Dissertation

submitted to the

Combined Faculty of Mathematics, Engineering and Natural Sciences

of Heidelberg University, Germany

for the degree of

Doctor of Natural Sciences

Put forward by

Heiko, Mager

born in: Villingen, Germany

Oral examination: 03.07.2025

Investigation of the ferroelectric and DC-conductive properties and their coupling in organic ferroelectrics

Referees:

Prof. Dr. ir. Martijn Kemerink

Prof. Dr. Peer Fischer

Zusammenfassung

In dieser Arbeit wurden die ferroelektrischen Eigenschaften und die Leitfähigkeit von einer Reihe von fluorinierten Cyclohexanverbindungen sowie von diversen organischen Ladungstransferkomplexen untersucht. Für erstere wurde ferroelektisches Schalten der Polarisation in dünnen Filmen mittels elektrischen Doppelwellenmessungen und Kapazitäts-Spannungs-Messungen für leitende und nicht-leitende Molekülderivate nachgewiesen. Die ferroelektrischen Parameter wurden durch analytische Modelle zur Schaltung der Polarisation gut beschrieben. Die Diskrepanz zwischen den gemessenen und den theoretischen Polarisationswerten in einigen dieser Materialien konnte durch die Modulation ihrer Leitfähigkeit durch die ferroelektrische Polarisation erklärt werden. Die Entdeckung einer signifikanten Leitfähigkeit war unerwartet, da die Materialien keine ausgedehntes π-Elektronen System besitzen, was gemeinhin als Voraussetzung für elektronischen Ladungstransport in organischen Materialien gesehen wird. Die Leitfähigkeit wurde elektrisch charakterisiert und der Einfluss der durch Rasterkraftmikroskopie und Röntgenstreuung beobachteten strukturellen supramolekularen Ausrichtung quantifiziert. Es wurden allgemeine Voraussetzungen formuliert, die von Materialien erfüllt werden müssen, um diese Art Leitfähigkeit zu zeigen und diese wurden durch experimentelle Untersuchungen an weiteren Materialien bestätigt. Ferroelektrizität wurde in zwei der Ladungstransferkomplexen nachgewiesen und die Temperaturabhängigkeit ihrer Leitfähigkeit deutet auf einen möglichen Übergang von der neutralen in die ionische Phase hin.

Abstract

In this work the ferroelectric and DC-conductive properties of a series of fluorinated cyclohexane compounds and organic charge transfer complexes were investigated. For the former, ferroelectric polarization switching in thin films was proven by electrical double wave and capacitance-voltage measurements in conducting and non-conducting molecular derivatives. The ferroic parameters were well described by analytical polarization switching models. A mismatch of measured and theoretical polarization values in some of the materials could be explained by the modulation of their conductivity by the ferroelectric polarization. The finding of a significant conductivity was unexpected as the materials do not contain an extended π-electron system that is commonly seen as a requirement for electronic charge transport in organics. The conductivity was characterized electrically and the influence of structural supramolecular alignment observed in atomic-force microscopy and X-ray scattering was quantified. A general set of requirements for materials to exhibit this kind of conductivity was formulated and confirmed by extension of the experimental investigation to further compounds. Furthermore, ferroelectricity was proven for two of the charge-transfer complexes and their temperature dependent conductivity suggested a neutral-ionic transition with temperature. In stark contrast to previous results, the materials displayed ferroelectric behavior on both sides of the transition that is sitting just below room temperature.

Table of Contents

1. Introduction

With the ever-increasing digitalization of society, including a growing demand for wearable electronics, and the strive for low-cost, energy-efficient alternatives to traditional devices mandated by the challenges of climate change, organic electronics have increasingly entered the academic spotlight. Compared to their inorganic counterparts, organic electronics are flexible, cheaper, often bio-compatible and solution processable. The latter allows for low energy manufacturing on large scales, via printing or coating techniques. Furthermore, chemical additions or modifications of their functional groups enable tailoring the properties of organic materials to the requirements of different applications. However, considerable challenges of varying nature remain, as material stability and performance commonly lack behind their inorganic peers. While in some cases organic electronics have already arrived in day-to-day life in the form of organic light emitting diodes (OLEDs), further applications like organic photovolatics (OPVs), organic field effect transistors (OFETs) and organic memory (e.g. ferroelectric random-access memory - FeRAM), occupy only a small niche of their respective markets. For now, it remains the task of scientific fundamental research to develop new materials and device structures as well as to improve upon already known ones, to enable a definitive push towards industrial applicability.

The base of many electronic applications is the material's ability to conduct charges, be it ionic, semiconducting or metallic transport. In organics, long range electronic charge transport is commonly mediated by an extended system of π-electrons, resulting from the sp^2-hybridization of conjugated carbon atoms. Materials with extended π-systems have been shown to exhibit excellent semiconductive[1,2] and even metallic properties[3,4] in one and two dimensions.[5–8] Charge transport in organic materials is often described as a thermally activated hopping process, owed to their inherent structural and energetic disorder.[9,10] Electronic conduction without π-conjugation is a mostly unexplored phenomenon, although there are reports in the fields of bioelectrics, where electron hopping in self-assembled monolayers of an a α-helical peptide was observed, presumably along its amide groups.[11,12] In another case, intermolecular band-like charge transport over several micrometers was demonstrated in supramolecular nanofibers of a synthetic peptide.[13] Exploration into mechanisms of π-system-less conduction and its discovery in new and old materials has the

potential to greatly expand our understanding of charge transport in organic materials. It may even provide pathways to existing or even entirely new applications.

One less talked about, but nevertheless important subgroup of organic electronics are ferroelectric materials. Their characteristic properties are a bi-stable dipolar polarization, which can be switched directionally between two states by applying a sufficiently strong external electric field, called the coercive field. Concomitantly, all ferroelectric materials are pyroelectric, meaning that local temperature differences give rise to a potential built up, while applying a bias yields a change in temperature across the material. In addition, ferroelectric materials are also piezoelectric, which means that stretching, compressing, shearing or other deformation of the materials results in a potential built up. As with pyroelectricity, the reverse effect is possible, i.e. deformation of the material under an external bias. Piezoelectric materials excel as actuators and transducers[14–16], pyroelectrics are used as infra-red detectors in thermal cameras, gas sensors and calorimeters[17–19], and ferroelectrics enable non-volatile memory devices like ferroelectric field effect transistors (FeFETs) and FeRAM.[20–22]

While the first discovered ferroelectric, Rochelle salt in 1921[23], is an organic material, the following years of research were dominated by inorganic materials like barium titanate (BTO) and lead zirconium titanate (PZT).[24–27] The majority of commercially available applications are based on these two materials. On the organic side, polyvinylidene fluoride (PVDF) on its own and as co-polymer together with trifluoroethylene (P(VDF-TrFE)) has garnered the attention of the scientific community over the years and has even found commercial use for its piezoelectric properties.[28–32] So far, no organic material has made the step towards commercialization solely for its ferroelectric properties. The reasons are similar to other fields of electronics: lower benchmark performance than their inorganic counterparts often coupled with stability and endurance issues. Due to their inherently less ordered morphology, organics may never achieve comparable key metrics. However, with their aforementioned advantages in other areas entirely new avenues for applications are opening up. Examples are wearable electronics[33–36] and implants[36], where flexibility, softness and bio-compatibility are often a prerequisite.

A promising aspect of (ferroelectric) organic materials is their potential for multifunctionality, combining a selection of conducting, optical, magnetic and ferroelectric properties in one material.[37–40] Obtaining a conductivity coupled to the ferroelectricity polarization of a

material is highly desirable for memory applications. A simple crossbar array structure is made of ferroelectric capacitors[41], with each memory bit represented by the two states of polarization. Reading out the memory state, however, means flipping the polarization and is therefore destructive, requiring a rewrite for read-only operations. A non-destructive readout is preferable, halving the number of required operations, therefore reducing stress and saving energy. This can be realized by either creating blends of ferroelectric and semiconducting materials[42,43] or using a ferroelectric material with a polarization-modulated conductivity.[39] The latter simplifies architecture and manufacturing considerably, while increasing memory density at the same time. Depending on the polarization direction, the magnitude of the readout current signals the on- or off-state which can therefore be probed non-destructively.

The fundamental base for device creation and improvement is the search for new ferroelectric materials and their in-depth characterization regarding structural and electrical properties, which often are intertwined. In this thesis, two different groups of organic materials are experimentally investigated, the fluorinated cyclohexane C3 amide (FCH-C3-A) and its molecular derivatives, as well as a series of charge-transfer-complexes (CTCs) based on the electron donating material NHTA-557 in combination with the electron acceptors tetracyanoethylene (TCNE), 7,7,8,8-tetracyanoquinodimethane (TCNQ) and 2,3,5,6-tetrafluoro-7,7,8,8-tetracyanoquinodimethane (F4TCNQ). Both material groups were probed (ferro)electrically by dielectric spectroscopy (DS), the double wave method (DWM)[44], capacitance-voltage (CV) sweeps, as well as structurally via X-ray diffraction (XRD) measurements, atomic force microscopy (AFM) and by light microscopy. FCH-C3-A and its derivatives were additionally investigated by a variety of current-voltage (I-V) measurements.

FCH-C3-A is a liquid crystalline material that has been shown to undergo supramolecular polarization in solution, forming a double helix structure[45]. It contains two separate dipolar groups, a fluorinated cyclohexane ring and an amide group. Supramolecular structures have been shown to increase the total dipole moment beyond the sum of the dipoles of their constituent molecules in a cooperative manner.[46–48] The presence of two separate dipolar moieties potentially offers the exciting possibility of two independently switchable ferroic sublattices. Indeed, in addition to finding evidence for simple ferroelectric polarization switching, the experimental data implies the existence of two partially independent sublattices. FCH-C3-A is one of the first materials to exhibit such a phenomenon, thus

demonstrating the versatility of organic electronics. The ferroelectric properties of FCH-C3-A were studied experimentally over an extensive parameter space to determine the influence of temperature, applied field strength and frequency on the ferroelectric parameters.

During the ferroelectric characterization, it became increasingly obvious that FCH-C3-A possessed the ability to conduct current beyond what could be explained by mere leakage. This was surprising, as according to its molecular structure and electronic band structure, the material was expected to be an insulator, missing the usual delocalized electrons of conjugated π-systems. Investigation of the conducting properties allowed the exclusion of trivial explanations like ionic impurities, electric double layer formation and degradation. The conductivity proved to be time stable, as well as both temperature- and electric field-activated. AFM imaging and grazing-incident wide-angle x-ray scattering (GIWAXS) showed a strong correlation between conductivity increase and the formation of supramolecular fibers, aligned along the electric field direction. Comparable measurements on molecular derivates with similar structure and with either a thioamide group in place of or without the amide group showed the necessity for dipolar activity and highlighted the importance of the amide group for the charge transport. Keeping these results in mind, a set of requirements for molecules to exhibit the same kind of conductivity was formulated. Further electrical and structural measurements on discotic tricarboxamides (BTAs, CTAs), and triphenylamines (TPAs), allowed the generalization of the approach to a wider variety of material classes.

Naturally, the interplay of ferroelectric polarization and conductivity in FCH-C3-A was investigated. Electrical measurements, making use of various voltage pulse shapes, revealed a modulation of the bulk conductivity via the ferroelectric polarization. This explained the non-saturating and abnormally high polarization values, as well as making FCH-C3-A a truly multifunctional material.

CTCs have been promising candidates for ferroelectric behavior for a long time.[49,50] Investigating a series of charge-transfer complexes with a fixed donor molecule and varying acceptor molecules was expected to provide insight into the dependence of ferroelectric parameters on the degree of charge transport. NHTA-557 was chosen as a donor for its tendency of forming CTCs with a variety of acceptors. Dielectric spectroscopy revealed singularities in the capacity-temperature behavior for combinations of NHTA-557 with each acceptor molecule, a strong indication of a phase transition.[51] However, this phase transition

was shown to not be a paraelectric to ferroelectric transition, as ferroelectric behavior was observed in DWM measurements in the temperature ranges above and below the transition temperature. In NHTA:TCNQ and NHTA:TCNE, the conductivity in the vicinity of the phase transition exhibited analogous behavior to other CTCs from literature, which was attributed to the presence of neutral-ionic domain walls and spin solitons.[52,53] The experimental ferroelectric data of NHTA:TCNQ and NHTA:TCNE was well described by analytical polarization switching models. A similar temperature dependence of conductivity and ferroelectricity of NHTA:TCNQ and NHTA:TCNE suggested that both properties are governed by the same microscopic processes. Films of all donor-acceptor combinations exhibited stability and reproducibility issues which were resolved by changing to single crystals. The relationship between the ferroelectric properties and the degree of charge transfer remained inconclusive.

This thesis is structured as follows. Chapter two introduces the theoretical background, which is thematically split in parts about conductivity in organic materials and ferroelectricity, followed by the showcase of measurement methods and materials in chapter three. In chapter four the conducting properties of non π-conjugated materials are investigated. Then follows the discussion of the ferroelectric properties of FCHs and the interplay of their ferroic and conducting properties in chapter five. In chapter six the ferroelectric and conducting properties of the CTCs are presented. Chapter seven gives a summary of the results of this work, how they fit into the wider context of organic electronics research, and possible future research opportunities.

2. Theoretical background

2.1 Organic (semi)conductors

In this subsection, the established theory of electronic conduction in organic materials is introduced, beginning with the recollection of *sp*-hybridization in carbon atoms. This is followed by an explanation of the typical mechanics of hopping transport occurring in organic materials. The subsection concludes with a brief description of charge injection from metal contacts into organic films and a subsequent explanation of space-charge limited current behavior.

2.1.1 Carbon *sp*-hybridization

Organic materials can be classified in two categories, small molecules and polymers. Polymers are chains of repeated molecular units, so called monomers, that can reach hundreds of nanometers in length. For both classes, the basic building blocks are carbon atoms. Depending on their configuration, i.e. number and nature of neighboring atoms, carbon atoms undergo orbital hybridization.[54] Here, a slight increase in energy of the 2*s* electrons to form molecular hybrid orbitals made from a linear combination of *s*- and *p*-orbitals results in a large gain of negative binding energy and therefore a reduction of the total energy when overlapping with the hybrid orbitals of the neighboring atoms. All hybrid orbitals are energetically degenerate. Depending on the number of *p*-orbitals participating in the hybrid orbital formation the process is called *sp*, sp^2 or sp^3-hybridization. The resulting bond geometries are linear, planar and tetrahedral, respectively. In materials with sp^3 hybridized carbon atoms, the formation of so called σ-bonds via the overlap of all four sp^3-orbitals with those of neighboring atoms is observed. The σ-bonds are strongly binding with highly localized electrons, resulting in sp^3-materials being insulators or wide-gap semiconductors, like for example diamond.[55]

In contrast, sp^2-hybridized carbon atoms enable the formation of a partially delocalized electron system. Here, the sp^2-hybrid orbitals form three highly stable planar σ-bonds, while the non-hybridized p_z-orbital stands orthogonally out of plane. Together with a neighboring p_z-orbital a so called π-bond is formed, which is much weaker bonding than the σ-bond. Figure 1 shows a schematic of sp^2-hybridization in ethene, displaying the two different bonds formed by the sp^2- and p_z-orbitals respectively. The π-orbitals split into an energetically lower bonding molecular orbital and an energetically higher antibonding molecular orbital. In the ground state, the electrons occupy the bonding orbital, leaving the antibonding one empty.

Therefore, they are commonly referred to as highest occupied molecular orbital (HOMO) and lowest unoccupied molecular orbital (LUMO) and can be understood as the organic equivalent to the valence and conduction band in inorganics. Their energy difference is accordingly called bandgap. The presence of multiple π-bonds leads to the formation of the HOMO and LUMO of the complete molecule and enables the delocalization of the participating electrons along the chain of carbon atoms. These systems, where carbon bonds are alternating between single σ- and double σ-π-bonds are called conjugated π-systems and are to this day the fundamental base of semiconductivity in organic materials. The prototypical π-system is benzene, and while its large band gap of 7 eV makes it an insulator, aromatic cycles are part of the majority of organic semiconductors.[56] Some of the most prominent examples are pentacene, poly(3-hexylthiophene-2,5-diyl) (P3HT) and C60 (also known as Buckminster fullerene or buckyball).[57–62] For graphene and carbon nanotubes, π-conjugation even enables (semi)metallic conduction.[5,8]

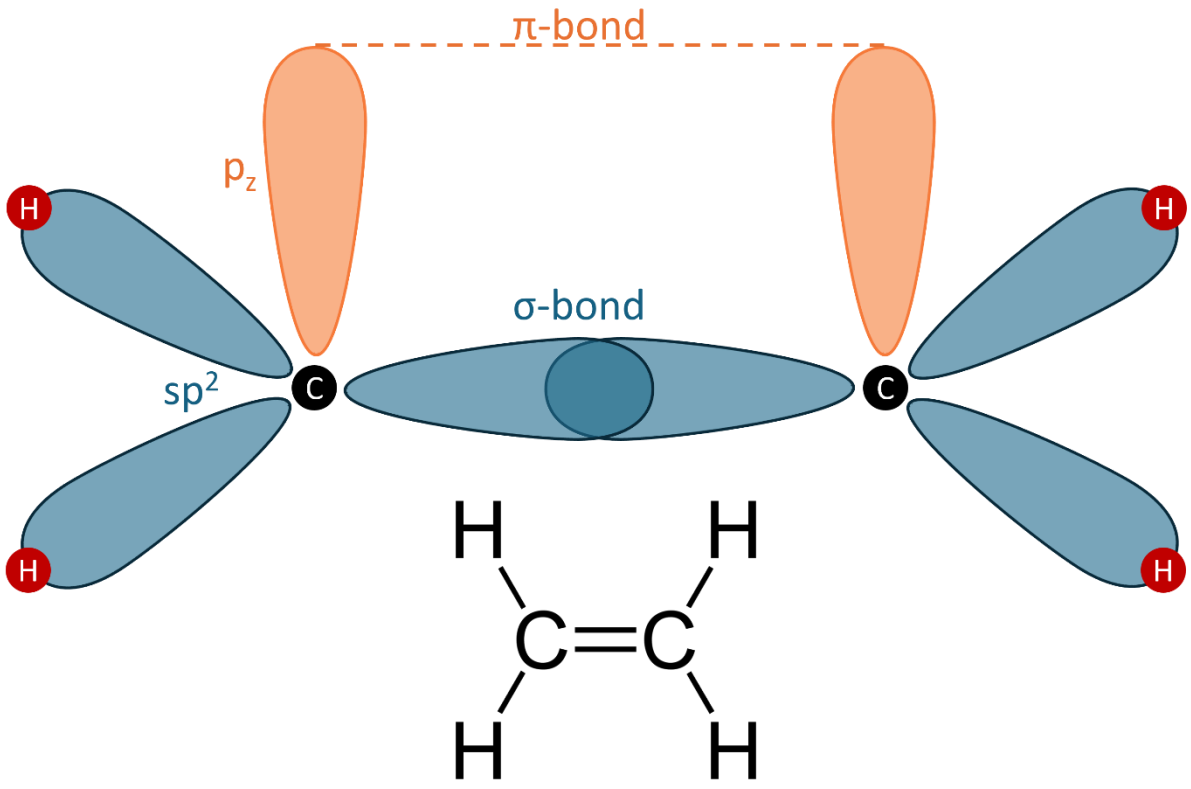

Figure 1. Schematic of *sp*^{2}-hybridization in ethene. The overlap of two *sp*^{2}-orbitals as well as the overlap of two p_z-orbitals results in the formation of σ- and π-bonds respectively.

2.1.2 Hopping transport – A question of disorder

Depending on the structural order and the electronic coupling between charge carrying sites (usually molecules or monomers) of the organic material in question, adequate models to describe the charge transport range from band-like to polaronic or disorder mediated hopping transport. Following M. Pope and G. M. Swenberg, a general understanding of charge transport can be derived from a one-electron Hamiltonian, that incorporates electronic and vibronic excitations, electron transfer and various types of disorder.[63] An in-depth theoretical overview is beyond the scope of this theses and the interested reader is forwarded to the original reference[63] or to the following reviews.[10,64] Instead, an overview is given of the different molecular electronic properties, how they determine the dominant charge transport mechanism, and what this means for the dependences of relevant physical parameters. Parts of this overview are based on the textbook "Electronic processes in organic semiconductors", by Köhler and Bässler.[65]

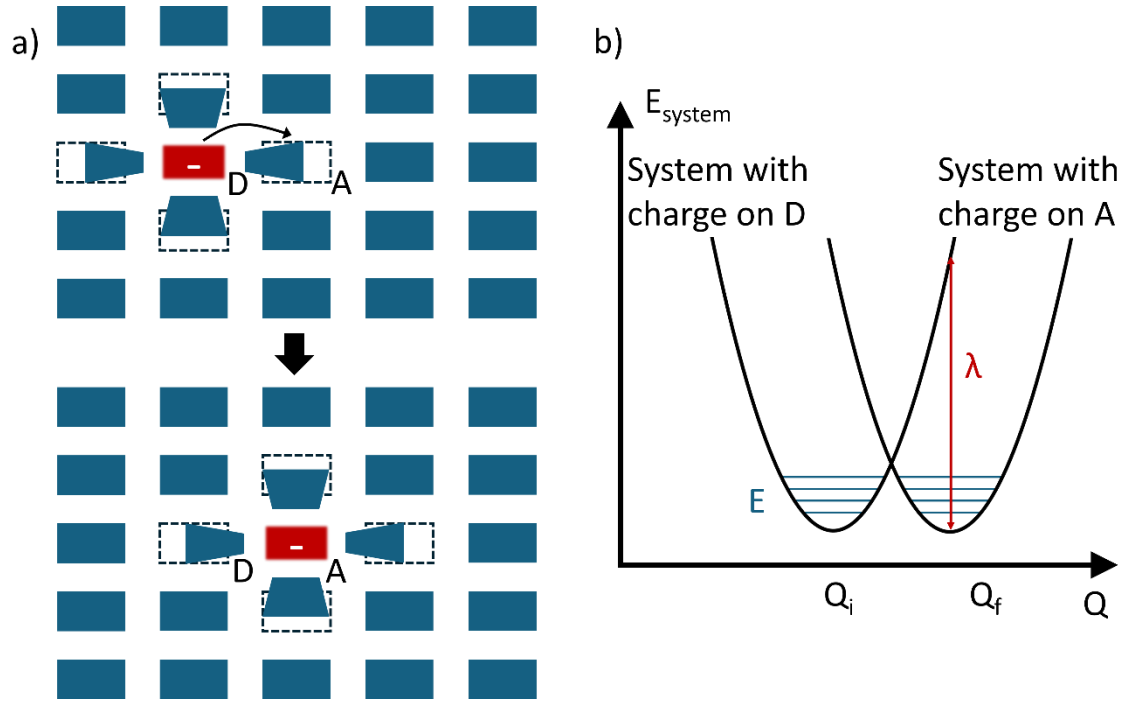

Figure 2. Schematic of Marcus hopping. a) shows the transfer of a negative polaronic charge from molecule D to molecule A and the resulting restructuring of the surrounding lattice. b) depicts the total energy of the system, which is comprised of the energy of each molecule D, A and of the surrounding lattice. Adapted from Köhler and Bässler, 2015[65]

Very pure organic single crystals, for example made from rubrene or naphtalene, have high structural order and strong electronic coupling and can therefore exhibit band-like charge transport akin to inorganic semiconductors.[66,67] The majority of investigated materials,

however, do not exhibit the structural order and long-range electronic coupling strength necessary for band-like transport. They are usually processed as amorphous films, with varying degrees of (poly)crystalline share. As a result of the reduced structural and energetic order, as well as the weaker electronic coupling compared to single crystals, the disorder terms in the one-electron Hamiltonian begin to dominate. One commonly differentiates two types of disorder, dynamic and static. The former describes the interaction between the electronic excitation and lattice vibrations, so called polaronic effects. They occur in organic materials because their dielectric constants are rather low (around 3) compared to inorganic semiconductors and therefore Coulomb interactions between electrons and the lattice are hardly screened. As a result, an additional (or missing) charge sitting on a site alters the surrounding lattice geometry which in turn changes the energy landscape felt by that charge. When propagating through the material, the charge is accompanied by a lattice distortion and this charge-phonon coupling is called a polaron.[68] Polaron propagation is commonly described by Marcus hopping[69], which is schematically depicted in Figure 2a). Here the transfer of a polaron from molecule D to a spatially adjacent molecule A is considered. For a negative charge, the system changes from the initial state of D^-+A to the final state of D+A^-. Marcus theory assumes a parabolic potential energy surface for the polaronic distortion, characterized by the reorganization energy λ. λ is the energetic cost that is connected with bringing the state D^-+A in geometric equilibrium with the state D+A^- or vice versa. It describes the energy that is required to readjust the internal molecular geometry and the surrounding lattice of initial and final polaron sites to the changed energy landscape. The reorganization energy depends on the overlap of the molecular orbitals of molecules A and D which additionally determines the crossing point of the potential energy surfaces. To hop from one molecule to another by thermal activation, the required energy is given by this crossing point, which can be determined by simple geometric reasoning to be $E_\mathrm{a} = \lambda/4$. Figure 2b) shows the energy of the total system, consisting of molecule D, A and their surroundings, in the initial state Q_i and final state Q_f. Following Holstein[70], the charge hopping rate is given by

$$R_{ET} = \frac{J^2}{\hbar}\sqrt{\frac{\pi}{2E_\mathrm{pol}kT}}\exp\left(-\frac{E_\mathrm{pol}}{2kT}\right) \quad (1)$$

where J is the transfer integral, $\hbar$ the reduced Planck's constant, E_pol the polaron activation energy that is equal to $\lambda/2$, k the Boltzmann constant and T the temperature. With the

Einstein relation $\mu = eD/kT$ an Arrhenius-type temperature dependence is obtained for the mobility in the three-dimensional case:

$$\mu = \frac{ea^2J^2}{6\hbar(kT)^{\frac{3}{2}}}\sqrt{\frac{\pi}{2E_{\mathrm{pol}}}}\exp\left(-\frac{E_{\mathrm{pol}}}{2kT}\right) \tag{2}$$

Here, e is the elemental charge, D the diffusion constant and a is the distance between sites. For realistic polaron activation energies, the $T^{-3/2}$ term only becomes relevant for temperatures above 600 K. A commonly used approach is to sum up the terms before the exponential into a temperature independent pre-factor mobility μ_0, which is only valid at low temperatures and simplifies equation 2 to

$$\mu = \mu_0 \exp\left(-\frac{E_{\mathrm{pol}}}{2kT}\right) \tag{3}$$

This leaves the static disorder term to be discussed. Static disorder describes the condition that in most organic semiconductor films not only the energy of individual carrier sites varies locally, but the distance between single sites as well. Consequently, the variation in intermolecular coupling is significant. Therefore, charge transport occurs as incoherent hopping, with the carries becoming temporary localized on the sites. The most prominent description of disorder mediated charge transport is the Gaussian disorder (GDM) model introduced by Bässler, which has been continuously extended over the years.[9] It assumes that charge carriers hop along a large variety of sites with energetic and inter-site spacing given by a Gaussian distribution. The energy levels of charge carrier sites are therefore distributed as

$$g(\epsilon) = \frac{1}{\sqrt{2\pi}\sigma}\exp\left(-\frac{(\epsilon-\epsilon_0)^2}{2\sigma^2}\right) \tag{4}$$

where ϵ is the energy of an individual site and the standard deviation σ determines the degree of disorder. Equation 4 is commonly referred to as Gaussian density of states (DOS). Compared to polaronic transport, disorder hopping occurs between two sites of different energies and therefore requires an asymmetric hopping rate. In case of a hop upwards in energy, thermal activation is required, implying a Boltzmann factor, while for downwards hops, energy is dissipated to the surrounding lattice. To account for the variation in electronic coupling strength by hopping site distance, an exponential exchange coupling rate can be

considered. These considerations where first taken into account by Miller and Abrahams in 1960[71] when they formulated the now commonly used Miller-Abrahams hopping rate:

$$w_{ij} = \nu_0 \exp(-2\gamma r_{ij}) \times \begin{cases} \exp\left(-\frac{\epsilon_j - \epsilon_i}{kT}\right), & \epsilon_j > \epsilon_i \\ 1, & \epsilon_j \leq \epsilon_i \end{cases} \quad (5)$$

Here ν_0 is an attempt frequency, usually comparable to typical phonon frequencies, γ is the inverse localization length of the carrier wavefunction, r_{ij} is the jump distance between sites i and j and ϵ is the site energy. A useful concept to understand how charge carries move through disordered materials is the so called effective transport energy.[72,73] In a low carrier density environment, the carriers are localized and occupy the tail states of the DOS. If one of these carriers is excited into a higher energy state by thermal activation, the local site distribution determines its probability to either relax back into its initial state or hop further away along suitable sites. The energy where the latter is the prominent effect is the transport energy E_T.

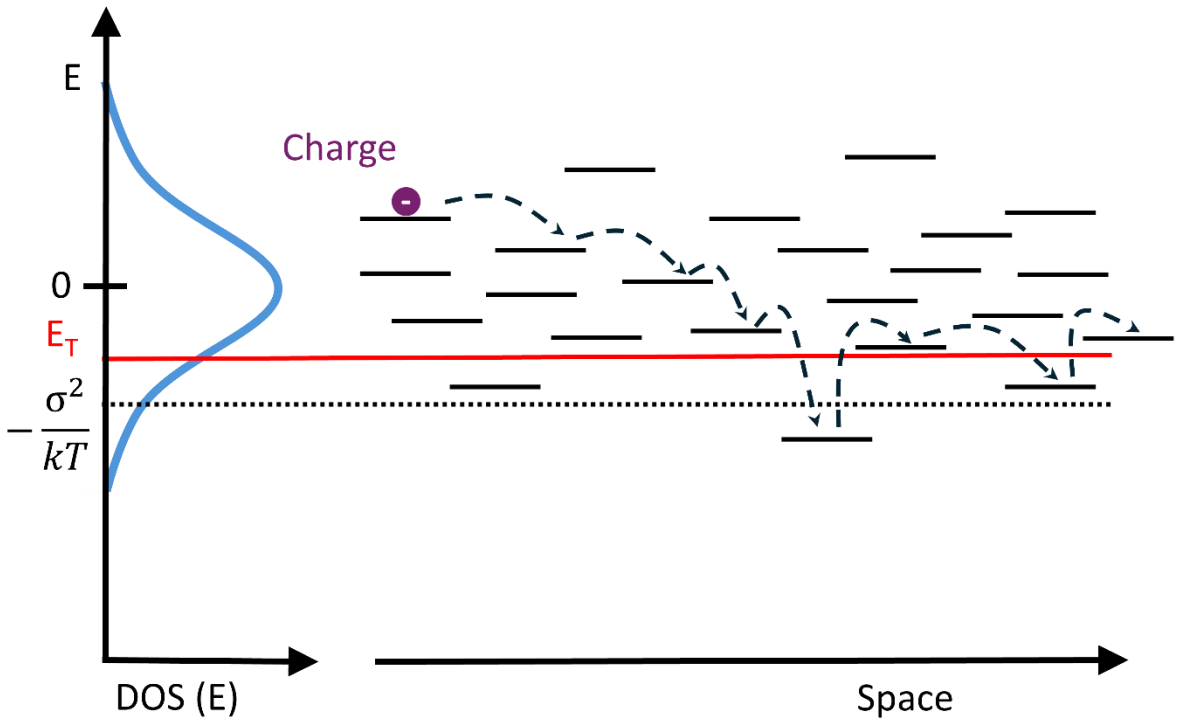

Figure 3. Schematic of a charge hopping in a Gaussian density over time and space after being generated at elevated energies. In the long time limit it will equilibrate at the equilibrium energy $\epsilon_\infty = -\sigma^2/kT$. The transport energy E_T is indicated in red.

A measure of the thermal activation required for carriers to reach the transport energy can be obtained by considering the density of occupied states (DOOS). As mentioned previously, the charge carriers are usually found in the tail end of the DOS. To see why, we can consider qualitatively what happens to several newly created carriers at random sites near the center of the DOS. To begin with, all carriers find abundant sites of lower energy in close vicinity, meaning their movement is dominated by downhill hops. After some time and reduction of the initial charge carrier energy, thermally activated upwards hops begin to appear, until a quasi-equilibrium between downward and upward jumps is found. The equilibrium energy $\epsilon_\infty = -\sigma^2/kT$ with respect to the center of the DOS is found as the statistically weighted average energy using the Gaussian DOS as weighing function in the limit of long timescales.[74,75] This equilibrium energy is the center of the DOOS, with has the same standard deviation and variance as the DOS. The average thermal activation energy for a charge carrier to become mobile is therefore the difference between transport and equilibrium energy.

As the equilibrium energy explicitly decreases (relative to the center of the DOS) with temperature, a simple Arrhenius picture for the temperature dependence of the mobility is insufficient and as a result the following relation is commonly used:

$$\mu = \mu_0 \exp\left(-C\left(\frac{\sigma}{kT}\right)^2\right) \tag{6}$$

Here C is a numerical coefficient that for pure disorder hoping reaches 0.44 and is lower in case of overlapping polaronic and disorder effects.[65] Equation 6 has been verified by numerical and analytical calculations.[74,75] Figure 3 shows a schematic of a carrier diffusing via hopping in a Gaussian DOS, with equilibrium and transport energy indicated. It has to be noted that before equilibrium is reached, the transport of multiple carriers is dispersive over time, as initial energy and the local energy landscape have a deciding influence on the carrier motion.

The question of whether a system exhibits polaronic, disorder or a combination of both kinds of charge transport is not easily answered and has been extensively discussed.[76,77] One reason is that the temperature dependence of the mobility is ambiguous as experimental data can often be fitted by both models, polaronic and disordered transport, following equations 3 and 6, respectively. Fishchuk *et al.* provided extensive theoretical considerations that

conclude with a critical temperature above which transport is of more polaronic nature and below which transport is mostly disorder mediated:[78]

$$T_c = C\frac{2\sigma^2}{kE_{pol}} \tag{7}$$

Here σ is the energetic disorder and $E_{pol} = \lambda/2$ the polaronic activation energy. For typical values of $\sigma = 80$ meV and $E_{pol} = 100$ meV the critical temperature is 650 K.

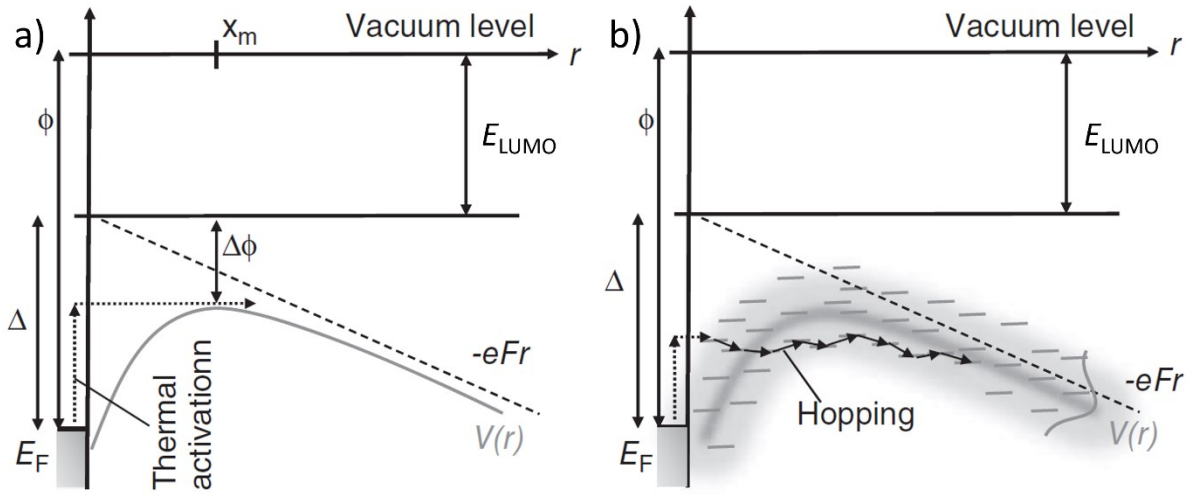

Figure 4. a) Energy landscape for the thermionic emission injection process for electrons. Carriers have to overcome the energy difference between work function ϕ and LUMO E_{LUMO}. The barrier is reduced by the image charge potential Δϕ and the potential of the applied external electric field. b) Energy landscape for the case of electron injection into a disordered organic field with a Gaussian DOS. Notice the softening of the injection barrier by the energetic disorder. Adapted from Köhler and Bässler (2015).[65]

2.1.3 Charge injection

For common electrical measurements, the organic materials are sandwiched between metal electrodes, from which charge carriers can be injected into the material. The intrinsic charge carrier concentration is negligibly small. This is because the energy gap between HOMO and LUMO is commonly above 2 eV resulting in a minor population of thermally excited carriers. Additionally, insufficient screening originating from average dielectric constants of 3-4 results in significant Coulombic binding energies of excitons (electron-hole pairs created by elevating an electron from HOMO to LUMO).[65] Therefore, charge carriers have to be injected externally from the contacts. The relevant physical parameters that govern charge injection are the work function of the electrode metal(s) and, depending on whether electron or hole transport is considered, the HOMO or LUMO of the organic material. The energy difference between

metal work function and relevant molecular orbital determines the magnitude of the barriers charge carriers must overcome. As a result, the conductive behavior of a device can vary significantly depending on the electrode material.

For inorganic semiconductors, injection-limited behavior is often described by thermionic emission.[79] Nevertheless, the thermionic emission model serves as an adequate basis to understand charge injection into organic (semi)conductors. Figure 4a) shows a schematic of the energy landscape at the contacts. The actual injection barrier is the potential difference between the work function of the metal and energy level of the relevant molecular orbital of the semiconductor, reduced by the applied electrostatic potential and the image charge potential $\Delta\phi$. For the latter, a charge placed near an equipotential surface (metal surface) creates a potential that can be described by the resulting dipole potential obtained by mirroring the original charge on the surface with inverted sign. With this, the effective injection barrier at distance r from the interface is given by

$$V(r) = (\Phi - E_{\mathrm{LUMO}}) - \frac{e^2}{16\pi\epsilon_0\epsilon_{\mathrm{r}} r} - eFr \tag{8}$$

Φ is the work function of the metal, E_{LUMO} the LUMO energy level, e the elemental charge, ϵ_{r} the dielectric constant and F the externally applied electric field. The maximum of the injection barrier is reached at the distance x_{m} from the interface. In the case of disordered organic materials however, the distance a carrier has to travel to overcome the injection barrier is unreasonably long under realistic operating conditions.[80] When dealing with organic conductors, the hopping mechanism of charge transport and its disordered nature must be kept in mind. Considering this, Arkhipov *et al.* developed an analytical model for charge injection into (Gaussian) disordered organics based on the ideas of Gartstein and Conwell.[80,81] They proposed that efficient transport away from the contact occurs if and only if the injected charge finds itself nearby sites of lower energy, as otherwise its tendency to recombine with its image charge takes precedence. The energy where the former occurs predominantly is again the transport energy introduced in section 2.1.2. As the analytical models are complex and an in-depth overview is beyond the scope of this thesis, the interested reader is referred to the previously mentioned articles as well as further work.[82,83] Figure 4b) schematically shows carrier injection into disordered organic materials, in contrast to the thermionic injection in Figure 4a). If the charge injection barrier is small enough or even vanishes

completely, carriers can be injected unobstructed, and the device conduction is completely determined by its bulk properties. This is usually referred to as ohmic contact and in the case of organic materials often results in space-charge limited behavior, as will be explained in the following subsection. Insight into the transition from injection-limited to bulk-limited behavior in case of disordered mediated bulk transport can be gained by comparing the energetic disorder and the injection barrier. The most energetically costly hops are roughly estimated on the order of twice the energetic disorder and hence a device changes from injection- to bulk-limited when the magnitude of the injection barrier drops below twice the energetic disorder. Unfortunately, the transition from injection-limited to ohmic contacts is not a discrete switch but happens continuously, meaning devices can exhibit a convolution of both injection regimes. As a result, a quantitative analysis of the respective contribution is not trivial and requires a careful evaluation of field- and temperature-dependencies.

2.1.4 Space charge limited current

In the case of ohmic injection, an infinite current through a device may seem possible. However, there are self-limiting effects, for highly conductive materials an equilibrium between carrier injection and extraction will be reached, while for less conductive materials the buildup of a space-charge potential from the injected carriers will ultimately compensate the applied potential. Organic materials generally are part of the latter group and are accordingly often described with space-charge limited current (SCLC) models. Originally introduced by Clement Child for thermionic emission in vacuum tubes, it was later adapted by Mott and Gurney to describe conduction in solids.[84,85] Combining Poisson's equation

$$-\frac{d^2\phi}{dx^2} = \frac{dF}{dx} = \frac{ne}{\epsilon_0 \epsilon_\mathrm{r}} \tag{9}$$

with the continuity equation

$$j = en\mu F - De\frac{\mathrm{d}n}{\mathrm{d}x} \tag{10}$$

and the Einstein relation

$$eD = kT\mu \tag{11}$$

gives the Mott-Gurney law:

$$j = \frac{9}{8}\mu\epsilon_0\epsilon_r\frac{V^2}{L^3} \tag{12}$$

Here ϕ is the electrostatic potential, n the charge carrier density, j the current density, V the applied bias and L the distance between injecting and extracting electrode. This derivation assumes unipolar charge transport, no intrinsic charge density, a field independent mobility and that carrier drift dominates. While the Mott-Gurney law is generally suitable for inorganic semiconductors, it does not universally fit all experiments, and the disordered nature of organic materials only amplifies these deviations.

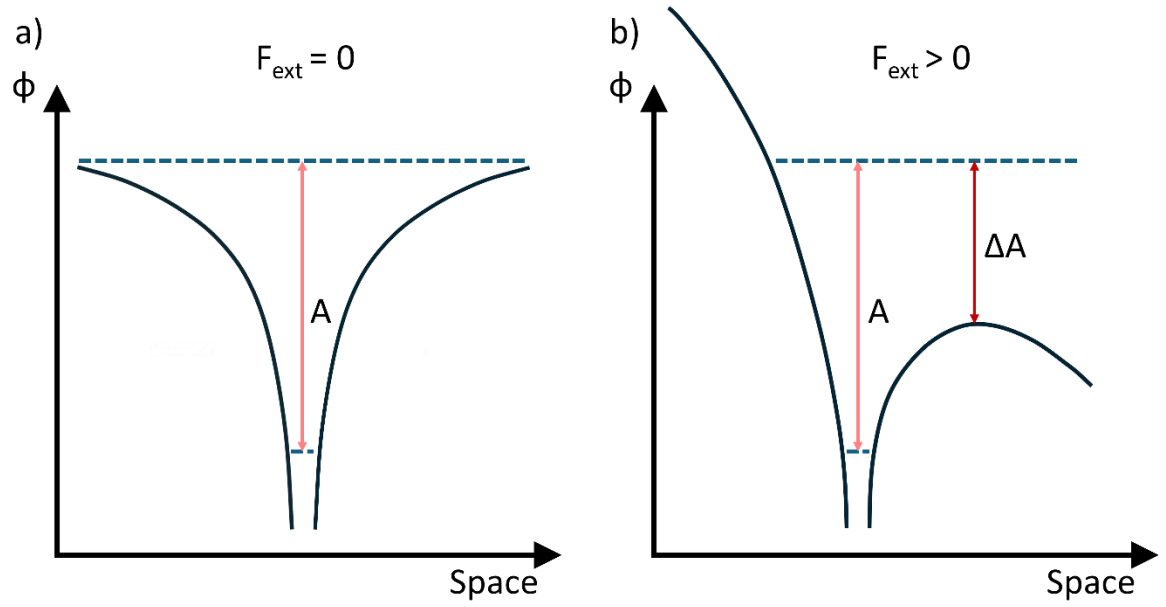

Figure 5. Schematic of a coulombic trap potential without a) and with b) an external electric field. As a result, a potential maximum in distance r_0 of the trap center is created and the trap depth reduced.

An important reason is the presence of charge traps in the conducting medium, which are not accounted for in the Mott-Gurney law. Traps are potential sinks in the energetic landscapes, from which a charge, once entered, cannot escape without obtaining a substantial amount of energy via thermal or potential means. A simple assumption for a trap density distribution in the case of electron transport is a single set of shallow traps sitting at an energy E_t below the LUMO.[86] The portion of free carriers θ is then given by:

$$\theta = \frac{n_f}{n_f + n_t} = \frac{N_{LUMO}}{N_t}\exp\left(-\frac{E_t}{kT}\right) \tag{13}$$

n_f and n_t are the free charge carrier and the trap density respectively, while N_f and N_t are the corresponding densities of states. An analog derivation to the Mott-Gurney-Law leads to

$$j = \frac{9}{8}\mu\epsilon_0\epsilon_\mathrm{r}\theta\frac{V^2}{L^3} \tag{14}$$

Mark and Helfrich developed an analytical model for the case of an exponential trap density distribution resulting in[87]

$$j \propto \frac{V^{l+1}}{L^{2l+1}} \tag{15}$$

For a Gaussian trap density multiple analytical approaches exist for the case of $n_f \ll n_t$, considering a field independent mobility and with different assumptions regarding trap depth.[88,89] However, to cover all charge densities and to include a possible field dependence of the mobility, numerical simulations are required.[90]

A simple way of introducing a field dependent mobility was proposed by Murgatroyd for the case of a constant trap level.[91] Following the work of Frenkel, he considered coulombic trapping of electrons in an external field. Figure 5 shows a schematic of the corresponding potential landscape.[92] The electron potential energy in distance r to a trap is the given by

$$U(r) = \frac{e^2}{4\pi\epsilon_0\epsilon_\mathrm{r}r} + eFr \tag{16}$$

It has a maximum at the distance

$$r_0 = \sqrt{\frac{e}{4\pi\epsilon_0\epsilon_\mathrm{r}F}} \tag{17}$$

of magnitude

$$U(r_0) = 2e\sqrt{\frac{eF}{4\pi\epsilon_0\epsilon_r}} = \alpha\sqrt{F} \tag{18}$$

Incorporating equation (18) into the trap density (13) leads to

$$\theta = \frac{n_f}{n_f + n_t} = \frac{N_\mathrm{LUMO}}{N_t}\exp\left(-\frac{E_t - \alpha\sqrt{F}}{kT}\right) \tag{19}$$

Calculating the current density for this carrier density is not possible analytically and it has to be approximated numerically, with the result given by

$$j = \frac{9}{8}\mu_0\epsilon_0\epsilon_\mathrm{r}\frac{V^2}{L^3}\exp\left(0.891\gamma\sqrt{\frac{V}{L}}\right) \tag{20}$$

Here, μ_0 is the zero-field mobility and the parameter γ describes the field dependence of the mobility. Equation (20) is commonly fitted to current-voltage characteristics measured on OSCs to obtain the zero-field mobility.[93]

2.2 Ferroelectric materials

This section introduces the physical properties of ferroelectric materials, including relevant parameters and models commonly used to describe them. A short recollection of the different types of electrically active materials is followed by the phenomenological description of ferroelectricity after Landau. Afterwards, an overview of the characteristic macroscopic ferroelectric parameters and their dependencies on experimental conditions is given. This is followed by a collection of models describing the macroscopic switching which derived from microscopic considerations. The section concludes with a short paragraph on polarization decay and an introduction to (semi)conducting ferroelectrics and their special properties.

2.2.1 Electrical properties of solids

On a superficial level, solid materials can be divided into two classes regarding their electrical properties. Those who conduct a current under bias application are called conductors while those that do not are called insulators. The difference is caused by the behavior of the valence electrons surrounding the atomic nuclei, in conductors they are predominantly delocalized and able to freely move through the bulk of the material while in insulators they are more tightly bound to their respective nuclei. This does not mean, however, that insulators are completely unaffected by an externally applied electric field. Without an external field, the electron clouds of insulators are usually symmetrically distributed around the atomic cores to minimize the total energy. Application of a constant external electric field breaks this equilibrium state as it slightly displaces the electron clouds from their equilibrium positions, leading to a small macroscopic polarization over the material with electric polarization commonly defined as volumetric charge density. These materials are called dielectrics and their polarization changes linearly with the applied electrical field as $P = \chi_e \epsilon_0 F$. The dielectric susceptibility $\chi_e = (\epsilon_r - 1)$ is a measure of the degree to which a material reacts to external electric fields. The common polarization versus field dependence is shown in Figure 6a).

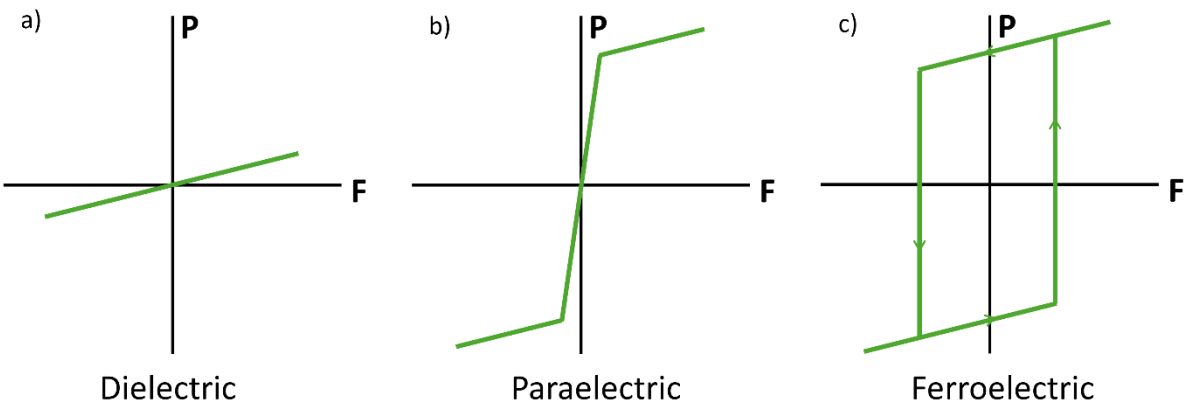

Figure 6. Polarization as a function of the applied electric field for dielectric, paraelectric and ferroelectric materials.

There are, however, materials, that have an inherent dipole moment originating from an asymmetric charge distribution, owed to the variations in the electronegativity of their constituent atoms. A simple example is the molecule H2O. In the solid state these materials are usually arranged in a way that neutralizes the dipole moment over the bulk of the material. If, under the influence of an external field, the constituent atoms or the molecular moiety they are part of, are displaced, a macroscopic bulk polarization is created. This is a result of the microscopic ordering of dipolar units. Once the external electric field is removed, the material returns to its disordered neutral state, the dipolar order disappears, and the polarization vanishes. The polarized state is energetically unfavorable and in absence of an external field the materials belong to a centrosymmetric space-group. These materials are called paraelectric.

If the material belongs to a non-centrosymmetric space-group at zero-field, stays stable after removing the external field and even remains so under fields of opposite sign up until a certain threshold field, the material is called ferroelectric. Theoretically ferroelectric materials should exhibit spontaneous polarization without the need for an external field, owed to their energetic ground state, however this is rarely observed in real materials because of defects and depolarization fields. Figure 6b) and c) demonstrate the polarization versus field behavior of paraelectric and ferroelectric materials respectively. The designation is inspired by ferro- and paramagnetism, however the “ferro” part tends to be misleading as ferroelectrics have no inherent connection to iron (lat. ferrum). Most ferroelectric materials exhibit a phase transition at a critical temperature T_0, where they lose their polarization and enter a

paraelectric phase. Analogous to magnetism, the order parameter is the (here electric) polarization and the corresponding dielectric susceptibility is described by the Curie-Weiss law:

$$\chi = \frac{1}{a_0(T - T_0)} \tag{21}$$

a_0 is a factor originating from the Landau-Devonshire theory of ferroelectrics that is discussed in the next subsection and its inverse is often called the Curie or Weiß temperature. The ferro- to paraelectric phase transition is accompanied by symmetry breaking, with the material changing its structure to one of the non-centrosymmetric crystallographic point groups. Not all materials in this point group however are also ferroelectric, some of them exhibit only piezoelectricity and some piezo- and pyroelectricity. Piezoelectricity describes a material's property to build up a bulk potential when subjected to mechanical stress. The effect is reversible, application of an external electric field leads to a deformation of the material. Pyroelectric materials exhibit a potential built-up when heated or cooled and application of an external field results in a temperature change. All pyroelectric materials are piezoelectric, and all ferroelectric materials are also pyroelectric. However, the reverse case does not hold true. A detailed description of the theory behind piezo- and pyroelectricity will be omitted, as they are beyond the scope of this thesis.

2.2.2 Landau-Devonshire-Theory

The ability of ferroic materials to switch between two stable polarization states has its origin in the existence of two equivalent global energy minima. Based on the work of Landau on phase transitions[94,95], Devonshire introduced a phenomenological description of the thermodynamic properties of ferroelectrics.[96–98] Considering the Gibbs free energy of a ferroelectric material near the phase transition, and, neglecting any strain effects, the free energy density can be expanded in terms of the polarization P:

$$G_{\mathrm{P}} = \frac{1}{2}\alpha P^2 + \frac{1}{4}\beta P^4 + \frac{1}{6}\gamma P^6 - FP \tag{22}$$

Here, α β and γ are parameters describing the nature of the phase transition and F is the external electric field. Figure 7 shows the Gibbs free energy of ferroelectric materials depending on the polarization, above and below the critical temperature. The equilibrium

state is found by minimization of the free energy density $\delta G_P/\delta P = 0$, which gives the field as a function of polarization:

$$F = \alpha P + \beta P^3 + \gamma P^5 \tag{23}$$

The linear electric susceptibility is given by $\chi^{-1} = \delta F/\delta P$ and in the paraelectric state above the transition temperature T_0, where $P = 0$, the Curie-Weiß law is recovered:

$$\chi = \frac{1}{\alpha} = \frac{1}{a_0(T - T_0)} \tag{24}$$

Here $\alpha = a_0(T - T_0)$ is an assumption from Landau theory with a positive coefficient a_0. The nature of the transition to the ferroelectric phase is given by the parameter β. If $\beta < 0$ and $\gamma > 0$, the transition is of first order and the susceptibility as well as the polarization change discontinuously. Here, only the simpler case of the continuous phase transition with $\beta > 0$ is considered, the interested reader is referred to other work for a description of first order transitions.[98,99] Below the transition temperature in equilibrium at zero field and only considering terms up to fourth order, the spontaneous polarization is found

$$P_0 = \pm\sqrt{\frac{a_0}{\beta}(T_0 - T)} \tag{25}$$

and $\chi = 1/\big(2a_0(T_0 - T)\big)$ for the electric susceptibility. With equation 22 the energetic barrier between the polarization states $w_\mathrm{b} = \alpha^2/(4\beta)$ is obtained, that is generally far higher than kT and therefore not easily overcome by thermal fluctuations alone. The corresponding electrical field needed to overcome this barrier, which is called the intrinsic coercive field, is given by $F_\mathrm{c,i} = \alpha\sqrt{\alpha/\beta}/4$. In this idealized case, the dipoles of the material are all part of one single domain and flip at the same time, which is not realistic for real materials. Here, polarization switching occurs extrinsically, meaning that there are many different domains that are switched consecutively, often via nucleation followed by domain growth. This is discussed more in-depth in a later section.

2.2.3 Ferroelectric polarization

The trademark of ferroelectric materials is the polarization versus field hysteresis loop, that is schematically shown in Figure 6c). Some of the characteristic ferroic parameters can be extracted from hysteresis loops. A completely depolarized ferroelectric is considered as starting point, which is a common case for untreated ferroic materials as spontaneous

polarization tends to be suppressed by defects and depolarization mechanics. Without an external field, the dipoles are randomly distributed in a way that the total polarization of the bulk is zero. Applying a steadily increasing external field starts pushing the system, in the energetic picture of Figure 7a), up the potential hill between the polarization states. The dipoles remain unaligned, however, until a field of sufficient strength is reached. This field is called the coercive field. Approaching its vicinity, single dipolar domains begin to flip until, at the coercive field F_C, all remaining domains align into one polarization state. Compared to the intrinsic coercive field introduced earlier for ideal ferroelectrics, the coercive field in real materials is drastically reduced and depends on the exact experimental conditions.

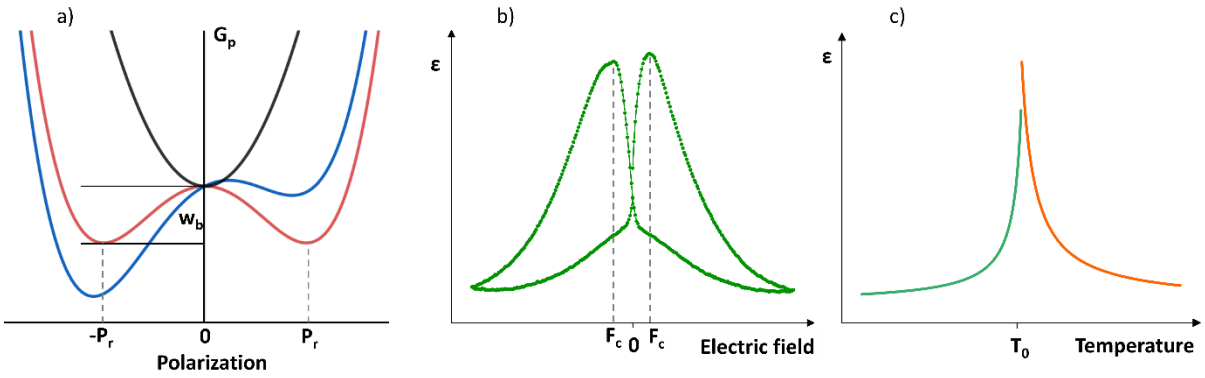

Figure 7. a) Gibbs free energy depending on the polarization of a paraelectric (black), a ferroelectric (red) and a ferroelectric under an applied external field (blue). The remnant polarization P_r and the energy barrier w_b are indicated. b) Permittivity of a ferroelectric depending on the applied electric field. The heightened dipolar sensitivity around the coercive field results in the characteristic "butterfly" shape. c) The dielectric permittivity around the ferro- to paraelectric phase transition temperature usually follows the Curie-Weiß law, here schematically shown for a second order transition. It must be noted that experimental data can deviate significantly from this schematic.

Temperature, field sweep rate, material morphology and device structure all influence the coercive field value, preventing it from being a universal material characteristic.[100,101] Comparing coercive fields of different ferroic materials is therefore only sensible within limits. Beyond the coercive field, once all dipoles are flipped, the polarization growth saturates and the polarization value in this regime is called the saturation polarization P_{sat}. The saturation of the polarization is an important sanity check for proper ferroelectric behavior. If the polarization keeps increasing with applied field strength to values far beyond what theoretical calculations of the dipolar density of the material predict, then the apparent polarization cannot be of purely ferroic origin. Decreasing the field towards zero typically leads to a slight

decrease in polarization for real materials, as depolarization effects switch back some of the dipoles. The remaining polarization at zero field is called the remnant polarization P_r. When reaching the coercive field of opposite polarity, all dipoles reverse their alignment, and the material enters the state of opposite polarization.

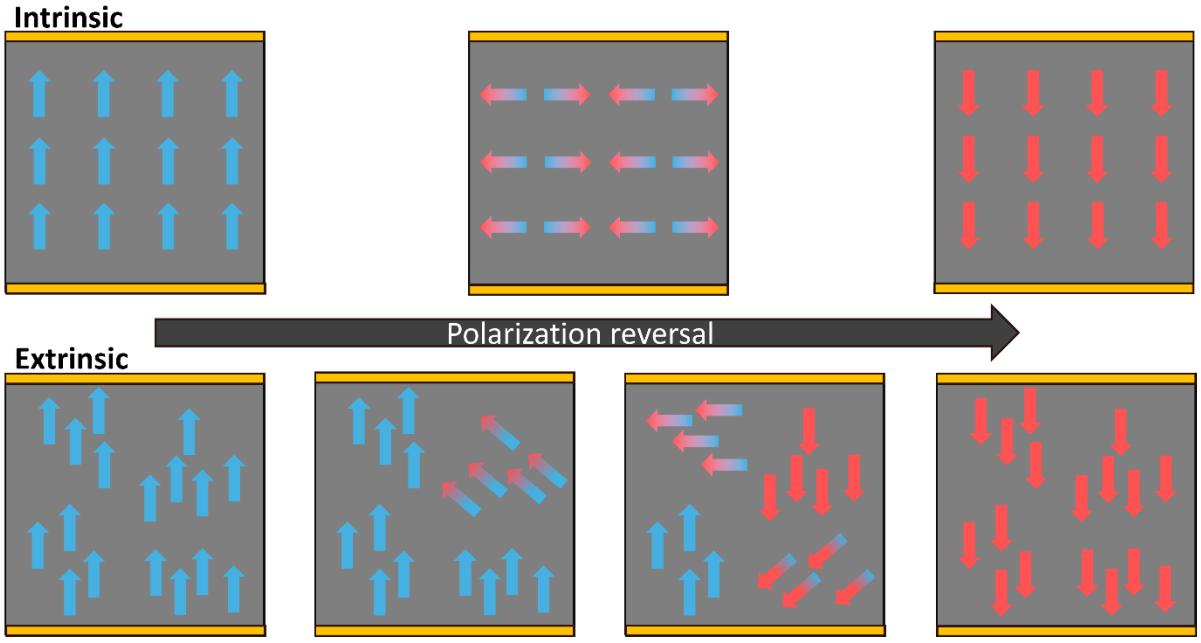

Figure 8. Comparison of intrinsic (top) and extrinsic (bottom) polarization switching in a ferroelectric capacitor. The arrows denote dipoles and their orientation. It has to be noted that in the limit of fields far beyond the coercive field, the time scales are vastly different, with intrinsic switching happening instantaneously and extrinsic switching orders of magnitude slower. For the extrinsic case the switching of single domains (a group of dipoles) occurs successively.

While in idealized ferroelectrics the polarization reversal at the coercive field occurs in a step-like fashion, real materials generally exhibit sloped flanks for their hysteresis loops, due to domain formation and nucleation processes. Figure 8 schematically shows the intrinsic (top) and extrinsic (bot) polarization reversal process. For the former, all dipoles switch at the same time, forming one single domain. In the latter, polarization reversal is a nucleation-driven process, where the flipping of a single domain results in consecutive switching of nearby domains over time. The timescales between these two processes vary greatly, as intrinsic switching is magnitudes quicker than extrinsic switching. This holds only true for fields far beyond the coercive field, which for intrinsic materials is seldom accessible in experiments.

The dipolar behavior in ferroic materials additionally results in a strong field dependence of the dielectric permittivity in proximity of the coercive field. Here, the dipolar ordering is highly

unstable and therefore very sensitive to even small external perturbations. Figure 7b) shows a common electric permittivity versus field curve of ferroic materials, with peaks at the coercive field in switching sweep directions. Passing the coercive field on the way back to zero field does not result in an increase of permittivity, as the dipoles are already in a stable configuration. The dipoles probed in these measurements are those that can be reversibly switched and their portion of the total polarization is commonly small. Integration of the CV-loops yields a polarization hysteresis loops for the reversible polarization.[102] Because of the shape resembling the wings of a butterfly, CV-curves are often called butterfly loops. Polarization hysteresis loops, butterfly loops and Curie-Weiß behavior of the dielectric susceptibility/permittivity are the electrically measurable proof that a material is a ferroelectric. The experimental methodology is presented later in the method section.

2.2.4 Analytical description of polarization switching

This subsection introduces different approaches to describe field dependence and kinetics of ferroelectric polarization reversal.

Kolmogorov-Avrami-Ishibashi (KAI) model

Based on the work of Kolmogorov and Avrami on crystallization theory, Ishibashi and coworkers developed a theoretical model to describe ferroelectric domain switching for ferroic single crystals.[103–105] They assumed random nucleation followed by domain growth at constant velocity under a constant applied electric field, obtaining the following equation for the polarization change with time:

$$\Delta P(t) = 2P_{\mathrm{s}}\left(1 - \exp\left(-\left(\frac{t}{\tau}\right)^{d}\right)\right) \tag{26}$$

Here τ is the characteristic switching time proportional to the inverse domain wall propagation velocity and d a dimensionality factor. The latter is given by the dimension of the domain wall propagation ($d = 1,\ 2,\ 3$), if nucleation is instantaneous at $t = 0$ and from there on domain wall propagation dominates. For a constant nucleation rate, d is given by the dimensionality of domain wall propagation reduced by one. In further work, the KAI model was extended to include dependence on the frequency of the probing signal:[106,107]

$$F_{\mathrm{C}} \propto f^{\frac{d}{\alpha}} \tag{27}$$

α is a geometric factor that is around 6 for sinusoidal and triangular waves. This is needed as for high sweeping frequencies, nucleation and domain wall growth cannot follow the changing field anymore. The KAI model and its extension are well-suited for single crystals and ordered materials where polarization switching is governed by domain wall growth. It tends to struggle with more disordered materials, which organic ferroelectrics often are.[108]

Du-Chen-Model

In a different approach, Du and Chen declared the nucleation rate as the limiting factor for polarization switching instead of domain wall propagation speed.[109] They assumed that at low fields, the domain walls are immobilized by a potential well until a nucleus of sufficient size has formed, with the formation time weighted by a Boltzmann factor. As soon as the nucleus is formed, domain wall movement occurs in a fast manner. The resulting dependence of the coercive field is given by:

$$F_C(f,T) = B'/\sqrt{kT \cdot \ln(f_0/f)} \tag{28}$$

Here B' is typically used as an empirical fitting parameter that includes the domain wall energy, the binding energy between domain wall and structural defects as well as the polarization change effected by the passing of the domain wall. f_0 is the frequency above which the nucleation rate is no longer the limiting factor. Together with the frequency dependence resulting from the nucleation rate, a temperature dependence is introduced, describing the increasing probability of critical nucleus formation with temperature. The Du-Chen model has been shown to accurately fit frequency dependence of the coercive field in inorganic and organic thin-film polycrystalline ferroelectrics.[108,110]

Thermally activated nucleation limited switching (TA-NLS)

Based on the KAI model and the Landau-Devonshire theory introduced earlier, Vopsaroiu and colleagues developed a nucleation driven polarization switching model, that not only considered thermally activated nucleation, but also included the influence of the externally applied electrical field as well as the depolarization field (see section 2.2.6) on the probability of nucleus formation.[111,112] Furthermore, they assumed a randomly distributed, fixed number of nucleation sites existing in the bulk at any time. Once the polarization reversal at one site reaches a critical volume V^*, the domain begins to expand rapidly and consumes the other nucleation sites until the bulk polarization is reversed. The time limiting step is therefore the

polarization rate of a single site to reach critical volume and not the nuclei expansion or formation rate. This time dependence is described by a non-equilibrium statistical model and solved in terms of a Pauli master equation approach. The resulting polarization dependence on time is equal to the one from the KAI model in equation 26 with $d = 1$. For the switching time t_{sw}, which is the time it takes for one nucleation site to reach the critical volume, they obtained

$$t_{\mathrm{sw}}(F,T) = \frac{1}{\nu_0}\exp\left(\frac{(w_{\mathrm{b}} - P_{\mathrm{s}}F)V^*}{k_{\mathrm{b}}T}\right) \tag{29}$$

from which the temperature and frequency dependence of the coercive field can be derived:

$$F_{\mathrm{C}}(f,T) = \frac{w_{\mathrm{b}}}{P_{\mathrm{s}}} - \frac{k_{\mathrm{b}}T\ln\left(\frac{\nu_0}{\ln(2)\,f}\right)}{V^*P_{\mathrm{s}}} \tag{30}$$

Here, ν_0 is an attempt frequency, usually akin to typical phonon frequencies of the material and w_{b} corresponds to the energy barrier per unit volume given by Landau-Devonshire theory. The first term therefore represents the intrinsic coercive field and the second term the reduction by the thermally activated nucleation process. Note that the assumptions made by Vopsaroiu *et al*. are similar to those made by Du and Chen, but the resulting frequency dependence is different. The TA-NLS model has been show to correctly describe switching kinetics and coercive field dependency in thin films of inorganic and organic ferroelectric materials.[100,112] Cornelissen *et al*. combined the TA-NLS model with the well-known, semiempirical Merz law for the switching time $t_{\mathrm{sw}} = t_\infty \exp(F_{\mathrm{a}}/F)$ and introduced a field dependence of the critical nucleation volume $V^* \propto 1/F$, combining the macroscopically observed Merz law with the microscopic process of nucleation.[113,114]

2.2.5 Preisach distribution

A conceptually important model to describe microscopic polarization switching is the Preisach model, originally developed for magnetic hysteresis loops, it has been shown to be valid for ferroelectrics as well.[115–118] The foundation of the model is the division of the ferroelectric bulk into single parts, called hysterons, which in principle are equivalent to dipolar domains. Each of these hysterons has its own ideal polarization hysteresis loop, characterized by certain up- and down-switching field values (denoted as U and V in the following), as shown in Figure 9a), that result from the local energetic landscape of the hysteron. This can be understood as

every hysteron having its own Landau-Devonshire double well potential, with many of those being asymmetric. The distribution of the hysterons' up- and down-switching fields is often assumed to be of Gaussian shape around the macroscopic coercive field, as depicted in Figure 9b), but can vary significantly for organic materials, depending on morphology. The summation over the polarization of all hysterons yields the macroscopic polarization. An average coercive field can be obtained by $F_c = \frac{U-V}{\sqrt{2}}$. This average coercive field, together with an "imprint" field $F_i = \frac{U+V}{\sqrt{2}}$ that describes the deviation from the former, can be used as an alternative description of the hysteron properties and corresponds to a coordinate transformation of U and V, as shown in Figure 9b). Urbanavičiūtė *et al*. unified the Preisach model and the TA-NLS model, obtaining a comprehensive theory to describe polarization switching in disordered organic ferroelectrics.[118] Every hysteron can be described in terms of the TA-NLS model with its own critical volume and corresponding switching time.

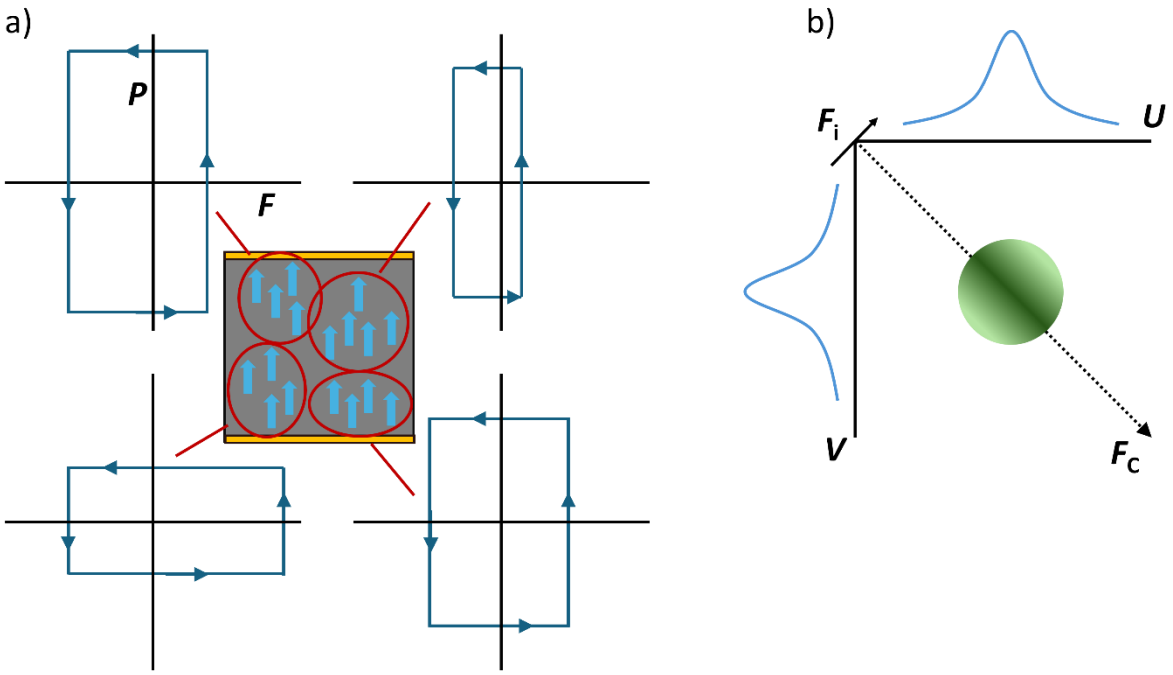

Figure 9. a) shows a schematic depiction of single hysterons (circled in red) and their corresponding polarization hysteresis loops that summed up yield the macroscopic hysteresis loop. b) depicts the gaussian distribution of the hysterons' up- (U) and down-switching fields (V) and the resulting distribution after coordinate transformation to the average coercive field F_C and the "imprint" field F_i.

Their framework explains the dispersive switching kinetics observed in various ferroelectric materials, which can be traced back to a distribution of hysteron switching times. For the investigated materials, the Preisach model gives a physical explanation for partial switching,

where even fields below the coercive field yield a finite polarization change. Additionally, the slope of the global hysteresis curve is determined by the width of the material's Preisach distribution, meaning for intrinsic switching the distribution is delta-function like.

2.2.6 Depolarization

A key parameter for ferroelectric materials considered for applications is the stability of the polarization state, over time and against thermal variations. The parameter describing the stability is the polarization retention, a measure of how much of the original remnant polarization remains after a certain amount of time has passed. Polarization retention is especially important for ferroelectric memory devices, where it determines the data storage time and commercial viability requires at least 10 years of storage time. As seen in the previous section, polarization switching is induced by thermally activated nucleation, and in absence of an external electric field, the polarization of a bulk material results in bound surface charges that give rise to a depolarization field of opposite sign, as shown in Figure 10a). As it is a surface effect, depolarization is especially problematic in thin films, while larger single crystals remain largely unaffected.[119,120] The strength of the depolarization field depends on the remnant polarization and the dielectric screening properties of the material, i.e. its dielectric permittivity, as $F_{\mathrm{Depol}} = -\frac{P_{\mathrm{r}}}{\epsilon_0 \epsilon_{\mathrm{r}}}$.

If not compensated for in some way, e.g. by the external field as shown in Figure 10b), the depolarization field leads to a rapid loss of polarization in the material. The state of full depolarization is reached once the dipoles are completely randomized again. In real devices, the ferroelectric is usually surrounded by metal electrodes and the charges on these can compensate the depolarization field as depicted in Figure 10c). However, dead layers, film inhomogeneities at the interfaces and a finite screening range diminish the compensation. This yields a finite depolarization field with a strength that is a fraction of the uncompensated one, as shown in Figure 10 d). A complete analytical description of polarization retention does not exist so far and can hardly be expected to fit the wide variety of organic ferroelectric materials with their different switching mechanisms. Experimental observations show dependencies in the form of a power law

$$P(t) \propto t^{-n} \tag{31}$$

or in log-linear form as

$$P(t) = P_{t_0} - m \log(t/t_0) \tag{32}$$

for timescales shorter than 100 seconds.[121–124] P_{t_0} is the polarization at t_0, a characteristic timestep, at which the log-linear behavior begins. For polarization decay in the long-time limit commonly a stretched exponential decay is observed:[124–127]

$$P(t) = P_0 \exp\left(-\left(\frac{t}{\tau}\right)^{\gamma}\right) \tag{33}$$

Here, P_0 is the polarization at $t = 0$, τ the characteristic decay time and γ the stretching exponent. A stretched exponential decay is often used in a phenomenological manner to describe disordered systems with a wide relaxation time distribution. The depolarization process is often exponentially magnified with increasing temperature as described by an Arrhenius law:[126]

$$\tau = \tau_0 \exp\left(\frac{E_a}{kT}\right) \tag{34}$$

Here, τ_0 is the decay time at infinite temperatures, equivalent to the reciprocal of the attempt frequency from equation 29 and E_a is the depolarization energy, typically on the order of 1 eV. Kinetic Monte Carlo simulations of molecular ferroelectrics showed that thermally activated depolarization begins at defects in the bulk of the material, suggesting that depolarization can be significantly reduced by improving film homogeneity.[128]

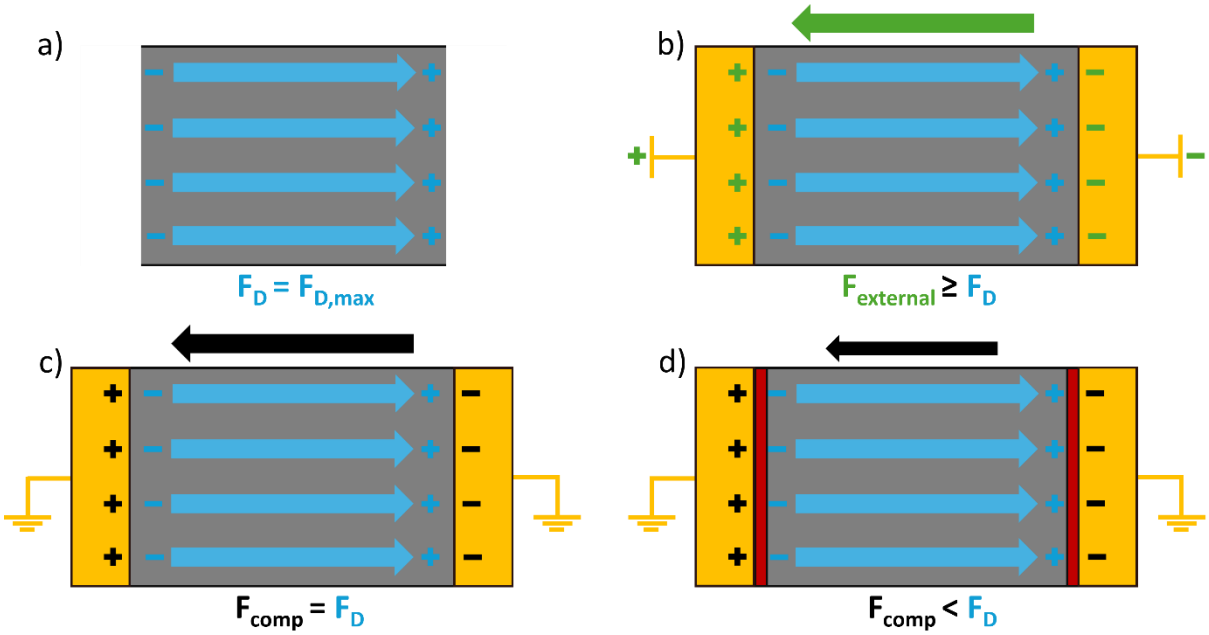

Figure 10. Schematic depiction of the depolarization field and possible screening via charge accumulation on metal electrodes. In a) for a theoretical free standing polarized ferroelectric film. b) Shows a ferroelectric between metal electrodes with an applied electrical field larger than the coercive field of the material. c) shows the case for grounded electrodes in the case of perfect ideal screening. d) depicts a more realistic case, where dead layers, indicated in red, and imperfect metal films result in a reduced screening of the depolarization field.

2.2.7 (Semi)conducting ferroelectrics and memory cells

Conducting properties of ferroic materials have been rarely investigated, as they are usually seen as detrimental to the ferroelectric properties and therefore, insulating materials are strongly preferred. Consequently, research in this area prominently focuses either on leakage currents and how to reduce them, or on conduction along domain walls in inorganic materials.[129–132] However, there are good reasons to develop (organic) materials that are ferroelectric as well as conducting, especially if a coupling between both properties exists. This will become clear after introducing the working principles of common ferroic memory devices, the ferroelectric field effect transistor (FeFET), the ferroelectric capacitor and ferroelectric diodes. In all of these, the memory function is enabled by the bistable, switchable polarization of ferroelectric materials, where the polarization states correspond to either the on- (1) or off-state (0).

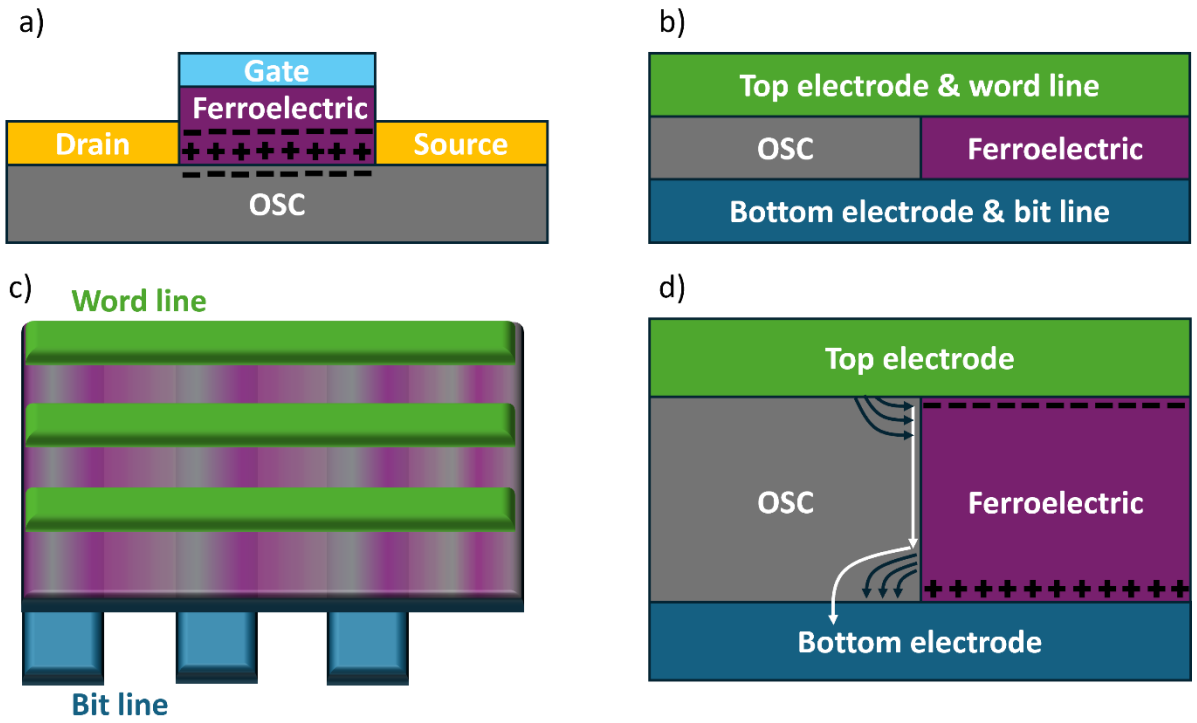

Figure 11. Schematic depictions of a ferroelectric field effect transistor in a), a ferroelectric diode in b) and its working principle in d) and a crossbar array consisting of 3x3 ferroelectric diodes in c).

FeFETs, schematically depicted in Figure 11a), have the same layout as the classic MOSFET transistor, except for the gate dielectric being replaced by a ferroelectric material. In the same manner as the dielectric, the ferroelectric material is used to modulate the conducting state of the transistor, by depletion or accumulation of charges at the ferroelectric-semiconductor interface. Contrary to MOSFETs, the conduction and corresponding memory state remains stable after removing the external field, making the FeFET a non-volatile memory on the timescale of the polarization retention. A detailed review of FeFETs is beyond the scope of this thesis and the reader is referred to the following literature.[133–135]

The optimal architecture regarding memory density is a simple crossbar array, as shown in in Figure 11c).[41,136] By contacting the $N = 3$ corresponding word and bit lines, all $N^2 = 9$ memory cells (here ferroelectric diodes) can be written and red-out. Since the crossbar requires two-terminal devices, the three-terminal FeFETs are not suitable and only ferroic capacitors and diodes can be integrated. Ferroic capacitors are the simplest memory cell layout usable but have the significant disadvantage that reading out the memory state (polarization) requires polarization reversal, which is destructive, and therefore the cell must

be rewritten for read-only operations. This increases device stress and fatigue and hence a non-destructive readout is preferable. Ferroelectric diodes are a natural way to realize non-destructive readout in crossbar arrays, combining an insulating ferroelectric with a semiconductor, schematically shown in Figure 11c). Asadi *et al*. created ferroelectric diodes by creating a blend of ferroelectric P(VDF-TrFE) and semiconducting P3HT, with a theoretically estimated memory density in the range of 1 GB/cm^2.[43,137]

Following the concept, van Breemen *et al*. managed to fabricate crossbar arrays of 1 kbit and a memory density of 10 kbit/cm^2.[138] The ferroelectric polarization modulates the injection barrier between the metal contacts and the semiconductor at the metal-semiconductor-ferroelectric interface. Depending on the polarization direction, charge injection is either facilitated, resulting in Ohmic contacts and a high current following SCLC behavior, or blocked, resulting in a low current.[42] In this way the on- and off-state of the memory cell are represented. This is depicted schematically in Figure 11d). A common problem with the crossbar architecture is crosstalk, especially when reading out a single low conductivity state surrounded by cells in the high conductivity state. In this case parasitic leakage currents diminish the on/off-ratio drastically. This can be prevented by incorporating a rectifying element, e.g. a diode, between the memory cells, at the cost of significantly increased device complexity.

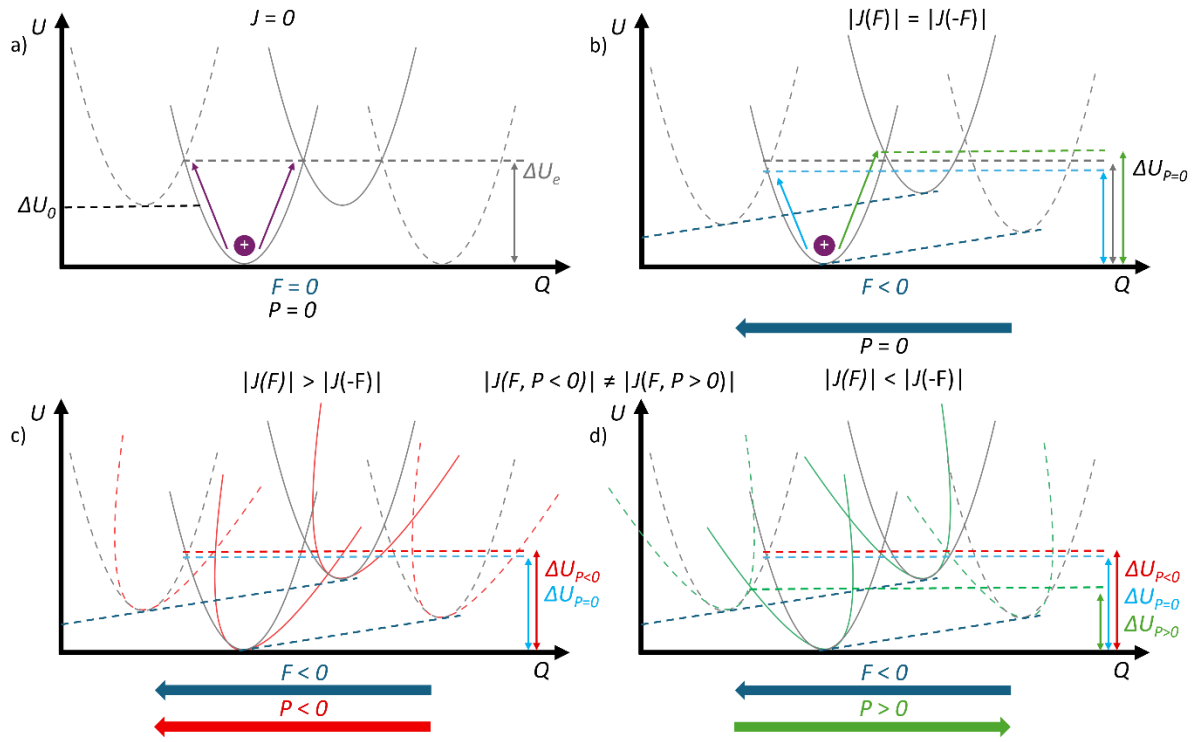

Figure 12. Schematic depiction of bulk conductivity modulation in (semi)conducting ferroelectrics. The top row shows the potential landscape in the unpolarized state, without a) and with b) an externally applied electric field. Fields of opposite direction result in an absolute current of same amplitude. The bottom row shows the potential landscape in the polarized state, where different polarization directions in c) and d) cause an asymmetric potential difference. Therefore, the absolute value of the current depends on the alignment of the external field relative to the polarization direction. Adapted from reference[139].

A further simplification of the crossbar architecture that does not rely on complicated multiple material blends can be obtained by using the previously mentioned conducting ferroelectrics, if the conductivity is modulated by the polarization state of the material. A natural approach is the use of organic materials containing (semi)conducting cores and dipolar groups. This idea was implemented successfully in various organic materials and resulted in resistive switching via injection barrier modulation (IBM)[140], via bulk conductivity modulation (or bulk conductivity switching, BCS)[141] and even the occurrence of both processes in a single material.[39] IBM works in the same way as the semiconductor-ferroelectric blends in the diodes, with the ferroic polarization modulating the injection barrier as

$$\phi = \frac{dP_s}{\epsilon_0 \epsilon_r} \tag{35}$$

Here d is the typical layer thickness of the injecting layer. Depending on the magnitude of the polarization and dielectric permittivity barrier modulations on the order of up to a few electron volts can be achieved. For a decrease in barrier height, the direction of the external electric field and the polarization has to be the same, for fields against polarization direction the contact will be blocking. Flipping the polarization will therefore modulate the conductivity accordingly.

BCS, as the name implies, is not an interface but a bulk effect and therefore only relevant when the injection barrier is sufficiently low. It describes the effect the ferroelectric polarization has on the charge transport through the bulk in a ratchet-like effect.[142] Contrary to IBM, the current-voltage behavior predominantly shows an increase in conductivity when applying fields against the direction of the polarization and decrease when field and polarization are aligned alongside. While no comprehensive theory exists yet, the conductivity modulation resulting from BCS was first modeled for columnar supramolecular units by Gorbunov *et al.* in terms of polaronic Marcus hopping.[141] This accounts for the change in site energy by the polarization. Considering a two-site model with periodic boundary conditions, they calculated the average hopping rate between carrier sites semi-analytically and with a kinetic Monte Carlo approach depending on field and polarization direction. The following paragraph explains the mechanism in more detail.

Figure 12a) schematically shows the carrier sites as Marcus parabolas in the unpolarized state at zero external field. Local differences in the potential landscape result in a site potential difference ΔU_0. The potential a charge has to overcome via hopping is indicated as $\Delta U_{\mathrm{F}=0}$. Applying an external field results in an effective potential shift, reducing the hopping barrier in field direction and increasing it against field direction. Inverting the field direction will invert the barrier change, meaning this is a symmetric process and the absolute currents for both field directions will be the same. In Figure 12c) and d) the ferroelectric polarization is introduced as a superimposed asymmetric potential, which results in a tilt of the Marcus parabolas of the carrier sites. Depending on the direction of the polarization and therefore of the tilt, the energetic hopping barrier is increased or decreased ($\Delta U_{P<0}$ or $\Delta U_{P>0}$), at constant external field. The hopping rates at finite fields become asymmetric and the resulting conductivity modulation (on/off-ratio) can be calculated semi-analytically. It has to be noted that in this model, depending on the exact parameters used, e.g. the reorganization energy

of the Marcus parabolas and their energy offset, the modulation can even fall below unity, resulting in an enhancement of currents for fields applied in polarization direction, similar to IBM.[141] However, this is only the case for a small part of the parameter space.

The BCS mechanism was further investigated on more fundamental theoretical basis by Johann *et al*. using a combination of molecular dynamics simulations and DFT calculations.[143] In a first step they reproduced the experimentally observed polarization switching of the ferroelectric semiconductor benzotrithiophene tricarboxamide (BTTTA) with molecular dynamics simulations. Then, by combining molecular dynamics with quantum mechanical DFT calculations they showed that the coupling between ferroelectric polarization and charge transport results in a conductivity modulation at high fields. Mobilities for charge transport in the case of antiparallel field and polarization exceeded those for the parallel case by a factor of around 1.7, confirming experimental observations and the validity of the BCS model by a higher-level theory.

3. Experimental methods and materials

In this section the experimental methods employed are introduced, and an overview of the investigated materials is given.

3.1 Electrical characterization

3.1.1 Substrates and electrode structure

All electrical measurements were done on films deposited on glass substrates patterned with in-plane, metal, interdigitated finger electrodes (IDE). These were either commercially available IDE from MicruX Technologies or homemade IDE produced by photo lithography. Micrux IDE have an electrode width and spacing of 5 µm, an electrode height of 50 nm titanium followed by 150 nm gold and a total length electrode length of 0.8 m. The homemade IDE had a height of 5 nm chromium followed by 25 nm of gold and electrode width and spacings of 1 µm, 2 µm and 5 µm, resulting in total electrode length of 10.10 m, 5.048 m and 2.018 m, respectively. A schematic of the IDE structure is shown in Fig. 13a). The lithography process to create the homemade IDE was developed by the author and Anton Kompatscher from the Kemerink Group during the course of this thesis, with the aim of obtaining higher signal to noise ratios as well as enabling the applications of higher electric fields. Prior to deposition of the active layer, all IDE substrates were chemically cleaned by sonication in acetone, followed by sonication in isopropanol and successively blow dried with nitrogen.

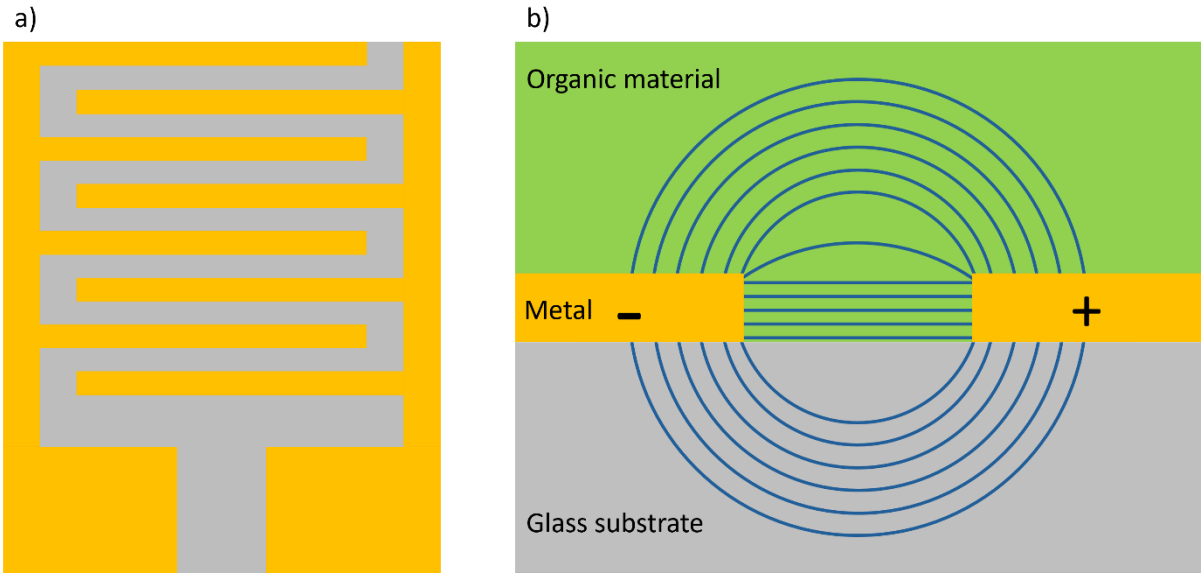

Figure 13. a) Top view schematic of the IDE layout. b) Side profile schematic of an organic dielectric film deposited on an IDE substrate with the field lines of an externally applied electric field depicted in blue.

Figure 13b) schematically depicts the electric field distribution in IDE devices with an organic film deposited on top. The in-plane geometry creates difficulties extracting the exact measured current density and polarization. More information is given in the description of each measurement type as well as ways of approximating the desired quantity. In addition, the field strength becomes inhomogeneous in the areas above (and below) the electrodes. For this reason, it is sensible to quantitatively only compare measurements on in-plane devices to each other, regarding characteristic parameters. Measurements on out-of-plane devices often show quantitative and qualitative deviations. Not only because the effective field is slightly different, but also because many materials tend to orient in a way that favors ferroelectric behavior either in in-plane or out-of-plane direction.

3.1.2 Electrical probe setups and current voltage characteristics

Electrical measurements were conducted in four different setups in various environments. For measurements in vacuum, either a Janis ST-100 continuous flow cryostat with fixed probe needle positions or a Janis probe station with adjustable probe arms was used. The sample stages in both can be cooled down to 77 K by liquid nitrogen and heated to 475 K and 450 K respectively. The typical vacuum level was between 2-5 $\times 10^{-5}$ mBar. Measurements in air were conducted either in an open probe station or a Linkam H600 stage. The stage in the former can be heated to around 450 K while the stage in the latter can reach temperatures of 870 K. Additionally, the Linkam stage was used to measure in nitrogen atmosphere, which allows cooling down the stage to 77 K. For all measurements with stepwise increasing or decreasing temperature samples were left to equilibrate between two (Linkam stage) and ten minutes (probe stations) at the temperature setpoint before measuring.

Current voltage (IV) and current over time at constant applied voltage (IV(t)) measurements were acquired in the Janis probe station in vacuum with a via a Keithley 2636B Source Meter Unit (SMU).

3.1.3 Dielectric spectroscopy

Dielectric spectroscopy (DS) is a powerful tool to measure the dielectric properties of materials over a wide temperature and frequency range. Here, it was employed to search for phase transitions in ferroelectric materials and only a brief explanation of the necessary theory for this experiment is given. For an in-depth overview of dielectric spectroscopy the reader is referred to one of various textbooks on the topic.[144] DS measurements were

conducted using a Zurich Instruments MFIA impedance analyzer in 2- and 4-probe geometry. The MFIA is a source measure unit (SMU) containing a lock-in amplifier and a frequency sweeping unit, that allows to measure the capacitance over frequencies of multiple orders of magnitude. In the experiment, an AC-voltage signal with an amplitude of 300 mV is applied and the resulting current amplified and frequency filtered by the lock-in amplifier to obtain an optimized signal to noise ratio. From the measured current I and its phase shift $\Delta\phi$ relative to the applied voltage V the impedance Z can be calculated:

$$Z = Z' + \mathrm{i}Z'' = \frac{|V|}{|I|}\exp(\mathrm{i}\Delta\phi) = |Z|\exp(\mathrm{i}\Delta\phi) \tag{36}$$

The impedance of a capacitor is given by

$$\mathrm{Z} = \frac{1}{\mathrm{i}\omega C} \tag{37}$$

with capacitance $C = 1/i\omega Z$ and frequency $\omega = 2\pi f$. By fitting an equivalent circuit model, in this case a RC-parallel circuit, to the measured data, the real and complex impedance, as well as the capacitance are obtained. The electric permittivity of the dielectric can be directly calculated from the capacitance as $\epsilon_\mathrm{r} = C/C_0$, with the capacitance of the capacitor without dielectric C_0. For a parallel plate capacitor $C_0 = \epsilon_0\epsilon_\mathrm{r}A/d$ is straightforward to calculate. However, for thin films on planar IDE the situation is more complicated as the permittivity of the substrate has to be considered, as well as the fact that the electric field lines are curved in some regions and their penetration depth into the film is unclear. While there are attempts in literature to model the capacitance of IDE structures, they are rather complicated, based on simplifications that might not hold true in real devices and for a different geometry.[145,146] For this reason and because DS in this thesis is only used to qualitatively search for phase transitions, only the capacitance will be considered. It is a sufficient proxy for the permittivity, as there is only a geometric proportionality factor between them.

3.1.4 Double wave method and capacitance-voltage measurements

Bulk polarization cannot be probed directly via electrical means. Instead, the current associated with charge carriers flowing onto the electrodes to compensate the field originating from the polarization is measured during polarization switching events. The double wave method (DWM) is the technique employed to measure ferroelectric polarization-field hysteresis loops by applying an electrical field and measuring the response

(switching) current.[44] To obtain complete hysteresis loops, the voltage pulse shown in Figure 14 is applied. To reduce sample stress and because of continuous effects of field annealing, single pulses were used instead of a periodic signal for most materials. The first negative triangular pulse is the "write" pulse used to polarize the sample. Triangle number two is a "read" pulse, where the current response includes the ferroelectric switching current and various background currents originating from leakage and displacement. Pulse number three with the same field direction reads in polarization direction and will therefore measure only the non-switching components. Subtracting the third from the second pulse corrects for all background currents and theoretically the pure ferroic switching current is obtained. How and why this does not always work is discussed in the results section of the thesis. The switching current per area is integrated over time and plotted against the corresponding external field to obtain the polarization hysteresis loop at positive fields.

$$\Delta P = \int \frac{I_{\mathrm{sw}}(t)}{A} \mathrm{d}t \tag{38}$$

Pulses number three and four yield the polarization at opposite field and complete the hysteresis loop. For later measurements a symmetric poling procedure of two upwards triangles followed by two downwards triangles was employed, to reduce the possible influence of ferroelectric imprinting.[147]

A brief disclaimer on the accuracy of the extracted polarization values has to be given. The in-plane geometry of the IDE again poses a few challenges. To obtain the relevant area to convert charge into charge density, i.e. polarization, the total effective length of the electrodes as well as the effective penetration depth (height) of the electric field into the ferroelectric are needed. The former is trivial to obtain, the latter however, is not. As almost all materials were drop-casted, see materials subsection, the obtained film roughness was high and on the order of hundreds of nanometers, resulting in an inhomogeneous film thickness. Additionally, there is no straightforward way of estimating the precise penetration depth of the electric field into ferroelectric materials, as they exhibit a drastically and non-linearly increased permittivity during polarization switching. A very simplifying approach is to assume that the field lines extend to a height equal to the distance between electrodes, following geometric arguments. Therefore, the film height was used as effective height when smaller than the electrode spacing, otherwise the electrode spacing was used as an upper

limit of the effective height. As a result, the given polarization values present a lower limit and should be seen as an “order of magnitude” indicator. Exact polarization values can be obtained from out of plane devices with a simple plate capacitor geometry. However, out-of-plane devices were no option for most of the materials investigated in this thesis as they formed rough and not fully closed layers. In out-of-plane devices this results in unavoidable shorts.

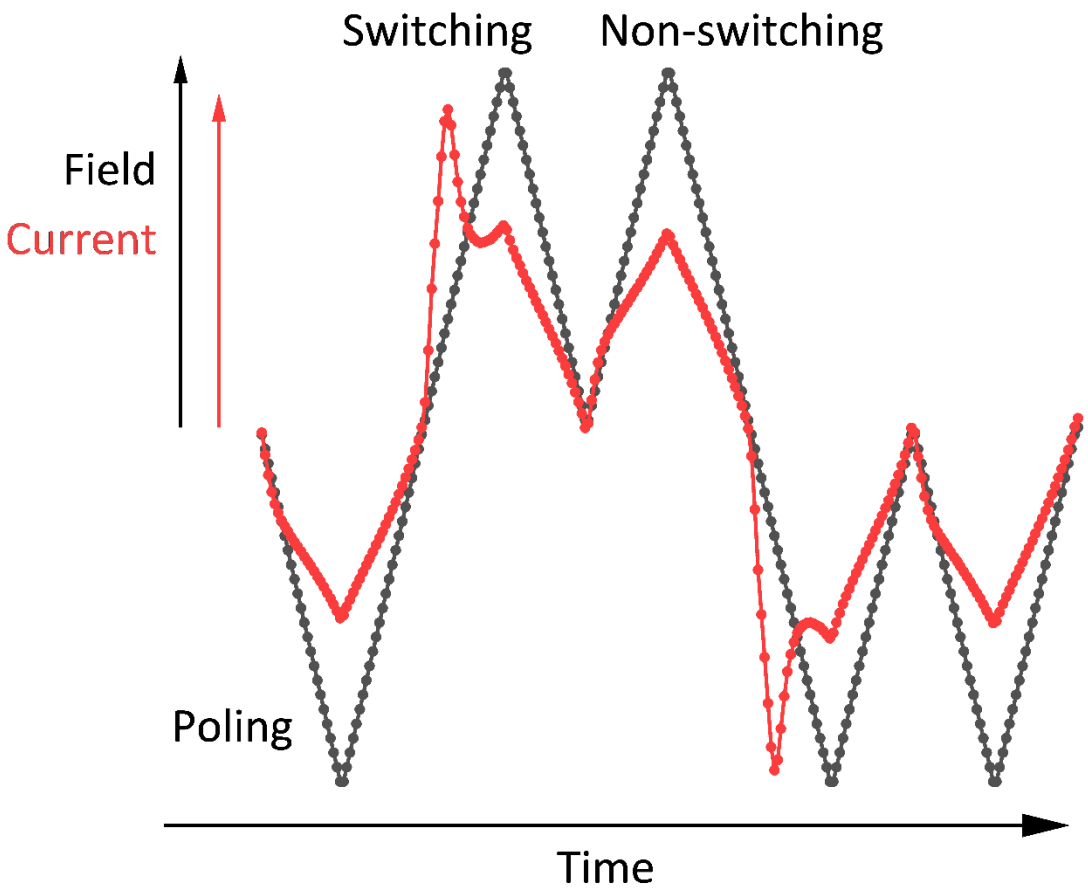

Figure 14. Schematic of the double wave measurement indicating poling, switching and non-switching pulses. The shape of the poling pulse varies for different measurements, for earlier data a single triangle was used for poling, while for more recent data a symmetric poling procedure of two upwards triangles followed by two downwards triangles was employed.

The capacitance-voltage (CV), DWM and “zig-zag” measurements were obtained with an aixACCT Systems Research Line DBLI together with a Linkam HFS600E-PB4 probe stage. For the CV-measurements, a DC-bias is swept back and forth with a small signal AC-bias overlaid to measure the capacitance. In this manner ferroelectric butterfly loops were probed, again with the capacitance as a proxy for the permittivity. When selecting the amplitude of the small

signal, it is important to keep it well below the coercive field, otherwise part of the polarization will be permanently switched back and forth, distorting the measurement.

3.2 Structural characterization

3.2.1 Atomic force microscopy

Atomic force microscopy (AFM) is a high-resolution structural characterization method, where the surface of planar samples is traced by an oscillating sharp tip, as shown schematically in Figure 15. The tip deflection in z-direction and its oscillation frequency is monitored by detecting the reflection of a laser directed at the tip surface. Piezoelectric positioners enable translation of the stage in x- and y-direction. All AFM images were obtained using a Bruker MultiMode 8-HR AFM operated in tapping mode.

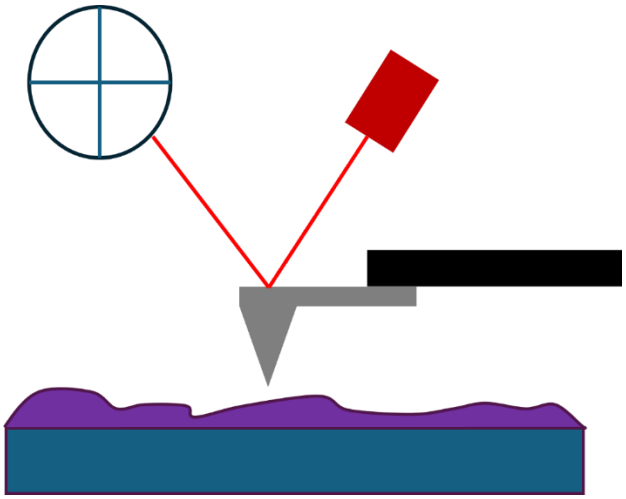

Figure 15. Schematic of the AFM imaging process, showing the holder (black) of the cantilever with tip (grey) that is probing a thin film (purple) on a substrate (blue). The deflection of the tip is measured by detecting the reflected laser light (bright red) from a diode laser (dark red).

3.2.2 Grazing incident wide angle X-ray scattering

Grazing incident wide angle X-ray scattering (GIWAXS) is a powerful tool to investigate structural ordering in thin films. It is based on X-ray-diffraction (XRD), a process where X-rays, with wavelengths on the order of atomic distances, are scattered elastically at the atoms of a crystal lattice as shown in Figure 16. The resulting circular waves interfere destructively unless Bragg's law $2d \sin\theta = n\lambda$ is satisfied. Here d is the interplanar distance, n a natural number indicating the diffraction order, λ the wavelength and θ the incident angle of X-rays. For GIWAXS, small incident angles are chosen to limit the probing depth and increase the resolution when measuring thin films. The detector is placed close to the sample stage to

capture a wide range of scattering angles including the large scattering angles resulting from small intermolecular distances like π-π-stacking. The experimental setup is shown in Figure 17a). For elastic scattering, the only wavevectors considered for scattering are the ones lying on the Ewald sphere, the three-dimensional equivalent of Braggs law in reciprocal space, meaning the resulting wavevectors differ by a vector in the reciprocal space. This is schematically shown in Figure 17b). The absolute values of the scattering reflexes in the reciprocal space are calculated from the measured scattering angles by

$$q = \frac{4\pi}{\lambda}\sin\left(\frac{\theta}{2}\right) \tag{39}$$

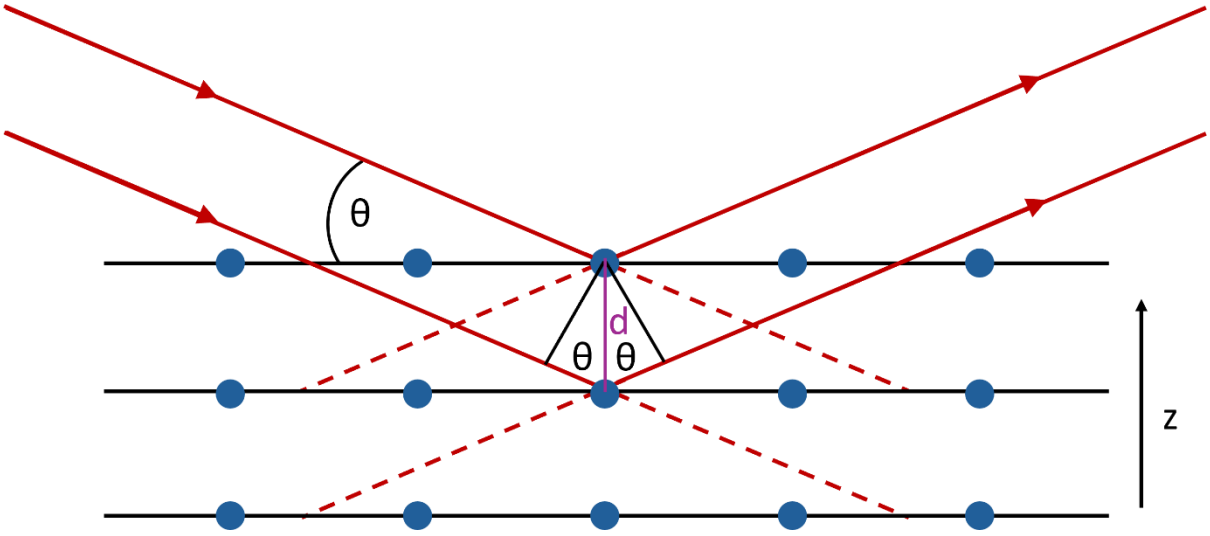

Figure 16. Schematic depiction of X-ray diffraction adhering to Bragg's law. The incoming and reflected X-rays are depicted as a solid red line with an incident angle θ. The interplanar distance of the atomic crystal planes is indicated as d.

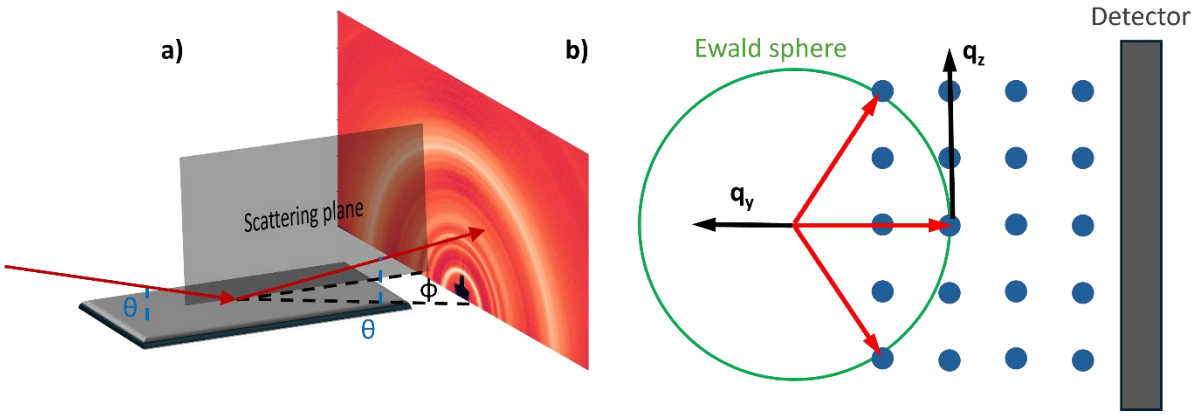

Figure 17. a) Depiction of the experimental GIWAXS geometry. b) Schematic of the scattering in reciprocal space, only wavevectors laying on the Ewald sphere result in a scattering reflex.

All XRD measurements were carried out using a Rigaku SmartLab setup employing a Cu source with a wavelength of 0.154 nm. The GIWAXS measurements were done in the 2D mode with an incident angle of 0.3° and an exposure time of one hour.

3.3 Materials

3.3.1 Fluorinated cyclohexanes

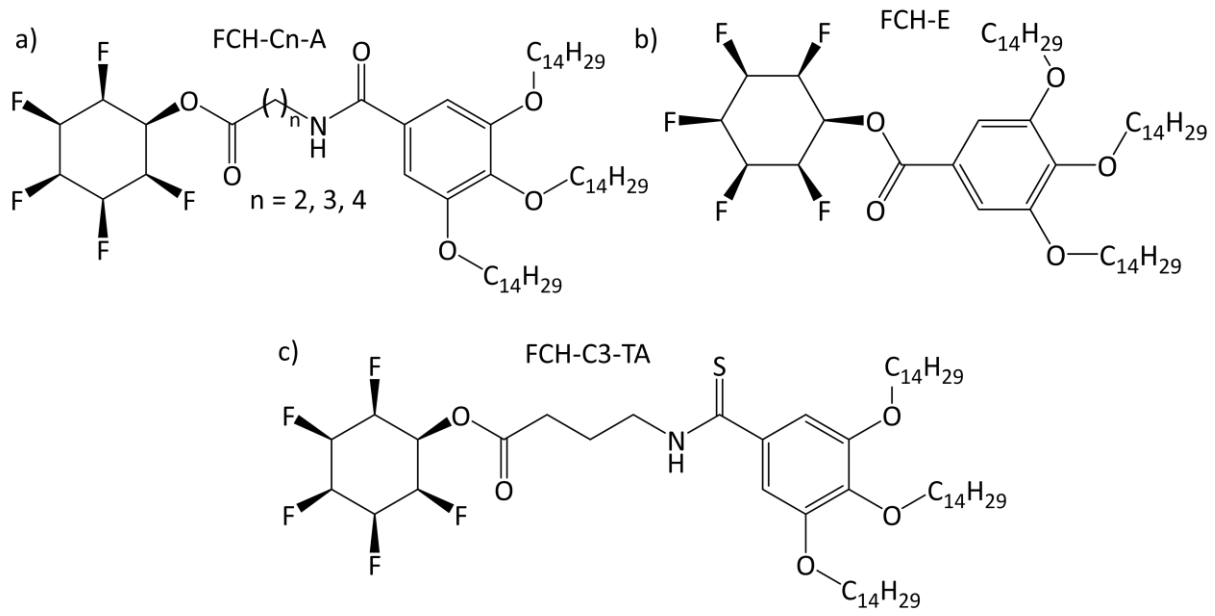

Figure 18. Molecular structure of the investigated fluorinated cyclohexanes.

The fluorinated cyclohexanes (1r,2R,3R,4s,5S,6S)-2,3,4,5,6-pentafluorocyclohexyl 3-(3,4,5-tris(tetradecyloxy)benzamido)-propanoate, -butanoate, -pentanoate, abbreviated **FCH-C2,3,4-A** respectively and shown in Figure 18a), were first introduced by Shyshov *et al*.[45] These small molecules have two strongly dipolar groups, a pentafluorocyclohexane group that amounts to around 6.2 Debye and an amide group with 3.7 Debye, separated by a short alkyl spacer. This makes them a prime candidate for ferroelectric behavior of the order-disorder type, where polarization occurs by ordering and alignment of the dipolar moieties. FCH-C3-A was shown to undergo supramolecular polymerization by H-bonding in solution, resulting in elongated molecular fibers when spin-coated on a silicon wafer. The different carbon spacer lengths result in a shift of the melting point to higher temperatures for shorter carbon chains, presumably caused by an increase in molecular rigidity and stability.

An excellent material to compare to the FCH-C*n*-As is the (1r,2R,3R,4s,5S,6S)-2,3,4,5,6-pentafluorocyclohexyl 3,4,5-tris(tetradecyloxy)benzoate, abbreviated **FCH-E**. It lacks the C*n*-spacer and the amide group and is shown in Figure 18b). Another molecular derivative, where the oxygen of the FCH-C3-A's amide group is replaced by sulfur is (1r,2R,3R,4s,5S,6S)-2,3,4,5,6-pentafluorocyclohexyl 4-(3,4,5-tris(tetradecyloxy)phenylthioamido)butanoate, short **FCH-C3-TA**, is depicted in Figure 18c). Substituting oxygen for sulfur facilitates oxidation

of the nearby nitrogen and decreases the energetic bandgap, see appendix Figure 1. All FCHs were synthesized by Shyamkumar Haridas from the von Delius group of Ulm University.

3.3.2 Discotic tricarboxamides

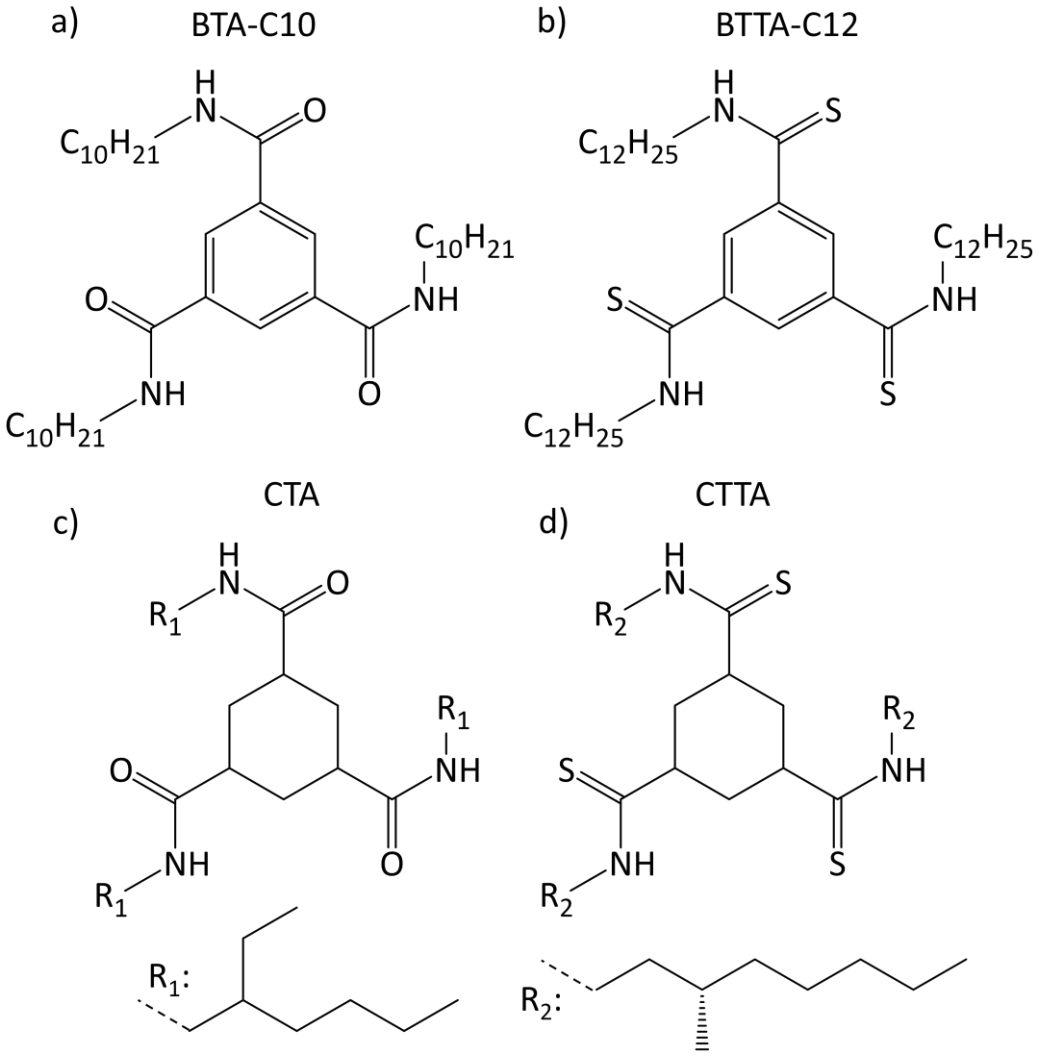

Figure 19. Molecular structure of the investigated molecular discotics.

The liquid crystalline benzene tricarboxamides (BTAs) are well known ferroelectrics, forming supramolecular columns under field annealing.[100,108] They each contain a π-stacking core with three polar (thio)amide groups and aliphatic chains for solubility. In this thesis the N1,N3,N5-tris(decyl)benzene-1,3,5-tricarboxamide (**BTA-C10**) and the N1,N3,N5-tridodecylbenzene-1,3,5-tris(carbothioamide) (**BTTA-C12**), depicted in Figure 19a) and b), were investigated. The cyclohexane tricarboxamides (CTAs) are structurally very similar to the BTAs, except that they have a non π-conjugated cyclohexane core. They were not yet extensively researched for possible ferroelectric behavior. The CTAs investigated in this thesis were the *N1,N3,N5*-Tris(2-

ethylhexyl)cyclohexane-1,3,5-tricarboxamide (**CTA**) and the *N1,N3,N5*-Tris((S)-3,7-dimethyloctyl)cyclohexane-1,3,5-tris(carbothioamide) (**CTTA**), shown in Figure 19c) and d) respectively.

3.3.3 Charge transfer complexes

Charge transfer complexes (CTCs) have been garnered the interest of researchers for a long time, resulting in the discoveries of various interesting properties such as metallic conductivity[4,148], superconductivity[148,149] and ferroelectricity.[150,151] CTCs are a combination of two different single semiconducting molecules, one with an affinity to take up charge and one with the tendency of donating charge. These parent molecules are accordingly denoted donor and acceptor, and CTCs are also often called donor-acceptor complexes. When combining, a fraction ρ ($0 < \rho \leq 1$), also denoted as the ionicity of the CTC, of an electron charge from the donor is transferred to the acceptor. This creates new energy levels with different HOMO and LUMO compared to the parent molecules, as shown in Figure 20c). The CTC LUMO lies energetically inside the bandgap of the donor while the CTC HOMO lies inside the bandgap of the acceptor. With a resulting bandgap generally smaller than those of the parent compounds, CTCs tend to offer improved semiconducting properties. However, the exact conductive properties can vary significantly, depending on the degree of charge transfer and the CTC stack morphology.[49] Likewise, the CTC bandgap and the degree of charge transfer depend on the HOMO and LUMO levels of the parent molecules.[152]

CTCs are usually arranged in either of two geometries, the mixed planar stack as shown in Figure 21a), were donor and acceptor molecules are alternating or the segregated planar stack as shown in Figure 21b). While for the former the 1:1 (D:A) stacking ratio is most commonly observed, other morphologies like 1:2, 1:3 and their inverse are possible. Many adjacent stacks make up to bulk material. This morphology generally leads to strongly anisotropic, quasi one-dimensional behavior, with most properties like for example conductivity are significantly enhanced in stack direction. Usually in mixed stack CTCs, complete ionization leads to insulating behavior, while partial ionization results in a semiconductor. Segregated stacking is a requirement for metallic conductivity but does not guarantee it.[49] Hence, while the conductive properties and the degree of charge transfer of a possible CTC consisting of an arbitrary donor-acceptor pairing cannot be predicted in detail in advance without a great deal of computational effort, assumptions can be made taking into

account the energy levels of the parent molecules and the stack morphology of related CTCs.[152] The ionicity of CTCs can be determined computationally or experimentally by vibrational spectroscopic means, where the neutral and ionized variants of the respective donor and acceptor molecule are compared.[153,154]

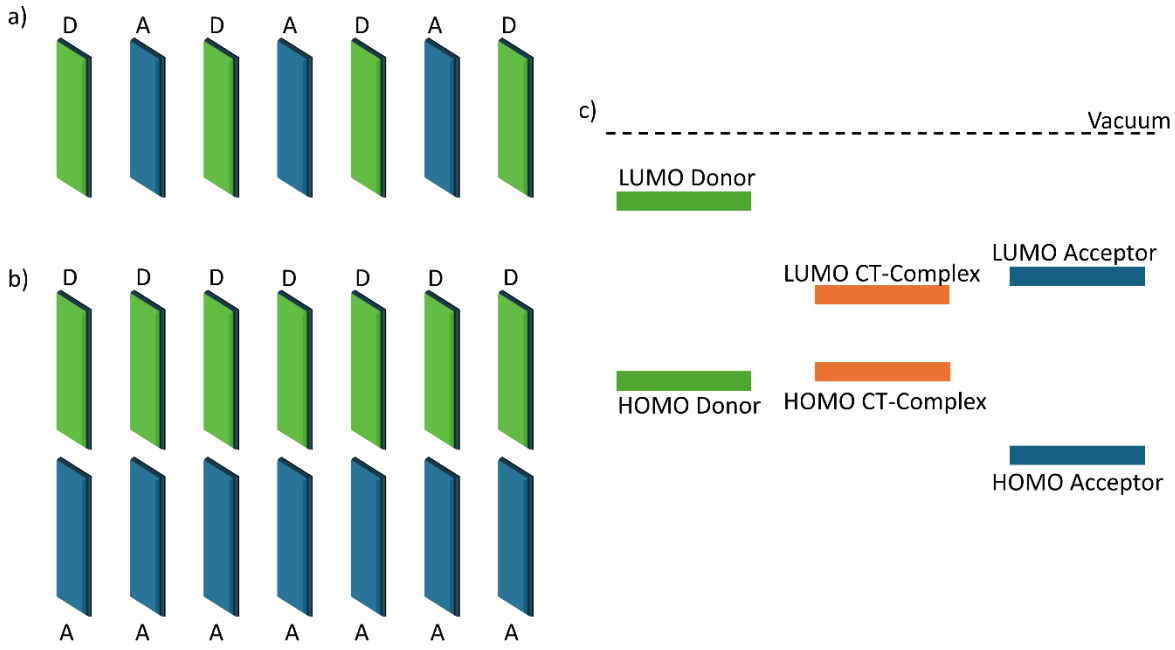

Figure 20. Schematics of a donor-acceptor charge transfer complex (CTC) in the mixed stack a) and segregated stack b) configuration. c) Schematic energy levels of a CTC.

Generally, ferroelectricity in CTCs is a little researched topic and so far, only a small number of materials have been investigated and shown to be ferroelectric. Ferroelectricity in CTCs does not usually originate from a disorder-order transition as in PVDF or BTA where the rotation and alignment of dipolar groups/atoms yields a macroscopic polarization, but from the displacement of charged molecules in mixed stack CTCs. To illustrate the process, the 1:1 stacking morphology with an arbitrary ionicity $\rho > 0$ is considered. It is easy to see that for a chain of periodic and evenly spaced alternating donor and acceptor molecules no macroscopic net polarization is obtained. However, a macroscopic polarization can be obtained by simultaneously displacing either all donor or all acceptor molecules, or both, to dimerize the chain into evenly spaced DA pairs. This is depicted in Figure 21a) on the left and usually occurs at a critical temperature or pressure, with the former being described by the Curie-Weiß law. Application of sufficiently large external electric fields shifts the direction of

the dimerization and concomitantly reverses the polarization, as depicted in Figure 21a) on the right.

This dimerization is also known as Peierls transition and occurs in some CTCs during temperature or pressure variation. The exact nature of the respective Peierls transition depends on the ionicity and possibly further parameters of the CTCs. Since the number of known ferroic CTCs is limited, no comprehensive description and classification of their Peierls(-like) transitions exists. Here, two truly distinct and somewhat representative cases are discussed, CTCs close to ionic salts with a ρ near unity and CTCs with partial charge transfer and hence fractional ionicity that undergo a transition from a quasi-neutral state to quasi-ionic one. An example of the former is the ionic CT-salt tetrathiafulvalene-*p*-bromanil (TTF-BA), with an ionicity of 0.95, which remains largely unchanged over all relevant temperatures. Kagawa *et al.* observed a para- to ferroelectric phase transition in TTF-BA at 53 K with a concomitant peak in the dielectric permittivity and the vanishing of a finite magnetic susceptibility.[155] From this and further measurements of suppressed ferroic behavior under external magnetic fields they concluded that TTF-BA can be described as a one-dimensional Heisenberg chain with spin 1/2, that undergoes dimerization at T_c via a spin-Peierls transition, concomitantly transitioning from para- to nonmagnetic.[156,157] In contrast stand CTCs with fractional ionicity, with tetrathiafulvalene-*p*-chloranil (TTF-CA) as one of the most prominently investigated examples. TTF-CA has been shown to undergo dimerization together with a paraelectric to ferroelectric phase transition at 81 K, while at the same time its ionicity changes from around 0.3 to 0.6.[158,159] This so called neutral to ionic transition (NIT) is a result of the ionization energy of the DA pair becoming smaller than the electrostatic energy of the respective ionic crystal, also known as Madelung energy.[160] Since the donor and acceptor molecules are only fractionally ionized and the electrons are shared between the molecules in a covalent fashion, TTF-CA does not undergo the classical spin-Peierls transition and its Peierls transition is more comparable to that of *trans*-polyacetylene, i.e. depending on electron-lattice interactions.[161,162]

The difference in electronic structure between TTF-BA and TTF-CA has further consequences for their ferroic and conductive properties. For TTF-BA, the spontaneous polarization along the main crystal stacking direction is 1.5 mC/m^2 while for TTF-CA it is 63 mC/m^2, despite the larger ionicity of the former. Horiuchi *et al.* explained this discrepancy by a significant

contribution of the electronic polarization in TTF-CA.[151] In short, the spontaneous polarization in TTF-BA matches the expected dipole density obtained by considering the ionicity and the molecular displacement in a simple classical picture, while for TTF-CA mostly the dynamical electron contributions enabled by the covalent character determine the magnitude of the polarization. The latter must then be calculated computationally using, for example density functional theory, and the Berry-phase approach.[163] A discussion of the theoretical background for these calculations is beyond the scope of this work and the interested reader is instead referred to the literature.[164–166]

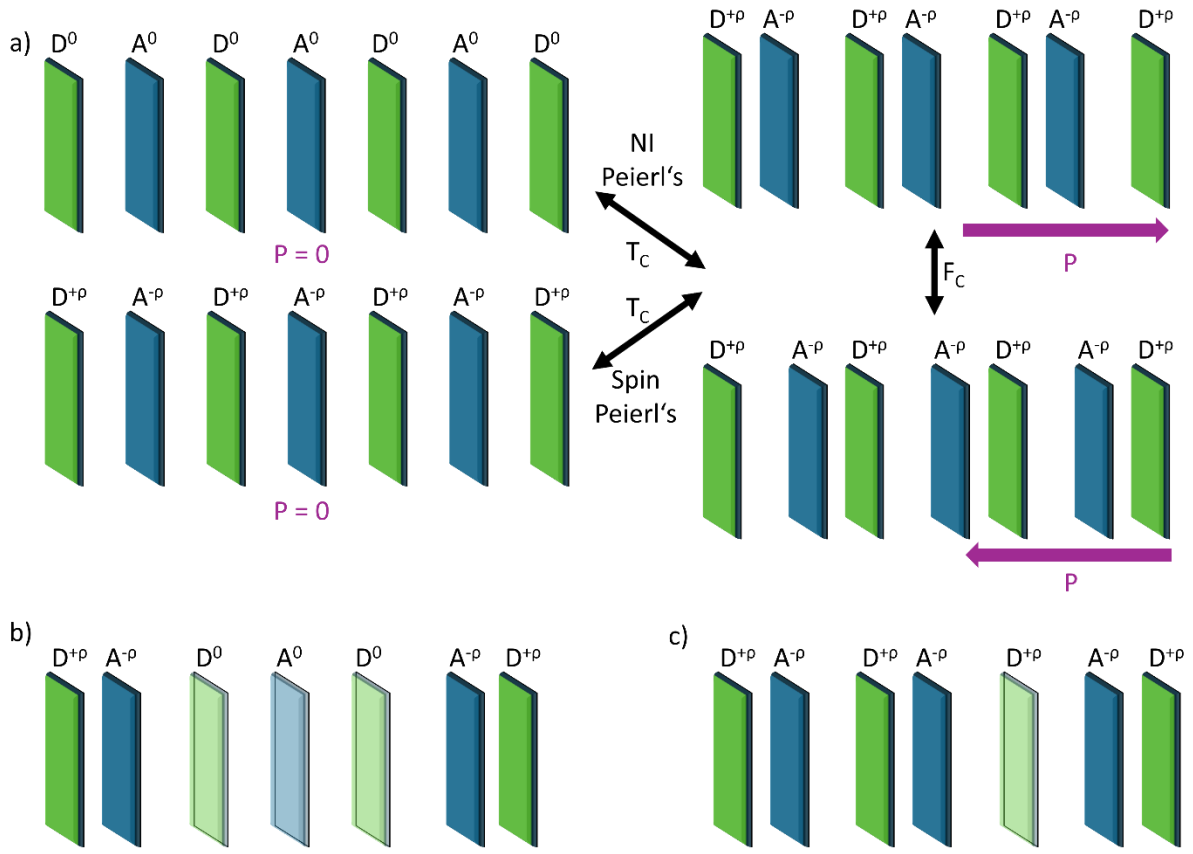

Figure 21. a) Schematic of a mixed stack donor-acceptor charge transfer complex (CTC) in the (quasi-)neutral phase on the upper left and in the (quasi-)ionic phase below. After passing the critical temperature both configurations dimerize with a resulting macroscopic polarization, as depicted on the right. Application of an external electric field inverses the dimerization and concomitantly the polarization direction. b) Example of a neutral-ionic domain wall in a segregated stack CTC, a possible defect in the quasi-neutral phase. c) Example of a spin-soliton defect in a segregated stack CTC.

Regarding the conductivity of the materials, TTF-BA is an insulating salt, while TTF-CA is a low bandgap semiconductor.[154] The conductivity of the latter exhibits a distinct temperature dependence around the NIT transition, that was attributed to low energetic excitations like

neutral-ionic domain-walls (NIDW) in the neutral phase or charged spin-solitons in the ionic phase.[52,167] Exemplary schematics of these NIDWs and spin-solitons are shown in Figure 21b) and c) respectively.

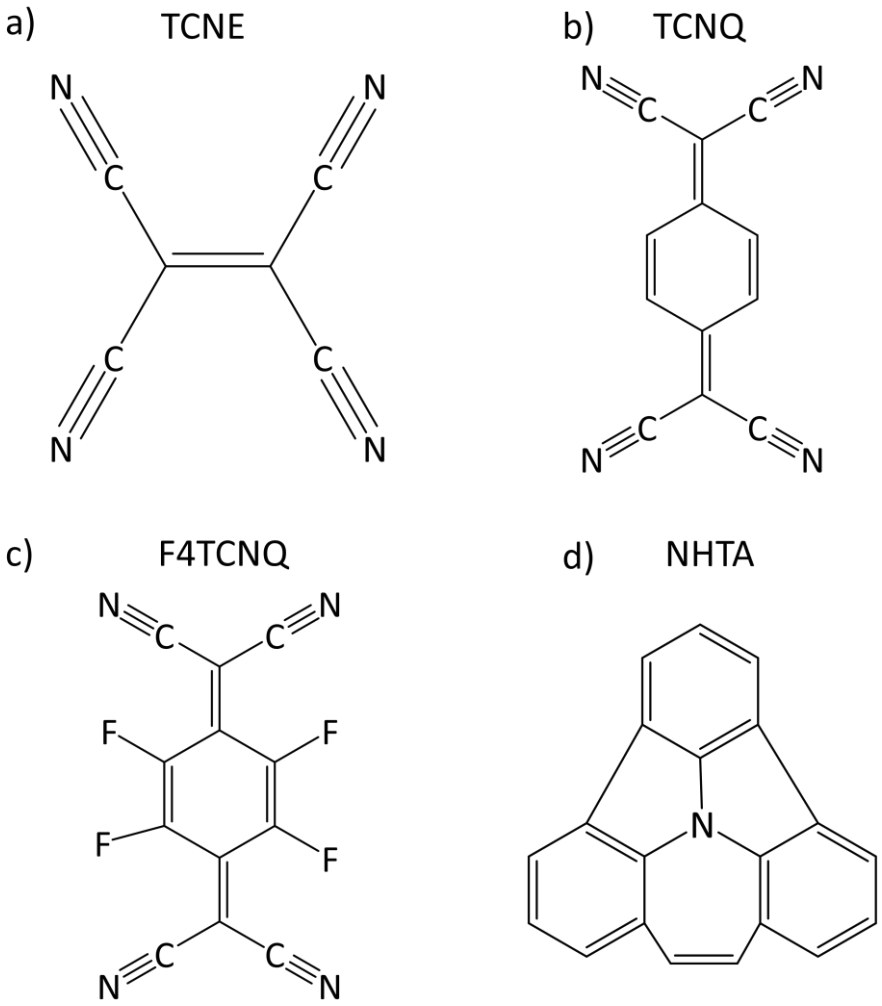

Figure 22. Molecular structure of the electron acceptor molecules TCNE, TCNQ and F4TCNQ a)-c) that form charge transfer complexes with the electron donor molecule NHTA in d).

The acceptor molecules used in this thesis are the well-known ethene-1,1,2,2-tetracarbonitrile (TCNE), 2,2'-(cyclohexa-2,5-diene-1,4-diylidene)dimalononitrile (TCNQ), and 2,2'-(perfluorocyclohexa-2,5-diene-1,4-diylidene)dimalononitrile (F4TCNQ), depicted in Figure 22a)-c). Together with a newly synthesized donor molecule, the 3a2-azabenzo[3,4]azuleno[2,1,8,7-jklm]fluorene (NHTA), shown in Figure 22d), they form CTCs with an alternating stack morphology of 1:1 for NHTA:TCNE and NHTA:TCNQ and of 2:1 for NHTA:F4TCNQ.[168] XRD data taken at -70°C showed a small displacement towards dimerization of 2 pm for NHTA:TCNE, between 3 and 5 pm for NHTA:TCNQ and of 10 pm for NHTA:F4TCNQ.

Michalsky *et al.* observed a slight redshift of the C≡N bond stretching vibration with respect to the unpaired acceptors, indicating a minor degree of charge transfer for the co-crystals.[168] Following Chappell *et al.,* the degree of charge transport in NHTA:TCNQ is estimated to be roughly around 0.1, with presumably slightly smaller values for TCNE and slightly bigger values for F4TCNQ.[169] The NHTA was synthesized by Ina Michalsky from the Kivala group at Heidelberg University.

3.3.4 Triphenylamines

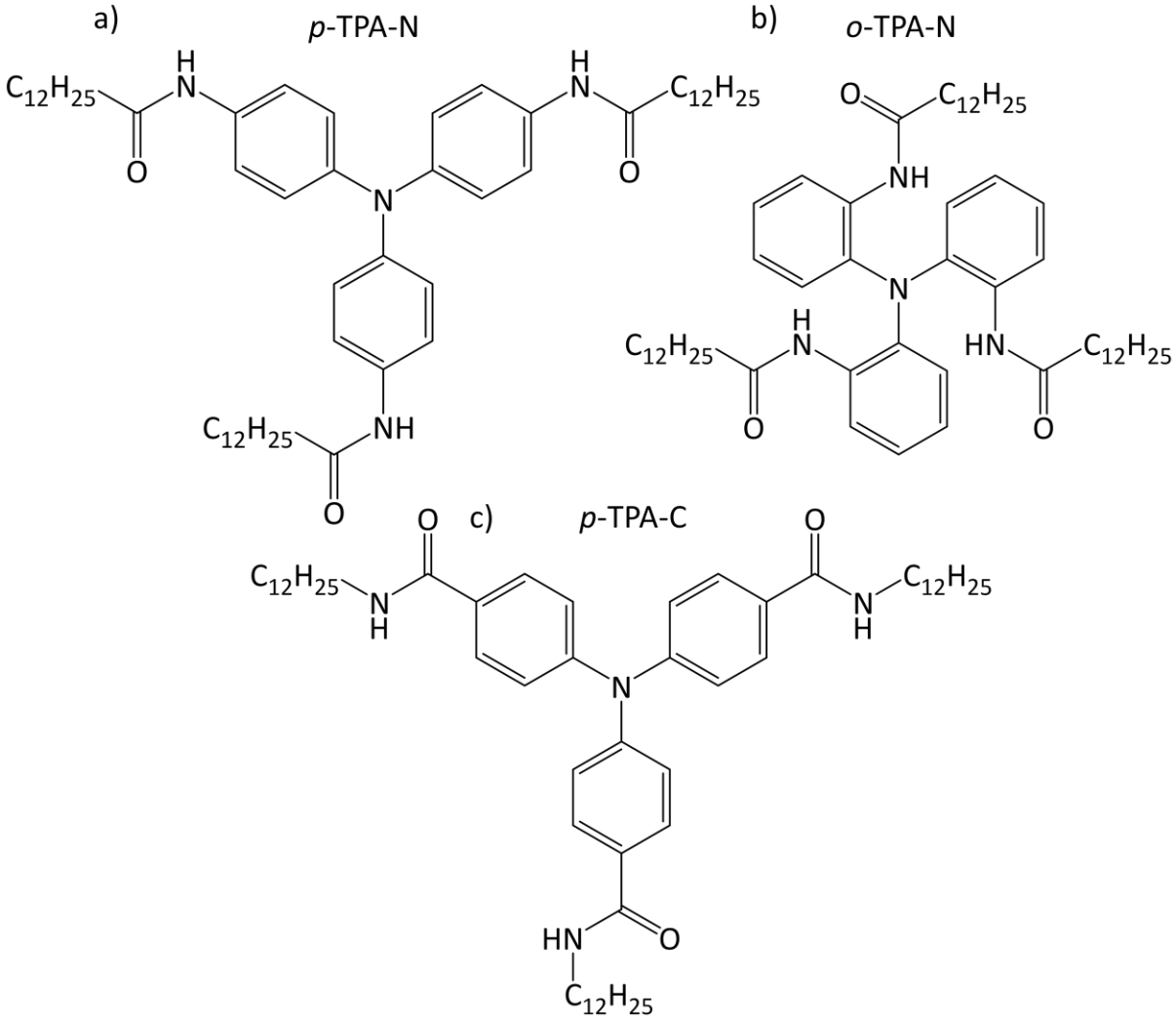

Figure 23. Molecular structure of the investigated triphenylamines.

Triphenylamines (TPAs) are a well-known motif for hole conduction in organic semiconductors. They contain a core made of three phenyl groups connected over a central nitrogen atom. The phenyl groups are connected in different ways to an amide group with an aliphatic chain attached to it. Their structure generally supports a delocalized π-system extending over the whole core. The investigated triphenylamines were the *N*,*N*',*N*''-

[Nitrilotri(4,1-phenylene)]tritridecanamide (***p*-TPA-N**), the *N*,*N*',*N*''-[Nitrilotri(2,1-phenylene)]tritridecanamide (***o*-TPA-N**) and the 4,4',4''-Nitrilotris(*N*-dodecylbenzamide) shown in Figure 23a)-c).

3.3.5 Film creation

All FCH and CTA films were created by drop-casting 2-5 times 4-5 µL drops from a 20 mg/mL solution in tetrahydrofuran (THF). The films were successively molten and cooled down on an aluminum block to improve film homogeneity. Drop-casted and molten films are called pristine in this thesis. All BTA films were created by drop-casting 2-5 times 4-5 µL drops from a 10 mg/mL solution in chloroform and successively field annealed at 70°C for 15 minutes to improve film homogeneity. All TPA films were created by drop-casting 5 µL drops from a 10 mg/mL solution of either pure THF (*p*-TPA-N and *p*-TPA-C) or a 50/50 mixture of THF and dichloromethane (*o*-TPA-N). All CTC films were obtained by drop-casting a single 4-5 πL drop from THF solutions of varying concentrations. A 10 mg/mL NHTA:TCNE solution for example was created by combining 10 mg/mL solutions of NHTA with TCNE. Therefore, the co-crystal solution is not really a 10 mg/mL solution, but the naming scheme was kept to easily reproduce the recipe. The THF used was stabilizer free and uninhibited, although it could not be determined whether that was necessary or if stabilized THF would have sufficed. It has to be noted that the CTC films generally exhibited reproducibility issues regarding (ferro)electric performance, which is attributed to a strong sensitivity to external parameters (humidity, air temperature, solvent purity, airflow) during film creation resulting in hardly controllable film morphologies. Additionally, the films suffered significant degradation under field and temperature stress. For this reason, the experimental investigations were switched to single crystal samples which proved more stable and hence the majority of data presented here is from single crystal samples.

CTC single crystals were drawn from saturated CTC solutions in THF and afterwards manually deposited on top of IDE. The crystals for all CTCs were thin needles of varying lengths. XRD studies showed that the direction of planar DA-stacking is along the long axis of the needle and the CTCs were aligned accordingly on the IDE substrates whenever possible.

Results and discussion

In the following three chapters, experimental results from three projects are analyzed and discussed. It starts with chapter 4 on the conducting properties of organic non-π-conjugated systems. An in-depth discussion of the conductivity in FCH-C3 is followed by comparison with the conducting properties of various further types of organic small molecules. This results in a generalized description of electric conduction in non-π-conjugated organic systems. The following chapter 5 treats the ferroelectricity of the FCHs and how polarization interacts with the conducting properties of FCH-C3-A. In chapter 6 the origin of and mechanisms behind conductivity and ferroelectricity in organic charge-transfer complexes (CTCs) formed by the donor molecule NHTA with three different well-known acceptors are discussed. All chapters begin with a short introduction specifying the contributions of all people involved in data gathering and evaluation. In all three chapters experimental data is presented, analyzed, and compared with literature and relevant theory.

4. Conductivity in organics without an extended π-system

In this chapter the experimental results regarding the conductivity in organic materials without extended π-system are presented and analyzed. DFT calculations were conducted by Jan Borstelmann from the Kivala group at Heidelberg University. X-ray fluorescence and differential scanning calorimetry data was provided by Shyamkumar Haridas of the van Delius group at Ulm University. Cyclic voltammetry and ultraviolet spectroscopy data was provided by Vivek Wakchaure of the van Delius group at Ulm University. All experimental data on the TPAs as well as AFM and GIWAXS measurements on BTA-C10 were collected by Andrey Butkevich of the Kemerink group at Heidelberg University. Analysis and interpretation of the experimental data gathered for the TPAs and BTA-C10 was shared equally between Andrey Butkevich and the author of this thesis. All TPA and BTA-C10 films were created by Andrey Butkevich. All GIWAXS plots were created by Andrey Butkevich. All other plots and all figures were created by the author of this thesis. All other experiments as well as the interpretation and evaluation of the resulting data were carried out by the author of this thesis. A large part of the data and many figures presented in this section are included in a submitted manuscript. The text in this section is almost completely original, with some exceptions like figure subtitles that are directly taken from the manuscript. The original main text of the manuscript was written by Heiko Mager, the author of this thesis and revised and improved upon mainly by Martijn Kemerink, Heiko Mager and to a lesser extent by the other co-authors of the manuscript.

4.1 The surprising conducting properties of FCH-C3-A

So far, (semi)conductivity in organics without conjugated π-systems has been rarely investigated or even observed. Faramarzi *et al.* demonstrated metal-like conductivity in supramolecular nanowires via illumination self-assembled triarylamine derivatives.[170] They hypothesized that charge transport is mediated by delocalized triarylamine radicals sharing their electronic wavefunctions with those of the metallic sample. In the field of bioelectronics Arikuma *et al.* demonstrated charge hopping along up to 11 nm long α-helical self-assembled monolayers of synthetical peptides.[11,12] They suggested that the amide groups function as hopping sides. Ing *et al.* observed metal like conduction in supramolecular α-helical nanofibers of synthetic peptides and while they could exclude the *π*-system as origin of the conductivity, the exact charge transport mechanism remained unclear.[13]

As discussed in subsection 2.1.1, conductivity in organic materials is generally mandated by the delocalized π-electrons of sp^2-hybridized carbon atoms. If the delocalization does not extend over the majority of the molecule, the resulting HOMO-LUMO gap tends to be large, and the material is insulating. This should be true for the FCH-C3-A introduced earlier, which has a π-system with its phenyl group and a large band gap of between 4 eV to 5.1 eV, as measured by UV-Vis-spectroscopy and calculated by density functional theory (DFT). An overview of molecular orbitals and energy levels as calculated by DFT and the relevant parameters of the latter are given in the appendix Figure 1. Originally investigated for its ferroelectric properties, it quickly became clear that the material conducts current beyond what would be expected as mere leakage. Coupled with the observation that this conductivity appeared to increase over the course of successive measurements, a detailed investigation of the conductive properties, including structural analysis, was deemed a necessary first step in understanding the material.

Here, a short disclaimer is given. Since the films were rough and inhomogeneous, converting the currents into meaningful conductivity values is difficult. However, as the average film thickness varies by not more than a factor of two to three, current is an adequate proxy for conductivity. The research presented in this section focuses mainly on the qualitative investigation of the conducting properties and their dependencies. It is not meant to deliver exact benchmarking, but a first understanding of how and why these materials conduct current on a fundamental level.

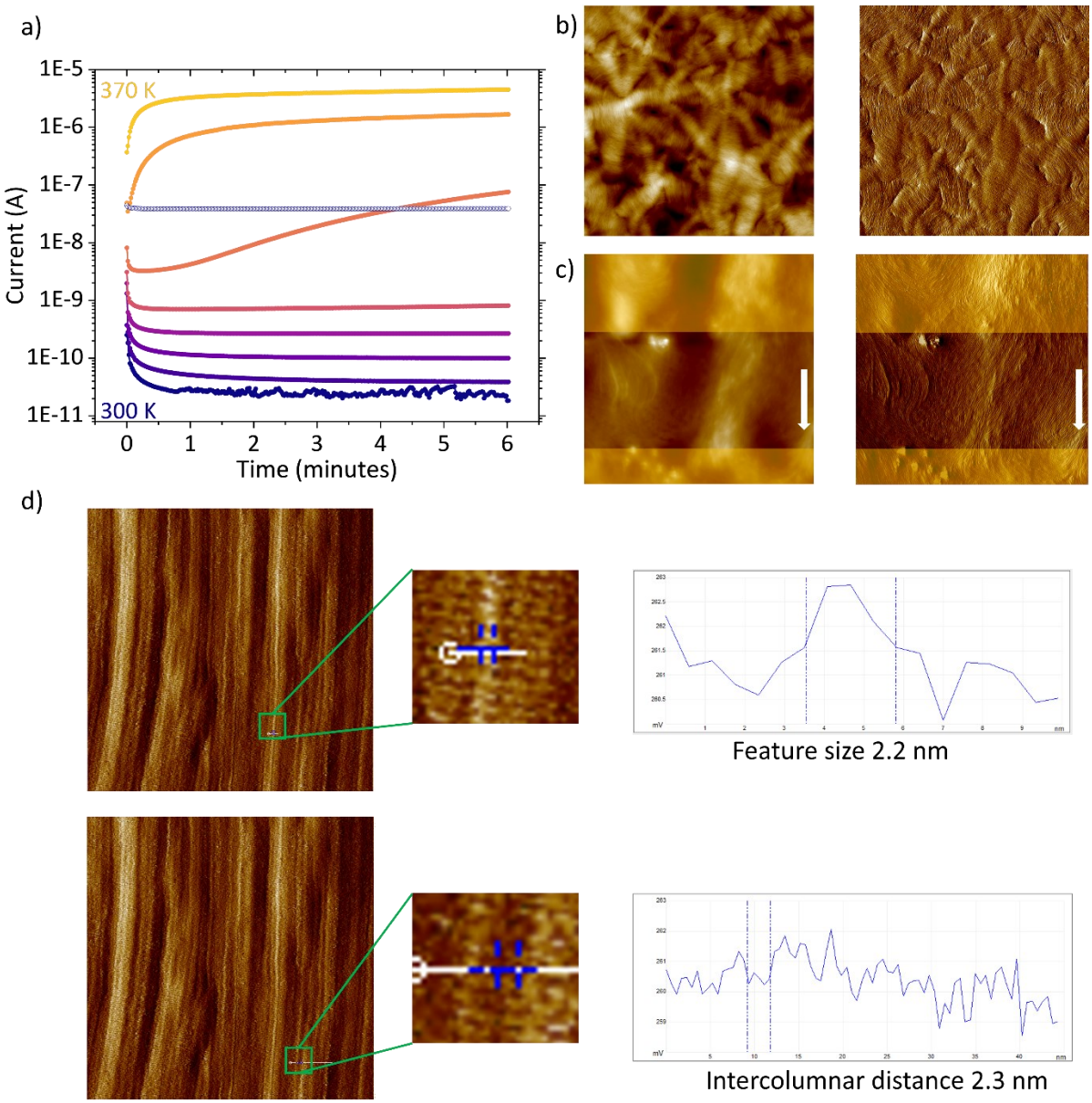

Figure 24. a) Measured current response over time at a constant applied field of a 20 V/µm for increasing temperature in 10 K steps. The empty blue symbols show the current response after cooling back down to 300 K. b) AFM images of a pristine FCH-C3-A film, height channel on the left, amplitude on the right. c) AFM images of an FCH-C3-A film annealed at 370 K for an hour with an externally applied field of 20 V/µm, height channel on the left, amplitude on the right. The image size is 10 x 10 µm. Submerged electrode structures are schematically overlaid in gold and the field direction is indicated by the white arrow. d) High resolution zoom-in of phase image in c) with dimensions of 250 nm x 250 nm that shows the approximate size of and the distance between the supramolecular fibers.

To capture possible effects of restructuring during field application, long-time current measurements at a constant applied voltage were conducted in vacuum for stepwise increasing and decreasing temperatures. The results for an FCH-C3-A film are shown in Figure 24a) for an applied field of 20 V/µm and temperatures ranging from 300-370 K. At

temperatures between 300 k and 340 K a decay in current is observed that plateaus on longer timescales are at a level comparable with currents measured on empty substrates (cf. Figure 25a). The former is attributed to ionic motion and the current amplitudes indicate little to no ability of the material to conduct current. At 350 K, the current begins to strongly increase during the measurement, which continues at higher temperatures. Over the whole temperature range an increase in conductivity of nearly six orders of magnitude is observed, indicating a temperature activated conductivity mechanism.

After cooling back down to 300 K, the conductivity remains permanently enhanced, as indicated by the open blue symbols in Figure 24a). This behavior, together with the conductivity increase during single measurements at 350 K and above strongly suggests a change in sample morphology. This was investigated by AFM imaging with the results shown in Figure 24b) and c), were a pristine FCH-C3-A film (drop-casted, molten and cooled down) and a field annealed film are depicted respectively. The pristine film shows local bundles of supramolecular fibers with maximum lengths of around 1-3 µm that are randomly oriented throughout the film. After field annealing the fibers are elongated reaching up to 6 µm and exhibit strong preferential long-range order in direction in the field direction. High resolution AFM images in Figure 24d) allow the identification of single fibers with width and spacing of roughly 2-3 nm. This is comparable to the length of a single FCH-C3-A molecule in the direction from the cyclohexane to the phenyl group, indicating that the supramolecular fibers are created by molecules stacking in normal direction to the cyclohexane rings, similar to what Shyshov *et al*. observed in solution.[45] This is consistent with the expectation that the dipolar groups are aligned into columns.

Fiber bundling is dramatically reduced after field annealing. This paints a consistent picture with the observed conductivity behavior, when considering that the onset of the conductivity increases at elevated temperatures possibly coincides with the beginning of the film morphology changing towards long-range ordered fibers. Enhanced conducting properties as a result of long-range ordering has been observed previously in organic polymers and is commonly attributed to an increase in crystallinity[171,172], while the supramolecular polymerization via field annealing bears a strong resemblance to what has been found in solution before[45] and in films of the liquid crystalline BTA.[173] It has to be noted that the sample measured in Figure 24a) does not exhibit the same degree of alignment after the

measurement, only for longer field annealing times images as in Figure 24c) are obtained. A natural explanation is that AFM is only probing the surface of the film, which is heated up less than the material at the substrate interface. Together with a smaller effective electric field owing to the curvature of the field lines, this results in the material at the top being aligned at a significantly slower rate than at the film/substrate interface.

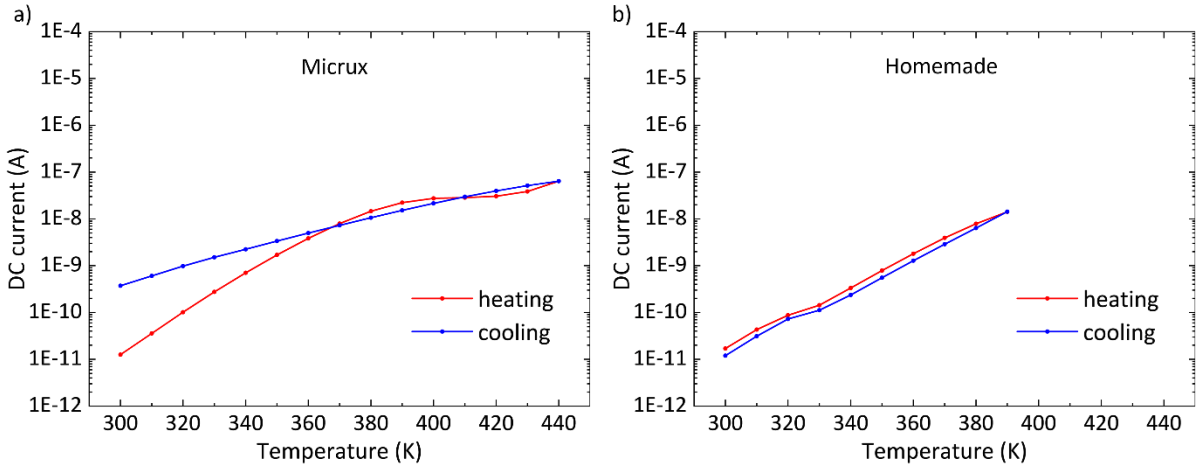

Figure 25. Measured DC-current at a constant applied field of 20 V/µm against temperature for an empty commercial Micrux IDE a) and an empty homemade b) IDE. The raw data is given in the appendix Figure 5.

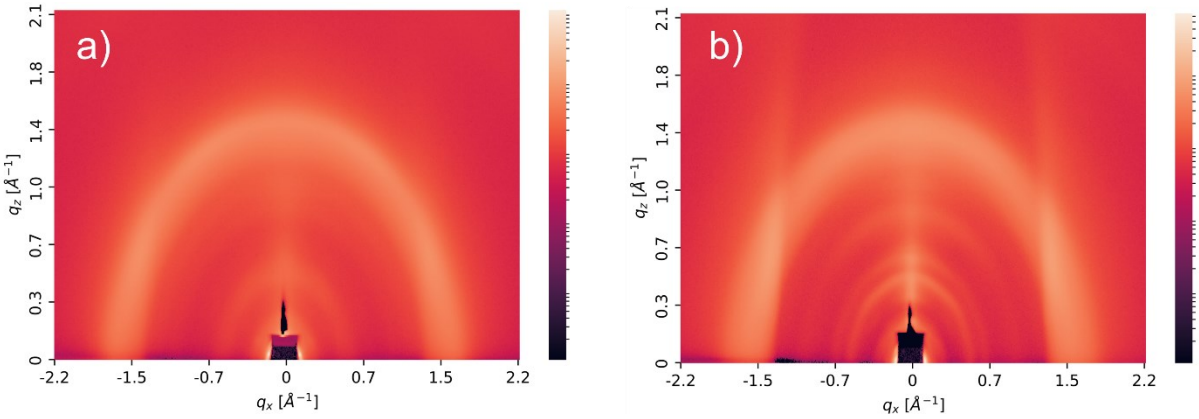

Figure 26. GIWAXS images of an FCH-C3-A film, before a) and after field annealing at 370 K under a constant applied field of 20 V/µm for 1 hour. The increased number of visible scattering reflexes at lower q-values indicates improved crystallinity after field annealing.

The structural analysis was finalized by GIWAXS measurements shown in Figure 26, that confirm the fiber spacing of around 2 nm obtained from AFM imaging and suggest a molecular stacking distance along the fiber axis of around 0.4 nm. The number of visible scattering reflexes increases after field annealing, hinting towards more discrete distances and heightened crystallinity, agreeing with the observation from AFM imaging.

To verify that FCH-C3-A truly exhibits DC-conductivity and to exclude transient phenomena, extended long-time (20 hours) current measurements were conducted at 370 K under an applied field of 20 V/µm in vacuum, the results are depicted in Figure 27. In the beginning of the current measurement, the formation and increasing long-range alignment of supramolecular fibers results in a steep increase in conductivity. A maximum is reached after about an hour measurement time and the conductivity transitions into a soft roll-off. A possible explanation for this behavior is found in the AFM images in Figure 27 (top – height and bottom – phase). As expected, the pristine films exhibit no long-range ordering. However, at the end of the 20-hour measurement, the fibers are not only aligned but also accumulated on top of the electrodes. The material is seemingly displaced by the applied field onto the electrodes. A natural explanation for the observed behavior is that long-range alignment and displacement are two competing effects, which results in the observed current versus time behavior. It has to be noted that the morphology changes drastically accelerate with increasing temperature and decelerate at lower temperatures. The latter enables a more controlled annealing procedure.

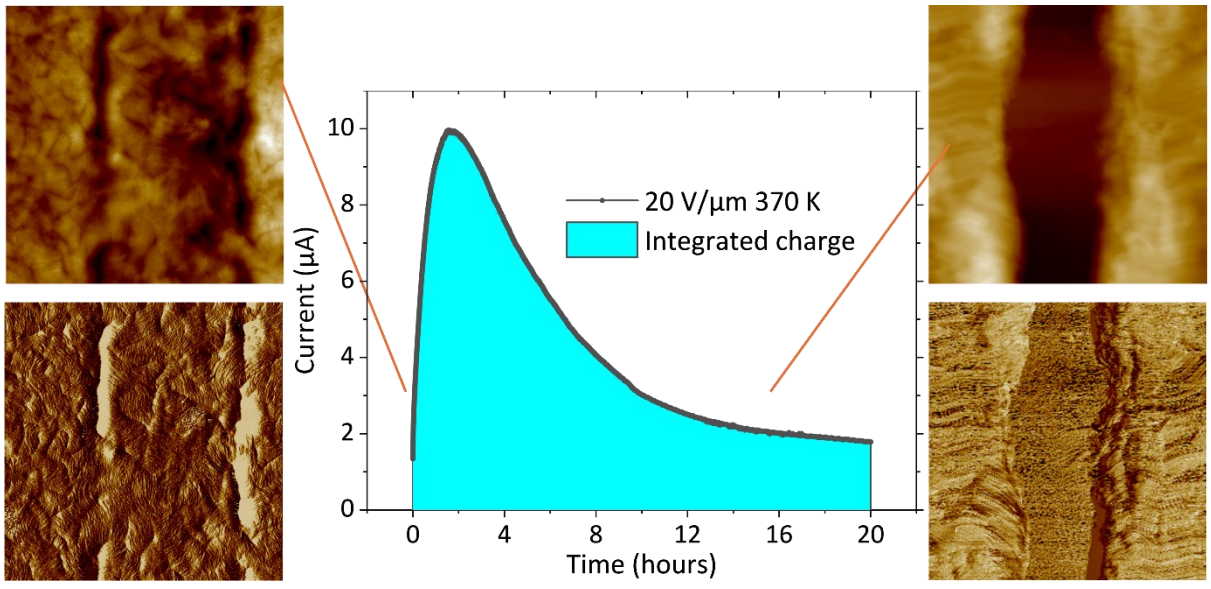

Figure 27. Long time current measurement of an FCH-C3-A film at 370K under a constant applied field of 20 V/µm with the cyan area indicating the conducted charge over the measurement, amounting to 307 mC. In the beginning of the measurement, field annealing drives the long-range ordering of the fibers resulting in a steep increase in conductivity that reaches its peak after an hour has passed and transitions into a soft roll-off. The 10 µm x 10 µm AFM images depict the corresponding surface topography at different stages of the alignment process, showing the unaligned bundles at the beginning and oriented fibers in the end. Surprisingly, most of the material is then found on top of the

electrodes, seemingly displaced by the applied field, which is a possible explanation for the observed roll-off.

Integrating the current over the shown measurement time yields a total charge of 307 mC. Comparing this with the maximally possible number of charged monomers, which is reached when every single monomer in the film is ionized, gives an answer to the question whether the long-time current could be caused by material degradation. Assuming a film drop-casted with 5 x 5 µL = 25 µL from a solution with a concentration of 20 mg/mL gives an upper limit of 500 µg FCH-C3-A in the film. With a molecular weight of 1003 u or $1.67 \cdot 10^{15}$ µg the film consists of roughly $3 \cdot 10^{17}$molecules. In the extreme case where every single one is ionized irreversibly, a total charge of 48.1 mC is obtained, which is exceeded by a factor of more than six by the measured charge in Figure 27. Therefore, material degradation cannot be the origin of the observed current.

Another possible cause could be the formation of an electric double layer. To calculate the upper limit of possible charge originating from double layer formation, we assume a high dielectric constant of 10. The total electrode surface area including the sides and the top amounts to 2.16 mm^2. With $C = \epsilon A/d$ and an understated double layer thickness of 0.4 nm, a double layer capacitance of 191.5 nF is obtained, which corresponds to a charge of 38.3 µC when applying 20 V/µm. Again, this is small compared to the integrated charge from the current measurement in Figure 27 and excludes double layer formation from causing the current.

Ionic impurities as origin of the conductivity were excluded from X-ray spectroscopy data, as shown in the appendix Figure 6, as the impurity concentration is far too small compared to the measured flown charge. Finally, proton conductivity can be excluded, as the conductivity in FCH-C3-A is observed at temperatures well below its melting point, in high vacuum and at temperatures above the evaporation temperature of H_2O.[174]

After excluding almost all other possibilities, electronic charge transport emerged as the likeliest candidate for the observed conductivity, which is truly DC in nature.

Further investigations showed that FCH-C3-A films can be arbitrarily switched between their high and low conductivity state, as melting the films returns their conductivity to the pristine level, see Figure 28a), while renewed field annealing restores the conductivity enhancement.

This is a further argument against film degradation. The state of enhanced conductivity at room temperature resets almost completely after remaining one week at ambient air, as shown in Figure 28b). Since the film alignment persists, the reduction in conductivity is hypothesized to be caused by the formation of oxygen and/or water traps, which is commonly observed for organic semiconductors.[175,176] Successive field annealing in vacuum restores the original state. Leaving the sample one week in vacuum leads to only a very minor reduction in conductivity, further supporting the trap hypothesis.

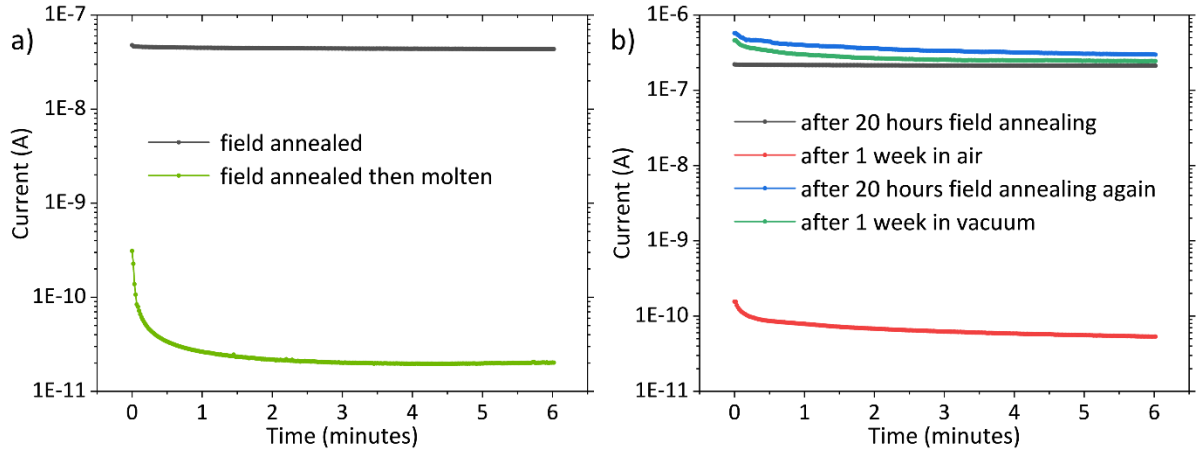

Figure 28. Current measurements of an FCH-C3-A device under a constant applied field of 20 V/µm at 300 K. a) Shows a device measured after field annealing (black) and after successive melting (green). The conductivity enhancement is undone by melting the film. Field annealing the device again will revert it into the state of enhanced conductivity again. b) Stability of the permanently enhanced conductivity at 300 K with the black line as the starting point, measured after long-time field annealing. Leaving the film in ambient air for a week results in the loss of conductivity (red line). Successive field annealing in vacuum recovers the original state (blue). Leaving the sample one week in vacuum leads to only a very minor reduction in conductivity (green).

In addition to FCH-C3-A, two closely related molecular derivatives were studied, FCH-C2-A and FCH-C4-A, with the only difference being the length of the carbon atom chain (also called the spacer) between the pentafluorocyclohexane group and the amide group. Both derivatives exhibit similar conductive behavior, which is again coupled with morphology changes resulting in supramolecular fiber formation, see appendix Figure 8. However, there is one difference found in the temperature dependence. Since scanning differential calorimetry (DSC) data indicate a continuous decrease in melting point with carbon spacer length, shown in appendix Figure 11, the maximum temperature in the temperature dependent current measurements was adjusted accordingly. The variance in melting point

stems presumably from different degrees of rigidity and therefore stability, which are anti-proportional to the spacer length. Temperature dependent current measurements under constant applied field for FCH-C2-A and FCH-C4-A are presented in Figure 29a) and b). The quantitative behavior of the conductivity with temperature is identical to what was observed in FCH-C3-A, an increase in conductivity over five to six orders of magnitude and a permanently enhanced conductivity at room temperature. Only the onset of the increase and presumably of the fiber alignment process occurs at different temperatures. In Figure 29c) the DC-current of the three FCH-C*n*-As is plotted against the temperature, showing how the temperature dependence of the conductivity rise correlates with the respective melting points. This is an example of how relevant parameters in organic systems can be tuned via chemical engineering.

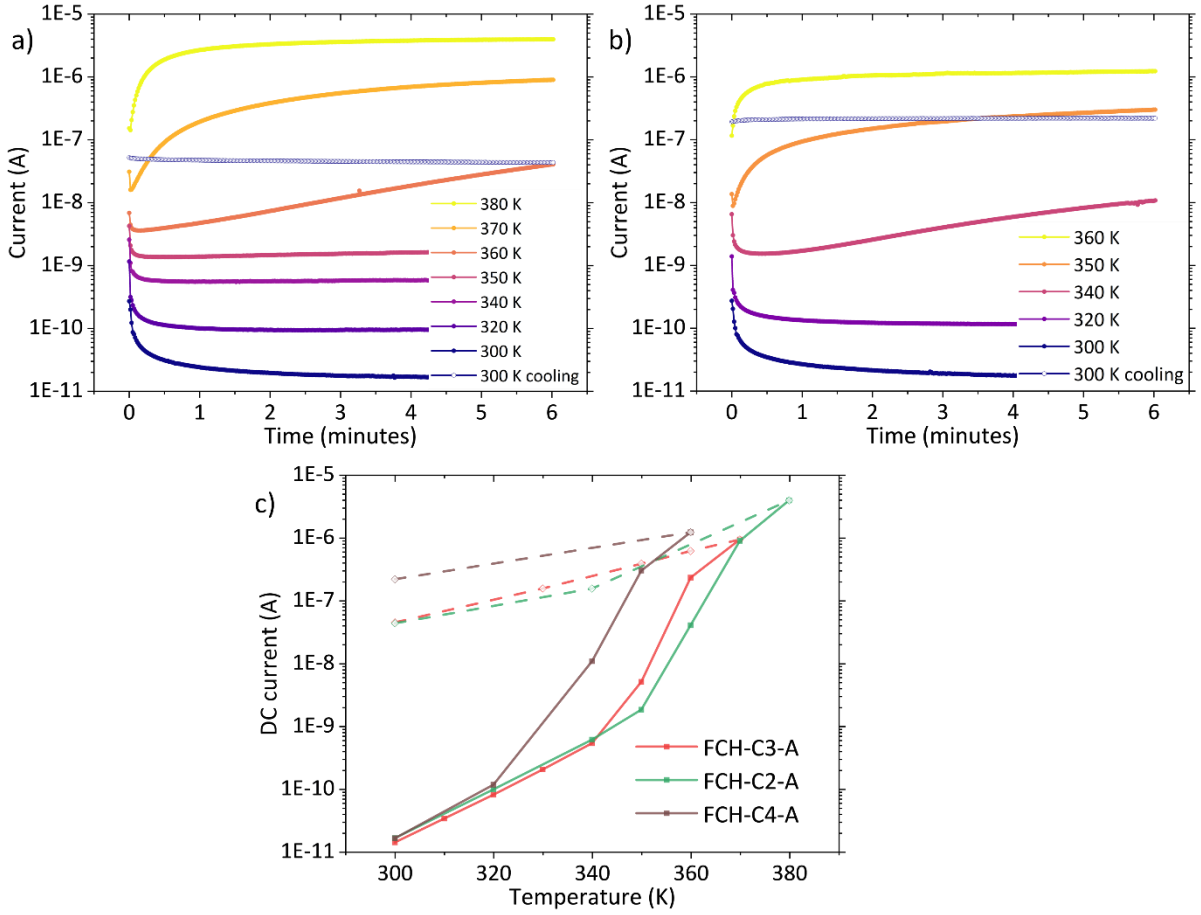

Figure 29. Currents measured under a constant applied field of 20 V/µm at increasing (closed symbols) and decreasing (open symbols) temperatures for FCH-C2-A a) and FCH-C4-A b). Both materials show analogous behavior to FCH-C3-A, with the onset of increasing conductivity shifted in relation to the corresponding melting point of the materials; see DSC traces in appendix Figure 11. This trend becomes clearer when looking at c), where the DC-

current taken from $IV(t)$ measurements is plotted against temperature for all FCH-C*n*-A materials. Solid lines indicate increasing temperatures, dashed lines decreasing temperatures.

4.2 Molecular origin of the conductivity

Following the discovery of the conducting properties of FCH-C3-A and their categorization as truly DC, the question remains what molecular properties/moieties enable electronic conduction in a material that should be insulating. A natural assumption would be that the π-system of the phenyl group governs the charge transport. A second possibility might be charge hopping along the amide groups, as proposed for charge hopping in peptides by Arikuma *et al.*[11,12] More information about the charge transport could therefore be expected from measurements of molecular derivatives with modifications to, or lack of either of the relevant molecular groups. For this reason, the molecules FCH-C3-TA and FCH-E were investigated. The former has the same structure as FCH-C3-A, except that the oxygen atom of the amide group is replaced by a sulfur atom. In the latter, the amide group and the carbon spacer are completely missing.

Analogous DC-current measurements as for FCH-C3-A were conducted and are depicted in Figure 30a) and b). As before, the temperature range was chosen to keep the same relative distance from the melting point as with FCH-C3-A. For FCH-E, the short transient decay in the beginning can again be attributed to ionic motion. While the conductivity rises by two orders of magnitude with increasing temperature, it does only barely exceed the background conductivity of the substrate, if at all (cf. Figure 25). A direct background correction for all measurements was not possible, as the background currents measured on the IDE were varying by up to a factor of two between different substrates and each film would have required a full separate background measurement beforehand. For FCH-E, even at elevated temperatures, no current increase is observed during the measurements and the conductivity reverts to its original value after cooling down. For this reason, the current observed in FCH-E is classified as leakage current of the material and the substrate. The AFM images in Figure 30c) indicate that FCH-E does not form supramolecular fibers and only minor structural changes after observed after annealing. An increase in crystallinity is indicated by the sharpening of the scattering reflexes in the GIWAXS measurements shown in Figure 30e), which does not appear to affect the conducting properties.

For FCH-C3-TA, the IV(*t*) curves paint a very different picture compared to both FCH-C3 A and FCH-E. While the 300K measurement differs only slightly from the background current of the substrate and is in the same order of magnitude as for the other FCHs, already at 310 K a significantly increased conductivity is observed. The rise in conductivity occurs already at low temperatures and does not exhibit the steep increase observed in the FCH-C*n*-As while ultimately reaching currents of a similar magnitude at the highest temperatures. At 360 K, the currents begin to slightly increase over time, however not in a comparable way to FCH-C3-A. After cooling back down, the conductivity falls back to its original value. This suggests a lack of permanent, conductivity enhancing, structural reordering, which is confirmed by the AFM images in Figure 30d). While the structure of the film changes from rather featureless to the appearance of small bundles of short fibers during field annealing, these are randomly oriented and not aligned along the field direction. Again, GIWAXS indicates an increase in crystallinity, but the structural changes do not result in a change of the remnant conductivity. It has to be noted that FCH-C3-TA also proved less stable over long-time measurements at the highest temperatures, showing signs of degradation in *IV(t)* and structural measurements after 5-10 hours. A complete series of AFM images is presented in appendix Figure 7.

Comparing the conducting properties of FCH-E, FCH-C3-TA and FCH-C3-A allows drawing first conclusions about the possible origin of the conductivity. FCH-C3-A demonstrates an enhanced conductivity at elevated temperatures that is accompanied by long-range ordering of supramolecular fibers and remains on a high level after cooldown and annealing. The sulfur substituted version FCH-C3-TA starts to conduct already at lower temperatures and reaches similar current magnitudes at higher temperatures, but the conductivity resets after cooling down and no long-range alignment of fibers occurs. This suggests on the one hand that the formation of long-range ordered supramolecular fibers is beneficial but not necessary for the charge transport and on the other hand that the sulfur substitution facilitates conductivity at low temperatures. Substituting the oxygen atom of an amide group by a less electronegative sulfur is known to decrease the ionization energy, which is underlined by the increase in HOMO level of FCH-C3-TA by between 0.13 eV and 0.76 eV compared to FCH-C3-A (-5.6 eV/-5.71 eV and -5.73/-6.47 eV respectively, cf. appendix Figure 1). The first values were determined experimentally via cyclic voltammetry and the second values from DFT calculations. In the case of hole injection from the gold electrodes into the organic film, FCH-

C3-TA has a lower injection barrier, giving a possible explanation as to why it starts conducting at lower temperatures than FCH-C3-A. The lack of significant conductivity in FCH-E is a strong indicator that the π-system of the phenyl group is not the driving force behind the conduction and a comparison with FCH-C3-TA suggests that a lack of long-range ordering is not a hinderance. From this it becomes clear that the missing amide group appears to play a significant role, which is further reinforced by the DFT calculations showing that the HOMO is at least partially localized on the nitrogen atom of the amide group in all materials exhibiting enhanced conductivity. On FCH-C3-A and FCH-E, the electron wavefunction is predominantly sitting on the phenyl group, while shifting more onto the thioamide group for FCH-C3-TA, in line with the shift to higher HOMO energies upon replacing the oxygen of the amide group by sulfur. With FCH-C3-A and FCH-C3-TA showing a pronounced conductivity and FCH-E not, this corroborates that the π-system is not essential for charge transport in these materials.

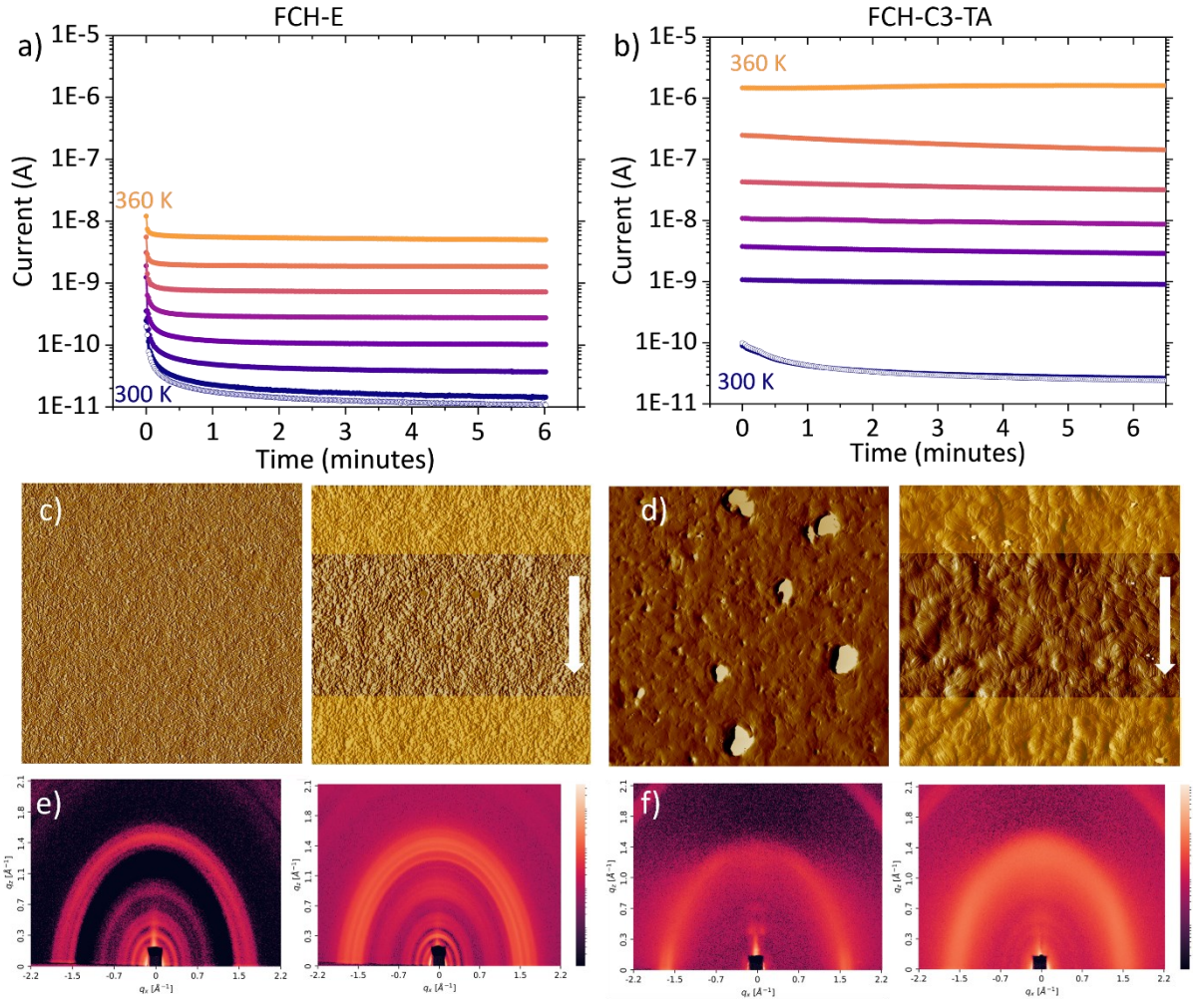

Figure 30. Currents measured under constant field application of 20 V/µm and stepwise temperature increase (ΔT = 10 K) for FCH-E a) and FCH-C3-TA. The empty symbols depict the

current at 300 K after cooling back down. The y-axis is chosen to facilitate comparison to Figure 24a). Measured on Micrux IDE. c) and d) are AFM amplitude images of FCH-E and FCH-C3-TA respectively, taken before (left) and after (right) field annealing at 360 K for one hour. The white arrow indicates the field direction, and the electrodes are overlaid in gold. Corresponding height images can be found in the appendix Figure 7. e) and f) GIWAXS data of the samples from c) and d).

4.3 Charge injection and charge transport

The observed conductivity in FCH-C3-A and some of its derivatives is completely unexpected, considering the lack of an extended π-system and the large HOMO (-5.73 eV/-6.47 eV) -LUMO (-1.73 eV/-1.31 eV) gap of 4.0 eV/5.16 eV, as obtained by cyclic voltammetry and from DFT calculations (cf. appendix Figure 1) respectively. After a lot of alternative explanations were ruled out section 4.1, the most sensible assumption is conductivity of electronic nature. With a substantial bandgap and in the absence of intentional or unintentional doping, which was deemed rather improbable as the impurity content was found to be small, no free charge carriers should be present in the material in the dark. This leaves solely charge injection from the gold electrons as mobile carrier source. However, with a gold work function of around -4.5 eV[177] and a HOMO of -5.73 eV/-6.47 eV, the hole injection barrier at the organic/gold interface is around 1eV to 2 eV, meaning next to no charges should be injected. The magnitude of the currents observed in the DC measurements as well as the space-charge limited current behavior presented later in the text in section 4.5 suggest that the injection barrier has to be reduced in some way.

Materials with permanent dipole moments have been shown previously to facilitate charge injection by barrier reduction when the dipoles are aligned along the field.[140] As demonstrated in a later section, FCH-C3-A and FCH-E are ferroelectric and FCH-C3-TA at least demonstrates dipolar activity. Therefore, all of the conducting materials are able to reduce the injection barrier that can be estimated by considering the potential shift due to a dipolar interface layer:

$$\Delta V = \frac{P_{\mathrm{r}}}{\epsilon_0 \epsilon_{\mathrm{r}}} d_{\mathrm{typ}} \tag{40}$$

Here P_r is the remnant dipolar polarization and d_{typ} the typical thickness of one interfacial dipole layer. The measurement of P_{r} in FCH-C3-A is not straight forward, as shown later in section 5.1. An approximate theoretical estimation is obtained by combining the dipole moment of the fluorinated cyclohexane ring, 6.2 Debye, with that of the amide group, 3.7

Debye, and dividing it by the molecular volume of around 0.4 nm^3. This gives a polarization of around 83 mC/m^2 which together with a typical static ϵ_r of 2-3 for organic materials results in a barrier reduction ΔV of around 1.87 eV to 1.25 eV. The reduced injection barrier for holes is then vanishingly small, enabling charge injection especially at higher temperatures and fields. The influence of the interface dipole density could be confirmed via Kelvin probe force microscopy, where potential steps of around 1 V were measured at the gold-organic interface, see appendix Figure 9. The minor deviation of the measured value from the theoretical ΔV is not surprising, as in a real film the material directly at the electrode edge might slightly misaligned. When using aluminum electrodes instead, the remaining barrier is expected to be 0.4-0.5 eV larger, ensuing a more limited injection. Experimentally, this indeed results in a reduction in current magnitude by more than a factor of two compared to gold electrodes, as seen in Figure 31, reinforcing the envisioned injection process. For FCH-C3-TA, the lower lying HOMO results in a smaller injection barrier from the start, explaining the earlier onset of enhanced conduction compared to FCH-C3-A.

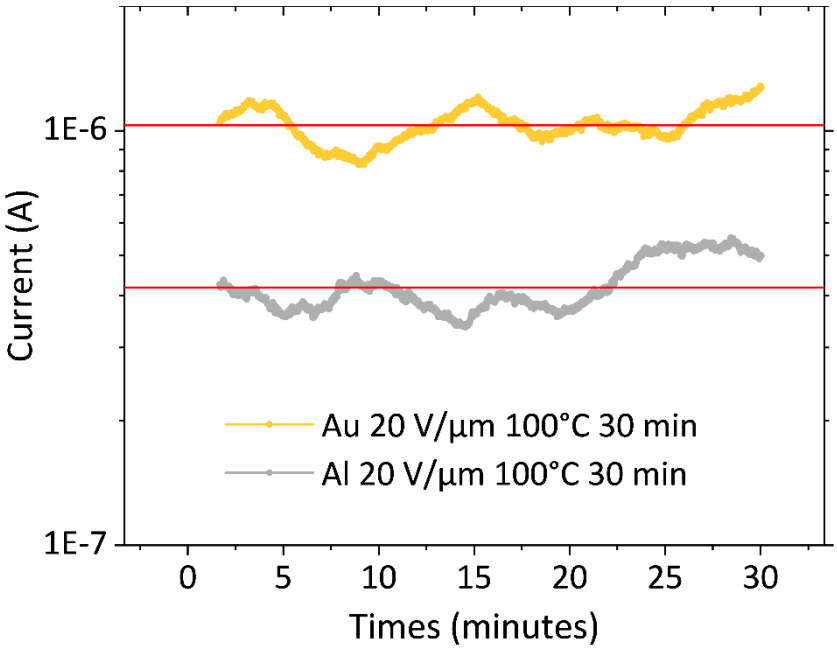

Figure 31. Current measured in FCH-C3-A films under application of a constant field of 20 V/µm at 100°C for gold and aluminum IDE. Both films were drop-casted in the same way from the same solution and treated/measured identically. The observed oscillations are a result of temperature variations owed to the PID control of the setup.

With the dipole density reducing the hole injection barrier, FCH-C3-A can be oxidized by electron transfer to the metal electrode. The charge transport in the bulk occurs then by inter-molecular charge transfer between adjacent molecules, which is facilitated by the formation

of long-range ordered supramolecular fibers. A schematic of the charge transport mechanism is presented in Figure 32, with real space depicted in the top row where the molecules are sandwiched between electrodes and the corresponding picture in energy space below. a) shows the system without external stimuli, at zero field and low temperature. In b) the external field is applied, but its magnitude and/or the temperature are too low, the molecules and their dipoles remain disordered, and the charge injection barrier remains unsurmountable. Once the combination of field and temperature is sufficient, the molecules and their dipoles align, and the resulting polarization leads to a reduction in charge injection barrier height as described above. Now oxidation is possible, charges can be injected and transported. It has to be noted that the crucial part for charge injection is the dipolar alignment, not the structural alignment of the molecules. The former causes injection barrier height reduction while the latter facilitates intermolecular charge transfer in the bulk and is not per se required for this kind of conductivity, as demonstrated by FCH-C3-TA. From the lack of conductivity found in FCH-E it is natural to assume that the (thio)amide group plays an important role in the oxidation process, i.e. the electron transfer to the electrodes.

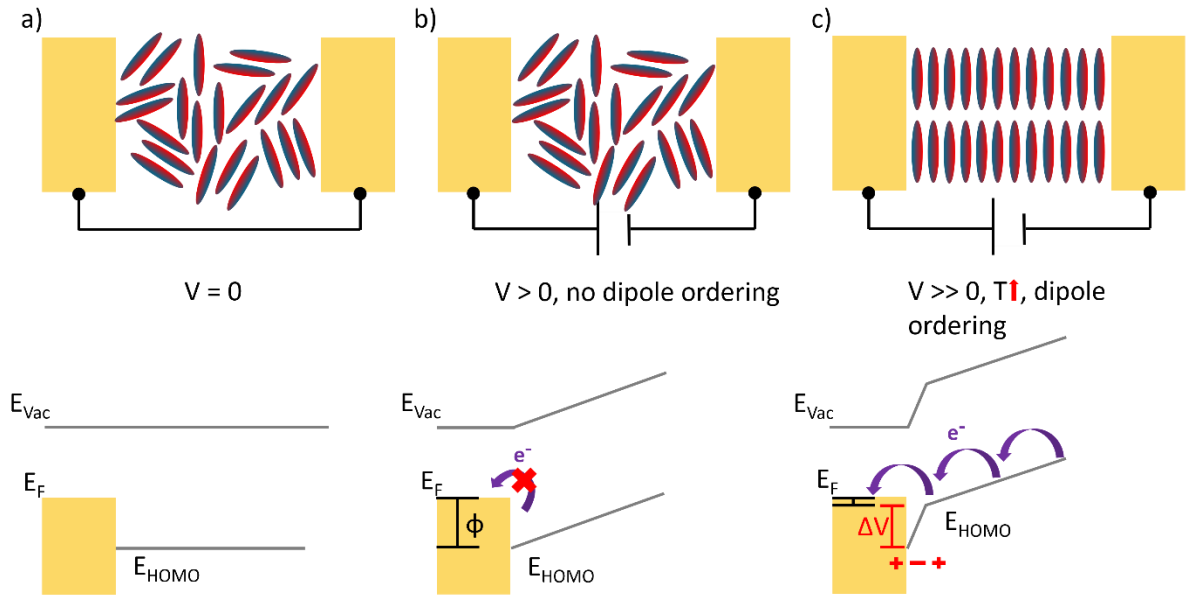

Figure 32. Schematic of the proposed charge transport mechanism in thin films of the investigated molecular compounds. The upper row depicts real space where the molecules containing dipoles are sandwiched between metal electrodes and the corresponding energy space picture is shown below. a) shows the system in its pristine state without an applied external field. The molecules are disordered and the total dipole moment averages to zero. In b) an external field is applied, however, it is of insufficient magnitude and/or the temperature is too low. As a result, the molecules stay disordered, no macro dipole is

formed and the injection barrier ϕ remains high. c) The combination of temperature and field is sufficient to induce molecular and dipolar ordering, resulting in the reduction of the injection barrier, enabling oxidation of the organic and intermolecular charge transport.

4.4 Generalization of the DC-conductivity in materials without extended π-system

Recalling the DC-current measurements of all FCH derivatives, a general list of requirements can be found, which, if satisfied, should enable and/or enhance this new kind of conductivity that does not require π-conjugation: (i) the presence of and oxidation center, (ii) strong dipoles and (iii) supramolecular polymerization by hydrogen(h)-bonding. To test the generality of this hypothesis, further compounds that are known or expected to meet these criteria were investigated. The first class of materials that chosen were the molecular discotics trialkylbenzene-1,3,5-tricarboxamide (BTA) and trialkylbenzene-1,3,5-triscarbothioamide (BTTA), that exhibit pronounced self-organization by H-bonding into stacks of supramolecular columns.[178] Arranged in a hexagonal lattice, the molecular stacks transition to a liquid crystalline phase at room temperature or slightly above. Similar to what was shown for FCH-C3-A, field annealing aligns the columns along the electric field direction. Each molecule possesses three amide groups attached to their benzene core with a combined dipole moment of 12 Debye that can be aligned along the stacks to obtain a switchable polarization. The thioamide variant BTTA was previously reported to show substantial “leakage” currents at elevated temperatures, which were tentatively attributed to electrochemical reactions induced by the sulfur in the vicinity of noble metals.[179]

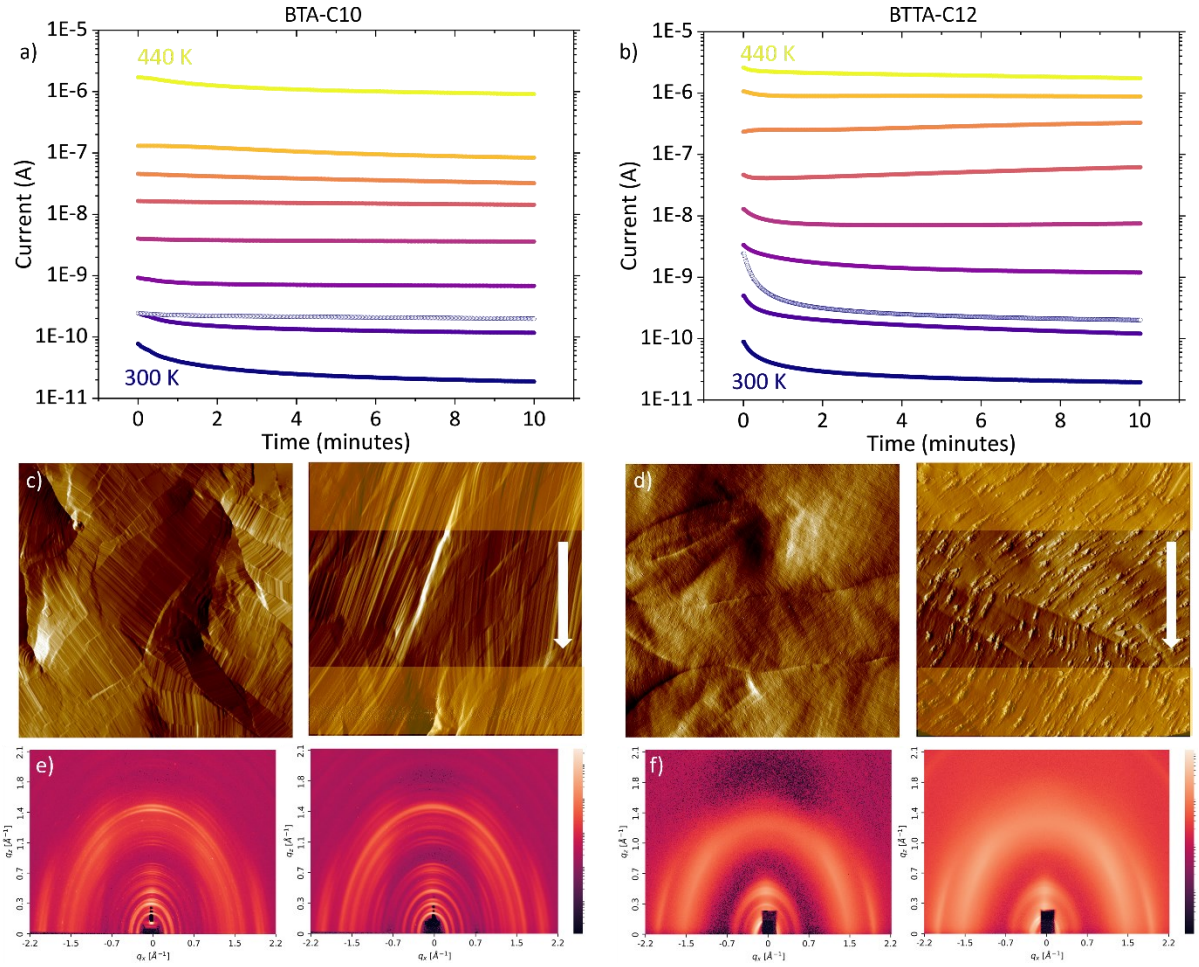

Figure 33. Currents measured under constant field application of 20 V/µm and stepwise temperature increase (ΔT = 20 K) for BTA-C10 a) and BTTA-C12. The empty symbols depict the current at 300 K after cooling back down. The y-axis is chosen to facilitate comparison to Figure 24a). Measured on Micrux IDE. c) and d) are AFM amplitude images of BTA-C10 and BTTA-C12 respectively, taken before (left) and after (right) field annealing via measurements in a) and b). The white arrow indicates the field direction, and the electrodes are overlaid in gold. Corresponding height images can be found in the appendix Figure 10. e) and f) GIWAXS data of the samples from c) and d).

Results of temperature-dependent current measurements under constant applied field on BTA-C10 and BTTA-C12 (see Figure 19a) and b) films on IDE are depicted in Figure 33a) and b) respectively. As the melting points of both materials lie beyond 470 K, the temperature range was adjusted accordingly.[108,179] BTA-C10 does indeed exhibit a DC-conductivity at temperatures beyond 390 K, however at temperatures below the currents are barely above the leakage currents of the substrate. No clear onset of long-range ordering is found during the temperature sweep and while the conductivity after cooldown at 300 K is slightly enhanced, this might just be a result of increased leakage substrate currents, cf. Figure 25. Nevertheless, the AFM images shown in Figure 33c) indicate significant long-range ordering

of supramolecular columns in direction of the applied field and the slightly sharper scattering reflexes observed in the GIWAXS data suggest a minor increase in crystallinity. The reduced conductivity compared to the conducting FCHs and the lack of a significant long-range alignment effect on the conductive properties is not unexpected. Considering that the HOMO level of BTA-C10 lies at -7.13 eV (cf. appendix Figure 2), the resulting energy barrier for hole injection amounts to roughly 2.6 eV and with a remnant polarization of 45 mC/m^2, the resulting barrier height reduction obtained from equation 40 amounts to around 1 eV. Consequently, the remaining injection barrier is too high for efficient charge injection and only at elevated temperatures the available thermal energy is large enough to enable charge injection. The devices are assumed to be strongly injection limited, overriding possible alignment effects that would influence the bulk behavior.

In comparison, the BTTA-C12 already begins to conduct notably at temperatures above 360 K and reaches slightly higher maximum currents than the BTA-C10. At elevated temperatures a slight increase in current with time is observed during the measurements, however the trend is weaker than for FCH-C3-A. A possible explanation is again the long-range alignment of the supramolecular columns, as suggested by AFM in Figure 33, with the blob-like features possibly indicating the onset of degradation at the highest temperatures. GIWAXS images do not show significant change in scattering reflexes and henceforth in crystallinity. A very slight decree in reflex sharpness corroborates the degradation theory. After cooling back down, a slightly enhanced remnant conductivity on a similar level as the substrate conductivity is observed. These observations fit well with what was found for the BTA-C10. Considering the HOMO level of BTTA-C12 lies a significant amount higher at -5.88 eV and therefore the remaining hole injection barrier to overcome is only around 0.4 eV, allowing for effective charge injection at already lower temperatures. The finite height of the barrier is sufficient that at room temperature no conductivity enhancement occurs.

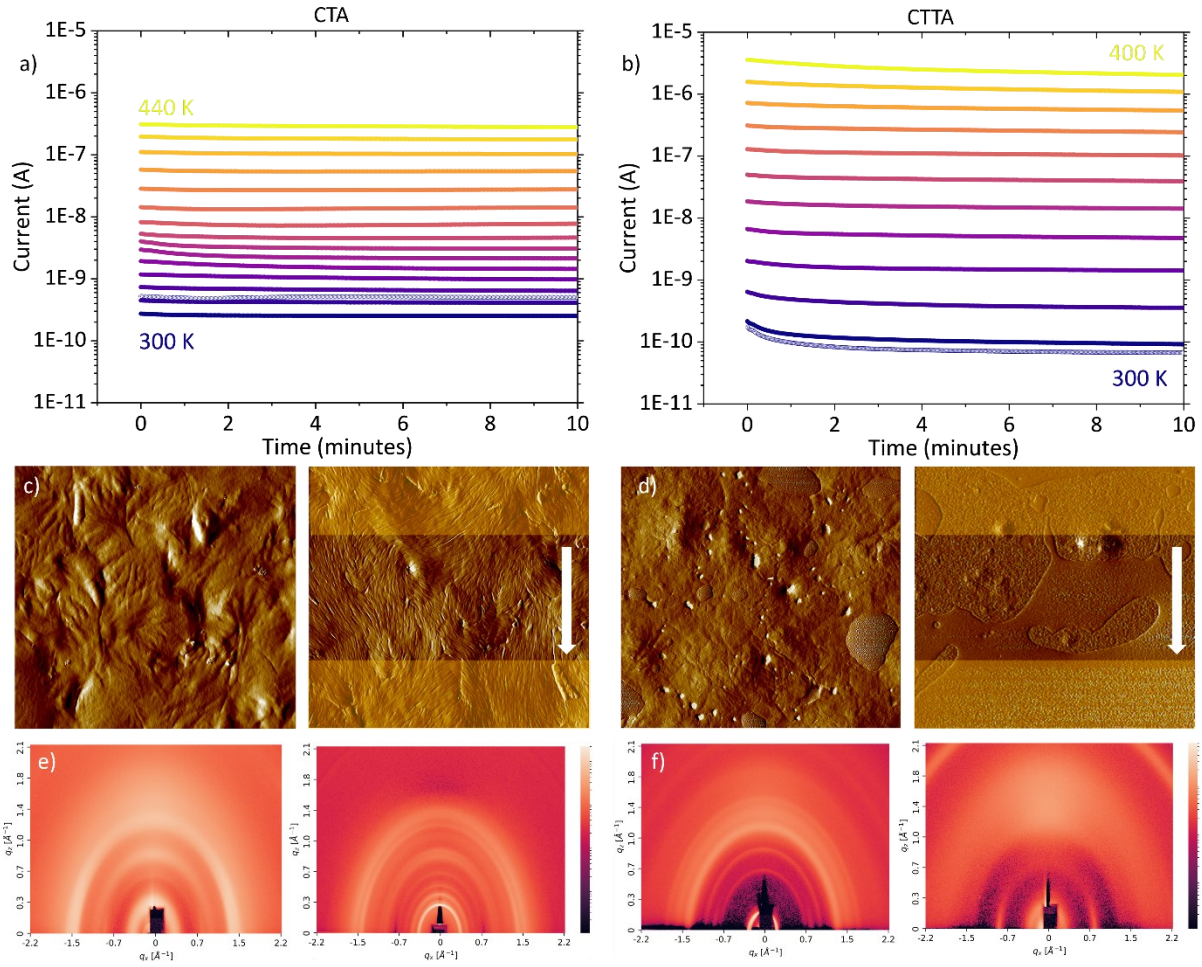

Figure 34. Currents measured under constant field application of 20 V/µm and stepwise temperature increase (ΔT = 10 K) for CTA a) and CTTA. The empty symbols depict the current at 300 K after cooling back down. The y-axis is chosen to facilitate comparison to Figure 24a). Measured on Micrux IDE. c) and d) are AFM amplitude images of CTA and CTTA respectively, taken before (left) and after (right) the measurements in a) and b) were conducted. The white arrow indicates the field direction, and the electrodes are overlaid in gold. Corresponding height images can be found in the appendix Figure 10. e) and f) GIWAXS data of the samples from c) and d).

While the BTAs exhibits similar conducting properties as the FCHs, they all contain a π-conjugated benzene core in addition to the amide groups, again leading to the question of where the conductivity originates. An excellent opportunity to reinforce the hypothesis whether the oxidation of the amide group being the driving factor was the investigation of the cyclohexane tricarboxamides (CTAs) shown in Figure 19c) and d). With a cyclohexane core instead of the π-conjugated benzene core the CTAs are structurally very close to the BTAs, containing the same three amide groups and similar aliphatic chains. The latter are mostly relevant for solubility and the minor differences in those between the BTAs and CTAs should not impact electrical measurements in a meaningful way. Ferroelectric switching has not been

observed yet in CTAs, however the very similar structure to BTA, their tendency to form supramolecular columns and the presence of the dipolar amide groups indicate a strong possibility of a dipolar interface layer.[180] This would be enough to reduce the injection barrier without requiring true ferroelectric polarization switching.

Analogous measurements on CTA and CTTA to those made for the BTAs are shown in Figure 34. Akin to the BTA-C10, the CTA only exceeds the substrate background conductivity in a meaningful way from 420 K on and neither shows an increase in current during a single measurement nor a permanently enhanced remnant conductivity beyond the substrate background conductivity. AFM images show partial long-range alignment and GIWAXS indicates an increase in crystallinity after field annealing, cf. Figure 34c) and e). With a HOMO level of -6.87 eV (cf. appendix Figure 3) and an estimated maximum injection barrier reduction of 1 eV the remaining hole injection barrier is almost as high as for the BTA-C10, explaining the very similar conductive behavior.

The thioamide containing CTTA however, already starts conducting considerably at 320 K and beyond. At the highest temperature of 400 K, the current begins to drop over time. Together with AFM and GIWAXS images of the film before and after measuring, where features smoothen and scattering reflexes disappear respectively, this might point towards the onset of material degradation. Nevertheless, the conductivity behavior is very reminiscent of what was measured for the other thioamide compounds, BTTA-C12 and FCH-C3-TA. Again, the higher lying homo level of -5.71 eV as compared to the CTA and the resulting significantly lower injection barrier result in the CTTAs improved conducting properties. The presence of a DC-conductivity similar to FCHs and BTAs in the CTAs further supports the notion that the charge transport occurs independent of π-conjugated electron systems.

To contextualize the conductivity qualitatively and quantitatively, a series of triphenylamine compounds (TPAs) that contain three peripheral amide groups (cf. Figure 23) were additionally investigated. The TPA-motif is well-established as basis for hole-conducting organic semiconductors, with three phenyl groups connected in a propeller-like fashion to a central nitrogen.[181] DFT calculations show that the HOMO wavefunction is distributed almost evenly over all three phenyl rings and the central nitrogen. Notwithstanding the large degree of delocalization, the HOMO levels and bandgaps are comparable to the FCH compounds, see appendix Figure 4. Similar to the FCH-As, the TPAs exhibit a conductivity increase over

multiple orders of magnitude with rising temperatures and a permanently enhanced conductivity after cooling back down to 300 K, see Figure 35a) and b). The latter can only tentatively be related to structural long-range alignment as AFM images show only minor restructuring and the GIWAXS data likewise indicate only slight changes in crystallinity. Despite extensive research, no dipolar activity was found in any of the TPAs. That the compounds still exhibit a similar behavior in conductivity as the FCH-As, reinforces the notion that the dipolar moieties are required to reduce the injection barrier and not for the charge transport in the bulk itself (see discussion of the CTAs).

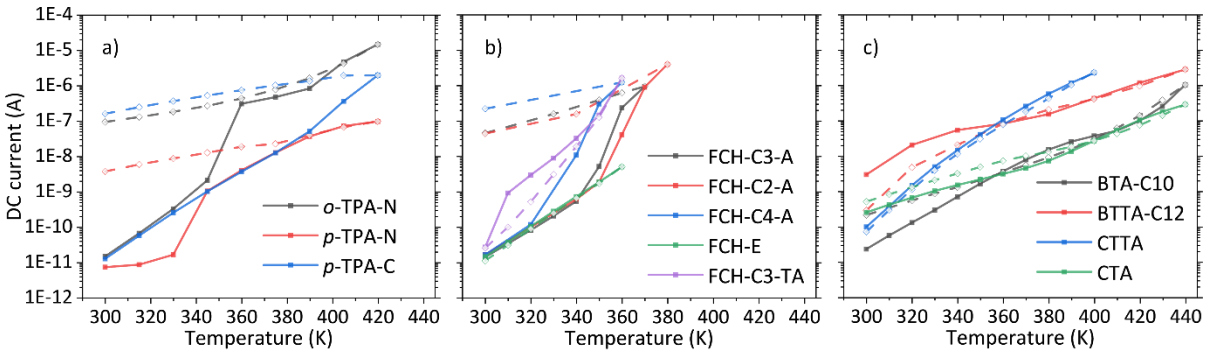

Figure 35. Measured DC-current vs. temperature for increasing (solid lines) and decreasing (dashed lines) temperatures, for (a) TPAs, (b) FCHs and (c) molecular discotics. Current values are measured at 20 V/µm, in quasi-steady state after 6 minutes.

Figure 35 summarizes the temperature dependence of the measured DC-conductivity for all investigated compounds. Besides the qualitatively similar behavior of the TPAs and FCH-As, the contrast between the thioamide compounds and the standard variants is clearly visible. The former consistently exhibit conductive properties already at lower temperatures in agreement with their reduced injection barriers. However, the thioamide compounds tend to be unstable at the higher temperatures, possibly entering a degradation regime, while for the normal variants no degradation was observed. For the thio-variants it remains unclear how much of a role fiber formation and alignment plays, as only the BTTA showed partial ordering that did not result in an enhanced remnant conductivity at room temperature. A direct correlation between long-range ordering and conductivity enhancement was observed for the FCH-C*n*-As, where the formation of supramolecular fibers aligned in field direction resulted in a strong increase in conductivity during a single measurement and in a permanently increased conductivity at room temperature. Similar behavior could be expected of the molecular discotics CTA and BTA-C10 on accord of their tendency to form

supramolecular columns. However, their deeper lying HOMO levels and smaller dipolar densities lead to comparatively bigger charge injection barriers, resulting in the devices becoming injection-limited at lower temperatures, presumably masking possible effects of long-range order and alignment in Figure 32c). As a compound with neither extended π-system nor (thio)amide group, FCH-E showed no significant conductive properties, serving as a necessary control compound.

The measurements so far suggest that the novel, non π-system mandated conductivity found in FCH-C3-A and its derivatives is indeed generalizable to a broader spectrum of organic small molecule compounds, as long as those contain sufficiently strong dipolar moieties and a prospective oxidation center. This enables charge injection and transport in materials commonly assumed to be insulating. Supramolecular polymerization was shown to significantly enhance conductivity but was not mandatory.

4.5 Charge transport mechanism

Insight about the charge transport in the bulk can be obtained from the temperature dependence of the conductivity, as described in section 2.1.2. Using current as proxy for the mobility, it was investigated whether a polaronic, equation 3 or a disorder ansatz, equation 6, describes the behavior best. For that, the logarithmic current of the cooling traces of FCH-C3-A, *o*-TPA-N and *p*-TPA-N from Figure 35 are plotted against the inverse and the squared inverse temperature in Figure 36. This allows fitting of equations 3 and 6 in their linear forms by the Levenberg-Marquardt least squares algorithm.[182,183] Only the materials with permanently enhanced remnant conductivity significantly exceeding the substrate background currents are fitted. The cooling traces were selected over the heating traces to minimize possible effects from morphology changes by field annealing. For the same reason the highest temperatures were disregarded. Both models seem to adequately describe the dependence at lower temperatures with only minor differences in fit quality (see appendix Table 1). The obtained polaron binding energies E_{pol} of approximately 360 meV for FCH-C3-A, 203 meV for *o*-TPA-N and 215 meV for *p*-TPA-N are significantly higher than the typical values for organic semiconductors of around 50 meV to 100 meV.[65] On the other hand, the resulting disorder values from the GDM fits are depending on the choice of the scaling parameter C. For purely disorder mediated hopping, $C \cong 0.44$ and the resulting energetic

disorder σ is about 76 meV for FCH-C3-A, 59 meV for *o*-TPA-N and 57 meV for *p*-TPA-N. These are quite sensible, as typical values for the disorder range between 50 meV to 150 meV.[65,184]

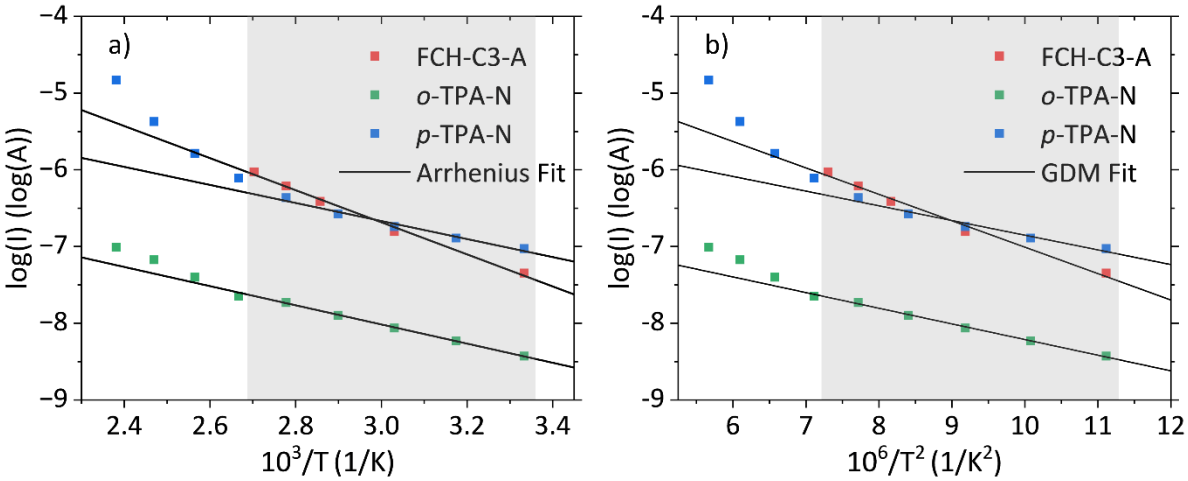

Figure 36. Logarithmic DC-current of FCH-C3-A, *o*-TPA-N and *p*-TPA-N devices when cooling down, plotted against the inverse temperature and the squared inverse temperature. a) shows fitting of an Arrhenius model while b) shows fitting of the Gaussian disorder model. The fitting range is indicated in grey, higher temperatures were excluded to avoid the influence of morphological changes.

Neither the goodness of fit nor the obtained fit parameters allow a decisive conclusion as to what the dominating transport process is or whether and to what degree a mixture of both is observed. However, the polaron binding energies obtained by Arrhenius fitting are considerably larger than typical values, while the energetic disorder from GDM fitting falls in line with commonly obtained values. Coupled with the fact that the critical temperature at which polaronic and disorder effects contribute equally is generally above 650 K, it is reasonable to assume that the GDM model is closest to reality. However, the existence of a small polaronic density cannot be excluded and would not be surprising. Since conventional organic semiconductors with extended π-systems are usually described by the GDM and the fact that FCH-C3-A is described by the GDM model just as well as the TPA compounds reinforces the notion that charge transport in organic materials with and without extended π-system occurs in a similar fashion.

In the previous sections it was assumed that the charge transport occurs by holes that are injected from the contacts, meaning the materials themselves are intrinsic. The lack of a considerable number of free charges at zero field is expected, since doping a material with a HOMO level at -6 eV or below is rather difficult and improbable to occur spontaneously, for

example by impurities. To obtain further corroboration of this hypothesis, the current-voltage (IV) dependence of the materials was characterized. The IVs were taken at room temperature whenever possible, to minimize any unwanted influence from possible morphological changes and/or degradation that might occur at elevated temperatures. For materials that do not show a permanently enhanced conductivity at room temperature, measurements from higher temperatures are considered instead. Figure 37 shows representative IVs of all materials investigated. It turned out that the SCLC-model with coulombic trapping as proposed by Murgatroyd (cf. equation 20) gives good fit results in the medium to high bias regimes for all compounds that exhibit an enhanced remnant conductivity at 300 K, see Figure 37a). This is more evidence that the materials are of intrinsic nature and charges are injected via the contacts, as SCLC-behavior originates from the buildup of space charge in the case of small or vanishing injection barriers, see section 2.1.4. Minor deviations from the SCLC behavior are presumably caused by substrate background currents or depolarization transients, which are too small to be seen at medium to high bias. For the *p*-TPA-N, a battery-like current is observed at low bias, which is attributed to motion of an unknown ionic species that becomes visible in the low bias regime due to the relatively low mobility of this compound.

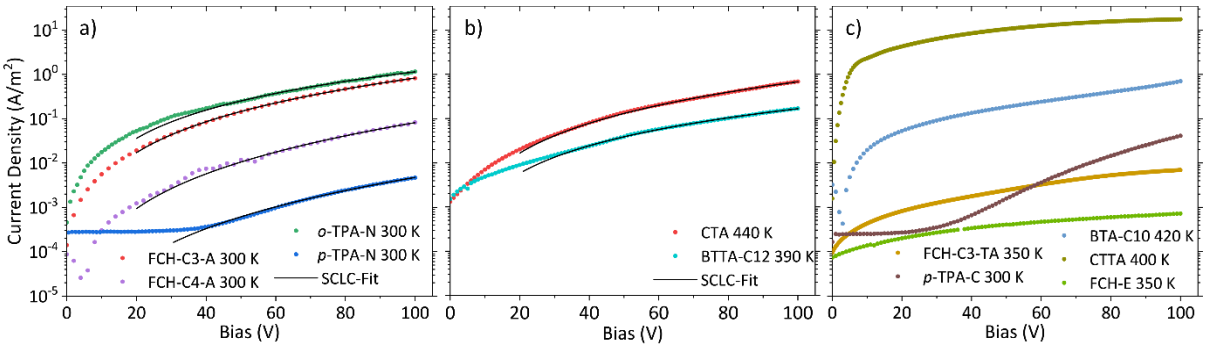

Figure 37. Representative current-voltage characteristics of all investigated compounds. Room temperature measurements are preferred, to minimize the influence from possible dipolar switching, morphological changes and or degradation. a) shows the materials that exhibit SCLC-like conduction at 300 K, b) the materials that exhibit SCLC-like conduction at elevated temperatures and c) the materials that cannot be described by known models, with the exception of FCH-E, which shows linear behavior. All films were measured on IDE with a 5 µm gap.

Of the materials without enhanced remnant conductivity, the CTA and BTTA-C12 clearly show SCLC-behavior at elevated temperatures (Figure 37b), while the rest of the compounds shown in Figure 37c) are not well described by known analytical models. Possible explanations for

this are manifold, for some materials the remaining injection barrier might result in complete or partial injection limited behavior (BTA-C10), for some the underlying dipolar properties might influence the resulting currents either directly (switching current) or indirectly (conductivity modulation) (FCH-C3-TA, BTA-C10) and for the thioamide compounds degradation could be a distorting factor (CTTA, FCH-C3-TA). FCH-E (bright green) poses an exception, demonstrating linear behavior, however, the current does not significantly exceed the background current from the substrate. This is consistent with the notion that the material has no significant conductive properties.

The obtained mobilities from SCLC fitting and the corresponding field dependence factor γ are given in table 1. With zero field mobilities around 10^{-8} to 10^{-6} cm^2/Vs, the materials without a conjugated π-system (FCH-C3/4-A, BTTA-C12, CTA) reach comparable mobility values to the established π-conjugated semiconductor motif TPA.

In this chapter, an unexpected DC-conductivity was discovered in the small organic molecule FCH-C3-A, which does not have an extended π-system. A rise in conductivity of nearly six orders of magnitude was observed in constant voltage current measurements when increasing the sample temperature from 300 K to 370 K. Cooling back down to 300 K revealed a permanently enhanced conductivity by three orders of magnitude compared to the pristine film. This and the observation of a steadily increasing current at temperatures of 340 K and above implied morphological changes due to field annealing. Indeed, the formation of long-range aligned supramolecular fibers after annealing was observed via AFM. Additionally, GIWAXS images showed a sharpening of the scattering reflexes, indicating a more ordered and crystalline structure. From the fiber withs and spacing in the AFM as well from the scattering reflexes it could be inferred that the molecules form fibers by face-to-face stacking, presumably forming separated columns of the individual dipolar groups. Long-time measurements in vacuum and air showed consistent behavior, ruling out proton hopping, degradation or ionic impurities as origin of the DC-conductivity.

Investigations of molecular relatives FCH-C3-TA, where the amide oxygen is replaced by sulfur, and FCH-E, which lacks the amide group completely, indicated the amide group playing a central role in the charge transport. The sulfur substitution in FCH-C3-TA facilitates oxidation of the nitrogen, resulting in an improved conductivity already at lower temperatures without the need for long-range ordering compared to FCH-C3-A, while for FCH-E no enhanced

conductivity was observed. For this reason, the oxidation of the amide group and successive hole transport was hypothesized to be the cause of the conductivity and a possible supramolecular long-range ordering presumed to be helpful, but not essential. All FCHs were shown to exhibit dipolar activity, which proved essential to enable charge injection by lowering the hole injection barrier, e.g. by around 1-2 eV for FCH-C3-A. Additionally, design rules for materials to exhibit this kind of conductivity were formulated: the presence of an oxidizable moiety, a sufficient dipolar density to facilitate injection and helpful but not necessary, the ability to form supramolecular long-range ordered structures. Indeed, similar conducting properties were found in the supramolecular, amide containing discotic systems BTA and CTA, including their sulfur substituted variants. Since the benzene core of BTA contains a π-system which the cyclohexane core of CTA lacks, the observation of similar conducting properties in both reinforced the idea of charge transport independent of the presence of an extended π-system.

Finally, a series of TPA molecules, a well-known semiconducting motif, were shown to exhibit a similar conductivity behavior, implying that the fundamental charge transfer between molecules occurs in a comparable way. This was further reinforced by the observation of SCLC behavior in IV-measurements and a conductivity-temperature dependence following the Gaussian disorder model, with energetic disorder parameters between 57 and 76 meV. Therefore, hole hopping through the bulk after oxidation near the contacts is the presumed charge transport mechanism. From the SCLC fits zero field mobilities of 10^{-8} to 10^{-6} cm^2/Vs were obtained for materials without extended π-system, similar values as for the semiconducting TPAs. Hence, efficient long-range charge transport in organic materials without extended π-system was characterized and proven to be possible.

5. Ferroelectric properties of fluorinated cyclohexane amides

This chapter focuses on the discovery and characterization of the ferroelectric properties of FCH-C3-A and FCH-E and how ferroelectricity is coupled to the conductivity of FCH-C3-A. All measurements and the interpretation and evaluation of the resulting data were carried out by Heiko Mager, the author of this thesis. All figures were created by Heiko Mager. The text was originally written for this section. Significant parts of this section, figures and data, are part of a submitted manuscript. The original text in the manuscript was written by Heiko Mager and revised and improved upon by Martijn Kemerink, Heiko Mager and to a lesser degree by the co-authors.

5.1 Ferroelectricity in FCH-C3-A

The fluorinated cyclohexane amide FCH-C3-A introduced earlier in Figure 18a) is a prospective candidate for ferroelectric behavior. It contains two strong dipolar moieties and undergoes polymerization into supramolecular fibers via H-bonding when field annealed. In the past, these ingredients were commonly found in organic ferroelectrics, with the supramolecular liquid crystalline BTA being a textbook-like example.

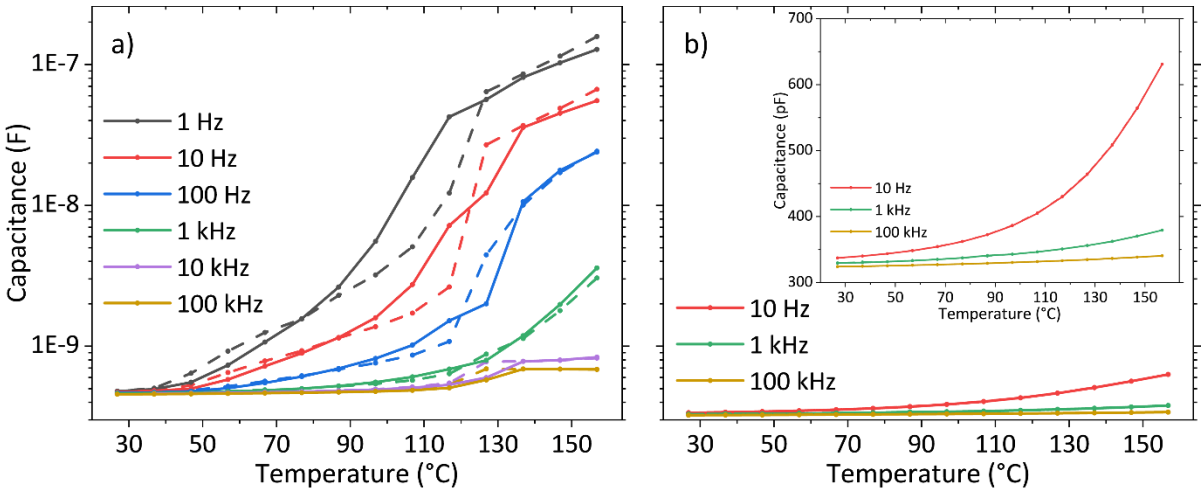

Figure 38. Dielectric spectroscopy data depicting measured capacitance on a logarithmic scale versus temperature at varying frequencies. Solid lines indicate heating traces, dashed line cooling traces. a) FCH-C3-A film on 1 µm IDE. b) DS data from an empty 1 µm IDE at comparable temperatures and frequencies with the same logarithmic y-axis scale. The inset shows the data on a linear scale.

When searching for ferroelectricity in untested materials, it is convenient to scan a vast temperature range for phase transitions, which might be of paraelectric to ferroelectric nature, or vice versa. The two methods usually employed are differential scanning calorimetry (DSC), where the heat flow from and into the material is detected and dielectric spectroscopy (DS) as described in subsection 3.1.3. In the DSC traces of FCH-C3-A shown in appendix Figure 11a) large peaks are observed at about 105°C (378 K) in the cooling trace and 130°C (403 K) in the heating trace, indicating the freezing and melting points respectively. A smaller and broader shoulder appears in both traces at around 75°C (343 K), possibly indicating a further phase transition. However, DS measurements of FCH-C3-A depicted in Figure 38a) lack a pronounced feature in the vicinity of 75°C at all measured frequencies. This leaves two possible explanations for the shoulder observed in the DSC traces. Either it results from a structural transition that does not significantly influence the dielectric properties of the material and is therefore not of paraelectric to ferroelectric nature, or the resulting dielectric response is drowned out by the observed strong general increase in dielectric sensibility. Again, this rules out a ferroic nature of the phase transition, as for those the dielectric response should be a (stronger) singularity at the transition temperature.

The continuous strong rise of the dielectric permittivity during heating up which by far exceeds any contribution from the substrate (cf. Figure 38b) is attributed to a gradual increase in mobility of the dipolar moieties. This continues until the melting point, beyond which the rise in permittivity slows down. As low frequencies exhibit a significantly stronger dielectric response with magnified temperature dependence, it is assumed that the dipolar moieties are not sufficiently mobile to follow the external field at higher frequencies. In the cooling traces the reverse behavior is observed together with a shift of the freezing to lower temperatures relative to the melting point. In neither trace any kind of Curie-Weiß-like behavior is observed, indicating that in this temperature range neither a ferroelectric to paraelectric phase transition nor the reverse case occurs. However, this does not mean that the material is not ferroelectric. As shown later, FCH-C3-A exhibits ferroelectric properties from around 85°C up to the vicinity of the melting point, indicating that the material melts before reaching the transition temperature. This is not uncommon and has been observed for example in the high temperature ferroic phase of $BaMnF_4$ or in blends of pure PVDF and P(VDF-TRFE).[185,186]

While not depicting Curie-Weiß behavior, the DS spectra indicate increased dipolar mobility at elevated temperatures and for low excitation frequencies. With that in mind, low frequency double wave method (DWM) measurements at elevated temperature were the next logical step. For FCH-C3-A, the conductive properties discussed in section 4 have to be kept in mind, as they result in the presence of a significant non-switching background current in all DWM measurements at elevated temperatures. Figure 39a) shows temperature dependent DWM measurements of a pristine FCH-C3-A film on Micrux IDE, with a maximum field of 40 V/µm. At around 85°C a shoulder starts to appear in the first and the third readout pulse. With increasing temperature, the shoulder evolves into a pronounced peak, that progressively shifts towards lower fields.

Possible origins of a peak with such behavior are ferroelectric polarization switching and/or the accumulation of a mobile ionic species at the electrodes. The latter can be ruled out with some confidence since ionic impurities and material degradation as probable sources of mobile ions were excluded previously in section 4.1. Measurements in ambient air and in nitrogen atmosphere show comparable results, excluding chemical reactions as origin. Therefore, polarization switching remains the most likely explanation for the observed current peak. The significant increase in background current is owed to the DC-conductivity of the material. While the resulting hysteresis loops show the characteristic shape of ferroelectric materials at first glance, no proper polarization saturation is observed, and the polarization values are up to eight times larger than the theoretically estimated value of 83 mC/m^2. Since the upper limit of the ferroelectric polarization is given by the dipole density in the bulk, the measured polarization cannot be entirely of ferroic origin.

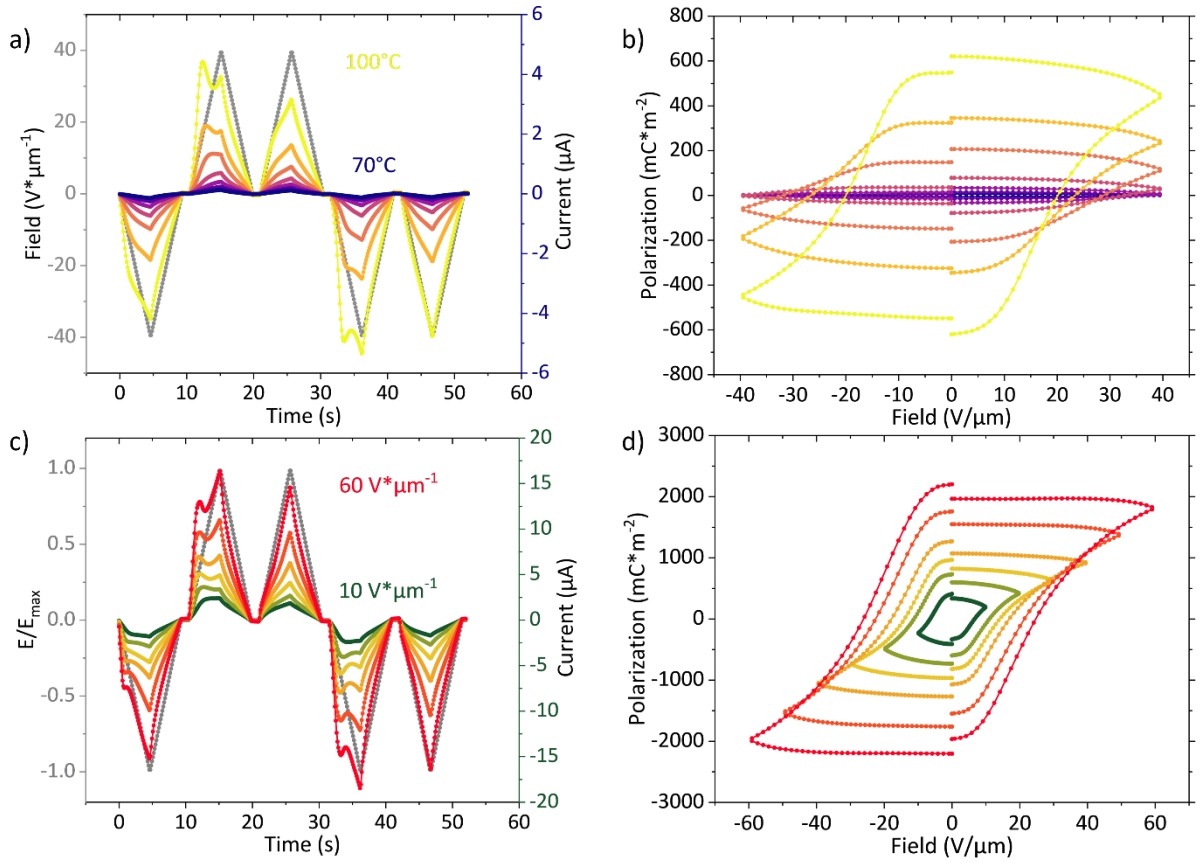

Figure 39. Double wave measurements of FCH-C3-A, current response on the left and resulting "polarization" hysteresis loops on the right. The polarization values cannot be of purely ferroelectric nature, reasons and explanations are given in the text and in later sections. In a) the temperature is stepwise increased by 5°C with an external maximum field of 40 V/µm and constant frequency of 25 mHz. In c) the external maximum field is varied from 10 V/µm up to 60 V/µm at 100°C and constant frequency of 25 mHz.

Further information on the polarization characteristics and possible saturation were obtained by field variation DWM measurements conducted at a constant temperature of 100°C shown in Figure 39b). At low fields, a shoulder is observed that grows into a peak with increasing field strength. The peak concomitantly shifts to earlier timestamps up to a maximum field of 40 V/µm, after which it remains constant. This is typical ferroelectric behavior, as for lower maximum fields the coercive field is not reached and only a subset of the hysterons is switched. Increasing the field towards the coercive field increases the number of switched hysterons and the current increases up until the coercive field is reached, beyond which the switching current stays constant. The peak shift in time relates to the frequency dependence of the coercive field discussed in subsection 2.2.4 and is investigated with a better suited measurement later in this section. Similarly, the increase of the coercive field with maximum applied field is caused by a concomitant increase in sweep rate. The corresponding hysteresis

loops reveal two issues: firstly, the polarization values vastly exceed the theoretical dipole density and secondly, the ever-growing size of the loops with increasing maximum field. Both observations again indicate that the “polarization” obtained from the DWM measurements contains significant non-ferroic contributions.

A natural suspect is the large background current, resulting from the significant conductive properties of FCH-C3-A. As seen in Figure 39a) and to a lesser extent in b), the background current peaks in the correction pulse are smaller compared to the readout pulse, resulting in an incomplete background correction. A possible explanation for the difference in background current peaks are residual ionic impurities in the material or substrate.[187] Additionally, if the measurement frequency is too high, a portion of the switching current is cut-off while the rest is superimposed with the background peak in the readout pulse, which does not happen in the correction pulse. While the frequency cut-off is solved by decreasing measurement frequency and/or increasing the applied maximum field, the ionic contributions (and other unknown transients) are rather difficult to exclude via experimental means. A common way to avoid ionic contributions is to increase the measurement frequency, but this can cause the switching current to be cut off. This is the case for FCH-C3-A, as will be shown later. Hence, the two problems have opposite solutions regarding the frequency. As they cannot be solved experimentally, the background correction of the DWM was modified. A straightforward way of correcting for the different magnitudes of the background currents is by directly scaling the current from the correction pulse to the peak value of the background current from the readout pulse, as schematically shown in Figure 40a). However, while the resulting polarization loops depicted in b) now show the polarization saturating for a single measurement, the polarization still exceeds the theoretical value by orders of magnitude and still grows for measurements of increasing maximum applied fields.

An alternative approach of subtracting a linearly fitted background is shown in Figure 40c), but again, the magnitude of the obtained polarization is far too high to be of purely ferroelectric origin. This indicates that the incomplete background correction is not the only reason for the behavior of the polarization. As discussed later in section 5.3, the modulation of the conductivity by the ferroelectric polarization turned out to be the origin of the far to large observed “switching” currents. For this reason, the observed current peaks are not really switching currents, but conductivity peaks that originate from polarization switching. The

magnitude of the actual switching current is far smaller and drowned out by the conductivity current. Since this part is about ferroelectric properties and since the position of the conductivity peak is the same as that of the switching peaks, when talking about switching peaks, what is really meant is the peak resulting from the combination of conductivity and switching current. This facilitates the discussion of ferroelectric phenomena and avoids confusing statements.

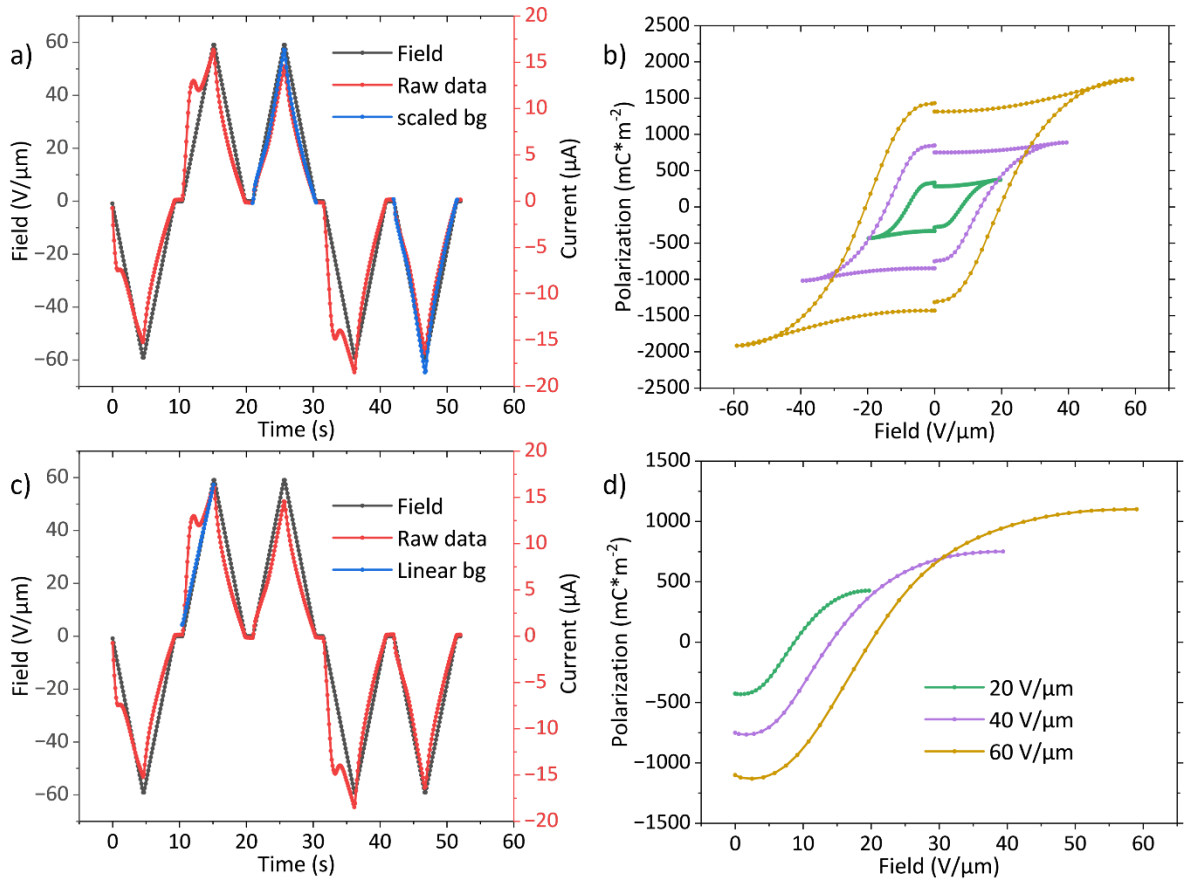

Figure 40. Different ways to adjust the DWM background correction. a) shows background correction by scaling the background peaks to the maximum of the corresponding readout peaks with the resulting polarization hysteresis loops in b). c) shows background correction by linear fitting of the left flank of the first readout peak. The resulting polarization is depicted in d). However, both methods are insufficient for extracting the pure ferroelectric switching current, as the resulting polarization values still exceed the theoretical value significantly.

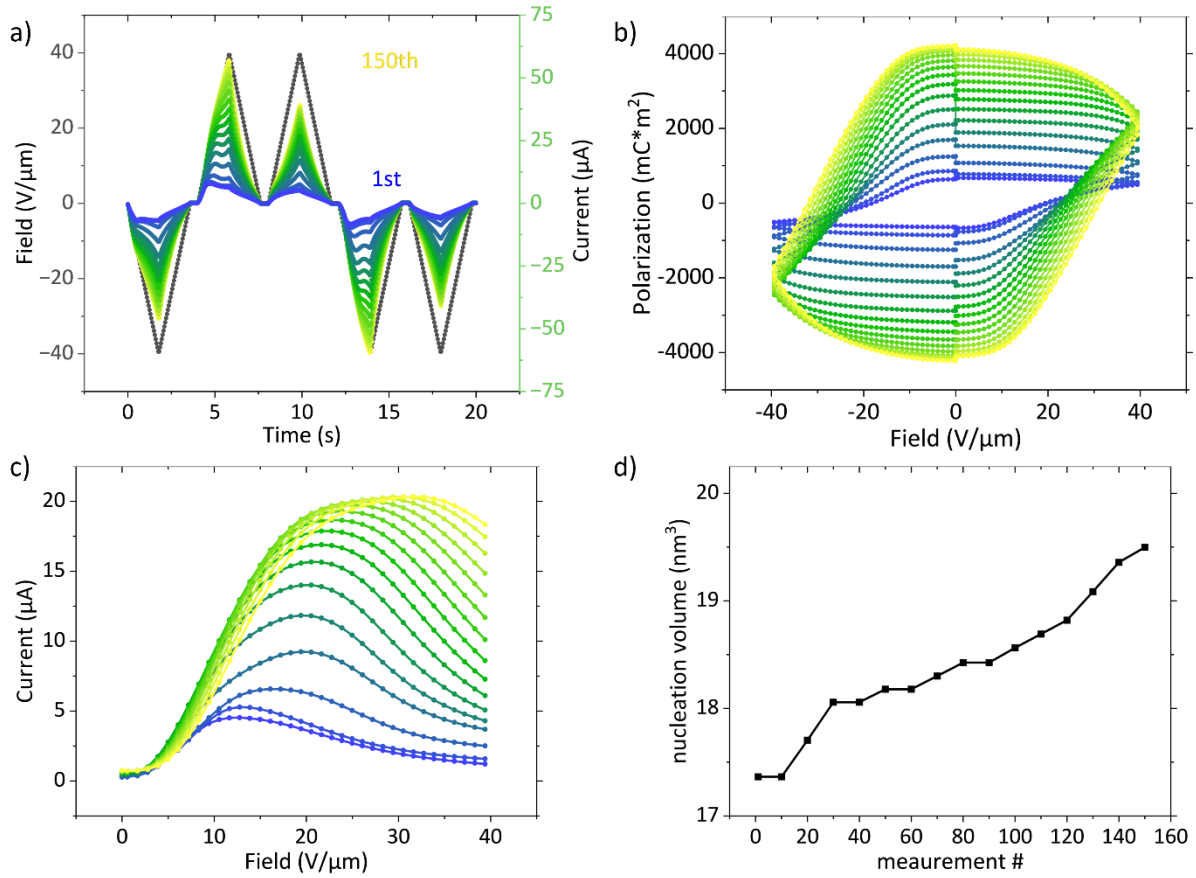

Figure 41. a) shows the first and then every tenth response current of 150 consecutive DWM measurements with a maximum field of 40 V/µm at 100°C and constant frequency of 67 mHz with the corresponding polarization hysteresis loops depicted in b). c) shows the "switching currents" extracted via the DWM that indicate an increasing coercive field with measurement number. d) With the coercive fields obtained from c) an increase in critical nucleation volume *V for consecutive measurements can be estimated in terms of the TA-NLS framework.**

Before further evidence for the ferroelectricity of FCH-C3-A is presented, the influence of "field annealing" on the DWM measurements has to be discussed. "Field annealing" in this context means the frequent repetition of DWM pulses at elevated temperatures. Figure 41 depicts currents and respective polarization hysteresis loops of 150 consecutive DWM pulses taken with a maximum external field of 40 V/µm at 100°C. The downtime between the measurements was around three seconds. A clear trend is observed for the background current. While for the first couple of measurements the presumed switching current is clearly visible and larger than the background current, the ratio shifts for consecutive measurements and even inverts beyond the 30th. Again, switching current in this context means the current peak resulting from the conductivity switching caused by the concomitant ferroelectric polarization reversal.

After 80 successive DWM pulses the background current has increased so far that the switching current is drowned out. This is not surprising, as the conductivity of FCH-C3-A has been shown to be significantly enhanced by field annealing, see section 4. A second observation is that the position of the switching peak versus time and field, i.e., the coercive field, shifts to higher fields, see Figure 41c). In the framework of the TA-NLS model (cf. 2.2.4), which is shown to be valid for FCH-C3-A later in this section, this is attributed to an increasing critical nucleation volume as shown in Figure 41d). This means that the ferroic switching transitions from a more extrinsic to a more intrinsic nature with the concomitant rise in coercive field. Still, the switching mechanism remains extrinsic and is far from ideal intrinsic switching. An increase in nucleation volume would be hardly surprising, as the field annealing results in the formation of supramolecular fibers, which has been shown to enhance the dipolar coupling between monomers. Therefore, larger units of monomers have to be switched together.

The behavior displayed in Figure 41 presents an additional difficulty in determining the ferroelectric parameters of FCH-C3-A, as higher fields (over 20 V/µm) and elevated temperatures (over 95°C) are required for complete ferroelectric switching. However, under these conditions the measurements itself result in structural changes which in turn enhance the conductivity and complicate the determination of the ferroelectric parameters. In addition, since drop-casting and successive melting leads to films of varying morphology, finding a consistent starting point for ferroic measurements was only possible within limits. To allow for a certain degree of consistency, all measurement series were conducted on freshly made, close to pristine samples. Pristine in this context means drop-casted on IDE, heated over the melting point and then cooled down again.

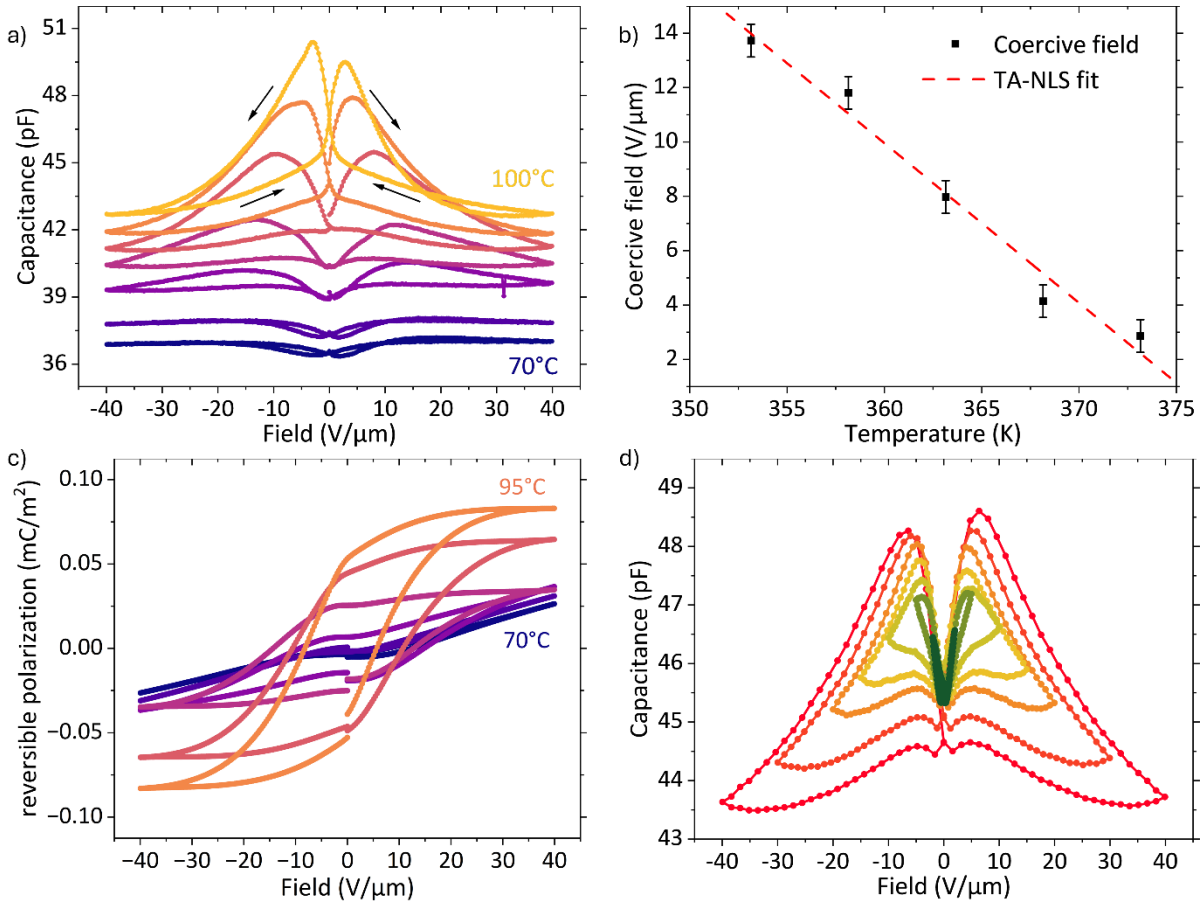

Figure 42. CV-curves of FCH-C3-A measured with a small signal of frequency 1 kHz and peak-to-peak amplitude of 600 mV/µm. In a) the temperature was stepwise increased from 70°C to 100°C in 5°C steps. The black arrows indicate the loop sense. b) shows the positive coercive fields obtained from a) plotted against the temperature and fitted with the TA-NLS model. c) depicts the reversible polarization, obtained from integrating the baseline corrected CV-traces in a). In d) the evolution of the CV-loop for a stepwise increasing maximum DC-field at a constant temperature of 100°C is depicted. The loop sense is the same as in a). a) and d) were measured on two different samples.

Additional evidence for the notion that the observed behavior is indeed ferroelectric is found in the capacitance-voltage measurements depicted in Figure 42. In a) the temperature is increased in intervals of 5°C between single measurements, starting from 70°C. At low temperatures, no notable features are observed, until at 85°C two broad peaks appear at 13 V/µm and -16 V/µm respectively that evolve into the characteristic ferroelectric butterfly shape with further increasing temperatures. At the same time, the peaks, which indicate the coercive field, shift towards smaller values, as shown in Figure 42b) for the positive fields. The asymmetry can be explained by imprint effects.[147] The temperature dependence of the coercive field is well described by TA-NLS theory, equation 30 is fit to the data with an estimated theoretical polarization of $P_r = 31$ mC/m^2, a typical attempt frequency $v_0 = 10$

THz and a frequency $f = 2$ mHz of the DC-field sweep. The value for the remnant polarization corresponds to that of the amide group only, as later measurements indicate that the peaks originate from the amide dipole alone. v_0 is approximated from the typical phonon frequencies of other supramolecular organics.[100,188] The resulting energy barrier $w_\mathrm{b} = 43$ meV is slightly smaller and the critical nucleation volume of $V^* = 27.6$ nm^3 slightly bigger than in the comparable organic ferroelectric BTA.[100,127] Nevertheless, the values are reasonable and of a comparable order of magnitude. The complete fit parameters are given in the appendix Table 2. Together with the fact that the temperature dependence of the CV-loops is consistent with the behavior of the presumably ferroic switching peak in the DWM measurements, the validity of the TA-NLS model for the coercive field dependence presents a strong case for ferroelectricity of FCH-C3-A.

Figure 42c) shows the portion of the polarization that is reversibly switchable, obtained from integrating the baseline corrected CV-traces in a). Compared to the theoretically estimated switchable polarization of 31 mC/m^2 the reversible portion of the polarization is very small. The reversible polarization being small compared to the irreversible polarization is commonly observed and expected, albeit usually not to such a large extent.[102] Unfortunately, direct comparisons to the measured irreversible polarization cannot be made, as the observed polarization values from DWM measurements are not the actual ferroelectric polarization but exaggerated by the conductive properties.

The stepwise DC-field increase shown in Figure 42d) shows typical ferroic characteristics. From low to high fields a clear evolution of the butterfly shape is observed, with the curves at low fields demonstrating incomplete switching as the coercive field is not reached. They are akin to unsaturated inner loops obtained from DWM measurements below the coercive field. For maximum DC-fields of 15 V/µm and above, the coercive field is exceeded and the complete butterfly shape observed. The values for the coercive field are $\pm$4.2 V/µm for the 15 V/µm measurement and increase slightly to $\pm$6.3 V/µm for 40 V/µm, with the increase presumably resulting from the increase in DC-field sweep rate.

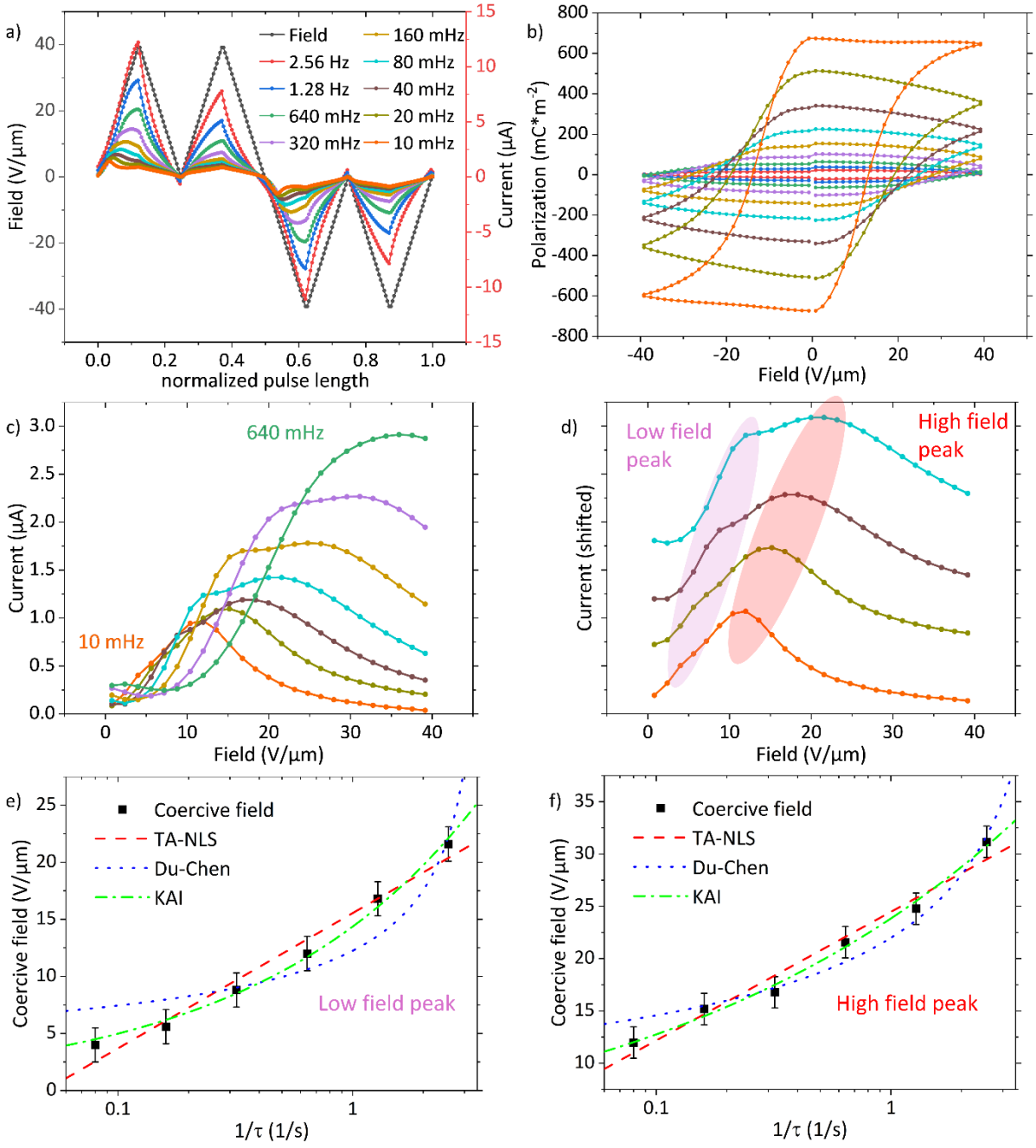

Figure 43. a) Currents obtained from DWM measurements of FCH-C3-A films at varying frequencies with a maximum applied field of 40 V/µm at a constant temperature of 110°C. Frequencies start at 10 mHz and are then doubled each measurement. The x-axis depicts the normalized pulse duration. Measured on aluminum IDE. b) shows the corresponding hysteresis loops. In c) the "switching" currents obtained from the correction of the first readout peak from a) are plotted. While the background correction is still insufficient (cf. Figure 40), the presence of two different peaks is clearly observable. d) shows the low frequency currents shifted for clarity while the markings indicate the position of the first and second switching peak. The corresponding coercive fields are plotted against the inverse rise time τ and fitted with various theoretical models that describe polarization switching in e) and f) for the first and second peak, respectively.

After obtaining additional reinforcement via the demonstration of typical ferroelectric behavior in CV-measurements that is describable in the TA-NLS framework and considering measurements of FCH-E in section 5.2, FCH-C3-A is classified as a true ferroelectric, despite the asterisk attached to the measured polarization values. To obtain further insight into the polarization switching dynamics, frequency resolved DWM measurements were conducted. Figure 43a) shows currents measured at frequencies from 10 mHz to 2.56 Hz under a maximum applied field of 40 V/µm at 110°C, plotted against the normalized pulse duration. In contrast to other ferroelectric measurements, those were conducted on films on aluminum IDE, reducing the effect of the background conductivity. Going forward, ferroelectric measurements of FCH-C3-A are advised to be performed with aluminum or another lower work function metal as IDE material, however, during most of this work, aluminum IDE substrates were insufficiently available. In Figure 43a), a clear switching peak is observed for low frequencies, shifting to larger fields with increasing frequency. The increasing background currents with frequency result from the concomitant rise in displacement currents. Approaching higher frequencies, the switching peak is partially cut-off, as the dipolar motion cannot follow the driving field anymore and only the portion of hysterons with lower characteristic switching time flips. Therefore, complete ferroelectric switching can only be observed at low frequencies. This is an additional obstacle to estimating the true ferroelectric polarization, as high frequencies are advantageous to reduce the influence of unwanted background currents.

High frequencies allowed the measurement of polarization values closer to the theoretical value of 83 mC/m^2, but not without cutting off the switching current. This is seen in Figure 43b), where the top of the hysteresis loops increases for reducing field and only at 10 mHz a nearly constant polarization is observed, indicating complete switching. Switching times on the order of seconds indicate significant molecular rigidity which is expected considering the difficulty of reorienting the larger pentafluorocyclohexane group.

A closer look at the switching currents obtained from the DWM correction in Figure 43c) reveals the presence of two distinct peaks, one at lower and one at higher fields, for measurements taken at frequencies of 320 mHz and below. For clarity, the low frequency currents are shifted on the y-axis and the peaks are marked in Figure 43d). The low field peak appears especially at low frequencies as merely a shoulder. Until the 320 mHz measurement

both peaks are visible, beyond that at least one peak is fully cut off. In the measurements presented previously only the high field peak was observed and shown to be of ferroic nature. After excluding various non-ferroelectric sources for the current peak at higher fields in the beginning of this section, the same holds true to some extent for the "new" peak at low fields. Therefore, a ferroic origin of the low field peak is probable. A natural explanation for the observation of two distinct ferroelectric switching peaks would be the presence of two, partially independent ferroic sublattices. FCH-C3-A with its two spaced out dipolar moieties meets the prerequisites to exhibit such a phenomenon. However, before such a claim is made, further evidence for the ferroic nature of the low field peak is required.

Figure 43e) and f) depict the frequency dependence of the peak position, which is equivalent to the coercive field, from the low and the high field peak. To fit polarization switching models to the data, the relevant frequency that E_c is plotted against is the inverse rise time τ of a single triangular pulse and not the frequency of the whole DWM pulse which is given in Figure 43a). This distinction is important as the models generally describe only the polarization switching from one state to another and not the full DWM process. For both peaks the data was fitted with the TA-NLS, Du-Chen and KAI models introduced in section 2.2.4. For TA-NLS a typical attempt frequency of $\nu_0 = 10$ THz and theoretically estimated polarization values of 31 mC/m^2 and 52 mC/m^2 are used for the low and high field peaks, respectively. Here, the assumption was made that the low field peak belongs to the amide group while the high field peak belongs to the fluorinated cyclohexane ring. The cause for this assignment is presented later in the section. Since the functional dependence does not change for choosing different polarization values, the exact choice does not influence whether the model is a good fit to the data or not. The fitting parameters are the critical nucleation volume V^* and the energy barrier w_b. For the Du-Chen model B' and f_0 were taken as fit parameters, while for the KAI model α was set to 6 for the triangular waveform and d used as fit parameter.

It is evident that the Du-Chen model does not capture the full physics of the polarization switching for either peak. However, the TA-NLS and the KAI model describe the data well for both peaks, with the KAI model fitting better especially for the low field peak. Complete fit parameters are given in appendix Table 3-5. While the fit parameters show a slight preference for the KAI model which is more pronounced for the low field peak, the TA-NLS model is presumably more appropriate considering the nature of the investigated material. FCH-C3-A

is better described as a disordered organic than an organic crystal. Together with the fact that the temperature dependence is also fit well by the TA-NLS model (cf. Figure 42b), it is more likely to be the model that actually describes the microscopic mechanism behind polarization switching in FCH-C3-A. That the coercive field dependence of the low field peak is analogous to that of the high field peak of ferroic origin and well described by polarization switching models, implies a ferroelectric nature of the low field peak.

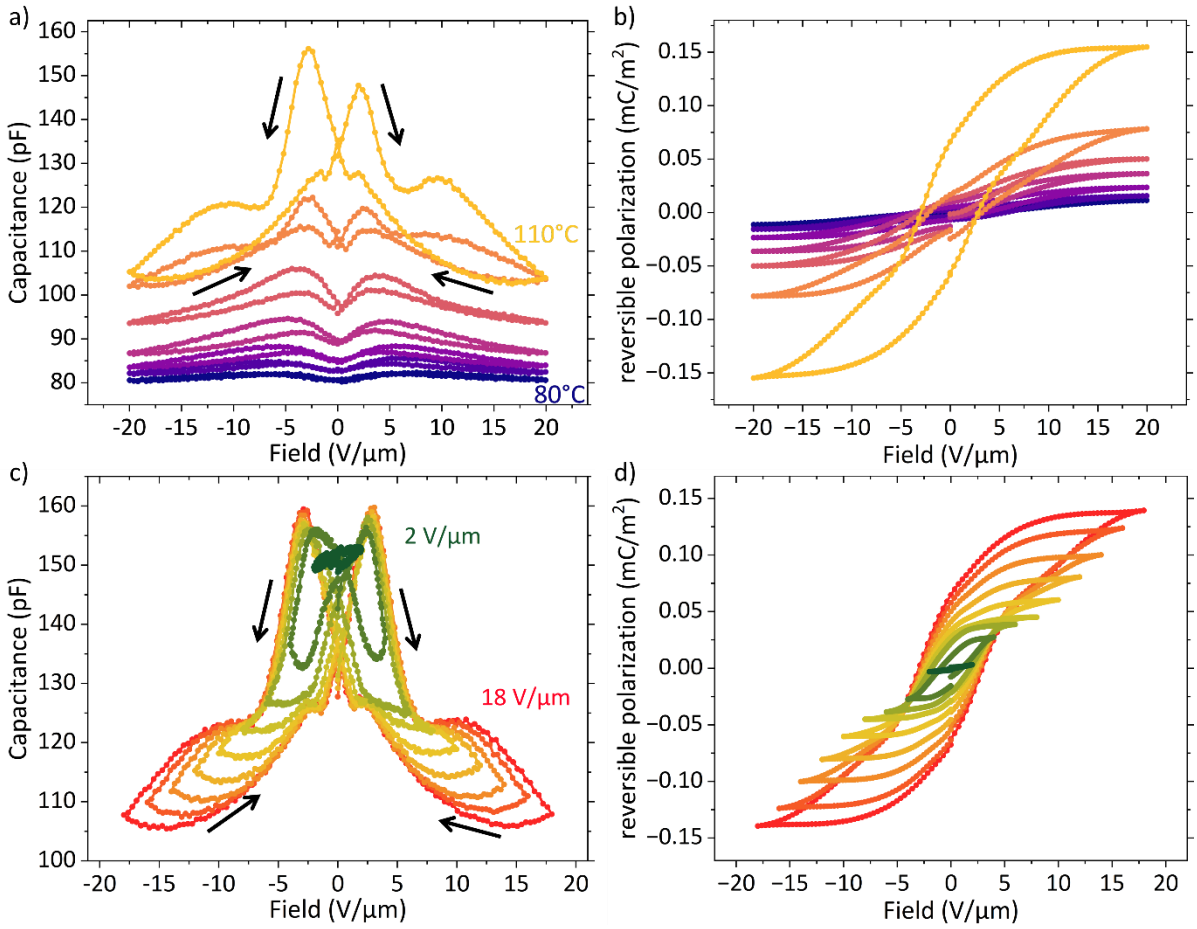

Figure 44. CV-measurements of FCH-C3-A with a small signal peak-to-peak amplitude of 200 mV/µm and a frequency of 100 Hz. The large signal DC-field was swept from 0 to 20 to -20 to 0 V/µm. a) shows temperature dependent measurements from 80°C to 110°C in increments of 5°C. c) shows CV-measurements for varying maximum DC-field from 2 V/µm to 18/µm in increments of 2 V/µm at a constant temperature of 110°C. The large signal DC-field was swept from 0 to maximum field to negative maximum field to 0 V/µm. The black arrows indicate the loops sense. b) and d) show the respective reversible polarization obtained by integrating the baseline corrected CV-traces.

Further evidence for the ferroic nature of the low field peak is found in the CV-measurements shown in Figure 44. Compared to the measurements shown before in Figure 42 the small signal frequency was reduced from 1 kHz to 100 Hz and higher temperatures were explored.

In Figure 44a) the temperature is stepwise increased by 5°C between measurements. Heating up to 100°C, the emergence of the butterfly shape is observed with the coercive field shifting to lower fields, consistent with what was observed previously. However, at 105°C an additional set of shoulders appears at higher fields evolving into a more peak-like shape at 110°C. A similar picture is painted for field dependent measurements at 110°C shown in Figure 44c). Small fields result in incomplete inner-loop butterflies, until at around 6 V/µm the complete loop is observed. Further increasing the maximum DC-field reveals another set of peaks at higher fields. The coercive fields obtained peaks at higher maximum DC-fields are around 2.9 V/µm and 10 V/µm, which are in good agreement with the coercive field values obtained for low frequencies via DWM (cf. Figure 43 e) and f). While coercive field values from CV and DWM measurements are usually not directly comparable because of the different measurement conditions, an approximate agreement nevertheless underlines the presumed ferroelectric nature of both peaks and demonstrates consistent behavior. Considering the energetic cost of rotating the dipolar groups allows a tentative assignment of the two peaks to their corresponding dipolar moiety. The lower field peak is therefore assigned to the less energetically demanding reorientation of the amide group while the more energetically costly movement of the full fluorinated cyclohexane ring is assigned to the high field peak. Ferroelectric measurements on FCH-E shown later in section 5.2 further reinforce this hypothesis by comparing the coercive field values and fit parameters obtained from analytical models.

The on first glance contradicting magnitude of the two switching peaks when comparing CV to DWM measurements can be explained twofold: The apparent magnitude of the switching peaks in DWM measurements is predominantly determined by the conductivity current and not the polarization switching current. Additionally, the CV loops measure only the reversibly switchable polarization (shown in Figure 44b) and d) and hence no correlation between the amplitudes between DWM and CV are expected. In Figure 44b) the significant growth in reversible polarization at higher temperatures is observed, due to the emergence of the high field peak. Similar behavior is seen in d), where up to 8 V/µm only the low field peak is contributing to the polarization which appears to saturate. For higher maximum DC-fields the high field peak starts to contribute, and no saturation of the polarization is observed. This indicates that the coercive field of the high field peak might not have been reached and/or

implies that even for DC-fields above the coercive field a portion of mobile domain walls that contribute to the dielectric permittivity remain. The latter has been observed in literature before and in this case no saturation would be expected.[189,190]

The lack of the high field peak of the fluorinated cyclohexane in lower temperature CV-measurements implies a stronger temperature dependence of reversible switching compared to the amide group. This is not unexpected given the different sizes and geometries of the dipolar groups, implying a higher steric rigidity of the fluorinated cyclohexane group, which is more easily overcome with increased available thermal energy. Alternatively, lowering the small signal frequency to 10 Hz allowed the observation of the peak corresponding to the cyclohexane group down to 95°C, see appendix Figure 12b).

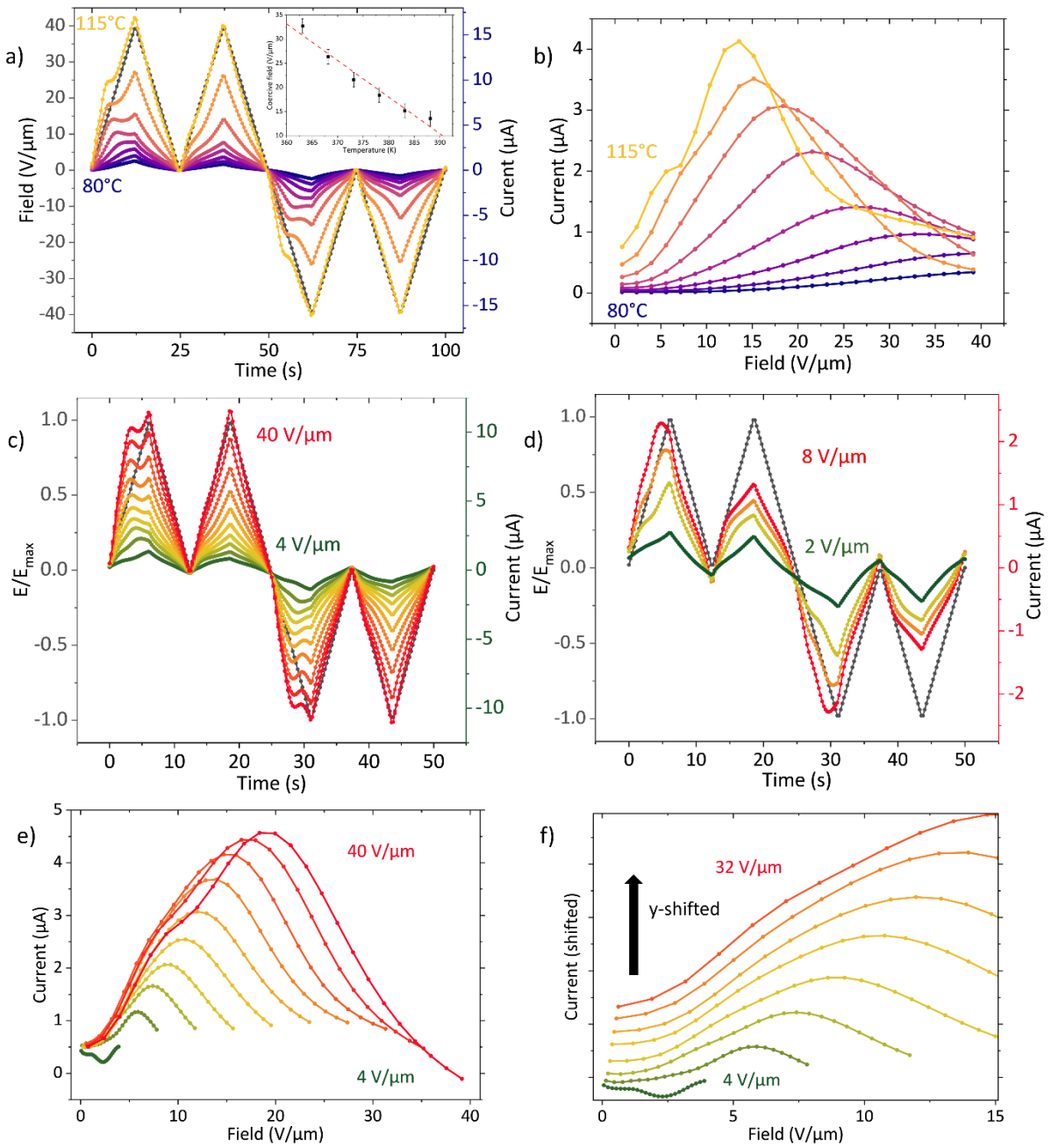

Figure 45. Further DWM measurements of FCH-C3-A. a) DWM currents at temperatures varying from 80°C to 115°C in 5°C steps with an applied maximum field of 40 V/µm and a frequency of 10 mHz. The inset shows a plot of the coercive field against the temperature, fitted with the TA-NLS model. b) shows the switching currents obtained from a). Currents obtained by DWM with varying maximum fields in 4 V/µm steps measured at 110°C and a frequency of 20 mHz are depicted in c) with a zoom in on low fields in d). e) shows the resulting switching currents from c) with maximum fields increasing in 4 V/µm steps. f) shows a zoom in of e) at low fields where the measured currents are offset in y-direction for clarity.

In Figure 45 the best of initial experimental attempts to further characterize and possibly disentangle the two distinct ferroelectric switching peaks by adjusting the temperature and

applied field are presented. DWM measurements with 5°C stepwise increasing temperatures between 80°C and 115°C are shown in a). Since for lower temperatures only the high field peak is visible, no further insight into a possible peak separation is gained from the raw data. In the resulting switching currents shown in b) only at temperatures of 110°C and 115°C an additional shoulder is observed in addition to the high field peak. Comparing the peak behavior with Figure 44a) this comes as a surprise, as in the CV measurement the low field peak is visible at lower temperatures and the high field peak appears at elevated temperatures, which is not observed in the DWM measurements.

A possible explanation is that since the peaks in the DWM are conductivity peaks and not switching peaks, the lack of a visible low field peak at lower temperatures in the DWM (cf. Figure 45a) and b) could be attributed to the presence of a finite injection barrier, which is only overcome once the pentafluorocyclohexane group becomes mobile at higher temperatures. This would be consistent with the injection barrier limited behavior seen at low fields in Figure 51e) in section 5.3 later. However, the actual amide switching current should then be observed. The reason it is not observed is probably that compared to the magnitude of the measured current, the switching current portion is small and likely drowned out. Another thing to consider is that the temperature dependence of the conductivity modulation, especially the interplay between injection barrier modulation and bulk conductivity switching for different temperatures, is unclear at present.

In addition, considering Figure 43c) and d) it can be argued that the two peaks are quite close to each other and if under slightly different conditions the coercive fields shift closer, a separation might not be possible anymore. Depending on the morphology of the sample and considering the effect of annealing (cf. Figure 41), slight variations in the coercive fields due to both effects are expected. Calculating the temperature dependence of the two coercive fields from the TA-NLS law, shows that the peaks actually shift slightly further apart by 0.4 V/µm when changing the temperatures from 115°C to 90°C, theoretically making a separation at 90°C a little bit easier. However, for even slightly reduced amplitudes of the amide conductivity switching peak relative to the pentafluorocyclohexane peak, the former is likely to be swallowed by the latter and/or the general current magnitude.

In contrast to the DWM, the CV measurements depicted in Figure 44 show actual reversible ferroelectric switching, therefore the low field peak of the amide group is already visible at

lower temperatures, independent of injection barriers. Reversible switching of the pentafluorocyclohexane group is assumed to be energetically costlier, meaning higher temperatures and lower frequencies are required. As a side note, in the inset of Figure 45a) the coercive field of the high field peak is plotted against the temperature, which again is well described by the TA-NLS model.

Field dependent DWM measurements at 110°C are shown in Figure 45c). Again, the raw data shows nearly only the high field peak of the fluorinated cyclohexane group, only when looking closer at low field measurements in Figure 45d) a shoulder a small shoulder of the amide peak is observed clearly in the 4 to 8 V/µm measurements. From 4 V/µm on the switching peak of the cyclohexane ring begins to appear, however, it remains partially cut off till higher fields are reached. This is also the reason for the apparent big differences in background current peak between first and second peak which is resolved at higher fields once the coercive field is reached. The appearance of a shoulder in the second triangular pulse can be explained in at least three ways in a ferroic picture. Firstly, possible antiferroelectric behavior of the amide group might result in such a current peak. Another possibility is the field dependence of the Curie temperature, where going towards zero field the material falls below the Curie temperature and loses its spontaneous polarization. When increasing the field again the Curie temperature rises, and the material becomes ferroelectric once again. Such behavior has been observed previously in BTO and P(VDF-TrFE).[191,192] Both mechanisms would additionally explain the small peak in the CV-loops of Figure 44 when sweeping back to zero field.

However, antiferroelectricity would lead to a kink in the right decreasing flank of the first triangular pulse from the partial dipole reversal, which is not observed. For the loss of ferroelectricity through the field dependent Curie temperature the dipoles do not reverse but enter a disordered and hence depolarized state. This depolarization might occur over a longer time and therefore result in a less peak like current. However, the Curie-Weiß law not being observed in the dielectric spectroscopy measurements contradicts this hypothesis. The third and most probable explanation is simply that the shoulder is caused by the incomplete switching of the cyclohexane group, resulting in the switching of leftover hysterons in the second triangular pulse. However, the peaks in the CV-loops when going towards zero field cannot be explained this way. The data does not yield a clear conclusion and hence the observed behavior has to be partially attributed to further unknown effects.

The corrected “switching” currents from Figure 45c) are shown in e) and a zoom in to lower fields with the currents shifted in y-direction for clarity in f). Here the amide shoulder is more clearly seen at higher fields and weakly visible at low fields. The latter is caused by the unwanted shoulder in the correction peak, due to the incomplete switching of the cyclohexane group.

In summary, a clear separation of the two switching peaks with temperature via DWM measurement proved difficult, caused by the variable injection barrier height due to the temperature dependent mobilization of the pentafluorocyclohexane group and the small current amplitude of the amide peak. However, DWM measurements with varying maximum applied field strength at high temperatures showed that the amide switching peak could be isolated for very small fields, providing a basis for further research into the properties of the two independent ferroic lattices and into potential applications exploiting the presence of two distinct coercive fields, e.g. multi-bit ferroic memory.[193]

5.2 Ferroelectricity in FCH-E

With a similar structure to FCH-C3-A, but missing the carbon chain spacer and the amide group, FCH-E was chosen as a promising candidate to obtain further insight into the ferroelectric polarization switching mechanism of FCH-C3-A. As presented earlier, FCH-E does not have the same conducting properties as FCH-C3-A, facilitating the investigation of its ferroelectric properties. The dielectric spectroscopy measurements at various frequencies shown in in Figure 46 do not exhibit any features besides a strong increase around the melting point of around 105°C, which is in agreement with DSC measurements, see appendix Figure 11.

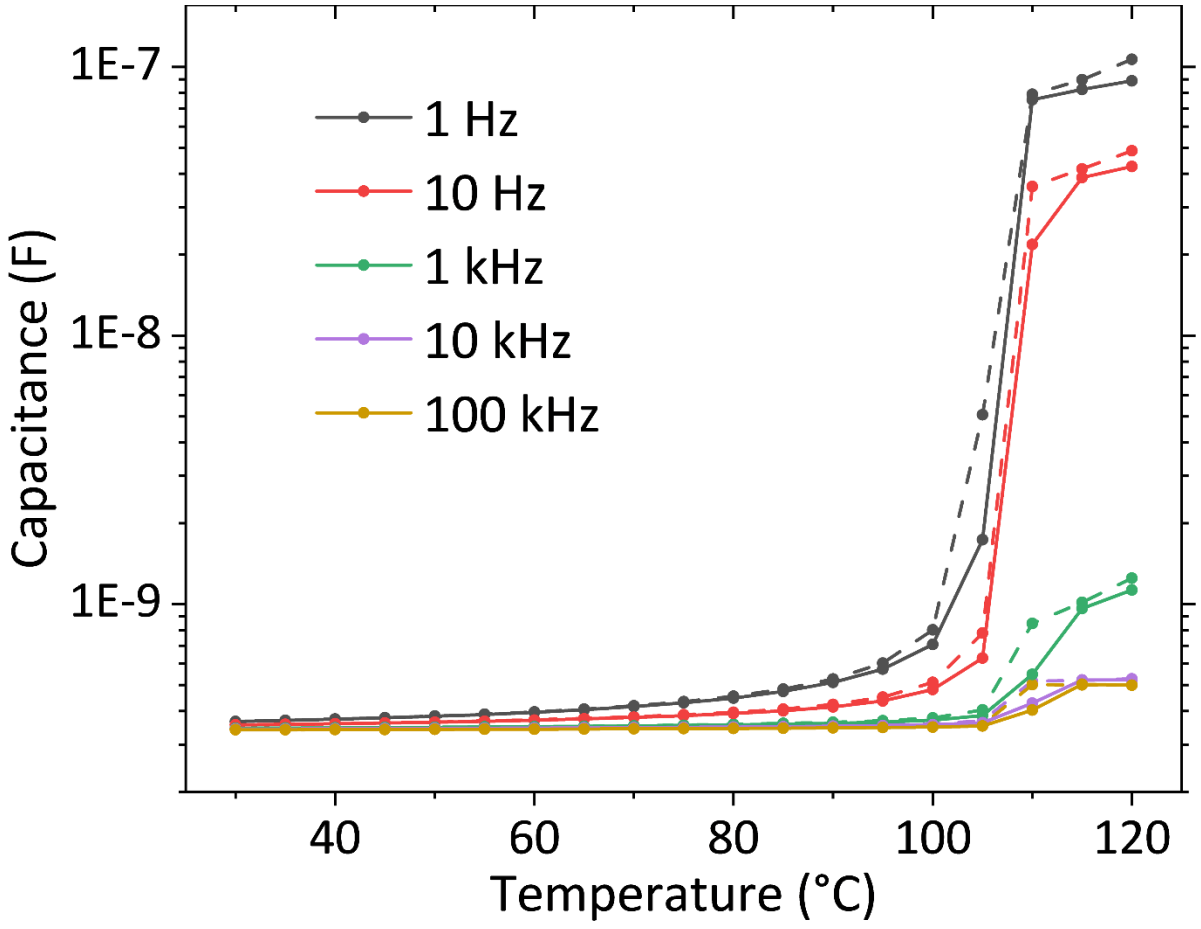

Figure 46. Dielectric spectroscopy measurements of FCH-E at various frequencies. Solid lines denote heating, dashed lines cooling traces.

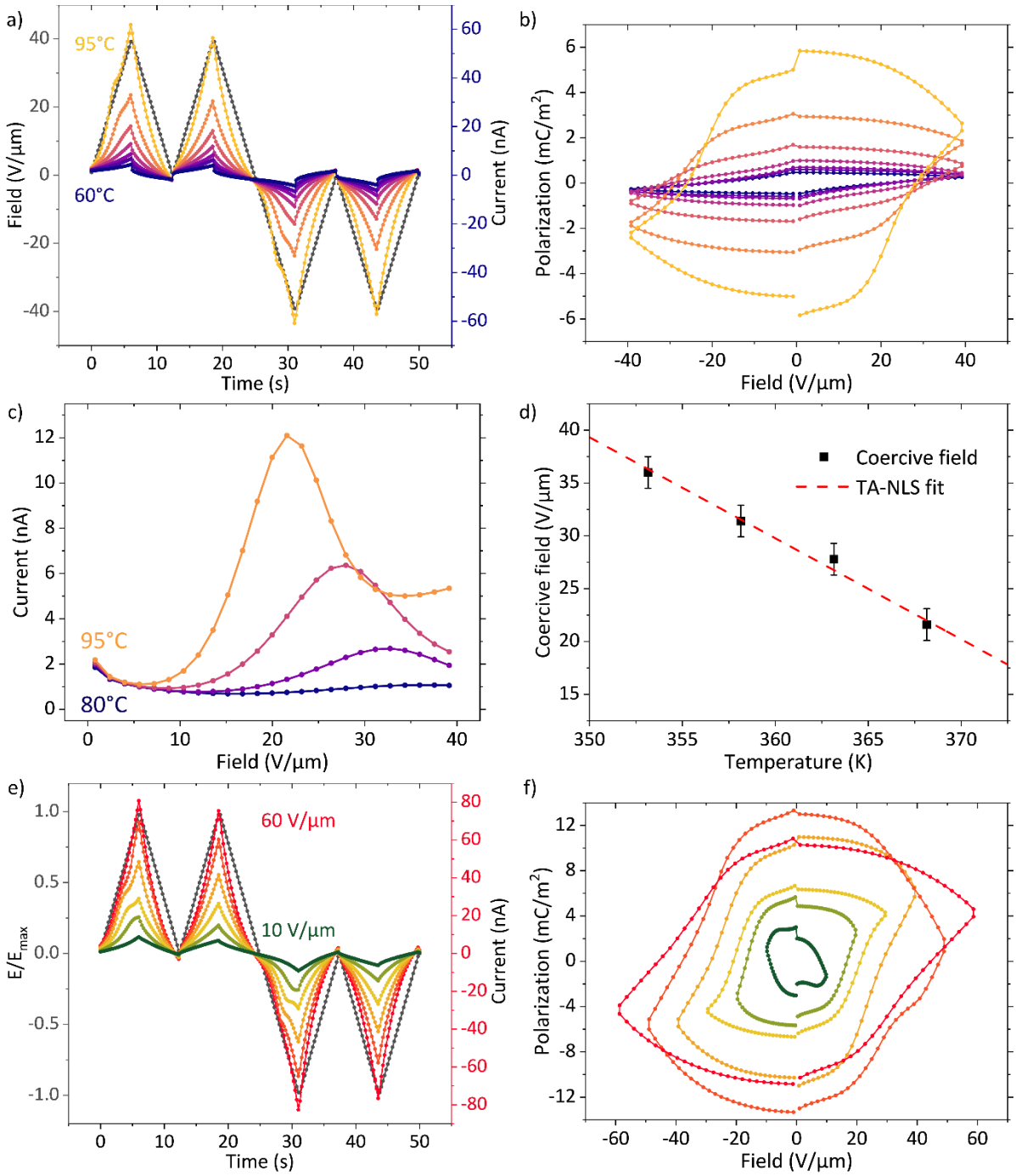

Figure 47. DWM measurements on FCH-E. a) shows measured DWM currents at fixed frequency of 20 mHz and an applied maximum field of 40 V/µm for temperatures between 60°C and 95°C increasing in steps of 5°C. b) shows the corresponding polarization hysteresis loops and c) the corresponding switching currents. In d) the coercive field obtained from c) is plotted against the temperature and fitted with the TA-NLS model. e) shows DWM currents measured at 95°C and a fixed frequency of 20 mHz for applied maximum fields increasing from 10 V/µm to 60 V/µm in 10 V/µm steps.

Since no information on a ferroelectric phase could be obtained from DS measurements, a natural approach was to conduct DWM measurements at similar parameters as done for FCH-

C3-A. Figure 47a) shows DWM measurements on FCH-E at a constant frequency of 20 mHz and a maximum applied field of 40 V/µm for increasing temperature in 5°C steps between 80°C and 95°C. The latter was chosen as maximum temperature to avoid effects from the onset of melting at temperatures above. From 85°C on a shoulder appears that becomes slightly more pronounced at higher temperatures, and which is identified as polarization switching current. Compared to FCH-C3-A and as expected, the background currents are far smaller. However, especially for the 95°C measurement the background current of the first pulse exceeds the background current of the following correction pulse significantly, indicating some ionic presence. As a result, the corresponding hysteresis loops shown in b) do not saturate and are slightly asymmetric. Therefore, the obtained polarization values are overestimating the actual measured switched polarization by a small margin (around 9.3% at 95°C). The magnitude of the polarization values is physically sensible, albeit rather small for ferroelectric switching, considering the theoretically estimated polarization of 69 mC/m^2. The same 6.2 Debye of the cyclohexane ring are now distributed over a smaller volume of around 0.3 nm^3.

DWM measurements with varying applied maximum fields are shown in Figure 47e). The data suggests that the coercive field is fully surpassed from the 30 V/µm measurement, while the corresponding hysteresis loops keep growing until 40 V/µm, which shows similar polarization values as 60 V/µm. After correcting for the presumably ionic background, the approximate value for the polarization is 5.1 ± 0.8 mC/m^2. To correct for ionic contributions and further unwanted transient currents, the background currents were scaled as shown previously in Figure 40. The resulting negative parts of the polarization loops are plotted in appendix Figure 14. The uncorrected hysteresis loop of the 50 V/µm measurement clearly shows the influence of ionic contributions. That the polarization loops do not grow significantly beyond 40 V/µm indicates that all switchable dipoles are flipped. This leaves the question as to why the measured polarization is around 10 times smaller than the theoretically estimated polarization.

There are a multitude of possible explanations, a straightforward one is that the switching mechanism is unknown, so the theoretical polarization state where all five fluorine atoms of the cyclohexane group are pointing in the same direction might not be the actual configuration. In reality, steric constraints might prevent a full reorientation of the

cyclohexane rings fluorine atoms, resulting in only a fraction of the theoretical polarization value. Another possibility is the lack of long-range order in the film, as indicated by AFM images (cf. Figure 30). Random orientation of the single molecules means that the dipoles might not be able to fully align with the applied field and therefore only a fraction of their dipole moment contributes to the overall bulk polarization. This fraction can be roughly estimated by considering the average effective dipole moment of completely randomly oriented dipolar groups in three dimensions, which is given by $\mu_{\mathrm{effective}} = \mu \cdot 2/\pi \approx \mu \cdot 0.64$. Here it was assumed that all dipole moments point along field direction and the structural orientation of the molecule determines the effectiveness. This does not give the missing factor 10 and would introduce an additional field dependence, as the effective field driving the polarization switching would show a similar angle dependence. Since no strong field dependence of the switching is observed beyond 40 V/µm, the effect cannot be too large. The third explanation is an overestimation of the effective film thickness, as discussed earlier in section 3.1.4.

None of the effects discussed are exclusive and expected to be strong enough on their own, indicating that the reduced polarization value may be the result of a combination of some or even all of them, with no straightforward way of disentangling the various contributions. Switching to out-of-plane devices would solve the issue of the unknown effective film thickness and in-plane field lines, but FCH-E films were not suitable for out-of-plane device geometries. In-situ XRD measurements on poled samples might possibly provide insight into the structural polarization configuration, but the present experimental setup did not allow the in-situ field application and temperature variation necessary for ferroelectric poling.

Figure 47c) shows the switching currents obtained from the temperature dependent DWM measurements in a), with the extracted coercive field values plotted in d) against the temperature. Again, the data is well described by the TA-NLS model, with an energy barrier of 161 ± 6 meV and a critical nucleation volume of 6.7 ± 0.3 nm^3. The values together with further fit data are discussed and compared to the values for FCH-C3-A in a later part of the section.

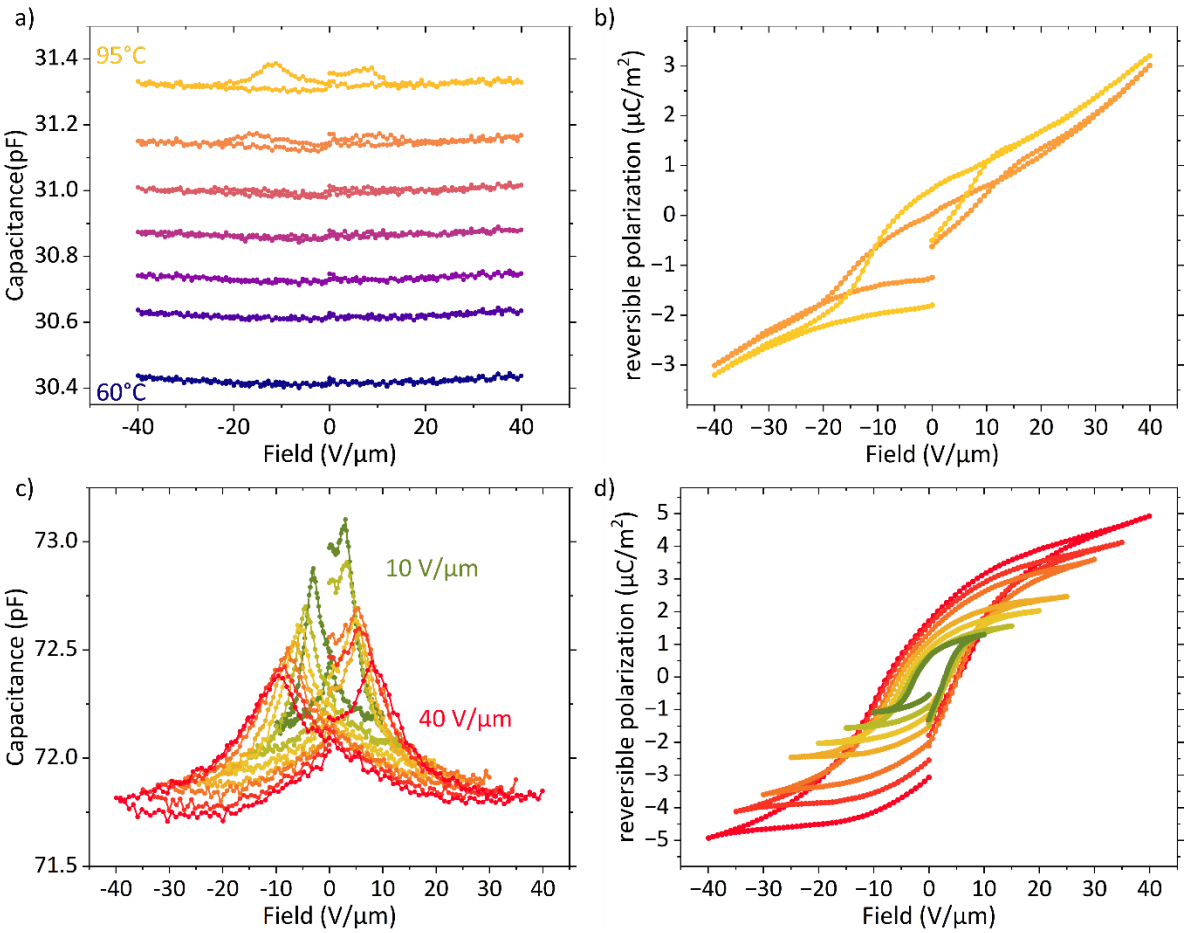

Figure 48. Capacitance-voltage measurements of an FCH-E film. a) shows curves taken at temperatures increasing in 5°C increments, with a small signal frequency of 1 kHz and a small signal peak-to-peak field of 1 V/µm. c) shows curves taken at increasing maximum DC-field with a small signal frequency of 10 Hz and a small signal peak-to-peak field of 1 V/µm at 95°C. b) and d) depict the corresponding reversible polarization obtained by integrating the CV-traces.

Further proof of ferroic behavior is found in the temperature dependent CV-measurements of an FCH-E film depicted in Figure 48a). Here curves measured at temperatures increasing in 5°C increments from 60°C to 95°C depicted, with a small signal frequency of with a small signal frequency of 1 kHz and a small signal peak-to-peak field of 1 V/µm. The increasing baseline is a result of the temperature dependence of the electric permittivity of the organic film and the glass substrate, as seen in the DS data in Figure 46. For low temperatures the measured curves remain flat over the complete DC-field range, only from 90°C on the peaks of a typical butterfly appear with the typical loop sense. The CV response is generally weak considering the peak amplitudes, which can be further quantified by the obtained reversible polarization plotted in Figure 48b) that is orders of magnitude smaller (1-5 µC/m2) than the theoretical polarization of 69 mC/m^2 and the experimentally measured polarization of 5.1 mC/m^2. This

can be explained by the large steric rigidity of the cyclohexane ring, which due to the absence of a carbon spacer can be expected to be larger than in FCH-C3-A. The very small reversible polarization results in incomplete polarization loops in in Figure 48b). Nevertheless, the temperature dependent behavior of the CV-loops is consistent with the DWM measurements.

CV-loops measured on an FCH-E film at 95°C for increasing maximum DC-field with a small signal frequency of 10 Hz and a small signal peak-to-peak field of 1 V/µm are depicted in Figure 48c) with the corresponding reversible polarization plotted in d). A very low small signal amplitude of 10 Hz was chosen as for FCH-C3-A the double peak was only sensed after increasing the parameter space. This was done as an additional sanity check to make sure double peaks are only observed for the material with two dipolar moieties and are not caused by some unknown artifact. However, even for large DC-fields and very low small signal frequency no additional peak is observed. Instead, the evolution of a typical butterfly peak is observed, with a coercive field of around 10 V/µm for the saturated loops. This agrees nicely with the coercive field obtained for the high field peak from CV measurements on FCH-C3-A (cf. Figure 44c) and reinforces the assignment of the high field peak to the fluorinated cyclohexane group. Since no saturation of the reversible polarization is observed in Figure 48d), it is assumed that some domains remain mobile up to high DC-fields similar.[189,190]

Frequency dependent measurements shown of an FCH-E film are shown in Figure 49a). Here, response currents measured at various frequencies and at a fixed temperature of 95°C with an applied maximum field of 40 V/µm are plotted against the normalized pulse duration. The corresponding hysteresis loops are depicted in b) and the extracted switching currents in c). Increasing frequency reduces the influence of the ionic background as seen in the hysteresis loops from 10 mHz to 40 mHz, however, at 80 mHz and beyond a portion of the switching current is cut off. Like in FCH-C3-A, the ferroelectric switching occurs on longer time scales. In Figure 49d) the coercive field taken from the peak of the switching currents in c) is plotted against the frequency and fitted with various analytical models that describe ferroelectric polarization switching. Again, the TA-NLS model and the KAI model fit well to the measured data, while the Du-Chen model does not deliver an adequate description. As with FCH-C3-A, it is not clear from the data which model is the more appropriate choice that describes the physical reality the best. To differentiate, presumably data over a larger frequency range is required. Due to the large switching times of FCH-E, higher frequencies are not accessible.

Going to much lower frequencies is possible, however, there the influence of unwanted (ionic) background currents is further amplified. However, similar to FCH-C3-A. the disordered nature of FCH-E implies that the TA-NLS model gives a more appropriate description than the KAI model.

The fact that the frequency dependence of the current peak is described well by analytical models for ferroelectric polarization switching together with the ferroic butterfly loops obtained in the CV-measurements (cf. Figure 48) presents sufficient evidence to classify FCH-E as ferroelectric. In a way, this is an additional point of evidence that FCH-C3-A is indeed ferroelectric, as it shows that the pentafluorocyclohexane ring on its own can be ferroelectrically switched.

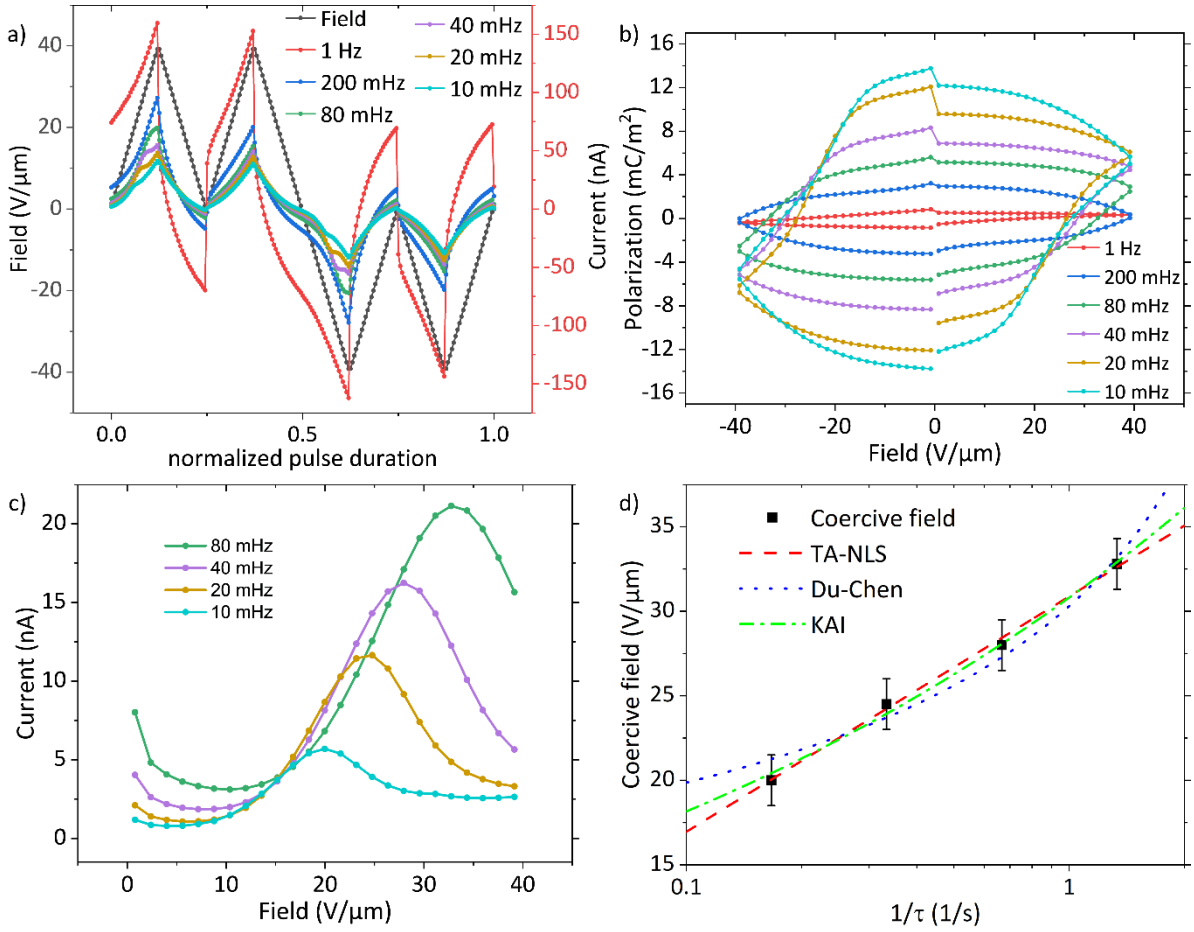

Figure 49. a) DWM currents measured at 95°C with a maximum applied field of 40 V/µm for various frequencies plotted against the normalized pulse duration. b) shows the corresponding polarization hysteresis loops and c) the corresponding switching currents obtained by DWM correction. In d) the coercive field is plotted against the inverse rise time τ and fitted by various analytical polarization switching models.

Here, a short summary of the fit parameters obtained for FCH-E from the data shown in Figure 47d) and Figure 49d) is given and how they compare to the ones obtained for FCH-C3-A in various measurements presented in section 5.1. As mentioned previously, for both molecules the KAI and the TA-NLS models provided adequate fits to the frequency dependent data. Since the former was developed for ferroelectric crystals, the TA-NLS model is presumed to be the model that most likely describes the switching mechanics in the disordered FCHs. The KAI model does not include a temperature dependence for the coercive field; therefore, data of the latter was only fitted by the TA-NLS model. Since the Du-Chen model did not capture the dependencies of the data for either molecule, it is disregarded in further analysis.

Starting with the KAI model, a dimension parameter d of 1.38 ± 0.08 is obtained for FCH-E, while for FCH-C3-A the low field peak that is attributed to the switching of the amide group yields $d = 2.8 \pm 0.1$ and the high peak attributed to the switching of the fluorinated cyclohexane $d = 1.63 \pm 0.07$. While not agreeing within the error margins, the d obtained from FCH-E being a lot closer to the latter than the former is noteworthy. At this point it has to be noted that the error margins come from the uncertainty of the determination of the coercive field and the corresponding fits. Therefore, statistical errors are not included as the amount of experimental data required for this was not obtainable given the material and time constraints. Furthermore, the exact quantitative values are not of significance to the conclusions drawn from the data. Onto the TA-NLS fits, where the relevant fit parameters are the critical nucleation volume V^* and the energy barrier density w_b. For FCH-E critical nucleation volumes of 6.7 ± 0.3 nm^3 (Figure 47d) and 12.2 ± 0.5 nm^3 (Figure 49d) with corresponding energy barriers of 161 ± 6 meV and 92.2 ± 0.3 meV are obtained. For comparison the high field peak attributed to the fluorinated cyclohexane for FCH-C3-A yields nucleation volumes of 11 ± 1 nm^3 (Figure 45a) inset) and 19 ± 2 nm^3 (Figure 43f) with corresponding energy barrier densities of 99 ± 1 meV and 60.4 ± 0.5 meV while the low field peak attributed to the amide group gives nucleation volumes of 28 ± 3 nm^3 (Figure 42c) and 33 ± 3 nm^3 (Figure 43e) with corresponding energy barrier densities of 42.9 ± 0.4 meV and 33.1 ± 0.3 meV. The ranges of the fit parameters for FCH-E overlap significantly with those of the high field peak from FCH-C3-A, further strengthening its assignment to the fluorinated cyclohexane group. In comparison to the cyclohexane group, the amide group exhibits higher nucleation volumes and lower energy barriers. This can be interpreted as a

larger hysteron size of the ferroic amide sublattice, presumably owed stronger long-range coupling between the amide moieties. The lower energy barrier can be traced back to the lower energetic cost of reorientation compared to the cyclohexane ring.

5.3 Conductivity switching in FCH-C3-A

In this subsection the coupling between the ferroelectric and conducting properties of FCH-C3-A is discussed, i.e. how the former modulate the latter. In the previous subsections FCH-C3-A was established as truly ferroelectric. However, the question of the non-saturating, nearly ever-growing polarization with values magnitudes higher than the theoretical dipole density remains open. Since further modifications to the background correction of the DWM aimed at removing ionic and other transient currents still proved insufficient, a natural assumption is the presence of a non-linear conductivity. As discussed earlier in section 2.2.7, ferroelectric polarization has been shown to modulate charge transport in semiconducting ferroelectrics in various ways. The essential mechanisms are briefly repeated in the following. There is injection barrier modulation (IBM), an interface effect where the polarization at the contacts facilitates or impedes charge injection into the semiconductor. Moreover, IBM was shown to be a major factor in the charge transport of non-π-conjugated organic materials including FCH-C3-A, see section 4. The other relevant mechanism is bulk conductivity switching (BCS), a bulk effect where the ferroelectric polarization influences the energy landscape of the charge carrier sites directly and hence modulates charge hopping. While for IBM the conductivity increases for fields applied along the polarization direction and decreases for fields applied against polarization direction, BCS was experimentally and computationally shown to have the opposite effect.[39]

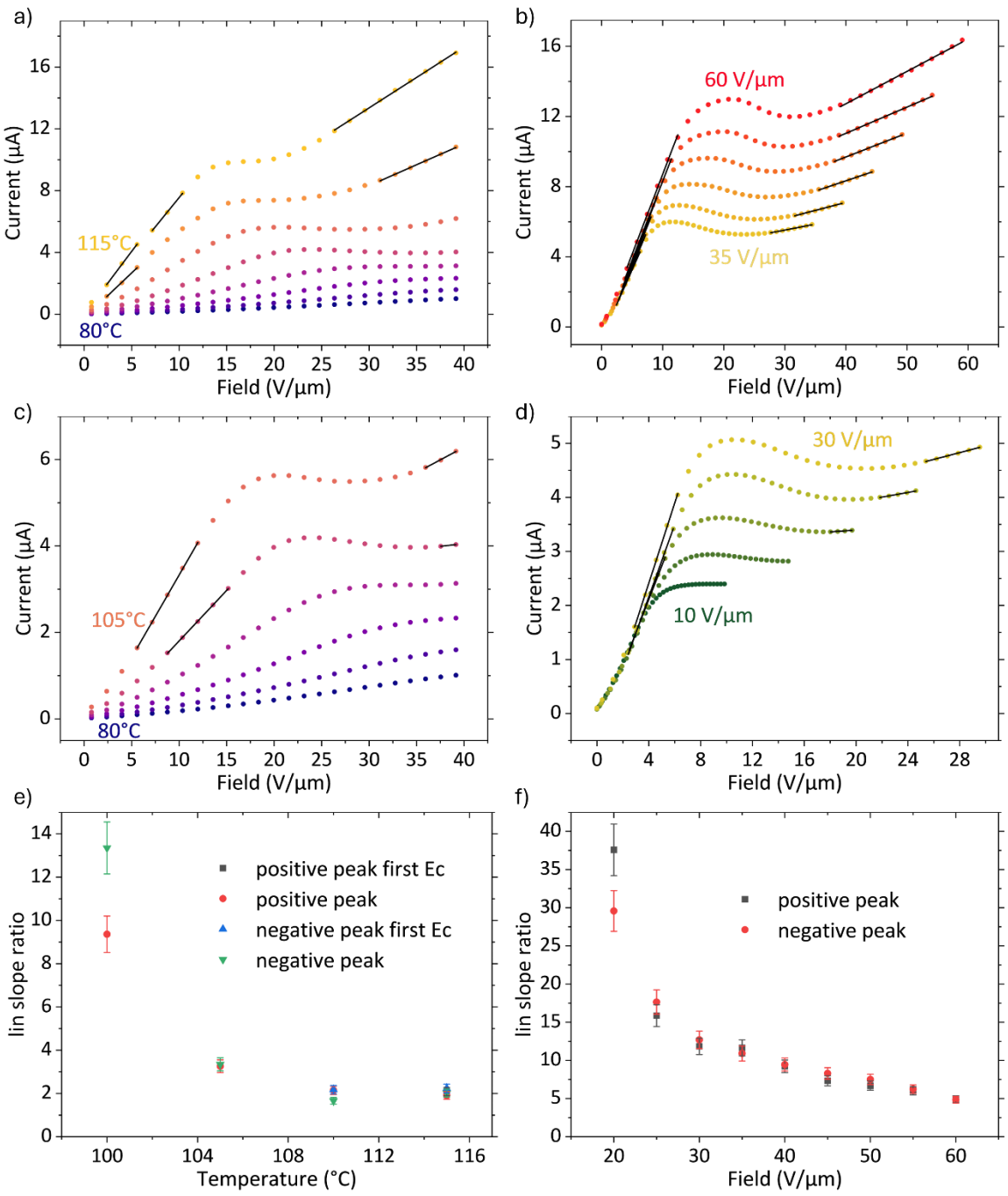

Figure 50. a) and b) show current-voltage characteristics obtained from the left flank of the first readout pulse (the one including polarization switching) from the temperature- and field-dependent DWM measurements shown earlier in Figure 45a) and Figure 39c), respectively. c) and d) show the corresponding low temperature and low field regimes. The black lines are linear fits to the slopes below and above the coercive field, i.e. before and after polarization switching. The ratios of the slopes "before" divided by "after" are plotted in e) and f) against temperature and field respectively and give the on/off-ratio or current modulation by the polarization in the framework of the BCS model.

First information about possible conductivity modulation in FCH-C3-A can be obtained by looking at the already presented DWM measurements. In a rough approximation, a measure for the conductivity can be obtained from the left flank of the first readout pulse (the one including polarization switching) by linearly fitting the slopes below and above the coercive field, i.e. before and after polarization switching. This is shown for the positive readout pulse in Figure 50 a), c) and b), d) for temperature and field dependent DWM measurements respectively. The fitting range was approximated by eye to exclude the regions where polarization switching is still ongoing, and the errors are estimated from slight variations of the fitting range. The corresponding on/off-ratios for all temperatures and fields are plotted in e) and f) for both, up- and down peaks of the DWM measurements. For low temperatures (below 105°C) and fields (below 30 V/µm) shown in c) and d) respectively, the effect of the incomplete switching on the high field slope could not be avoided completely, leading to reduced slopes and hence in significantly overinflated on/off-ratios.

For the high temperature measurements, the presence of the two separate coercive fields from the two dipolar groups has to be considered and for those cases two low field slopes are fitted, below the first and below the second coercive field. The resulting slope ratios in the sensible temperature and field ranges vary from 2 to 10. Ratios larger than one indicate that the conductivity is larger before polarization switching, meaning the conductivity is reduced for fields applied along the polarization direction and enhanced against, which is in line with the BCS mechanism. The variation of the modulation values for different measurement parameters are assumed to be caused by a field dependence of the modulation and variations in polarization loss between poling and readout (depolarization is temperature dependent, cf. with equation 34). By definition, the modulation obtained from the slope ratio is the required conductivity modulation to explain the magnitude and lack of saturation of the polarization with field observed in section 5.1.

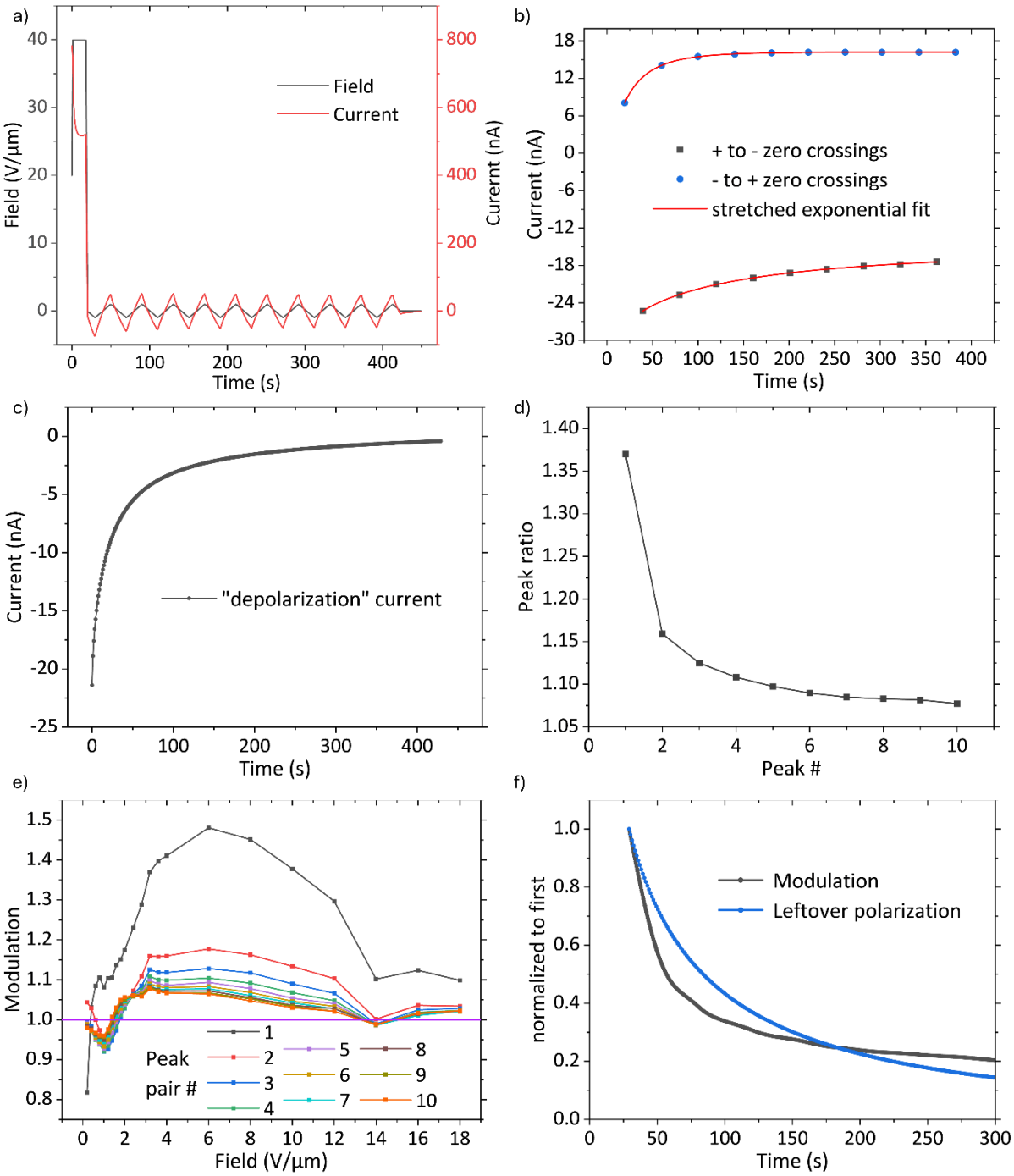

Figure 51. Conductivity modulation measurements on FCH-C3-A. a) shows an exemplary "zig-zag" measurement used to probe conductivity along and against field direction. Before the modulation can be obtained, the measurement has to be corrected for background currents. b) to d) show the correction process. In b) the currents from a) at the zero-crossings of the voltage from positive to negative and for the opposite case are plotted and fitted with a stretched exponential decay which includes a constant term capturing the displacement current. By averaging the resulting fit functions, the "depolarization" current in c) is obtained, which includes depolarization but also further transient currents that might arise due to ionic impurities. "Depolarization" current and displacement current are then used to correct the measured current in a) to obtain the modulation as the ratio of the downwards peak currents divided by the upwards peak currents, which is shown in d) for a

single field value. e) shows the modulation of each peak pair plotted against the field. In f) the extrapolated modulation of the 4 V/µm measurement is plotted against the averaged leftover polarization. Both are normalized to their starting values at $t = 29$ s.

To gain further insight into the conductivity modulation of FCH-C3-A and its possible field dependence, so called "zig-zag" measurements were conducted. For comparability with the DWM measurements, similar parameters and shapes were chosen. Figure 51a) shows an example of a "zig-zag" measurement. A rectangular poling pulse above the coercive field is employed to fully polarize the sample in one direction. It is followed by triangular field pulses with a constant maximum field and alternating sign. Depending on the amplitude of the triangular pulses in relation to the coercive field(s), asymmetric current responses are expected or not. The conductivity modulation is then obtained as the ratio between up and down current peaks. Before the current ratios are taken, the current data has to be corrected for various unwanted background currents. These include the constant displacement current from the continuously changing electric field as well as transient currents due to depolarization, ionic impurities and other effects. Depolarization is expected to be the main contribution and besides the direct effect of the added depolarization current it additionally results in a decrease of the modulation over time.

The "depolarization" current that includes all other transient currents as well as the displacement current can be obtained from the measured currents at the zero crossings of the voltage in a). Keeping in mind the opposite sign of the displacement current for crossing from negative to positive and vice versa two zero-field currents are obtained, with the 20 V/µm measurement (triangular amplitude) plotted as an example in Figure 51b). The zero-field current were then fitted with a stretched exponential decay to account for the depolarization current (see equation 33) with an added constant term that captures the displacement current. Sensible fits for the depolarization current could only be obtained for lower fields between 0.2 V/µm and 2 V/µm, as for higher currents the depolarization gets drowned out by the displacement current. With the fit parameters from the stretched exponential the depolarization current is reconstructed for both zero-crossing directions and averaged, the resulting depolarization current from the 1.8 V/µm measurement is plotted in c) as an example. Integrating the depolarization currents over time results in charge of around 270 mC/m^2 and varies between 125 mC/m^2 and 356 mC/m^2. This deviates not by magnitudes from the expected polarization of 83 mC/m^2 and can be explained by additional transient

currents from ionic impurities and by the finite zero-point voltage of the DBLI. With the obtained “depolarization” and displacement currents the original measurement is corrected and the peak ratios of the downwards peaks with their successive upwards peaks are taken, as shown for the 4 V/µm measurement in d). The peak ratios for each n^{th} peak pair are plotted against the triangular pulse amplitude in e).

Before evaluating the modulation versus field trend, it has to be noted that for triangular amplitudes above the coercive field any modulation should disappear, as then the polarization is switched during each triangle. Similarly, linear response theory demands a vanishing conductivity modulation, i.e. a current ratio of one, in the low field regime towards zero-field, as the derivative of the current with respect to the field must be well-defined at zero-field. Except for the first peak pair, the low field requirements are fulfilled by all peak pairs with only slight deviations. Larger deviations for the first peak pair, especially at lower fields, are not unexpected as there the depolarization current is still of considerable magnitude and even minor imperfections in the background correction have a large impact. Therefore, the modulation at lower fields for the first peak pair is to be taken with a grain of salt. Interestingly, for peak pairs besides the first the modulation drops below one before reversing and steadily climbing above unity. The modulation smaller than one is tentatively attributed to the effect of IBM. As discussed earlier in subsection 4.3, IBM plays a key role in enabling charge injection into FCH-C3-A and others. IBM and BCS are competing effects and it is not immediately clear as to how both can occur in the same device. However in the organic semiconducting ferroelectric benzotrithiophene tricarboxamide (BTTTA) different field dependencies allowed the observation of both effects in a single device, with IBM observed at low fields before giving way to BCS at high fields.[39] Keeping in mind that IBM occurs at the interfaces which tend to be more disordered in organic films, it is reasonable to assume that individual dipoles near contact regions are already reversed at much smaller fields than the bulk polarization. Hence IBM at low fields in some capacity is not unexpected.

The increasing modulation with field from 1 V/µm on up to fields of around 3-6 V/µm and is in line with what has been observed for BCS in the literature.[141] For fields beyond 3-6 V/µm, depending on peak pair, a steady decrease of the modulation is observed. This is attributed to the increasing amount of reversed polarization, as with increasing fields a larger number of hysterons are switched and the effective polarization that modulates the conductivity is

reduced. The data suggests that the high field coercive field is surpassed at 14 V/µm, which is in line with what was observed in section 5.1 for the high field coercive field in FCH-C3-A. The slight increase in modulation afterwards is unexpected and might be an effect of polarization imprint keeping a portion of the dipoles locked in the same configuration. The steady decrease of the modulation with peak pair is a direct result of depolarization. An additional way of characterizing the modulation is obtained by linearly interpolating the peak currents of up- and downwards peak and smoothing the resulting ratio of the interpolated data. An example is given in appendix Figure 15, which also includes a graph of the modulation plotted against the field for different time stamps, showing qualitative and quantitative behavior that is in good agreement with the peak ratios in Figure 51e). The in this way obtained continuous modulation is plotted for the 4 V/µm measurement in Figure 51d) together with the depolarization current, with both normalized to their starting value at $t = 29\text{s}$. While no one-to-one correlation is observed, the qualitative behavior is quite similar, indicating that indeed the reduction in modulation with peak pair (or over time) is caused by depolarization. The depolarization current can be seen as a proxy of the remaining polarization as its integral is equal to the polarization lost so far.

Finally, the modulation values from the “zig-zag” measurements are compared to those from the linear slopes obtained from the DWM measurements, see Figure 50. The latter showed modulation values of around 2 to 10 depending on the exact measurement conditions, while the former only resulted in modulation values of 1.3 to 1.5. This discrepancy can be mainly explained by the effect of depolarization. The first modulation value in time, peak ratio or from extrapolation, is only obtained after 29s. Considering the depolarization current shown in Figure 51c), after 29s its amplitude and therefore the remaining polarization, is reduced to around one-third of its starting value. As shown in e), the modulation is reduced concomitantly with the polarization. The modulation obtained from the linear slope method of the DWM measurements only suffers marginally from depolarization. For a similar depolarization in the DWM measurements, modulation values of 1.3 to 4 would be obtained. These agree well with the modulation values given by the “zig-zag” measurements. Therefore, to obtain a closer match of the modulation values from “zig-zag” and DWM measurements, the former need to be conducted with a greatly increased frequency, to reduce the influence of depolarization. However, this would result in drastically increased displacement currents,

making the extraction of the depolarization currents nearly impossible. In addition, when the displacement currents become large relative to the DC currents, the background correction becomes more erroneous, as the measured data now consists of a large amount of background current and only a small amount of relevant signal. For future measurements, variations in “zig-zag” frequency and probe temperature might yield further insight into the conductivity modulation. For now, the “zig-zag” measurements are consistent with the notion that the conductivity modulation is the cause of the large polarization values and the lack of saturation of the polarization with field observed for FCH-C3-A in section 5.1.

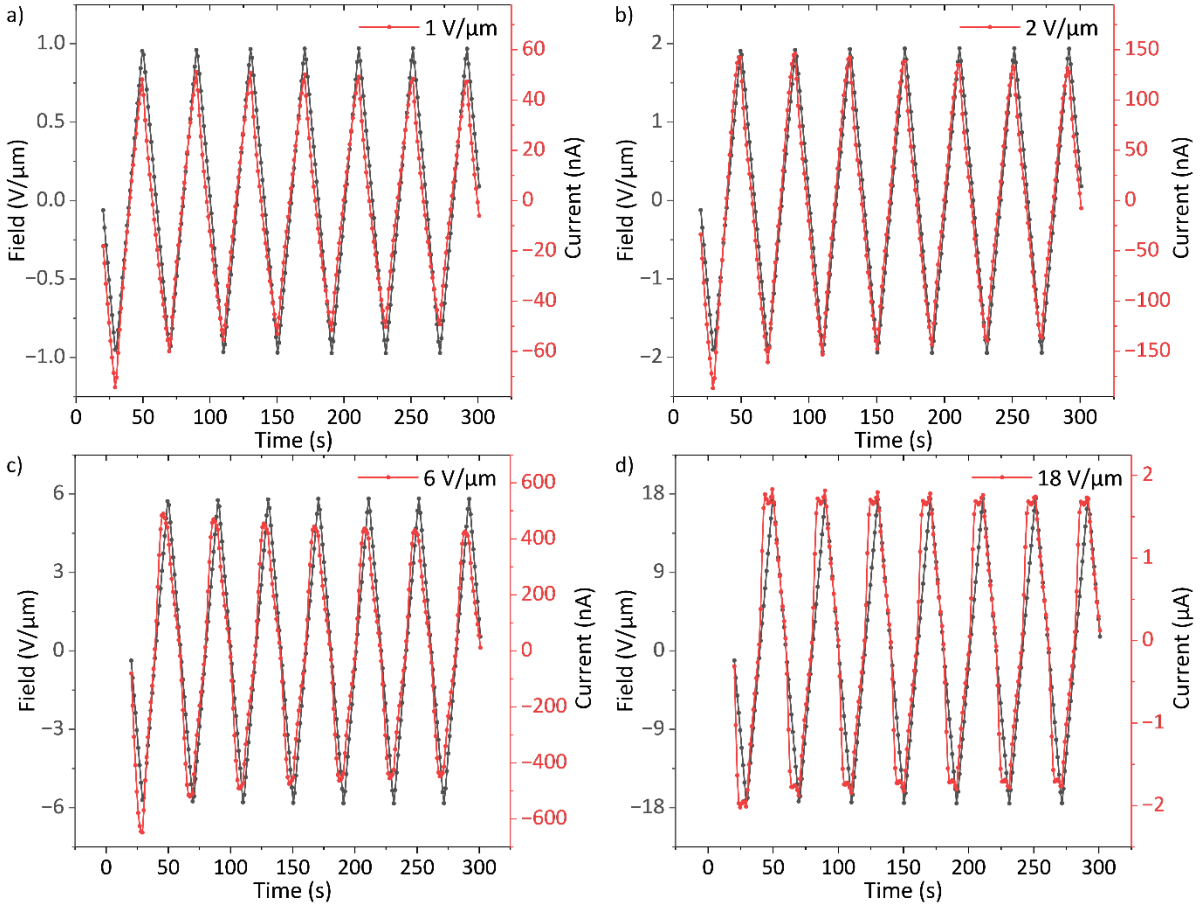

Figure 52. Raw data of the current plotted against time for “zig-zag” measurements with triangular amplitudes of 1 V/µm a), 2 V/µm b), 6 V/µm c) and 18 V/µm d). The rectangular poling peak and the last six triangles were left out for clarity.

The question of the behavior of the individual ferroic sublattices and whether their influence can be separated remains. In previous measurements, the low field coercive field of the amide group was observed to be as low as 2 V/µm (cf. Figure 44c). Looking at the raw data of the zig-zag measurements, presented for representative fields in Figure 52, no sign of polarization switching is found for 1 V/µm and only a slight hint for 2 V/µm. At 6 V/µm, partial switching

is observed in every triangle. The partial switching current is superimposed on the modulated DC-current and is expected to be the same magnitude in for up- and down-peaks. At 18 V/µm, a distinct switching peak is observed, indicating that the coercive field likely has been exceeded. This is consistent with the obtained modulation in Figure 51e). The switching peak is assigned to the fluorinated cyclohexane group. However, a clear separation between the switching of the two dipolar moieties is not observed in this measurement series, which is mostly attributed to the effect of IBM suppressing the amide switching peak. Still, some uncertainty remains as to their individual influence regarding the conductivity modulation.

In this chapter the ferroelectric properties of FCH-C3-A and FCH-E were investigated and proven to be ferroelectric. Neither material showed an indication for a ferroelectric to paraelectric phase transition, as now Curie-Weiß behavior was observed in dielectric spectroscopy measurements. FCH-E exhibited ferroelectric polarization hysteresis above 85°C with a saturating polarization at fields of 40V/µm and beyond with values of 5.1 ± 0.8 mC/m^2. The discrepancy to the theoretical dipole density of 69 mC/m^2 can be explained by an incomplete rotation of the pentafluorocyclohexane group during switching, by a reduction in polarization due to a lack of long-range order, by an overestimation of the effective film thickness or by a combination of the previous effects. The coercive fields ranged between 10 V/µm and 30 V/µm, with a temperature and frequency dependence following the TA-NLS model, indicating a nucleation limited switching process and reinforcing the ferroic nature of the material. CV measurements showed the butterfly shape characteristic for ferroelectric materials, but only at temperatures of 90°C and above. Together with the very small reversible polarization, this indicates that the polarization switching is dominated by irreversible processes.

Polarization hysteresis measurements on FCH-C3-A revealed ferroic like behavior from 85°C on in DWM and CV measurements, however with a non-saturation polarization of a magnitude far exceeding the dipolar density of the material. This discrepancy was traced back to the conductivity of the material, which was shown to be modulated by its ferroelectric polarization, meaning the observed peaks in the DWM measurements are conductivity peaks and not classical ferroelectric switching peaks. To this end, so called “zig-zag” measurements were employed that measured the current response to applied fields along and against polarization. These revealed a conductivity modulation with a field dependence similar to the

bulk conductivity switching observed by Gorbunov *et al.*[141] A comparison of the modulation with the IV-slopes from polarization switching measurements considering depolarization effects, confirmed that the conductivity modulation is the cause for the large magnitude of the polarization as well as its lack of saturation. Hence, FCH-C3-A is classified as ferroelectric. Furthermore, the observation of two separate peaks in DWM and CV measurements indicates the presence of two partially independent ferroic sublattices in FCH-C3-A. The coercive fields of the peaks varied between 3 V/µm to 15 V/µm and 10 V/µm to 30 V/µm, depending on frequency and temperature. The temperature and frequency dependence of the two coercive fields is well described by the TA-NLS model and a comparison of the fit parameters as well as the coercive field values with those obtained for FCH-E allowed the assignment of the low and high field peaks to the switching of the amide- and the pentafluorocyclohexane group, respectively.

6. Ferroelectric and conducting properties of charge-transfer complexes

In this chapter experimental data from investigations of possible ferroelectricity and conductivity of a series of charge-transfer-complexes (CTCs) of the donor molecule NHTA-557 with the three different acceptor molecules TCNE, TCNQ and F4TCNQ are presented, analyzed and compared to data and theory from literature. As the acceptor strength increases continuously from TCNE over TCNQ to F4TCNQ and hence the degree of charge transfer in the respective CTC complexes, possible correlations of the latter with ferroic and conducting properties were a central point of interest. To facilitate comparison, the data from the same type of experiment for all CTC combinations is shown in the same figure. Since the CTC films were prone to degradation and showed poor reproducibility (see section 3.3.5), all data shown is from single crystals unless mentioned otherwise. From here on, NHTA:TCNE will be labeled as CTC1, NHTA:TCNQ as CTC2 and NHTA:F4TCNQ as CTC3.

Single crystal solutions were created by Jan Borstelmann from the Kivala group at Heidelberg University. The majority of CTC films were created by Heiko Mager, the author of this thesis, the remaining ones by Master student Ramon Jannasch. All measurements unless stated otherwise were conducted by Ramon Jannasch under the supervision of Heiko Mager. Analysis and evaluation of the experimental data was shared equally between Ramon Jannasch and Heiko Mager.

6.1 Dielectric properties of NHTA-557 based CTCs

As with the other materials, initial investigations into the possible ferroelectric nature of the CTCs began with dielectric spectroscopy measurements. Preliminary measurements on CTC films showed an increasing tendency for material degradation above 30°C while no features in the capacitance were observed in the temperature from -180°C to -80°C. Dielectric spectroscopy measurements in the temperature range of interest are shown in Figure 53 for CTC1 in a), CTC2 in b) and CTC3 in c). The heating traces of all CTC (top row) look qualitatively similar, with a peak of the capacitance (and therefore dielectric permittivity) at -2°C for CTC1 and CTC2 and at -6°C for CTC3. All three exhibit a rapid decrease in capacitance for temperature above the peak and a weaker gradual decay for temperatures below. Considering the inverse slope of the capacitance for temperatures below and above it is obvious that the ratio is by far exceeding the factor of two that would be expected from

Landau-Devonshire theory for a para- to ferroelectric phase transition, see section 2.2.2. Hence, it is improbable that the peak in dielectric permittivity signals a ferro- to paraelectric Curie-Weiß transition. This is confirmed later, as ferroelectric-like behavior was found below and above the peak temperature. Since the temperature of the peak does not shift notably with frequency for any of the CTCs, the peak is not caused by a dielectric relaxation (e.g. from an induced dipolar rotation).[194] The cooling traces show a peak in capacitance at lower temperatures for all CTCs, at -26°C for CTC1, between -22°C and -26°C for CTC2 and at around -25°C for CTC3. As the peak again does not shift with frequency for any of the compounds and as there is no feature at the original peak position, the cooling trace peak is attributed to the same transition that gives rise to the large peak in the heating trace. A hysteretic shift of the transition temperature is a well-known property of first order phase transitions.[195] However, while unlikely, it could not be excluded that the peak in the cooling traces originates from another phase transition altogether.

The shoulders observed for temperatures below the peak in the heating trace of all CTCs tend to shift to higher temperatures with increasing frequency until they almost completely disappear, which is a common sign of a dielectric relaxation.[194] Similar arguments can be made for the increase in capacitance for temperatures below the peak in the cooling traces, since for larger frequencies a maximum appears which presumably sits at lower, not measured temperatures for lower frequencies. For all CTCs, the peak in the cooling traces shows additional substructure, e.g. in the form of a shoulder at lower temperatures that does not change with frequency. As of now the origin of the substructure is unknown.

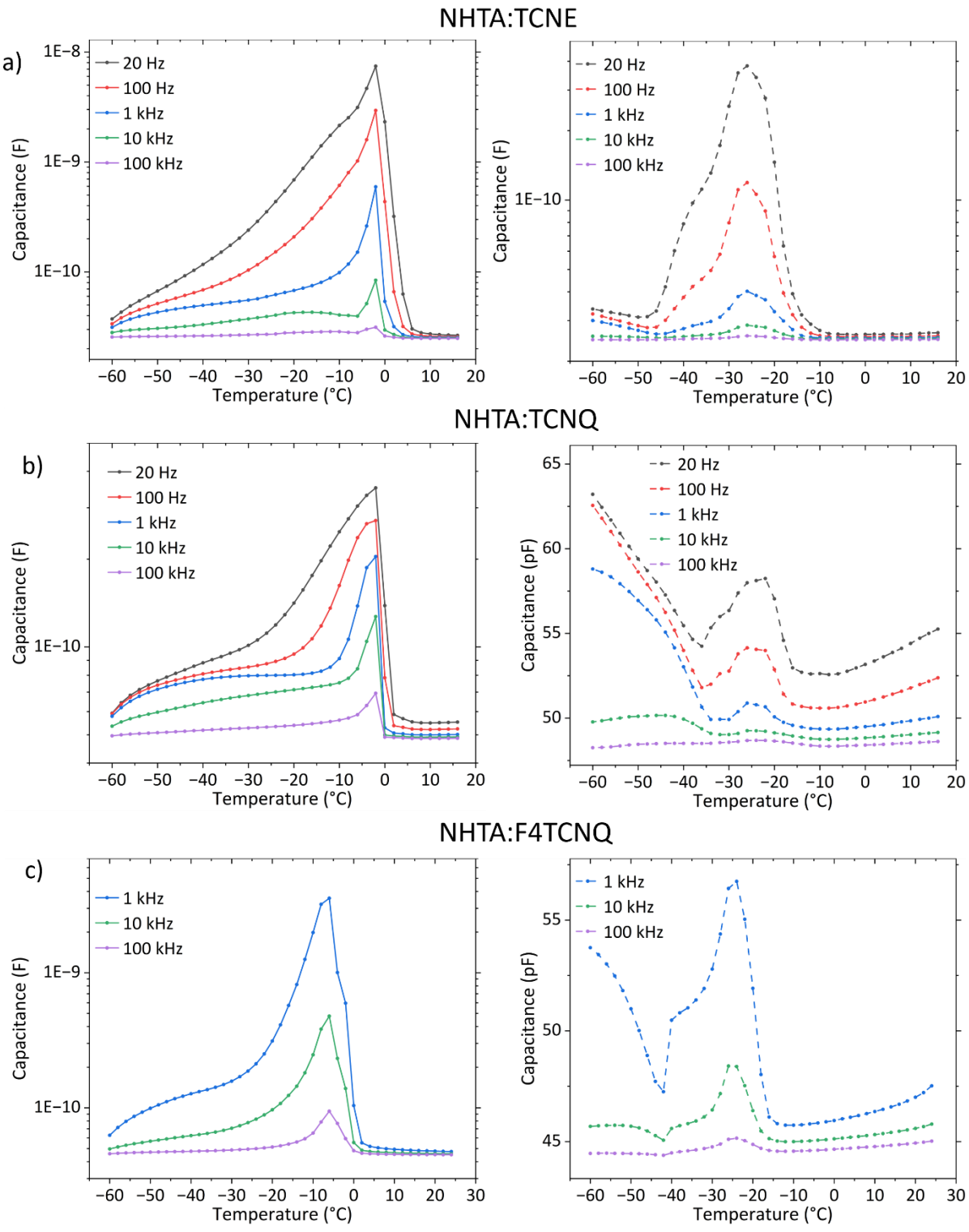

Figure 53. Dielectric spectroscopy measurements of CTC1 a), CTC2 b) and CTC3 c). The measured capacitance is plotted against the temperature for various frequencies. Solid lines in the top graphs depict heating traces, dashed lines in the bottom graphs cooling traces. Note that the y-scales are different for heating and cooling. a) and c) are from single crystals, b) from a drop-casted film. The measured currents at frequencies below 1 kHz in c) exceeded the measuring range for the heating trace and were therefore disregarded. All measurements were conducted in nitrogen atmosphere.

Finally, the peaks being close to 0°C in the heating traces raises the question whether they originate from the melting of frozen water. However, there are considerable arguments against water as origin. The measurements were conducted in nitrogen atmosphere and repeated measurements of CTC1 showed the heating peak occurring at slightly different temperatures with similar magnitude, see appendix Figure 16. Trapped water released at temperatures above 0°C would be expected to condense and freeze on the liquid nitrogen lines, resulting in a sharp decrease in peak signal for repeated measurements, which was not observed. Additionally, the phase transition of melting ice tends to occur in a stepwise manner, with a permanently enhanced dielectric permittivity after melting.[196,197] Therefore water is an unlikely explanation for the observed transition. The cause of the significant dielectric permittivity peak observed in the dielectric spectroscopy is discussed further in section 6.3, considering additional data from DWM measurements.

6.2 Ferroelectric investigation of NHTA-557 based CTCs

Ferroelectric polarization switching was investigated via the DWM over a large temperature range. From the dielectric spectroscopy measurements, it was originally assumed that the ferroelectric phase during heating (cooling) is below 0°C (-25°C) down to lower temperatures, while the paraelectric phase was assumed to be above 0°C (-25°C). However, from temperatures of -180°C to -50°C only leakage and displacement currents were observed with no sign of ferroelectric activity. Generally, at temperatures near the phase transition temperature in the dielectric spectroscopy signs of ferroelectric switching appeared. Figure 54a) to c) show temperature dependent DWM measurements of CTC1, CTC2 and CTC3, respectively. Measurements below 0°C are shown on the left, above 0°C on the right. For CTC1, the data comes from a single sample, measured consecutively at stepwise increasing temperatures. For CTC2 and CTC3 measurements below and above 0°C are from different samples, for stepwise decreasing (CTC2) and increasing (CTC3) temperatures. Because of short-circuiting and degradation issues, large measurement series were difficult to obtain on single samples. Starting with the analysis of CTC1 in a), from -30°C on a distinct shoulder is observed in the first readout pulse that evolves further into a peak until -10°C. From there on the peak begins to vanish until it completely disappears at 0°C. Besides the remark that all CTCs have non-negligible conductivity, background currents are discussed later in section 6.3. While the observations so far agree well with a possible ferro- to paraelectric phase transition

at around 0°C, a further increase in temperature leads again to an increasing background current and the re-appearance of a shoulder at 10°C, which evolves into a distinct peak at higher temperatures up to 50°C. This is especially clear in the third triangular pulse. Therefore, the observed phase transition in the dielectric spectroscopy cannot be the ferro- to paraelectric Curie-Weiß transition. Interestingly, the presumably ferroelectric behavior is detected at temperatures above and below the phase transition indicated by dielectric spectroscopy, but not in the immediate vicinity of the transition point (at -2°C).

Similar observations can be made for the CTC2 in Figure 54b), though it has to be kept in mind that this is a measurement for decreasing temperatures. Starting with temperatures above 0°C on the right, a clear peak is observable from 40°C down to 0°C. On the left below zero, the peak vanishes at -5°C and -10°C before re-appearing as shoulder at -15°C, evolving into a peak below -25°C and finally vanishing again at -45°C. Note that the large steps at zero field for the -25°C measurement is caused by displacement current, amplified by the peak in dielectric permittivity near the phase transition. Considering the dielectric spectroscopy data from Figure 53b) on the right, the -25°C measurement is practically measured at the transition temperature, confirming this hypothesis. Again, the phase transition is presumably not a ferro- to paraelectric transition, as a possible switching peak is still observed at -40°C.

On first glance, the data for the CTC3 shown in Figure 54c) depicts a similar behavior, where again, the data on the left and on the right were taken from different samples. When heating up from -40°C, a shoulder emerges at -35°C that evolves into a distinct peak for increasing temperatures up until 0°C, where the background conductivity too is at its highest. At 5°C any signs of possible ferroelectricity and the background conductivity vanish. In contrast, the other measurement in Figure 54c) on the right shows presumably ferroic behavior from -3°C to +14°C, before it vanishes together with the conductivity at 20°C. In the data on the right in Figure 54c) shoulders/peaks are also seen in the second and fourth pulse, indicating incomplete switching or a very short retention time.

It has to be noted that CTC3 was by far the least stable CTC in addition to the crystals being very small. The latter posed a significant challenge as it was impossible to place only one single crystal aligned in field direction onto the IDE and instead a multitude of small crystals with random alignment were deposited. Depending on its alignment relative to the field direction, each crystal is only exposed to a fraction of the applied external field, which in theory should

lead to a distribution of the coercive fields, if the observed current peaks are caused by polarization switching. While this is not clearly observed in all measurements, presumably because the resulting switching currents of singular crystals are quite small, it is a possible explanation for the occurrence of multiple peaks and substructures. Additionally, ferroelectric switching might occur not only along the main crystal stacking axis, but also orthogonal to it, if multiple DA-stacks are aligned adjacently and offset by half a period. This might result in additional peaks/substructures at coercive fields different from the main stack direction. In general, the data for CTC3 has to be considered as less reliable than the data for CTC1 and CTC2 and no strong claims can be made. For the latter two alignment in field direction was commonly achieved, but possible contributions from off-axis switching cannot be excluded completely.

As mentioned before, CTC3 was shown to crystalize in a 1:2 stoichiometry and to the best of the authors knowledge no ferroic behavior was shown in literature for CTCs with that stoichiometry so far. It is therefore not entirely clear what ferroelectric behavior can be expected from such a material.

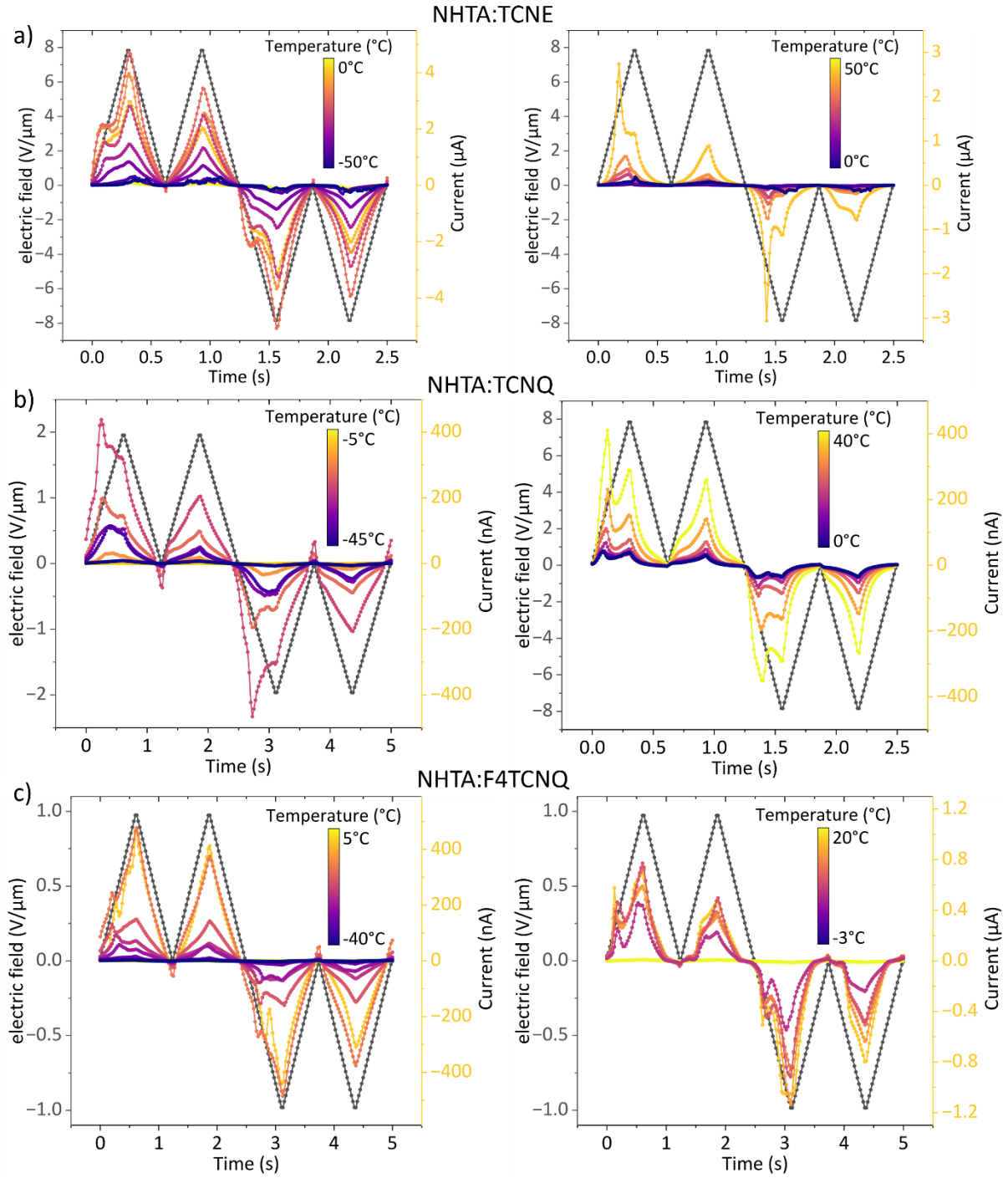

Figure 54. DWM measurements of single crystals on IDE of CTC1 a), CTC2 b) and CTC3 c), depicting measured current versus time for varying temperatures. The applied field is shown as black lines. Temperatures below 0°C are shown on the left, above 0°C on the right. a) and c) are measured for increasing and b) for decreasing temperatures. For CTC1 all measurements were consecutively measured on the same sample, for CTC2 and CTC3 the left and right data comes from separate measurements.

The corresponding polarization hysteresis loops to Figure 54 are shown in the appendix Figure 17. The increase in polarization after reaching maximum field indicates a significant transient

contribution in the low temperature regime for CTC1 and CTC2, which is also seen in the difference in background current magnitude between first and second as well as between third and fourth triangular pulse in Figure 54. To calculate the polarization, the effective area had to be approximated by considering the area of the crystal(s) and taking an effective height of 5 µm (electrode spacing) as the crystal thickness significantly exceeded 5 µm. Light microscope images of the crystals are shown in appendix Figure 18. For CTC1 and CTC2, the polarization values for the low temperature phase are dominated by the transient background current and reach values of 500 mC/m^2. Therefore, most of the "polarization" is not of ferroelectric origin. In the high temperature phase, the values are more reasonable between 50 mC/m^2 and 200 mC/m^2 and presumably reflect the actual switched dipole density more closely. The exact nature of the transient current is unknown, a common candidate would be ionic impurities. The significant conductivity and difficult to estimate area result in extremely large polarization values for the CTC3 on the order of several C/m^2, making the estimation of a possible ferroelectric polarization impossible. Therefore, further attempts to extract approximate polarization values were limited to CTC1 and CTC2.

To further investigate the nature of the observed current peaks and check for the saturation of the observed hysteretic polarization, field dependent DWM measurements were conducted. The resulting currents are shown in Figure 55 on the left and the corresponding polarization hysteresis loops on the right. To compensate for the transient currents and to obtain a realistic value for a possible ferroelectric polarization, the background conductivity peaks were scaled as shown earlier in Figure 40a). An important note is that all DWM measurements with field variation were taken on samples that were heated up from low temperatures and are therefore in the phase indicated by the corresponding heating trace in the dielectric spectroscopy measurements (c.f. Figure 53). Figure 55a) shows data for CTC1 measured at -20°C. First signs of a possible ferroic current can already be seen at a maximum field of 0.6 V/µm with a distinct peak appearing at 3 V/µm. Considering the hysteresis loops on the right, the coercive field is not reached for the former but almost for the latter. A further increase in maximum field to 5 V/µm and beyond shows saturation of the polarization hysteresis loops, i.e. little increase of the saturation polarization with increasing maximum field, indicating the coercive field is already reached for 5 V/µm. The increase of the coercive field despite the saturating polarization is a side effect of the increase in maximum applied

external field at constant frequency, which increases the sweep rate. Therefore, a single exact coercive field cannot be given, but its values are distributed around 2V/µm. At the highest fields of 10 V/µm and above the conductivity begins to increase substantially and kinks appear. These are the first signs of electrical breakdown of the material, which occurred when the field was further increased. Excluding the measurements for fields near the breakdown field, an average saturation polarization of 144 mC/m^2 is obtained. Considering the stack geometry and the fact that the all of the CTCs presumably have only a small ionicity of around 0.1, see section 3.3.3, an ionic polarization smaller than for TTF-BA (2.4 mC/m^2) is expected. An upper limit of the possible ionic ferroelectric polarization can be calculated by considering an overestimated ionicity of 1, the observed displacement from XRD measurements[168] and an estimated unit cell volume of 9 Å^3, which would result in an ionic polarization of around 1 mC/m^2. As the measured polarization is orders of magnitude above the possible values from ionic polarization, is likely significant electronic contributions as in TTF-CA.[151] In comparison to the 67 mC/m^2 obtained for the latter, the measured polarization for CTC1 is significantly larger but still on a comparable and reasonable level. A computational estimation of the electronic polarization of CTC1 is needed in the future to the hypothesis of the electronic ferroelectric polarization. The saturation of the observed polarization and its realistic magnitude strongly imply that CTC1 is indeed ferroelectric.

DWM measurements of CTC2 at -15°C with varying applied maximum fields are shown in Figure 55b) on the left. Already at 4 V/µm clear peaks are observed in the first and third triangular pulse that only slightly increase in magnitude for higher fields, indicating that in case of ferroelectric origin the coercive field is already reached. Confirmation is found in the resulting polarization hysteresis loops on the right, where the polarization increases from 4 V/µm to 5 V/µm significantly and then saturates for even higher applied maximum fields. The only exception is the 7 V/µm measurement, which shows a higher polarization than even the 8 V/µm measurement. A possible explanation is again the onset of electrical breakdown, as for measurements from 6 V/µm on noisy substructures, characteristic for sample degradation, begin to appear that interfere with the background correction via the DWM. The small shoulders in the triangular pulses two and four that do not decrease with field indicate a short polarization retention time. An average saturation polarization of around 127 mC/m^2 is obtained, which is comparable to the polarization measured for CTC1. For the same reason

as for CTC1, no single coercive field can be given but the values are distributed around 2 V/µm. Considering their similar morphology and ionicity the same considerations for the origin of the polarization and its magnitude hold true. With reasonable polarization values and polarization saturation, CTC2 is assumed to be ferroelectric below room temperature.

Additionally, DWM measurements with varying applied maximum fields for CTC2 were taken at +20°C and twice the frequency of the -15°C measurement, shown in Figure 55c) on the left. At 2 V/µm maximum field a shoulder is observed that evolves into a full peak at 4 V/µm. The peak grows with rising applied maximum field up to 6 V/µm but stops increasing in a significant way from here on out. In case of a ferroic origin of the peak, this signals that the coercive field has been exceeded. This notion is further reinforced when considering the change in the peak amplitude compared to the change in the background current peak. Finally, the corresponding polarization hysteresis loops on the right confirm these observations, showing a significant increase in polarization early on that seemingly saturates at higher fields. To fully conclude saturating behavior, additional measurements at higher fields are needed. The polarization values at high fields range from 166 mC/m^2 to 196 mC/m^2 and are hence significantly larger than in the low temperature regime. Here, two remarks are made. Firstly, in both cases contributions from the conductivity cannot be excluded completely and the higher background currents in the 20°C measurement might inflate the polarization values compared to the low temperature measurement. Secondly, it is not clear whether the actual dipolar density is the same at both temperatures, as they are separated by the phase transition observed in the dielectric spectroscopy (c.f. Figure 53) and the different phases might exhibit different dipolar densities.

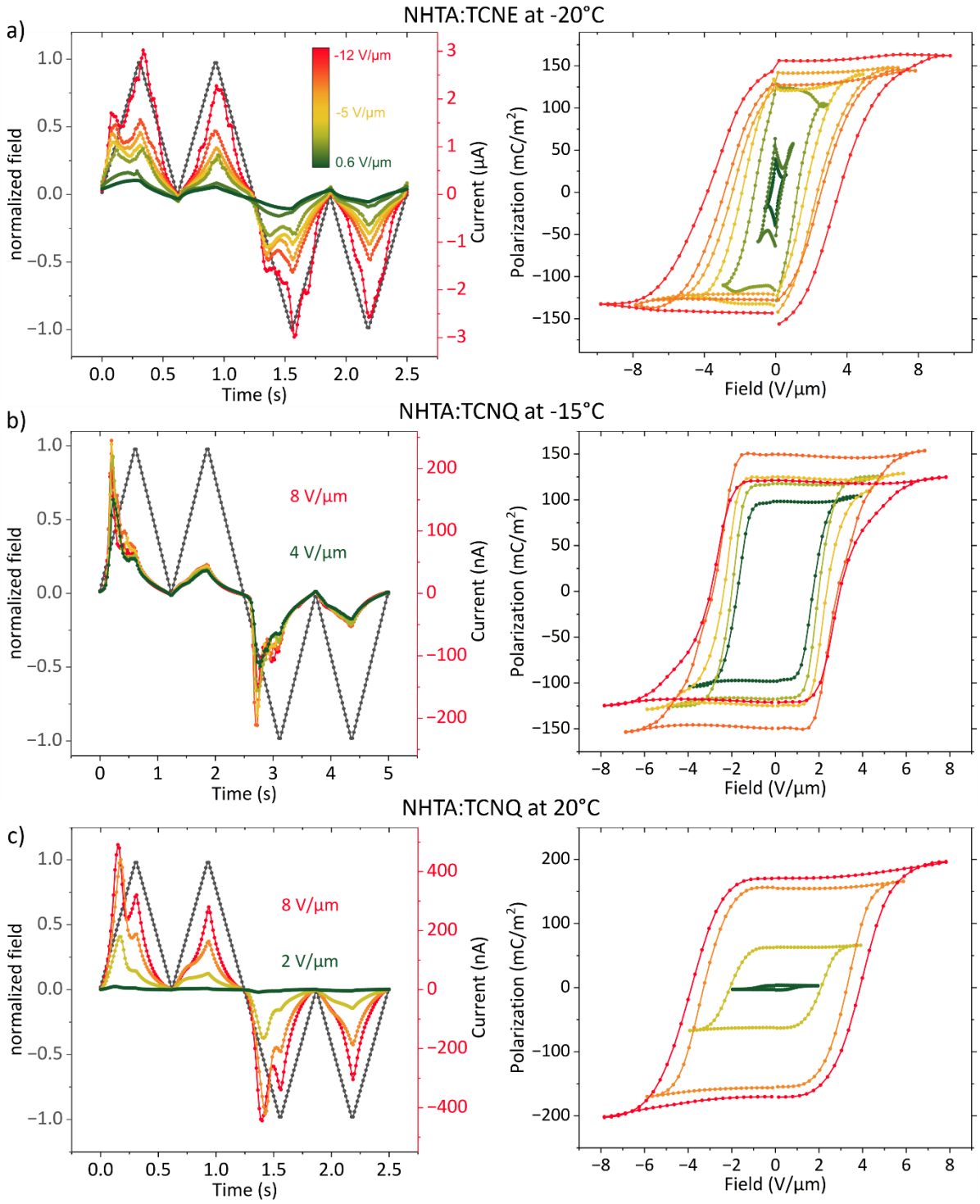

Figure 55. On the left, DWM measurements of CTC1 at -20°C a) and of CTC2 at -15°C b) and 20°C c) for successively increasing applied maximum field at constant frequency are shown. ΔF is 1 V/µm in b) and 2 V/µm in c) while the step size in a) is not constant. The corresponding polarization hysteresis loops are depicted on the right. On the left the raw data is shown while for the polarization hysteresis loops on the right the currents were scaled as demonstrated in Figure 40a) to account for transient currents and to obtain a realistic value for possible ferroelectric polarization.

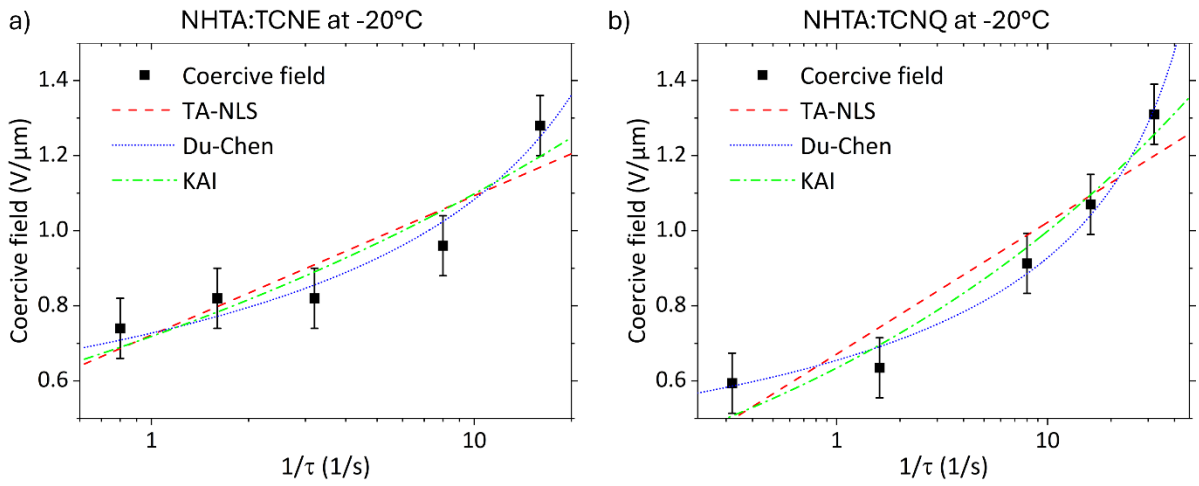

Figure 56. Frequency dependence of the coercive field of CTC1 a) and CTC2 b), measured at -20°C. Note that the coercive field is plotted against one over the reverse sweep time of a DWM triangular pulse. The corresponding raw data is shown in appendix Figure 19. The colored lines are fits of three different analytical polarization switching models with the fit parameters given in the appendix in Table 11-13.

While the magnitude and saturation of the observed polarization in CTC1 and CTC2 make a compelling argument for them being ferroelectric, further proof is required to strengthen the claim. To this end, the frequency dependence of the coercive field was measured by the DWM. In Figure 56a) and b) the resulting data at -20°C is presented for CTC1 and CTC2, respectively. The corresponding raw data is shown in appendix Figure 19. Various analytical models described in section 2.2.4 were fit to the data. For both materials, the TA-NLS model (red lines) does not adequately describe the data as seen by eye and considering goodness of fit parameters, see Table 11-13 in the appendix.

Better fits are obtained for the KAI model (green lines), which gives a dimensionality factor of $d = 1.1 \pm 0.2$ for CTC1 and 1.2 ± 0.2 for CTC2. Depending on the nucleation process, the KAI model predicts domain growth in either d or $d + 1$ dimensions, the former for instant nucleation and no further nucleation rate and the latter for a constant nucleation rate. This would result in either one or two-dimensional domain growth for the CTCs, which both would be feasible. Here, it has to be considered that while the DA-stacks are quasi one-dimensional, the crystals are made up of multiple adjacent DA-stacks. Therefore, possible interstack coupling can result in two-dimensional domain growth.

The Du-Chen model, which is also a thermally activated nucleation-limited switching model, delivers the best description of the data with upper frequency limits of $f_0 = 70 \pm 20$ Hz for

CTC1 and 100 ± 10 Hz for CTC2. While from these preliminary measurements only limited conclusions regarding a possible microscopic polarization switching mechanism can be drawn, it demonstrates the coercive field aligning with behavior generally found in ferroelectric (semi-)crystalline materials and hence is a further indication of the ferroic nature of CTC1 and CTC2. CV-measurements of all CTCs showed no activity at all or inconclusive behavior that was partially associated with degradation, indicating that the portion of reversible switching is small in the CTC single crystals.

6.3 Nature of the observed phase transition and analysis of the conductivity

Besides the observation of a clear phase transition in the dielectric spectroscopy, the temperature dependent DWM measurements of especially CTC1 and CTC2 shown in Figure 54 indicated significant changes in polarization and conductivity in the temperature range of the phase transition. Ferroelectric behavior was detected at temperatures below and above the phase transition point found in dielectric spectroscopy measurements, which together with the fact that the capacitance slopes below and above do not follow the Curie-Weiß law, indicates that the transition is of a different nature than a ferroelectric to paraelectric transition. To gather more information about this phase transition, the temperature dependence of polarization and conductivity was further investigated. As the qualitative behavior is of interest, current is used as proxy for conductivity.

Hence, in Figure 57a), c) and e), the polarization as well as the currents from the peak voltage of the DWM correction peak for CTC1, CTC2 and CTC3 are plotted against the temperature. For CTC1 and CTC3 the temperature was stepwise increased, for CTC2 decreased and the phase transitions occur around -2°C for heating and around -25°C for cooling, c.f. Figure 53. The data for CTC2 and CTC3 is taken from two different measurement series each, one below and one above 0°C. In the case of CTC2 the different voltages were used and hence the currents are scaled to approximately account for the difference. Considering CTC1 in Figure 57a) first, a qualitative very similar behavior of conductivity and polarization is observed. For temperatures far below the transition point, ferroelectric behavior and hence the polarization vanishes, and the conductivity becomes comparably small. Approaching the phase transition from below, a strong increase in polarization and conductivity is observed. Both reach a peak before the transition temperature (-2°C) is reached at -15°C and -10°C respectively. After

peaking both decrease rapidly with the polarization vanishing at the phase transition and the conductivity falling to a global minimum. Increasing the temperature from there on results in the reappearance of the ferroelectric polarization and a concomitant increase of the conductivity. The qualitative behavior of conductivity and polarization is nearly the same in CTC2, albeit shifted in temperature as expected when measuring for decreasing temperatures. For both CTC1 and CTC2, conductivity and polarization exhibit nearly identical qualitative temperature dependence, an indication that both might be coupled and/or governed by the same microscopic processes.

It has to be noted that an increasing conductivity often leads to an overestimation of the ferroelectric polarization obtained by DWM measurements, which can be seen in the polarization values around the conductivity peak, especially for CTC2. Therefore, one might gain the impression that the change in polarization is only a direct consequence of the changing conductivity and not an actual variation of the dipolar density. However, the peaks of polarization and conductivity for CTC1 are shifted by one temperature step. As both values taken from the same measurement, refuting the notion that the polarization change is purely driven by the changing conductivity. For CTC3 shown in Figure 57e), the conductivity shows a similar increase and peak when approaching the phase transition followed by a drop around the phase transition to a level higher than before the transition. From there on the conductivity remains roughly constant until at 20°C it drops significantly, together with the disappearance of any kind of ferroic-like behavior. Polarization follows conductivity only to a limited extent, i.e. at temperatures well below the phase transition, but no clear correlation as for CTC1 and CTC2 is observed. It has to be noted that the polarization values for CTC3 are by far exceeding any kind of physically possible ferroelectric polarization, due to a high conductivity and a difficult to estimate area, making quantitative estimations impossible.

On the right side of Figure 57 the logarithm of the current is plotted against the inverse temperature. In this depiction, the temperature dependent conductivity of CTC1 and CTC2 bears a strong resemblance to the kink-like temperature dependence of the conductivity near the neutral-ionic phase transition in TFF-CA.[167,198,199] As discussed in section 3.3.3 in more detail, TTF-CA undergoes a neutral ($\rho = 0.3$) to ionic ($\rho = 0.6$) phase transition at 83 K with a concomitant transition from the para- to the ferroelectric state.[158] In TTF-CA the DC-conductivity near the NIT in the neutral state is assumed to be dictated by the dynamics of

neutral-ionic domain walls (NIDW, c.f. Figure 21b), which have been detected via spectroscopic means and are hypothesized to enable DC-conduction.[52,200] Approaching the phase transition from above (neutral state) presumably leads to an increase in NIDWs that compensates the temperature-mediated decrease in conductivity resulting in a small plateau. At the phase transition temperature, the formation of charged spin-soliton-like defects (c.f. Figure 21c) is assumed to explain the sudden jump in conductivity.[200,201]

Tokura *et al.* obtained activation energies from Arrhenius fitting the conductivity above and below the transition temperature, obtaining values around 0.1 eV.[167] This implies that low energy excitations are determining the conductivity, which agrees with the presumed presence of NIDW and solitons. At first glance, the conditions appear to be quite similar to those found in CTC1 and CTC2, suggesting that the observed phase transition might be of neutral-ionic nature. However, there are a few distinct differences, making the assignment not straightforward. As mentioned previously, the CTCs in this work have ionicities around 0.1 at room temperature, meaning they are in the neutral state above the phase transition. For TTF-CA, the NIT is occurring simultaneously with a para- to ferroelectric phase transition, i.e. the CTC is paraelectric in the neutral state. In contrast, the compounds presented in this thesis all exhibit ferroelectric-like behavior at room temperature in the neutral state. This indicates that the ferroelectricity does not require an ionic state. If the phase transition of the CTCs is accompanied by a change in ionicity, ferroic behavior would be conserved during either a neutral to neutral ($\rho \approx 0.1 \rightarrow 0.1 < \rho < 0.5$) transition or during an actual neutral to ionic transition ($\rho \approx 0.1 \rightarrow 0.5 < \rho \leq 1$), depending on $\Delta\rho$. While the temperature dependence of the conductivity of CTC1 and CTC2 lacks the plateau observed for TTF-CA and the activation energies obtained by Arrhenius fitting are significantly larger, between 0.4 eV and 1 eV (see Figure 57b) and d), the similarity still implies a neutral-ionic character. To answer the question of the ionicity, the CTCs need to be investigated by temperature dependent vibrational spectroscopy in the future. Temperature dependent XRD measurements might provide further insight into possible changes in dimerization with temperature. Additionally, electron spin resonance measurements might reveal information on the presence of spin-soliton-like defects. For now, the exact nature of the observed phase transition remains speculative.

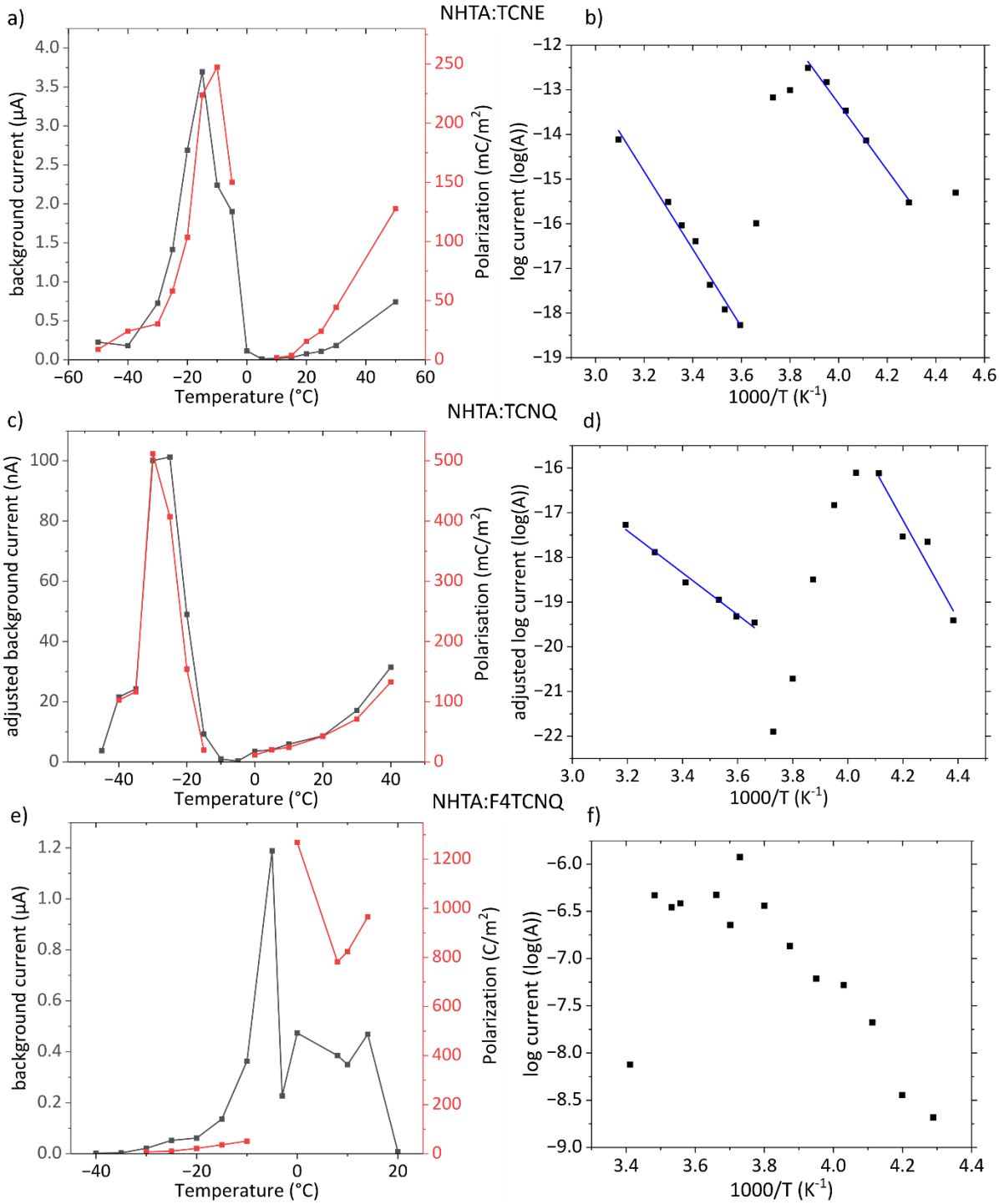

Figure 57. a), c) and e) show the polarization and the corresponding current peak of the correction pulse from DWM measurements plotted against the temperature for CTC1, CTC2 and CTC3, respectively. The data for CTC2 and CTC3 comes from two separate measurement series, one above and one below 0°C. In the case of CTC2 they were taken with different fields, therefore the currents are scaled to account for the field difference. In b), d) and f) the logarithm of the current is plotted against inverse temperature. The blue lines are Arrhenius fits.

Summarizing, in this chapter three different CTCs based on the electron donor NHTA-557 were investigated regarding their ferroelectric and conductive properties. In all investigated CTCs, dielectric spectroscopy measurements revealed a significant peak of the dielectric permittivity around -2°C when heating shifted to -25°C when cooling. The slopes before and after the transition do not follow the Curie-Weiß law, implying that the transition is not of para-to ferroelectric nature. This is confirmed by ferroelectric-like behavior measured with the DWM for temperatures above (up to 40°C to 50°C) and below (down to 30°C to 40°C) the phase-transition temperature. For CTC1 and CTC2 saturation of the polarization with applied external field was observed, with respective realistic values of 144 mC/m^2 and 181 mC/m^2 for the ferroelectric polarization. While vastly exceeding the dipolar density obtained by considering an ionic picture, it was shown in literature that the partial degree of charge transfer allows for large electronic contributions to the polarization. The latter is to be calculated computationally in the future. Considering the saturation of the polarization, its sensible magnitude and that the frequency dependence of the coercive field is well described by analytical models for ferroelectric polarization switching, CTC1 and CTC2 are classified as ferroelectric materials.

For CTC3, the high conductivity and hardly definable sample area resulted in polarization values multiple orders of magnitude higher than what could be explained by ferroelectric means, leaving the ferroelectric status of the material in question.

The temperature dependent conductivity of CTC1 and CTC2 exhibited a characteristic kink-like behavior, resembling findings from other ferroelectric CTCs in literature that undergo a transition from a neutral to an ionic state at a critical temperature. Contrary to those, the CTCs investigated in this work exhibited ferroelectric behavior in the quasi-neutral state, showing that even CTCs of low ionicity can be ferroelectric. A similar temperature dependence of conductivity and ferroelectric polarization around the phase transition was found for CTC1 and CTC2, indicating that both properties are either coupled and/or influenced by the same underlying microscopic mechanisms around the transition. While the behavior of the conductivity suggests that the observed phase transition is neutral to ionic in nature, definitive proof can only be obtained from a direct measurement of the temperature-dependent ionicity which is a natural next step in the research progression.

7. Summary

The research presented in this thesis is to a large degree focused on two distinct groups of organic materials, the fluorinated cyclohexane amides (FCHs) which are small molecules with a tendency to form supramolecular structures and series of charge-transfer-complexes (CTC) based on combinations of the electron donor NHTA-557 together with well-known acceptor molecules TCNE, TCNQ and F4TCNQ. All materials were systematically investigated experimentally regarding possible ferroelectric properties, for unusual conductivity behavior and in some cases, regarding coupling between ferroic and conducting properties.

The small molecule FCH-C3-A was deemed a prime candidate for potential ferroelectric behavior, with two strong dipolar moieties, a pentafluorocyclohexane ring and an amide group connected via a carbon chain spacer. The material has been known to form H-bonded, supramolecular structures in solution and if these supramolecular structures could be replicated in thin films in an ordered fashion, alignment of the dipolar moieties was expected to result in a macroscopic polarization. Indeed, preliminary electric characterization by the double wave method (DWM), probing polarization switching, and capacitance-voltage (CV) sweeps, probing dipolar mobility, demonstrated ferroelectric-like behavior. However, the measured polarization values vastly exceeded the physical dipole density of the material, even after the inclusion of extensive background current correction schemes. The background conductivity of FCH-C3-A was surprisingly high for a material lacking an extended π-system , which should be insulating due to its large bandgap.

It became increasingly clear that the contribution of the conductivity to the polarization could not be easily corrected for, without a better understanding of its fundamental nature and origins. Further investigations into the conducting properties of FCH-C3-A revealed that the conductivity is time-stable and an intrinsic material property, not originating from artifacts like double-layer formation, ionic impurities or degradation. Between 300 K and 370 K the conductivity increased over five orders of magnitude and field annealing resulted in a permanently enhanced conductivity by three orders of magnitude. This was connected to the formation of supramolecular fibers in FCH-C3-A films that aligned in field direction during field annealing, as observed via atomic-force microscopy. Grazing incident wide angle X-ray measurements confirmed alignment and enhanced ordering on larger scales. Analogous measurements on molecular derivatives FCH-C3-TA, where the oxygen of the amide group is

replaced by sulfur, and FCH-E, which lacks the amide group and the spacer, indicated that the amide group plays a central role regarding the observed novel conductivity. Furthermore, long-range alignment turned out to be a helpful, but not necessary condition. The electronic species responsible for charge transport are proposed to be holes. Initial oxidation of a suitable moiety, here presumably the amide nitrogen, via electron transfer to the metal electrode, is followed by hole transport through the bulk by inter-molecular charge transfer. This hypothesis is supported by the observation of space-charge-limited current (SCLC) behavior in current-voltage characteristics. While the experimental and theoretical estimated energy levels yield significant injection barriers for the gold electrodes used in the case of FCH-C3-A and hence should prevent injection and SCLC behavior, the dipole density of the material was estimated to lower the barrier sufficiently to permit efficient charge injection.

Hence, a general set of requirements for materials to exhibit this novel conductivity could be formulated: they need to have an easily oxidizable moiety, a sufficient interfacial dipole density and possibly H-bonding to allow supramolecular polymerization. The validity of this hypothesis was tested and confirmed by investigation of molecular compounds adhering to these requirements, the molecular discotic families of the benzetricarboxamides, (BTAs) with a π-conjugated core, the cyclohexanetricarboxamides (CTAs) without a π-system. Furthermore, triphenylamine derivatives (TPAs) with an extended π-system showed qualitatively and quantitatively similar conductive properties, e.g. SCLC mobilities and a Gaussian disorder-like temperature dependence of the conductivity. Hence, a strong similarity and possibly universality of charge transport in organic materials with and without extended π-system is implied.

With the conducting properties of FCH-C3-A sufficiently characterized, its ferroelectric properties and those of FCH-E were revisited. For neither material a para-to-ferroelectric Curie-Weiß-like transition could be observed, as they exhibited ferroelectric behavior from around 80°C up to their respective melting points. Both compounds showed characteristic CV-butterfly loops as well as polarization hysteresis loops, with a temperature and frequency dependence of their respective coercive fields that is well described by analytical model based on thermally activated nucleation-limited polarization switching (TA-NLS). While polarization saturation with increasing field strength was measured for the non-conducting FCH-E, the obtained values were too small by roughly a factor or ten, which was attributed to a

combination of lacking long-range order, possible off-axis dipole alignment and an eventual overestimation of the effective film height.

On the other hand, FCH-C3-A showed a non-saturating polarization with values exceeding the possible dipolar polarization by orders of magnitude. This behavior could be explained by taking into account the significant conductivity of the material, and how this conductivity is modulated by the dipolar polarization. A series of conductivity-switching measurements using "zig-zag" pulses showed that for higher fields FCH-C3-A exhibits bulk-conductivity switching (BCS), meaning that the conductivity is increased when the applied field is opposed to the direction of the ferroelectric polarization and reduced when it is aligned alongside. The field dependence of the modulation was measured, showing injection-barrier modulation at lower fields followed by BCS for further increasing fields. The occurrence of BCS gave an explanation for the non-saturation polarization and its order of magnitude. With that, FCH-C3-A was proven to be truly ferroelectric.

With the right choice of parameters, two different coercive fields could be resolved in DWM and CV measurements of FCH-C3-A. The temperature and field dependence of both fields is well described by the TA-NLS model, indicating that the two dipolar moieties of FCH-C3-A act as partially independent ferroelectric sublattices. Comparison of the coercive field values and their fit parameters with those obtained for FCH-E allowed the probable assignment of each coercive field to a corresponding dipolar moiety of FCH-C3-A.

The presence of two ferroelectric sublattices, as well as its conductivity(-switching properties) make FCH-C3-A a truly intriguing multifunctional material that showcases the flexibility of organic materials and serves as a promising basis for further research. While the discovery of a DC-conductivity in materials with no extended π-system is of more fundamental interest, the conductivity switching is a property highly sought after for memory applications.

A series of organic charge-transfer complexes (CTCs) consisting of combinations (called CTC1, CTC2 and CTC3) of the electron donor NHTA-557 with each of the acceptors TCNE, TCNQ and F4TCNQ were investigated for their ferroelectric properties. The CTCs exhibit a stack-like morphology with alternating donor and acceptor molecules arranged in one-dimensional stacks which when dimerized in a Peierls(-like) transition, are expected to yield a macroscopic polarization. As the films created from CTC solutions proved unstable and lacking in

reproducibility, single crystals with enhanced stability were used. Dielectric spectroscopy measurements revealed a strong dielectric peak across all frequencies in the heating trace around -2°C that was shifted when cooling to -25°C and is a strong indication for the occurrence of a phase transition. To begin with thought of as a para- to ferroelectric phase transition, deviations from the Curie-Weiß law sew doubts about the nature of the phase transition. Indeed, follow-up DWM measurements showed ferroelectric-like current peaks below and above the phase transition temperature for all CTCs. For CTC1 and CTC2, polarization saturation with field strength was observed with values far exceeding the possible ionic polarization. However, similar cases are known from literature, where the magnitude of the measured polarization could be explained by the electronic contribution to the polarization. While rarely occurring, it has been confirmed by theoretical and computational studies. Hence it is assumed that the polarization of the CTCs investigated in this work is dominated by the electronic contributions, as they show polarization values of similar magnitude and exhibit the partial charge transfer with concomitant covalency that is a prerequisite for electronic ferroelectricity. The frequency dependence of the coercive fields of CTC1 and CTC2 was well described by analytical polarization switching models with a dimension of one obtained as fitting parameter, in agreement with the morphology of the 1D donor-acceptor stacks. Hence, CTC1 and CTC2 are presumed ferroelectric while further proof is required for CTC3.

The conductivity of CTC1 and CTC2 was found to undergo a pronounced step-like increase when approaching the transition temperature from higher temperatures with the general temperature dependent behavior being reminiscent of what was found in literature for the CTC tetrathiafulvalene-*p*-chloranil (TTF-CA). TTF-CA undergoes a para-to-ferroelectric phase transition with a concomitant neutral to ionic phase transition where the ionicity ρ changes from 0.3 to 0.6. The temperature dependence of the conductivity has been linked to the presence of neutral-ionic-domain walls and the creation of spin solitons in the ionic phase, both low energy excitation hypothesized to carry charge. Compared to TTF-CA, CTC1 and CTC2 are ferroelectric in the neutral state ($\rho \approx 0.1$) above the phase transition temperature, showing that ferroelectricity can even be achieved for low ionicities. Nevertheless, the similar behavior of the conductivity around the phase transition implies that the transition is of neutral-ionic-nature, while conserving ferroelectricity. Furthermore, the observed

temperature dependence of conductivity and polarization was qualitatively nearly identical, implying a possible coupling and/or that the changes are driven by the same underlying microscopic mechanisms around the phase transition. To better understand the nature of the phase transition measurements of the temperature dependent ionicity need to be conducted in the future.

CTCs with ferroelectric behavior at room temperature extremely rare and so are materials undergoing neutral-ionic transitions. Together with the possible occurrence of spin-solitons, the CTCs investigated offer a rich phenomenology for future studies and a better understanding of the mechanisms behind their properties might push CTCs towards use in ferroelectric applications.

Acknowledgements

Now it is time to thank all the kind souls who, in one way or another, have helped me in the creation of this thesis.

First of all, I want to thank my supervisor Martijn Kemerink, who gave me the opportunity to conduct research on the topic of organic electronics, my favorite branch of condensed matter physics. Having had no real experience with ferroelectric materials beforehand, the start of this project felt a bit like a departure into the (exciting) unknown. Over time, organic ferroelectrics proved to be a fascinating subject, with some unexpected surprises in store and no small number of questions for me. Not only did Martijn do his best to answer the questions I was struggling with, he also provided exceptional guidance on which direction to take when the path forward seemed unclear. I deeply appreciate Martijn's supervision style, especially the open door policy and the large amount of time he dedicates to his students.

I am very grateful to Prof. Dr. Peer Fischer for taking the role of the second referee for this thesis, as well as to Prof. Dr. Hans-Christian Schultz-Coulon and Prof. Dr Tristan Bereau for taking the role of examiners for my PhD defense.

A big thank you to Prof. Max von Delius from Ulm University and his group, especially Shyamkumar, Oleksandr and Vivek, for providing the FCHs and their supporting data, as well as insightful comments and suggestions during the paper writing process.

I would also like to thank Prof. Milan Kivala from Heidelberg University and his PhD students. Ina for the synthesis of the NHTA and the TPAs, Jan for his DFT calculations and help with the synthesis of the single crystal charge transfer complexes and Angelina as well as their technician Frank for preliminary temperature dependent XRD measurements of the CTC single crystals that unfortunately won't be finished in time to be included into this thesis.

I am very thankful to the HGSFP for granting me financial aid for the finalization of this thesis.

Special thanks to Doro and Clemens, who provided invaluable support and guidance to not only to me, but to the whole group.

Many thanks to the IMSEAM administration and especially Henna, for being amazingly helpful with all kinds of administrative stuff.

I would like to thank the complete IMSEAM technical staff for keeping the institute and the clean room always running. In particular, thanks to Michael for his help with the diamond saw, all sorts of clean room and general technical issues, and to Stefan for his contributions to the development of Anton's and Mine's photolithography process.

Thanks to Finn from the Zaumseil group for his help with Raman spectroscopy measurements and the electron beam evaporator, and to Sebastian for help with the contact angle measurements.

A big thank you to all the people at the Kemerink group, it was a pleasure to work and play cards during the lunch break with all of you. Hopefully there will be many more rounds of TFM in the future! I especially want to thank my fellow PhD students Andrey, Anton, Maxi, Morty, Pria and Tobias for the fun times at and away from the institute. It was nice to always have someone to talk to (or sometimes rant :D) about your current research or life in general. The movie nights, board games, barbecues and generally going out together was always a great experience!

Special thanks to Maxi, Andrey, Anton, and to my students Ramon and Eric for their excellent cooperation during various projects.

Thanks to Sophia for continuing the research on FCH-C3-A and conducting first KPFM measurements, hopefully many more exciting findings await!

Thank you, Andrey and Kurti, for being great roommates, although one after the other, and Anton for being an entertaining office mate, I always enjoyed our little talks about politics and the world.

Another big thank you to all my other friends who were not involved in my work life, for providing entertainment during my free time ;).

I am very grateful to my family, my parents, grandparents and especially my brother, your continued support throughout my life has been nothing short of amazing.

Finally, and most importantly, thank you to Margot for making the recent years such a wonderful time. Your loving support and comedic genius always cheered me up when things were not going so well.

References

(1) Dong, H.; Wang, C.; Hu, W. High Performance Organic Semiconductors for Field-Effect Transistors. *Chem. Commun.* **2010**, *46* (29), 5211. https://doi.org/10.1039/c0cc00947d.

(2) Okamoto, T.; Kumagai, S.; Fukuzaki, E.; Ishii, H.; Watanabe, G.; Niitsu, N.; Annaka, T.; Yamagishi, M.; Tani, Y.; Sugiura, H.; Watanabe, T.; Watanabe, S.; Takeya, J. Robust, High-Performance n-Type Organic Semiconductors. *Sci. Adv.* **2020**, *6* (18), eaaz0632. https://doi.org/10.1126/sciadv.aaz0632.

(3) Alves, H.; Molinari, A. S.; Xie, H.; Morpurgo, A. F. Metallic Conduction at Organic Charge-Transfer Interfaces. *Nat. Mater.* **2008**, *7* (7), 574–580. https://doi.org/10.1038/nmat2205.

(4) Ferraris, John.; Cowan, D. O.; Walatka, V.; Perlstein, J. H. Electron Transfer in a New Highly Conducting Donor-Acceptor Complex. *J. Am. Chem. Soc.* **1973**, *95* (3), 948–949. https://doi.org/10.1021/ja00784a066.

(5) Ebbesen, T. W.; Lezec, H. J.; Hiura, H.; Bennett, J. W.; Ghaemi, H. F.; Thio, T. Electrical Conductivity of Individual Carbon Nanotubes. *Nature* **1996**, *382* (6586), 54–56. https://doi.org/10.1038/382054a0.

(6) Novoselov, K. S.; Geim, A. K.; Morozov, S. V.; Jiang, D.; Zhang, Y.; Dubonos, S. V.; Grigorieva, I. V.; Firsov, A. A. Electric Field Effect in Atomically Thin Carbon Films. *Science* **2004**, *306* (5696), 666–669. https://doi.org/10.1126/science.1102896.

(7) Castro Neto, A. H.; Guinea, F.; Peres, N. M. R.; Novoselov, K. S.; Geim, A. K. The Electronic Properties of Graphene. *Rev. Mod. Phys.* **2009**, *81* (1), 109–162. https://doi.org/10.1103/RevModPhys.81.109.

(8) Lu, G.; Yu, K.; Wen, Z.; Chen, J. Semiconducting Graphene: Converting Graphene from Semimetal to Semiconductor. *Nanoscale* **2013**, *5* (4), 1353. https://doi.org/10.1039/c2nr32453a.

(9) Bässler, H. Charge Transport in Disordered Organic Photoconductors a Monte Carlo Simulation Study. *Phys. Status Solidi B* **1993**, *175* (1), 15–56. https://doi.org/10.1002/pssb.2221750102.

(10) Coropceanu, V.; Cornil, J.; Da Silva Filho, D. A.; Olivier, Y.; Silbey, R.; Brédas, J.-L. Charge Transport in Organic Semiconductors. *Chem. Rev.* **2007**, *107* (4), 926–952. https://doi.org/10.1021/cr050140x.

(11) Arikuma, Y.; Takeda, K.; Morita, T.; Ohmae, M.; Kimura, S. Linker Effects on Monolayer Formation and Long-Range Electron Transfer in Helical Peptide Monolayers. *J. Phys. Chem. B* **2009**, *113* (18), 6256–6266. https://doi.org/10.1021/jp810200x.

(12) Arikuma, Y.; Nakayama, H.; Morita, T.; Kimura, S. Electron Hopping over 100 Å Along an α Helix. *Angew. Chem. Int. Ed.* **2010**, *49* (10), 1800–1804. https://doi.org/10.1002/anie.200905621.

(13) Ing, N. L.; Spencer, R. K.; Luong, S. H.; Nguyen, H. D.; Hochbaum, A. I. Electronic Conductivity in Biomimetic α-Helical Peptide Nanofibers and Gels. *ACS Nano* **2018**, *12* (3), 2652–2661. https://doi.org/10.1021/acsnano.7b08756.

(14) Zhang, S.; Li, F.; Jiang, X.; Kim, J.; Luo, J.; Geng, X. Advantages and Challenges of Relaxor-PbTiO3 Ferroelectric Crystals for Electroacoustic Transducers – A Review. *Prog. Mater. Sci.* **2015**, *68*, 1–66. https://doi.org/10.1016/j.pmatsci.2014.10.002.

(15) Park, S.-E.; Shrout, T. R. Relaxor Based Ferroelectric Single Crystals for Electro-Mechanical Actuators. *Mater. Res. Innov.* **1997**, *1* (1), 20–25. https://doi.org/10.1007/s100190050014.

(16) Cross, L. E. Ferroelectric Materials for Electromechanical Transducer Applications. *Mater. Chem. Phys.* **1996**, *43* (2), 108–115. https://doi.org/10.1016/0254-0584(95)01617-4.
(17) Lew, W.; Lytken, O.; Farmer, J. A.; Crowe, M. C.; Campbell, C. T. Improved Pyroelectric Detectors for Single Crystal Adsorption Calorimetry from 100 to 350 K. *Rev. Sci. Instrum.* **2010**, *81* (2), 024102. https://doi.org/10.1063/1.3290632.
(18) Schreiter, M.; Gabl, R.; Lerchner, J.; Hohlfeld, C.; Delan, A.; Wolf, G.; Blüher, A.; Katzschner, B.; Mertig, M.; Pompe, W. Functionalized Pyroelectric Sensors for Gas Detection. *Sens. Actuators B Chem.* **2006**, *119* (1), 255–261. https://doi.org/10.1016/j.snb.2005.12.042.
(19) Sixsmith, A.; Johnson, N.; Whatmore, R. Pyroelectric IR Sensor Arrays for Fall Detection in the Older Population. *J. Phys. IV Proc.* **2005**, *128*, 153–160. https://doi.org/10.1051/jp4:2005128024.
(20) Scott, J. F. Applications of Modern Ferroelectrics. *Science* **2007**, *315* (5814), 954–959. https://doi.org/10.1126/science.1129564.
(21) Shu-Yau Wu. A New Ferroelectric Memory Device, Metal-Ferroelectric-Semiconductor Transistor. *IEEE Trans. Electron Devices* **1974**, *21* (8), 499–504. https://doi.org/10.1109/T-ED.1974.17955.
(22) Ishiwara, H. Ferroelectric Random Access Memories. *J. Nanosci. Nanotechnol.* **2012**, *12* (10), 7619–7627. https://doi.org/10.1166/jnn.2012.6651.
(23) Valasek, J. Piezo-Electric and Allied Phenomena in Rochelle Salt. *Phys. Rev.* **1921**, *17* (4), 475–481. https://doi.org/10.1103/PhysRev.17.475.
(24) Damjanovic, D. Ferroelectric, Dielectric and Piezoelectric Properties of Ferroelectric Thin Films and Ceramics. *Rep. Prog. Phys.* **1998**, *61* (9), 1267–1324. https://doi.org/10.1088/0034-4885/61/9/002.
(25) Haertling, G. H. Ferroelectric Ceramics: History and Technology. *J. Am. Ceram. Soc.* **1999**, *82* (4), 797–818. https://doi.org/10.1111/j.1151-2916.1999.tb01840.x.
(26) Jaffe, H. Piezoelectric Ceramics. *J. Am. Ceram. Soc.* **1958**, *41* (11), 494–498. https://doi.org/10.1111/j.1151-2916.1958.tb12903.x.
(27) Acosta, M.; Novak, N.; Rojas, V.; Patel, S.; Vaish, R.; Koruza, J.; Rossetti, G. A.; Rödel, J. BaTiO3-Based Piezoelectrics: Fundamentals, Current Status, and Perspectives. *Appl. Phys. Rev.* **2017**, *4* (4), 041305. https://doi.org/10.1063/1.4990046.
(28) Chen, X.; Han, X.; Shen, Q. PVDF-Based Ferroelectric Polymers in Modern Flexible Electronics. *Adv. Electron. Mater.* **2017**, *3* (5), 1600460. https://doi.org/10.1002/aelm.201600460.
(29) Han, K. S.; Lee, S.; Kim, M.; Park, P.; Lee, M. H.; Nah, J. Electrically Activated Ultrathin PVDF-TrFE Air Filter for High-Efficiency PM $_{1.0}$ Filtration. *Adv. Funct. Mater.* **2019**, *29* (37), 1903633. https://doi.org/10.1002/adfm.201903633.
(30) Knopfmacher, O.; Hammock, M. L.; Appleton, A. L.; Schwartz, G.; Mei, J.; Lei, T.; Pei, J.; Bao, Z. Highly Stable Organic Polymer Field-Effect Transistor Sensor for Selective Detection in the Marine Environment. *Nat. Commun.* **2014**, *5* (1), 2954. https://doi.org/10.1038/ncomms3954.
(31) Legrand, J. F. Structure and Ferroelectric Properties of P(VDF-TrFE) Copolymers. *Ferroelectrics* **1989**, *91* (1), 303–317. https://doi.org/10.1080/00150198908015747.
(32) Lee, J.; Yoon, H.; Kim, T. Y.; Gupta, M. K.; Lee, J. H.; Seung, W.; Ryu, H.; Kim, S. Micropatterned P(VDF-TrFE) Film-Based Piezoelectric Nanogenerators for Highly

Sensitive Self-Powered Pressure Sensors. *Adv. Funct. Mater.* **2015**, *25* (21), 3203–3209. https://doi.org/10.1002/adfm.201500856.
(33) Jang, S.; Jang, S.; Lee, E.-H.; Kang, M.; Wang, G.; Kim, T.-W. Ultrathin Conformable Organic Artificial Synapse for Wearable Intelligent Device Applications. *ACS Appl. Mater. Interfaces* **2019**, *11* (1), 1071–1080. https://doi.org/10.1021/acsami.8b12092.
(34) Sekine, T.; Sugano, R.; Tashiro, T.; Sato, J.; Takeda, Y.; Matsui, H.; Kumaki, D.; Domingues Dos Santos, F.; Miyabo, A.; Tokito, S. Fully Printed Wearable Vital Sensor for Human Pulse Rate Monitoring Using Ferroelectric Polymer. *Sci. Rep.* **2018**, *8* (1), 4442. https://doi.org/10.1038/s41598-018-22746-3.
(35) Petritz, A.; Karner-Petritz, E.; Uemura, T.; Schäffner, P.; Araki, T.; Stadlober, B.; Sekitani, T. Imperceptible Energy Harvesting Device and Biomedical Sensor Based on Ultraflexible Ferroelectric Transducers and Organic Diodes. *Nat. Commun.* **2021**, *12* (1), 2399. https://doi.org/10.1038/s41467-021-22663-6.
(36) Parvez Mahmud, M. A.; Huda, N.; Farjana, S. H.; Asadnia, M.; Lang, C. Recent Advances in Nanogenerator-Driven Self-Powered Implantable Biomedical Devices. *Adv. Energy Mater.* **2018**, *8* (2), 1701210. https://doi.org/10.1002/aenm.201701210.
(37) Dutta, S.; Vikas; Thangavel, V.; Munshi, P. Ferroelectricity and Uniaxial Negative Thermal Expansion in a Purely Organic Multifunctional Material. *ACS Appl. Electron. Mater.* **2021**, *3* (8), 3633–3640. https://doi.org/10.1021/acsaelm.1c00544.
(38) Tu, Z.; Wu, M.; Zeng, X. C. Two-Dimensional Metal-Free Organic Multiferroic Material for Design of Multifunctional Integrated Circuits. *J. Phys. Chem. Lett.* **2017**, *8* (9), 1973–1978. https://doi.org/10.1021/acs.jpclett.7b00636.
(39) Casellas, N. M.; Urbanaviciute, I.; Cornelissen, T. D.; Berrocal, J. A.; Torres, T.; Kemerink, M.; García-Iglesias, M. Resistive Switching in an Organic Supramolecular Semiconducting Ferroelectric. *Chem. Commun.* **2019**, *55* (60), 8828–8831. https://doi.org/10.1039/C9CC02466B.
(40) Ji, W.; Yao, K.; Liang, Y. C. Bulk Photovoltaic Effect at Visible Wavelength in Epitaxial Ferroelectric $BiFeO_3$ Thin Films. *Adv. Mater.* **2010**, *22* (15), 1763–1766. https://doi.org/10.1002/adma.200902985.
(41) Scott, J. C. Is There an Immortal Memory? *Science* **2004**, *304* (5667), 62–63. https://doi.org/10.1126/science.1095520.
(42) Kemerink, M.; Asadi, K.; Blom, P. W. M.; De Leeuw, D. M. The Operational Mechanism of Ferroelectric-Driven Organic Resistive Switches. *Org. Electron.* **2012**, *13* (1), 147–152. https://doi.org/10.1016/j.orgel.2011.10.013.
(43) Asadi, K.; Li, M.; Blom, P. W. M.; Kemerink, M.; De Leeuw, D. M. Organic Ferroelectric Opto-Electronic Memories. *Mater. Today* **2011**, *14* (12), 592–599. https://doi.org/10.1016/S1369-7021(11)70300-5.
(44) Fukunaga, M.; Noda, Y. New Technique for Measuring Ferroelectric and Antiferroelectric Hysteresis Loops. *J. Phys. Soc. Jpn.* **2008**, *77* (6), 064706. https://doi.org/10.1143/JPSJ.77.064706.
(45) Shyshov, O.; Haridas, S. V.; Pesce, L.; Qi, H.; Gardin, A.; Bochicchio, D.; Kaiser, U.; Pavan, G. M.; Von Delius, M. Living Supramolecular Polymerization of Fluorinated Cyclohexanes. *Nat. Commun.* **2021**, *12* (1), 3134. https://doi.org/10.1038/s41467-021-23370-y.
(46) Mes, T.; Cantekin, S.; Balkenende, D. W. R.; Frissen, M. M. M.; Gillissen, M. A. J.; De Waal, B. F. M.; Voets, I. K.; Meijer, E. W.; Palmans, A. R. A. Thioamides: Versatile Bonds To

Induce Directional and Cooperative Hydrogen Bonding in Supramolecular Polymers. *Chem. – Eur. J.* **2013**, *19* (26), 8642–8649. https://doi.org/10.1002/chem.201204273.

(47) Albuquerque, R. Q.; Timme, A.; Kress, R.; Senker, J.; Schmidt, H. Theoretical Investigation of Macrodipoles in Supramolecular Columnar Stackings. *Chem. – Eur. J.* **2013**, *19* (5), 1647–1657. https://doi.org/10.1002/chem.201202507.

(48) Pratik, S. M.; Nijamudheen, A.; Datta, A. Janus All- *Cis* -1,2,3,4,5,6-Hexafluorocyclohexane: A Molecular Motif for Aggregation-Induced Enhanced Polarization. *ChemPhysChem* **2016**, *17* (15), 2373–2381. https://doi.org/10.1002/cphc.201600262.

(49) Goetz, K. P.; Vermeulen, D.; Payne, M. E.; Kloc, C.; McNeil, L. E.; Jurchescu, O. D. Charge-Transfer Complexes: New Perspectives on an Old Class of Compounds. *J Mater Chem C* **2014**, *2* (17), 3065–3076. https://doi.org/10.1039/C3TC32062F.

(50) Horiuchi, S.; Okimoto, Y.; Kumai, R.; Tokura, Y. Ferroelectric Valence Transition and Phase Diagram of a Series of Charge-Transfer Complexes of 4,4'-Dimethyltetrathiafulvalene and Tetrahalo- *p* -Benzoquinones. *J. Am. Chem. Soc.* **2001**, *123* (4), 665–670. https://doi.org/10.1021/ja0016654.

(51) Trainer, M. Ferroelectrics and the Curie-Weiss Law. *Eur. J. Phys.* **2000**, *21* (5), 459–464. https://doi.org/10.1088/0143-0807/21/5/312.

(52) Okamoto, H.; Mitani, T.; Tokura, Y.; Koshihara, S.; Komatsu, T.; Iwasa, Y.; Koda, T.; Saito, G. Anomalous Dielectric Response in Tetrathiafulvalene- *p* -Chloranil as Observed in Temperature- and Pressure-Induced Neutral-to-Ionic Phase Transition. *Phys. Rev. B* **1991**, *43* (10), 8224–8232. https://doi.org/10.1103/PhysRevB.43.8224.

(53) Horiuchi, S.; Hasegawa, T.; Tokura, Y. Molecular Donor–Acceptor Compounds as Prospective Organic Electronics Materials. *J. Phys. Soc. Jpn.* **2006**, *75* (5), 051016. https://doi.org/10.1143/JPSJ.75.051016.

(54) Pauling, Linus. THE NATURE OF THE CHEMICAL BOND. APPLICATION OF RESULTS OBTAINED FROM THE QUANTUM MECHANICS AND FROM A THEORY OF PARAMAGNETIC SUSCEPTIBILITY TO THE STRUCTURE OF MOLECULES. *J. Am. Chem. Soc.* **1931**, *53* (4), 1367–1400. https://doi.org/10.1021/ja01355a027.

(55) Fox, B. A.; Hartsell, M. L.; Malta, D. M.; Wynands, H. A.; Tessmer, G. J.; Dreifus, D. L. Electrical Properties of Diamond for Device Applications. *MRS Proc.* **1995**, *416*, 319. https://doi.org/10.1557/PROC-416-319.

(56) Berger, L. I. *Semiconductor Materials*, 1st ed.; CRC Press, 2020. https://doi.org/10.1201/9780138739966.

(57) Kitamura, M.; Arakawa, Y. Pentacene-Based Organic Field-Effect Transistors. *J. Phys. Condens. Matter* **2008**, *20* (18), 184011. https://doi.org/10.1088/0953-8984/20/18/184011.

(58) Yen-Yi Lin; Gundlach, D. I.; Nelson, S. F.; Jackson, T. N. Pentacene-Based Organic Thin-Film Transistors. *IEEE Trans. Electron Devices* **1997**, *44* (8), 1325–1331. https://doi.org/10.1109/16.605476.

(59) Yoo, S.; Domercq, B.; Kippelen, B. Efficient Thin-Film Organic Solar Cells Based on Pentacene/C60 Heterojunctions. *Appl. Phys. Lett.* **2004**, *85* (22), 5427–5429. https://doi.org/10.1063/1.1829777.

(60) Tremel, K.; Ludwigs, S. Morphology of P3HT in Thin Films in Relation to Optical and Electrical Properties. In *P3HT Revisited – From Molecular Scale to Solar Cell Devices*; Ludwigs, S., Ed.; Advances in Polymer Science; Springer Berlin Heidelberg: Berlin, Heidelberg, 2014; Vol. 265, pp 39–82. https://doi.org/10.1007/12_2014_288.

(61) Berger, P. R.; Kim, M. Polymer Solar Cells: P3HT:PCBM and Beyond. *J. Renew. Sustain. Energy* **2018**, *10* (1), 013508. https://doi.org/10.1063/1.5012992.
(62) Miller, B.; Rosamilia, J. M.; Dabbagh, G.; Tycko, R.; Haddon, R. C.; Muller, A. J.; Wilson, W.; Murphy, D. W.; Hebard, A. F. Photoelectrochemical Behavior of C60 Films. *J. Am. Chem. Soc.* **1991**, *113* (16), 6291–6293. https://doi.org/10.1021/ja00016a067.
(63) Pope, M.; Swenberg, C. E. *Electronic Processes in Organic Crystals and Polymers*, Second Edition.; Oxford University PressNew York, NY, 1999. https://doi.org/10.1093/oso/9780195129632.001.0001.
(64) Bässler, H.; Köhler, A. Charge Transport in Organic Semiconductors. In *Unimolecular and Supramolecular Electronics I*; Metzger, R. M., Ed.; Topics in Current Chemistry; Springer Berlin Heidelberg: Berlin, Heidelberg, 2011; Vol. 312, pp 1–65. https://doi.org/10.1007/128_2011_218.
(65) Köhler, A. *Electronic Processes in Organic Semiconductors: An Introduction*; John Wiley & Sons, Incorporated: Newark, 2015.
(66) Hasegawa, T.; Takeya, J. Organic Field-Effect Transistors Using Single Crystals. *Sci. Technol. Adv. Mater.* **2009**, *10* (2), 024314. https://doi.org/10.1088/1468-6996/10/2/024314.
(67) Warta, W.; Stehle, R.; Karl, N. Ultrapure, High Mobility Organic Photoconductors. *Appl. Phys. Solids Surf.* **1985**, *36* (3), 163–170. https://doi.org/10.1007/BF00624938.
(68) Landau, L. D. Electron Motion in Crystal Lattices. *Phys Z Sowjet* **1933**, *3*, 664.
(69) Marcus, R. A.; Sutin, N. Electron Transfers in Chemistry and Biology. *Biochim. Biophys. Acta BBA - Rev. Bioenerg.* **1985**, *811* (3), 265–322. https://doi.org/10.1016/0304-4173(85)90014-X.
(70) Holstein, T. Studies of Polaron Motion. *Ann. Phys.* **1959**, *8* (3), 343–389. https://doi.org/10.1016/0003-4916(59)90003-X.
(71) Miller, A.; Abrahams, E. Impurity Conduction at Low Concentrations. *Phys. Rev.* **1960**, *120* (3), 745–755. https://doi.org/10.1103/PhysRev.120.745.
(72) Monroe, D. Hopping in Exponential Band Tails. *Phys. Rev. Lett.* **1985**, *54* (2), 146–149. https://doi.org/10.1103/PhysRevLett.54.146.
(73) Arkhipov, V. I.; Heremans, P.; Emelianova, E. V.; Adriaenssens, G. J.; Bässler, H. Weak-Field Carrier Hopping in Disordered Organic Semiconductors: The Effects of Deep Traps and Partly Filled Density-of-States Distribution. *J. Phys. Condens. Matter* **2002**, *14* (42), 9899–9911. https://doi.org/10.1088/0953-8984/14/42/305.
(74) Schönherr, G.; Bässler, H.; Silver, M. Dispersive Hopping Transport via Sites Having a Gaussian Distribution of Energies. *Philos. Mag. B* **1981**, *44* (1), 47–61. https://doi.org/10.1080/01418638108222366.
(75) Movaghar, B.; Grünewald, M.; Ries, B.; Bassler, H.; Würtz, D. Diffusion and Relaxation of Energy in Disordered Organic and Inorganic Materials. *Phys. Rev. B* **1986**, *33* (8), 5545–5554. https://doi.org/10.1103/PhysRevB.33.5545.
(76) Schein, L. B. Comparison of Charge Transport Models in Molecularly Doped Polymers. *Philos. Mag. B* **1992**, *65* (4), 795–810. https://doi.org/10.1080/13642819208204920.
(77) Parris, P. E.; Kenkre, V. M.; Dunlap, D. H. Nature of Charge Carriers in Disordered Molecular Solids: Are Polarons Compatible with Observations? *Phys. Rev. Lett.* **2001**, *87* (12), 126601. https://doi.org/10.1103/PhysRevLett.87.126601.
(78) Fishchuk, I. I.; Kadashchuk, A.; Hoffmann, S. T.; Athanasopoulos, S.; Genoe, J.; Bässler, H.; Köhler, A. Unified Description for Hopping Transport in Organic Semiconductors

Including Both Energetic Disorder and Polaronic Contributions. *Phys. Rev. B* **2013**, *88* (12), 125202. https://doi.org/10.1103/PhysRevB.88.125202.
(79) Crowell, C. R.; Sze, S. M. Current Transport in Metal-Semiconductor Barriers. *Solid-State Electron.* **1966**, *9* (11), 1035–1048. https://doi.org/10.1016/0038-1101(66)90127-4.
(80) Arkhipov, V. I.; Wolf, U.; Bässler, H. Current Injection from a Metal to a Disordered Hopping System. II. Comparison between Analytic Theory and Simulation. *Phys. Rev. B* **1999**, *59* (11), 7514–7520. https://doi.org/10.1103/PhysRevB.59.7514.
(81) Gartstein, Yu. N.; Conwell, E. M. High-Field Hopping Mobility in Molecular Systems with Spatially Correlated Energetic Disorder. *Chem. Phys. Lett.* **1995**, *245* (4), 351–358. https://doi.org/10.1016/0009-2614(95)01031-4.
(82) van der Holst, J. J. M.; Uijttewaal, M. A.; Ramachandhran, B.; Coehoorn, R.; Bobbert, P. A.; de Wijs, G. A.; de Groot, R. A. Modeling and Analysis of the Three-Dimensional Current Density in Sandwich-Type Single-Carrier Devices of Disordered Organic Semiconductors. *Phys. Rev. B* **2009**, *79* (8), 085203. https://doi.org/10.1103/PhysRevB.79.085203.
(83) Burin, A. L.; Ratner, M. A. Temperature and Field Dependence of the Charge Injection from Metal Electrodes into Random Organic Media. *J. Chem. Phys.* **2000**, *113* (10), 3941–3944. https://doi.org/10.1063/1.1290697.
(84) Child, C. D. Discharge From Hot CaO. *Phys. Rev. Ser. I* **1911**, *32* (5), 492–511. https://doi.org/10.1103/PhysRevSeriesI.32.492.
(85) Mott, S., N. F. (Nevill Francis); Gurney, R. W. (Ronald W. *Electronic Processes in Ionic Crystals*, 2nd ed.; The international series of monographs on physics; Clarendon Press, 1948.
(86) Lampert, M. A. Simplified Theory of Space-Charge-Limited Currents in an Insulator with Traps. *Phys. Rev.* **1956**, *103* (6), 1648–1656. https://doi.org/10.1103/PhysRev.103.1648.
(87) Mark, P.; Helfrich, W. Space-Charge-Limited Currents in Organic Crystals. *J. Appl. Phys.* **1962**, *33* (1), 205–215. https://doi.org/10.1063/1.1728487.
(88) Hwang, W.; Kao, K. C. Studies of the Theory of Single and Double Injections in Solids with a Gaussian Trap Distribution. *Solid-State Electron.* **1976**, *19* (12), 1045–1047. https://doi.org/10.1016/0038-1101(76)90191-X.
(89) NeŠpůrek, S.; Smejtek, P. Space-Charge Limited Currents in Insulators with the Gaussian Distribution of Traps. *Czechoslov. J. Phys. B* **1972**, *22* (2), 160–175. https://doi.org/10.1007/BF01709967.
(90) Nicolai, H. T.; Mandoc, M. M.; Blom, P. W. M. Electron Traps in Semiconducting Polymers: Exponential versus Gaussian Trap Distribution. *Phys. Rev. B* **2011**, *83* (19), 195204. https://doi.org/10.1103/PhysRevB.83.195204.
(91) Murgatroyd, P. N. Theory of Space-Charge-Limited Current Enhanced by Frenkel Effect. *J. Phys. Appl. Phys.* **1970**, *3* (2), 151–156. https://doi.org/10.1088/0022-3727/3/2/308.
(92) Frenkel, J. On Pre-Breakdown Phenomena in Insulators and Electronic Semi-Conductors. *Phys. Rev.* **1938**, *54* (8), 647–648. https://doi.org/10.1103/PhysRev.54.647.
(93) Blakesley, J. C.; Castro, F. A.; Kylberg, W.; Dibb, G. F. A.; Arantes, C.; Valaski, R.; Cremona, M.; Kim, J. S.; Kim, J.-S. Towards Reliable Charge-Mobility Benchmark Measurements for Organic Semiconductors. *Org. Electron.* **2014**, *15* (6), 1263–1272. https://doi.org/10.1016/j.orgel.2014.02.008.

(94) ON THE THEORY OF PHASE TRANSITIONS. In *Collected Papers of L.D. Landau*; Elsevier, 1965; pp 193–216. https://doi.org/10.1016/B978-0-08-010586-4.50034-1.
(95) Landau, L. D.; Lifshitz, E. M.; Lifshi͡ts, E. M.; Pitaevskii, L. P. *Statistical Physics: Theory of the Condensed State*; Butterworth-Heinemann, 1980.
(96) Devonshire, A. F. XCVI. Theory of Barium Titanate: Part I. *Lond. Edinb. Dublin Philos. Mag. J. Sci.* **1949**, *40* (309), 1040–1063. https://doi.org/10.1080/14786444908561372.
(97) Devonshire, A. F. CIX. Theory of Barium Titanate—Part II. *Lond. Edinb. Dublin Philos. Mag. J. Sci.* **1951**, *42* (333), 1065–1079. https://doi.org/10.1080/14786445108561354.
(98) Devonshire, A. F. Theory of Ferroelectrics. *Adv. Phys.* **1954**, *3*, 85–130. https://doi.org/10.1080/00018735400101173.
(99) Chandra, P.; Littlewood, P. B. A Landau Primer for Ferroelectrics. In *Physics of Ferroelectrics: A Modern Perspective*; Springer: Berlin, Heidelberg, 2007; pp 69–116. https://doi.org/10.1007/978-3-540-34591-6_3.
(100) Urbanaviciute, I.; Meng, X.; Cornelissen, T. D.; Gorbunov, A. V.; Bhattacharjee, S.; Sijbesma, R. P.; Kemerink, M. Tuning the Ferroelectric Properties of Trialkylbenzene-1,3,5-tricarboxamide (BTA). *Adv. Electron. Mater.* **2017**, *3* (7), 1600530. https://doi.org/10.1002/aelm.201600530.
(101) Horiuchi, S.; Tokunaga, Y.; Giovannetti, G.; Picozzi, S.; Itoh, H.; Shimano, R.; Kumai, R.; Tokura, Y. Above-Room-Temperature Ferroelectricity in a Single-Component Molecular Crystal. *Nature* **2010**, *463* (7282), 789–792. https://doi.org/10.1038/nature08731.
(102) Bolten, D.; Böttger, U.; Waser, R. Reversible and Irreversible Polarization Processes in Ferroelectric Ceramics and Thin Films. *J. Appl. Phys.* **2003**, *93* (3), 1735–1742. https://doi.org/10.1063/1.1535748.
(103) Kolmogorov, A. N. On the Statistical Theory of the Crystallization of Metals. *Bull Acad Sci URSS Cl Sci Math Nat* **1937**, *3*, 335.
(104) Avrami, M. Kinetics of Phase Change. II Transformation-Time Relations for Random Distribution of Nuclei. *J. Chem. Phys.* **1940**, *8* (2), 212–224. https://doi.org/10.1063/1.1750631.
(105) Ishibashi, Y.; Takagi, Y. Note on Ferroelectric Domain Switching. *J. Phys. Soc. Jpn.* **1971**, *31* (2), 506–510. https://doi.org/10.1143/JPSJ.31.506.
(106) Hashimoto, S.; Orihara, H.; Ishibashi, Y. Study on D-E Hysteresis Loop of TGS Based on the Avrami-Type Model. *J. Phys. Soc. Jpn.* **1994**, *63* (4), 1601–1610. https://doi.org/10.1143/JPSJ.63.1601.
(107) Orihara, H.; Hashimoto, S.; Ishibashi, Y. A Theory of D-E Hysteresis Loop Based on the Avrami Model. *J. Phys. Soc. Jpn.* **1994**, *63* (3), 1031–1035. https://doi.org/10.1143/jpsj.63.1031.
(108) Gorbunov, A. V.; Putzeys, T.; Urbanavičiūtė, I.; Janssen, R. A. J.; Wübbenhorst, M.; Sijbesma, R. P.; Kemerink, M. True Ferroelectric Switching in Thin Films of Trialkylbenzene-1,3,5-Tricarboxamide (BTA). *Phys. Chem. Chem. Phys.* **2016**, *18* (34), 23663–23672. https://doi.org/10.1039/C6CP03835B.
(109) Du, X.; Chen, I.-W. Frequency Spectra of Fatigue of PZT and Other Ferroelectric Thin Films. *MRS Online Proc. Libr.* **1997**, *493* (1), 311–316. https://doi.org/10.1557/PROC-493-311.
(110) Nam, S.-M.; Kil, Y.-B.; Wada, S.; Tsurumi, T. Domain Switching Kinetics of Lead Zirconate Titinate Thin Films. *Jpn. J. Appl. Phys.* **2003**, *42* (12B), L1519–L1522. https://doi.org/10.1143/jjap.42.l1519.

(111) Vopsaroiu, M.; Blackburn, J.; Cain, M. G.; Weaver, P. M. Thermally Activated Switching Kinetics in Second-Order Phase Transition Ferroelectrics. *Phys. Rev. B* **2010**, *82* (2), 024109. https://doi.org/10.1103/PhysRevB.82.024109.
(112) Vopsaroiu, M.; Weaver, P. M.; Cain, M. G.; Reece, M. J.; Kok Boon Chong. Polarization Dynamics and Non-Equilibrium Switching Processes in Ferroelectrics. *IEEE Trans. Ultrason. Ferroelectr. Freq. Control* **2011**, *58* (9), 1867–1873. https://doi.org/10.1109/TUFFC.2011.2025.
(113) Merz, W. J. Domain Formation and Domain Wall Motions in Ferroelectric BaTi${\mathrm{O}}_{3}$ Single Crystals. *Phys. Rev.* **1954**, *95* (3), 690–698. https://doi.org/10.1103/PhysRev.95.690.
(114) Cornelissen, T. D.; Urbanaviciute, I.; Kemerink, M. Microscopic Model for Switching Kinetics in Organic Ferroelectrics Following the Merz Law. *Phys. Rev. B* **2020**, *101* (21), 214301. https://doi.org/10.1103/PhysRevB.101.214301.
(115) Preisach, F. Über die magnetische Nachwirkung. *Z. Für Phys.* **1935**, *94* (5), 277–302. https://doi.org/10.1007/BF01349418.
(116) Cima, L.; Laboure, E.; Muralt, P. Characterization and Model of Ferroelectrics Based on Experimental Preisach Density. *Rev. Sci. Instrum.* **2002**, *73* (10), 3546–3552. https://doi.org/10.1063/1.1505659.
(117) Bartic, A. T.; Wouters, D. J.; Maes, H. E.; Rickes, J. T.; Waser, R. M. Preisach Model for the Simulation of Ferroelectric Capacitors. *J. Appl. Phys.* **2001**, *89* (6), 3420–3425. https://doi.org/10.1063/1.1335639.
(118) Urbanavičiūtė, I.; Cornelissen, T. D.; Meng, X.; Sijbesma, R. P.; Kemerink, M. Physical Reality of the Preisach Model for Organic Ferroelectrics. *Nat. Commun.* **2018**, *9* (1), 4409. https://doi.org/10.1038/s41467-018-06717-w.
(119) Wurfel, P.; Batra, I. P. <no Title>. **1976**.
(120) Lou, X. J. Polarization Retention on Short, Intermediate, and Long Time Scales in Ferroelectric Thin Films. *J. Appl. Phys.* **2009**, *105* (9), 094107. https://doi.org/10.1063/1.3106663.
(121) Kim, D. J.; Jo, J. Y.; Kim, Y. S.; Chang, Y. J.; Lee, J. S.; Yoon, J.-G.; Song, T. K.; Noh, T. W. Polarization Relaxation Induced by a Depolarization Field in Ultrathin Ferroelectric ${\mathrm{BaTiO}}_{3}$ Capacitors. *Phys. Rev. Lett.* **2005**, *95* (23), 237602. https://doi.org/10.1103/PhysRevLett.95.237602.
(122) Jo, J. Y.; Kim, D. J.; Kim, Y. S.; Choe, S.-B.; Song, T. K.; Yoon, J.-G.; Noh, T. W. Polarization Switching Dynamics Governed by the Thermodynamic Nucleation Process in Ultrathin Ferroelectric Films. *Phys. Rev. Lett.* **2006**, *97* (24), 247602. https://doi.org/10.1103/PhysRevLett.97.247602.
(123) Benedetto, J. M.; Moore, R. A.; McLean, F. B. Effects of Operating Conditions on the Fast-decay Component of the Retained Polarization in Lead Zirconate Titanate Thin Films. *J. Appl. Phys.* **1994**, *75* (1), 460–466. https://doi.org/10.1063/1.355875.
(124) Jo, W.; Kim, D. C.; Hong, J. W. Reverse-Poling Effects on Charge Retention in Pb(Zr,Ti)O3(001)/LaNiO3(001) Heterostructures. *Appl. Phys. Lett.* **2000**, *76* (3), 390–392. https://doi.org/10.1063/1.125763.
(125) Hong, J. W.; Jo, W.; Kim, D. C.; Cho, S. M.; Nam, H. J.; Lee, H. M.; Bu, J. U. Nanoscale Investigation of Domain Retention in Preferentially Oriented PbZr0.53Ti0.47O3 Thin Films on Pt and on LaNiO3. *Appl. Phys. Lett.* **1999**, *75* (20), 3183–3185. https://doi.org/10.1063/1.125271.

(126) V. Gorbunov, A.; Meng, X.; Urbanaviciute, I.; Putzeys, T.; Wübbenhorst, M.; P. Sijbesma, R.; Kemerink, M. Polarization Loss in the Organic Ferroelectric Trialkylbenzene-1,3,5-Tricarboxamide (BTA). *Phys. Chem. Chem. Phys.* **2017**, *19* (4), 3192–3200. https://doi.org/10.1039/C6CP08015D.
(127) Urbanaviciute, I.; Bhattacharjee, S.; Biler, M.; Lugger, J. A. M.; Cornelissen, T. D.; Norman, P.; Linares, M.; Sijbesma, R. P.; Kemerink, M. Suppressing Depolarization by Tail Substitution in an Organic Supramolecular Ferroelectric. *Phys. Chem. Chem. Phys.* **2019**, *21* (4), 2069–2079. https://doi.org/10.1039/C8CP06315J.
(128) Cornelissen, T. D.; Biler, M.; Urbanaviciute, I.; Norman, P.; Linares, M.; Kemerink, M. Kinetic Monte Carlo Simulations of Organic Ferroelectrics. *Phys. Chem. Chem. Phys.* **2019**, *21* (3), 1375–1383. https://doi.org/10.1039/C8CP06716C.
(129) Meyer, R.; Waser, R.; Prume, K.; Schmitz, T.; Tiedke, S. Dynamic Leakage Current Compensation in Ferroelectric Thin-Film Capacitor Structures. *Appl. Phys. Lett.* **2005**, *86* (14), 142907. https://doi.org/10.1063/1.1897425.
(130) Sigov, A.; Podgorny, Yu.; Vorotilov, K.; Vishnevskiy, A. Leakage Currents in Ferroelectric Thin Films. *Phase Transit.* **2013**, *86* (11), 1141–1151. https://doi.org/10.1080/01411594.2013.790033.
(131) Jiang, J.; Bai, Z. L.; Chen, Z. H.; He, L.; Zhang, D. W.; Zhang, Q. H.; Shi, J. A.; Park, M. H.; Scott, J. F.; Hwang, C. S.; Jiang, A. Q. Temporary Formation of Highly Conducting Domain Walls for Non-Destructive Read-out of Ferroelectric Domain-Wall Resistance Switching Memories. *Nat. Mater.* **2018**, *17* (1), 49–56. https://doi.org/10.1038/nmat5028.
(132) Schröder, M.; Haußmann, A.; Thiessen, A.; Soergel, E.; Woike, T.; Eng, L. M. Conducting Domain Walls in Lithium Niobate Single Crystals. *Adv. Funct. Mater.* **2012**, *22* (18), 3936–3944. https://doi.org/10.1002/adfm.201201174.
(133) Naber, R. C. G.; Tanase, C.; Blom, P. W. M.; Gelinck, G. H.; Marsman, A. W.; Touwslager, F. J.; Setayesh, S.; de Leeuw, D. M. High-Performance Solution-Processed Polymer Ferroelectric Field-Effect Transistors. *Nat. Mater.* **2005**, *4* (3), 243–248. https://doi.org/10.1038/nmat1329.
(134) Hoffman, J.; Pan, X.; Reiner, J. W.; Walker, F. J.; Han, J. P.; Ahn, C. H.; Ma, T. P. Ferroelectric Field Effect Transistors for Memory Applications. *Adv. Mater.* **2010**, *22* (26–27), 2957–2961. https://doi.org/10.1002/adma.200904327.
(135) Kim, J. Y.; Choi, M.-J.; Jang, H. W. Ferroelectric Field Effect Transistors: Progress and Perspective. *APL Mater.* **2021**, *9* (2), 021102. https://doi.org/10.1063/5.0035515.
(136) Burr, G. W.; Kurdi, B. N.; Scott, J. C.; Lam, C. H.; Gopalakrishnan, K.; Shenoy, R. S. Overview of Candidate Device Technologies for Storage-Class Memory. *IBM J. Res. Dev.* **2008**, *52* (4.5), 449–464. https://doi.org/10.1147/rd.524.0449.
(137) Asadi, K.; de Leeuw, D. M.; de Boer, B.; Blom, P. W. M. Organic Non-Volatile Memories from Ferroelectric Phase-Separated Blends. *Nat. Mater.* **2008**, *7* (7), 547–550. https://doi.org/10.1038/nmat2207.
(138) Breemen, A. J. J. M. van; Steen, J.-L. van der; Heck, G. van; Wang, R.; Khikhlovskyi, V.; Kemerink, M.; Gelinck, G. H. Crossbar Arrays of Nonvolatile, Rewritable Polymer Ferroelectric Diode Memories on Plastic Substrates. *Appl. Phys. Express* **2014**, *7* (3), 031602. https://doi.org/10.7567/APEX.7.031602.
(139) Cornelissen, T. *Switching Kinetics and Charge Transport in Organic Ferroelectrics*; Linköping University Electronic Press, 2020.
(140) Gorbunov, A. V.; Haedler, A. T.; Putzeys, T.; Zha, R. H.; Schmidt, H.-W.; Kivala, M.; Urbanavičiūtė, I.; Wübbenhorst, M.; Meijer, E. W.; Kemerink, M. Switchable Charge

Injection Barrier in an Organic Supramolecular Semiconductor. *ACS Appl. Mater. Interfaces* **2016**, *8* (24), 15535–15542. https://doi.org/10.1021/acsami.6b02988.
(141) Gorbunov, A. V.; Garcia Iglesias, M.; Guilleme, J.; Cornelissen, T. D.; Roelofs, W. S. C.; Torres, T.; González-Rodríguez, D.; Meijer, E. W.; Kemerink, M. Ferroelectric Self-Assembled Molecular Materials Showing Both Rectifying and Switchable Conductivity. *Sci. Adv.* **2017**, *3* (9), e1701017. https://doi.org/10.1126/sciadv.1701017.
(142) Reimann, P. Brownian Motors: Noisy Transport Far from Equilibrium. *Phys. Rep.* **2002**, *361* (2), 57–265. https://doi.org/10.1016/S0370-1573(01)00081-3.
(143) Johann, T.; Xie, W.; Roosta, S.; Elstner, M.; Kemerink, M. Theory for Nonlinear Conductivity Switching in Semiconducting Organic Ferroelectrics. *Phys. Chem. Chem. Phys.* **2024**, *26* (27), 18837–18846. https://doi.org/10.1039/D4CP01632G.
(144) Kremer, F.; Schönhals, A. *Broadband Dielectric Spectroscopy*; Springer Science & Business Media, 2002.
(145) Kidner, N. J.; Meier, A.; Homrighaus, Z. J.; Wessels, B. W.; Mason, T. O.; Garboczi, E. J. Complex Electrical (Impedance/Dielectric) Properties of Electroceramic Thin Films by Impedance Spectroscopy with Interdigital Electrodes. *Thin Solid Films* **2007**, *515* (11), 4588–4595. https://doi.org/10.1016/j.tsf.2006.11.038.
(146) Blume, S. O. P.; Ben-Mrad, R.; Sullivan, P. E. Modelling the Capacitance of Multi-Layer Conductor-Facing Interdigitated Electrode Structures. *Sens. Actuators B Chem.* **2015**, *213*, 423–433. https://doi.org/10.1016/j.snb.2015.02.088.
(147) Zhu, G.; Luo, X.; Zhang, J.; Yan, X. Imprint Effect in Ferroelectric Poly(Vinylidene Fluoride-Trifluoroethylene) Thin Films. *J. Appl. Phys.* **2009**, *106* (7), 074113. https://doi.org/10.1063/1.3240200.
(148) Bryce, M. R.; Murphy, L. C. Organic Metals. *Nature* **1984**, *309* (5964), 119–126. https://doi.org/10.1038/309119a0.
(149) Jérome, D.; Mazaud, A.; Ribault, M.; Bechgaard, K. Superconductivity in a Synthetic Organic Conductor (TMTSF)2PF 6. *J. Phys. Lett.* **1980**, *41* (4), 95–98. https://doi.org/10.1051/jphyslet:0198000410409500.
(150) Tokura, Y.; Koshihara, S.; Iwasawa, N.; Saito, G. Domain-Wall Dynamics in Organic Charge-Transfer Compounds with One-Dimensional Ferroelectricity. *Phys. Rev. Lett.* **1989**, *63* (21), 2405–2408. https://doi.org/10.1103/PhysRevLett.63.2405.
(151) Horiuchi, S.; Kobayashi, K.; Kumai, R.; Ishibashi, S. Ionic versus Electronic Ferroelectricity in Donor–Acceptor Molecular Sequences. *Chem. Lett.* **2014**, *43* (1), 26–35. https://doi.org/10.1246/cl.130840.
(152) Torrance, J. B. An Overview of Organic Charge-Transfer Solids: Insulators, Metals, and the Neutral-Ionic Transition. *Mol. Cryst. Liq. Cryst.* **1985**, *126* (1), 55–67. https://doi.org/10.1080/15421408508084154.
(153) Girlando, A.; Marzola, F.; Pecile, C.; Torrance, J. B. Vibrational Spectroscopy of Mixed Stack Organic Semiconductors: Neutral and Ionic Phases of Tetrathiafulvalene–Chloranil (TTF–CA) Charge Transfer Complex. *J. Chem. Phys.* **1983**, *79* (2), 1075–1085. https://doi.org/10.1063/1.445833.
(154) Oison, V.; Katan, C.; Rabiller, P.; Souhassou, M.; Koenig, C. Neutral-Ionic Phase Transition: A Thorough *Ab Initio* Study of TTF-CA. *Phys. Rev. B* **2003**, *67* (3), 035120. https://doi.org/10.1103/PhysRevB.67.035120.
(155) Kagawa, F.; Horiuchi, S.; Tokunaga, M.; Fujioka, J.; Tokura, Y. Ferroelectricity in a One-Dimensional Organic Quantum Magnet. *Nat. Phys.* **2010**, *6* (3), 169–172. https://doi.org/10.1038/nphys1503.

(156) Jacobs, I. S.; Bray, J. W.; Hart, H. R.; Interrante, L. V.; Kasper, J. S.; Watkins, G. D.; Prober, D. E.; Bonner, J. C. Spin-Peierls Transitions in Magnetic Donor-Acceptor Compounds of Tetrathiafulvalene (TTF) with Bisdithiolene Metal Complexes. *Phys. Rev. B* **1976**, *14* (7), 3036–3051. https://doi.org/10.1103/PhysRevB.14.3036.
(157) Bulaevskii, L. N.; Buzdin, A. I.; Khomskii, D. I. Spin-Peierls Transition in Magnetic Field. *Solid State Commun.* **1978**, *27* (1), 5–10. https://doi.org/10.1016/0038-1098(78)91039-6.
(158) Kobayashi, K.; Horiuchi, S.; Kumai, R.; Kagawa, F.; Murakami, Y.; Tokura, Y. Electronic Ferroelectricity in a Molecular Crystal with Large Polarization Directing Antiparallel to Ionic Displacement. *Phys. Rev. Lett.* **2012**, *108* (23), 237601. https://doi.org/10.1103/PhysRevLett.108.237601.
(159) Torrance, J. B.; Girlando, A.; Mayerle, J. J.; Crowley, J. I.; Lee, V. Y.; Batail, P.; LaPlaca, S. J. Anomalous Nature of Neutral-to-Ionic Phase Transition in Tetrathiafulvalene-Chloranil. *Phys. Rev. Lett.* **1981**, *47* (24), 1747–1750. https://doi.org/10.1103/PhysRevLett.47.1747.
(160) McConnell, H. M.; Hoffman, B. M.; Metzger, R. M. Charge Transfer in Molecular Crystals*. *Proc. Natl. Acad. Sci.* **1965**, *53* (1), 46–50. https://doi.org/10.1073/pnas.53.1.46.
(161) Ashkenazi, J.; Pickett, W. E.; Krakauer, H.; Wang, C. S.; Klein, B. M.; Chubb, S. R. Ground State of Trans-Polyacetylene and the Peierls Mechanism. *Phys. Rev. Lett.* **1989**, *62* (17), 2016–2019. https://doi.org/10.1103/PhysRevLett.62.2016.
(162) Girlando, A.; Painelli, A.; Bewick, S. A.; Soos, Z. G. Charge Fluctuations and Electron–Phonon Coupling in Organic Charge-Transfer Salts with Neutral–Ionic and Peierls Transitions. *Synth. Met.* **2004**, *141* (1), 129–138. https://doi.org/10.1016/j.synthmet.2003.11.004.
(163) Ishibashi, S.; Terakura, K. First-Principles Study of Spontaneous Polarization in Tetrathiafulvalene-*p*-Chloranil (TTF-CA). *Phys. B Condens. Matter* **2010**, *405* (11, Supplement), S338–S340. https://doi.org/10.1016/j.physb.2009.11.019.
(164) Resta, R.; Vanderbilt, D. Theory of Polarization: A Modern Approach. In *Physics of Ferroelectrics: A Modern Perspective*; Springer: Berlin, Heidelberg, 2007; pp 31–68. https://doi.org/10.1007/978-3-540-34591-6_2.
(165) Resta, R. Theory of the Electric Polarization in Crystals. *Ferroelectrics* **1992**, *136* (1), 51–55. https://doi.org/10.1080/00150199208016065.
(166) King-Smith, R. D.; Vanderbilt, D. Theory of Polarization of Crystalline Solids. *Phys. Rev. B* **1993**, *47* (3), 1651–1654. https://doi.org/10.1103/PhysRevB.47.1651.
(167) Tokura, Y.; Okamoto, H.; Koda, T.; Mitani, T.; Saito, G. Nonlinear Electric Transport and Switching Phenomenon in the Mixed-Stack Charge-Transfer Crystal Tetrathiafulvalene-p-Chloranil. *Phys. Rev. B* **1988**, *38* (3), 2215–2218. https://doi.org/10.1103/PhysRevB.38.2215.
(168) Michalsky, I.; Gensch, V.; Walla, C.; Hoffmann, M.; Rominger, F.; Oeser, T.; Tegeder, P.; Dreuw, A.; Kivala, M. Fully Bridged Triphenylamines Comprising Five- and Seven-Membered Rings. *Chem. – Eur. J.* **2022**, *28* (34), e202200326. https://doi.org/10.1002/chem.202200326.
(169) Chappell, J. S.; Bloch, A. N.; Bryden, W. A.; Maxfield, M.; Poehler, T. O.; Cowan, D. O. Degree of Charge Transfer in Organic Conductors by Infrared Absorption Spectroscopy. *J. Am. Chem. Soc.* **1981**, *103* (9), 2442–2443. https://doi.org/10.1021/ja00399a066.
(170) Faramarzi, V.; Niess, F.; Moulin, E.; Maaloum, M.; Dayen, J.-F.; Beaufrand, J.-B.; Zanettini, S.; Doudin, B.; Giuseppone, N. Light-Triggered Self-Construction of

Supramolecular Organic Nanowires as Metallic Interconnects. *Nat. Chem.* **2012**, *4* (6), 485–490. https://doi.org/10.1038/nchem.1332.
(171) Kim, B.-G.; Jeong, E. J.; Chung, J. W.; Seo, S.; Koo, B.; Kim, J. A Molecular Design Principle of Lyotropic Liquid-Crystalline Conjugated Polymers with Directed Alignment Capability for Plastic Electronics. *Nat. Mater.* **2013**, *12* (7), 659–664. https://doi.org/10.1038/nmat3595.
(172) Han, W.; He, M.; Byun, M.; Li, B.; Lin, Z. Large-Scale Hierarchically Structured Conjugated Polymer Assemblies with Enhanced Electrical Conductivity. *Angew. Chem. Int. Ed.* **2013**, *52* (9), 2564–2568. https://doi.org/10.1002/anie.201209632.
(173) Urbanaviciute, I.; Meng, X.; Biler, M.; Wei, Y.; Cornelissen, T. D.; Bhattacharjee, S.; Linares, M.; Kemerink, M. Negative Piezoelectric Effect in an Organic Supramolecular Ferroelectric. *Mater. Horiz.* **2019**, *6* (8), 1688–1698. https://doi.org/10.1039/C9MH00094A.
(174) Kodchakorn, K.; Nimmanpipug, P.; Phongtamrug, S.; Tashiro, K. Experimental Confirmation of Proton Conductivity Predicted from Intermolecular Hydrogen-Bonding in Spatially-Confined Novel Histamine Derivatives. *J. Solid State Chem.* **2021**, *299*, 122182. https://doi.org/10.1016/j.jssc.2021.122182.
(175) Kalb, W. L.; Mattenberger, K.; Batlogg, B. Oxygen-Related Traps in Pentacene Thin Films: Energetic Position and Implications for Transistor Performance. *Phys. Rev. B* **2008**, *78* (3), 035334. https://doi.org/10.1103/PhysRevB.78.035334.
(176) Zuo, G.; Linares, M.; Upreti, T.; Kemerink, M. General Rule for the Energy of Water-Induced Traps in Organic Semiconductors. *Nat. Mater.* **2019**, *18* (6), 588–593. https://doi.org/10.1038/s41563-019-0347-y.
(177) Braun, S.; Salaneck, W. R.; Fahlman, M. Energy-Level Alignment at Organic/Metal and Organic/Organic Interfaces. *Adv. Mater.* **2009**, *21* (14–15), 1450–1472. https://doi.org/10.1002/adma.200802893.
(178) Cantekin, S.; De Greef, T. F. A.; Palmans, A. R. A. Benzene-1,3,5-Tricarboxamide: A Versatile Ordering Moiety for Supramolecular Chemistry. *Chem. Soc. Rev.* **2012**, *41* (18), 6125. https://doi.org/10.1039/c2cs35156k.
(179) Urbanaviciute, I.; Garcia-Iglesias, M.; Gorbunov, A.; Meijer, E. W.; Kemerink, M. Ferro- and Ferrielectricity and Negative Piezoelectricity in Thioamide-Based Supramolecular Organic Discotics. *Phys. Chem. Chem. Phys.* **2023**, *25* (25), 16930–16937. https://doi.org/10.1039/D3CP00982C.
(180) Kulkarni, C.; Meijer, E. W.; Palmans, A. R. A. Cooperativity Scale: A Structure–Mechanism Correlation in the Self-Assembly of Benzene-1,3,5-Tricarboxamides. *Acc. Chem. Res.* **2017**, *50* (8), 1928–1936. https://doi.org/10.1021/acs.accounts.7b00176.
(181) Metri, N.; Sallenave, X.; Plesse, C.; Beouch, L.; Aubert, P.-H.; Goubard, F.; Chevrot, C.; Sini, G. Processable Star-Shaped Molecules with Triphenylamine Core as Hole-Transporting Materials: Experimental and Theoretical Approach. *J. Phys. Chem. C* **2012**, *116* (5), 3765–3772. https://doi.org/10.1021/jp2098872.
(182) Levenberg, K. A Method for the Solution of Certain Non-Linear Problems in Least Squares. *Q. Appl. Math.* **1944**, *2* (2), 164–168. https://doi.org/10.1090/qam/10666.
(183) Marquardt, D. W. An Algorithm for Least-Squares Estimation of Nonlinear Parameters. *J. Soc. Ind. Appl. Math.* **1963**, *11* (2), 431–441. https://doi.org/10.1137/0111030.
(184) Yuan, J.; Zhang, C.; Qiu, B.; Liu, W.; So, S. K.; Mainville, M.; Leclerc, M.; Shoaee, S.; Neher, D.; Zou, Y. Effects of Energetic Disorder in Bulk Heterojunction Organic Solar Cells. *Energy Environ. Sci.* **2022**, *15* (7), 2806–2818. https://doi.org/10.1039/D2EE00271J.

(185) Scott, J. F. Phase Transitions in $BaMnF_4$. *Rep. Prog. Phys.* **1979**, *42* (6), 1055–1084. https://doi.org/10.1088/0034-4885/42/6/003.
(186) Meng, N.; Zhu, X.; Mao, R.; John Reece, M.; Bilotti, E. Nanoscale Interfacial Electroactivity in PVDF/PVDF-TrFE Blended Films with Enhanced Dielectric and Ferroelectric Properties. *J. Mater. Chem. C* **2017**, *5* (13), 3296–3305. https://doi.org/10.1039/C7TC00162B.
(187) van Reenen, S.; Kemerink, M.; Snaith, H. J. Modeling Anomalous Hysteresis in Perovskite Solar Cells. *J. Phys. Chem. Lett.* **2015**, *6* (19), 3808–3814. https://doi.org/10.1021/acs.jpclett.5b01645.
(188) K. Bejagam, K.; Kulkarni, C.; J. George, S.; Balasubramanian, S. External Electric Field Reverses Helical Handedness of a Supramolecular Columnar Stack. *Chem. Commun.* **2015**, *51* (89), 16049–16052. https://doi.org/10.1039/C5CC05569E.
(189) Damjanovic, D. Ferroelectric, Dielectric and Piezoelectric Properties of Ferroelectric Thin Films and Ceramics. *Rep. Prog. Phys.* **1998**, *61* (9), 1267–1324. https://doi.org/10.1088/0034-4885/61/9/002.
(190) Colla, E. L.; Hong, S.; Taylor, D. V.; Tagantsev, A. K.; Setter, N.; No, K. Direct Observation of Region by Region Suppression of the Switchable Polarization (Fatigue) in Pb(Zr,Ti)O3 Thin Film Capacitors with Pt Electrodes. *Appl. Phys. Lett.* **1998**, *72* (21), 2763–2765. https://doi.org/10.1063/1.121083.
(191) Merz, W. J. Double Hysteresis Loop of BaTi O 3 at the Curie Point. *Phys. Rev.* **1953**, *91* (3), 513–517. https://doi.org/10.1103/PhysRev.91.513.
(192) Ducharme, S.; Bune, A. V.; Blinov, L. M.; Fridkin, V. M.; Palto, S. P.; Sorokin, A. V.; Yudin, S. G. Critical Point in Ferroelectric Langmuir-Blodgett Polymer Films. *Phys. Rev. B* **1998**, *57* (1), 25–28. https://doi.org/10.1103/PhysRevB.57.25.
(193) Khikhlovskyi, V.; Gorbunov, A. V.; van Breemen, A. J. J. M.; Janssen, R. A. J.; Gelinck, G. H.; Kemerink, M. Multi-Bit Organic Ferroelectric Memory. *Org. Electron.* **2013**, *14* (12), 3399–3405. https://doi.org/10.1016/j.orgel.2013.09.006.
(194) Lunkenheimer, P.; Loidl, A. Dielectric Spectroscopy on Organic Charge-Transfer Salts. *J. Phys. Condens. Matter* **2015**, *27* (37), 373001. https://doi.org/10.1088/0953-8984/27/37/373001.
(195) Li, K.; Zhu, X. L.; Liu, X. Q.; Ma, X.; Sen Fu, M.; Kroupa, J.; Kamba, S.; Chen, X. M. Electric-Field-Induced Phase Transition and Pinched P–E Hysteresis Loops in Pb-Free Ferroelectrics with a Tungsten Bronze Structure. *NPG Asia Mater.* **2018**, *10* (4), 71–81. https://doi.org/10.1038/s41427-018-0013-x.
(196) Shinyashiki, N.; Shimomura, M.; Ushiyama, T.; Miyagawa, T.; Yagihara, S. Dynamics of Water in Partially Crystallized Polymer/Water Mixtures Studied by Dielectric Spectroscopy. *J. Phys. Chem. B* **2007**, *111* (34), 10079–10087. https://doi.org/10.1021/jp0730489.
(197) Bittelli, M.; Flury, M.; Roth, K. Use of Dielectric Spectroscopy to Estimate Ice Content in Frozen Porous Media. *Water Resour. Res.* **2004**, *40* (4). https://doi.org/10.1029/2003WR002343.
(198) Mitani, T.; Kaneko, Y.; Tanuma, S.; Tokura, Y.; Koda, T.; Saito, G. Electric Conductivity and Phase Diagram of a Mixed-Stack Charge-Transfer Crystal: Tetrathiafulvalene- *p* -Chloranil. *Phys. Rev. B* **1987**, *35* (1), 427–429. https://doi.org/10.1103/PhysRevB.35.427.
(199) Horiuchi, S.; Kumai, R.; Okimoto, Y.; Tokura, Y. Chemical Approach to Neutral–Ionic Valence Instability, Quantum Phase Transition, and Relaxor Ferroelectricity in Organic

Charge-Transfer Complexes. *Chem. Phys.* **2006**, *325* (1), 78–91. https://doi.org/10.1016/j.chemphys.2005.09.025.
(200) Nagaosa, N. Theory of Neutral-Ionic Transition in Organic Crystals. III. Effect of the Electron-Lattice Interaction. *J. Phys. Soc. Jpn.* **1986**, *55* (8), 2754–2764. https://doi.org/10.1143/JPSJ.55.2754.
(201) Mitani, T.; Saito, G.; Tokura, Y.; Koda, T. Soliton Formation at the Neutral-to-Ionic Phase Transition in the Mixed-Stack Charge-Transfer Crystal Tetrathiafulvalene - p - Chloranil. *Phys. Rev. Lett.* **1984**, *53* (8), 842–845. https://doi.org/10.1103/PhysRevLett.53.842.
(202) Gaussian 16, Revision C.01, Frisch, M. J.; Trucks, G. W.; Schlegel, H. B.; Scuseria, G. E.; Robb, M. A.; Cheeseman, J. R.; Scalmani, G.; Barone, V.; Petersson, G. A.; Nakatsuji, H.; Li, X.; Caricato, M.; Marenich, A. V.; Bloino, J.; Janesko, B. G.; Gomperts, R.; Mennucci, B.; Hratchian, H. P.; Ortiz, J. V.; Izmaylov, A. F.; Sonnenberg, J. L.; Williams-Young, D.; Ding, F.; Lipparini, F.; Egidi, F.; Goings, J.; Peng, B.; Petrone, A.; Henderson, T.; Ranasinghe, D.; Zakrzewski, V. G.; Gao, J.; Rega, N.; Zheng, G.; Liang, W.; Hada, M.; Ehara, M.; Toyota, K.; Fukuda, R.; Hasegawa, J.; Ishida, M.; Nakajima, T.; Honda, Y.; Kitao, O.; Nakai, H.; Vreven, T.; Throssell, K.; Montgomery, J. A., Jr.; Peralta, J. E.; Ogliaro, F.; Bearpark, M. J.; Heyd, J. J.; Brothers, E. N.; Kudin, K. N.; Staroverov, V. N.; Keith, T. A.; Kobayashi, R.; Normand, J.; Raghavachari, K.; Rendell, A. P.; Burant, J. C.; Iyengar, S. S.; Tomasi, J.; Cossi, M.; Millam, J. M.; Klene, M.; Adamo, C.; Cammi, R.; Ochterski, J. W.; Martin, R. L.; Morokuma, K.; Farkas, O.; Foresman, J. B.; Fox, D. J. Gaussian, Inc., Wallingford CT, 2016.
(203) Vosko, S. H.; Wilk, L.; Nusair, M. Accurate Spin-Dependent Electron Liquid Correlation Energies for Local Spin Density Calculations: A Critical Analysis. *Can. J. Phys.* **1980**, *58* (8), 1200–1211. https://doi.org/10.1139/p80-159.
(204) Lee, C.; Yang, W.; Parr, R. G. Development of the Colle-Salvetti Correlation-Energy Formula into a Functional of the Electron Density. *Phys. Rev. B* **1988**, *37* (2), 785–789. https://doi.org/10.1103/PhysRevB.37.785.
(205) Becke, A. D. Density-Functional Thermochemistry. I. The Effect of the Exchange-Only Gradient Correction. *J. Chem. Phys.* **1992**, *96* (3), 2155–2160. https://doi.org/10.1063/1.462066.
(206) Stephens, P. J.; Devlin, F. J.; Chabalowski, C. F.; Frisch, M. J. Ab Initio Calculation of Vibrational Absorption and Circular Dichroism Spectra Using Density Functional Force Fields. *J. Phys. Chem.* **1994**, *98* (45), 11623–11627. https://doi.org/10.1021/j100096a001.
(207) Krishnan, R.; Binkley, J. S.; Seeger, R.; Pople, J. A. Self-Consistent Molecular Orbital Methods. XX. A Basis Set for Correlated Wave Functions. *J. Chem. Phys.* **1980**, *72* (1), 650–654. https://doi.org/10.1063/1.438955.
(208) Clark, T.; Chandrasekhar, J.; Spitznagel, G. W.; Schleyer, P. V. R. Efficient Diffuse Function-augmented Basis Sets for Anion Calculations. III. The 3-21+G Basis Set for First-row Elements, Li–F. *J. Comput. Chem.* **1983**, *4* (3), 294–301. https://doi.org/10.1002/jcc.540040303.
(209) Grimme, S.; Antony, J.; Ehrlich, S.; Krieg, H. A Consistent and Accurate *Ab Initio* Parametrization of Density Functional Dispersion Correction (DFT-D) for the 94 Elements H-Pu. *J. Chem. Phys.* **2010**, *132* (15), 154104. https://doi.org/10.1063/1.3382344.
(210) Grimme, S.; Ehrlich, S.; Goerigk, L. Effect of the Damping Function in Dispersion Corrected Density Functional Theory. *J. Comput. Chem.* **2011**, *32* (7), 1456–1465. https://doi.org/10.1002/jcc.21759.

Appendix

Density functional calculations (DFT)

All DFT calculations were carried out by Jan Borstelmann from the Kivala group at Heidelberg University. The following is a direct citation from the SI of paper [ref] and describes the DFT calculations:

Quantum chemical calculations were performed using the Gaussian 16 program package.[202] Long alkyl chains were simplified to methyl groups to reduce computational cost. Ground state geometry optimizations were performed by employing the B3LYP[203–206] functional, the 6-311G(d,p)[207,208] basis set and Grimmes D3 dispersion correction[209] with BJ-damping.[210] Thereby, ultra-tight convergence criteria of the respective computational method were used. Frequency calculations at the same level of theory were employed to verify the geometries as local minima possessing no imaginary frequencies.

Figures

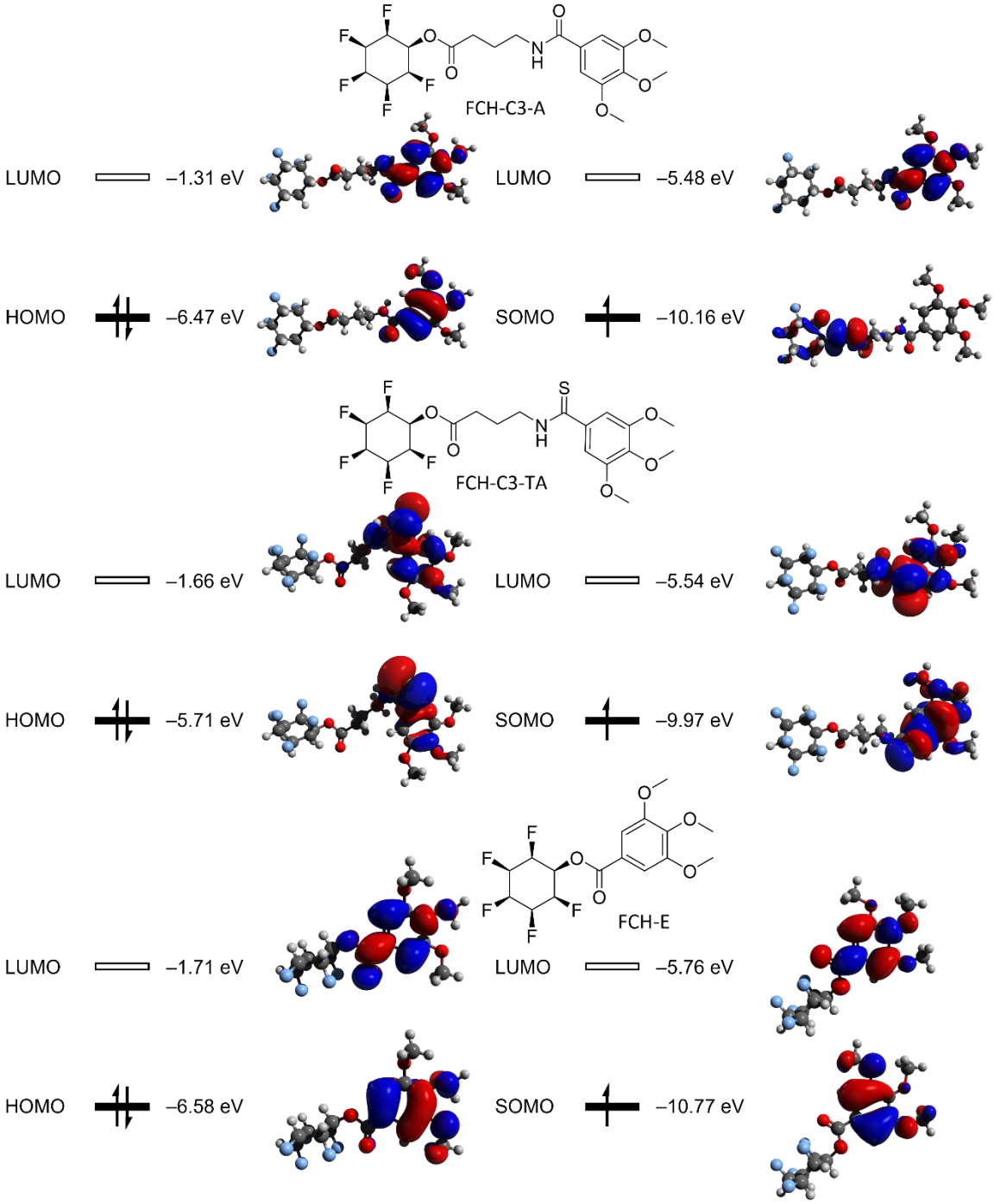

appendix Figure 1. Energy levels and electron wavefunction as calculated by DFT for FCH-C3-A, FCH-C3-TA and FCH-E in descending order.

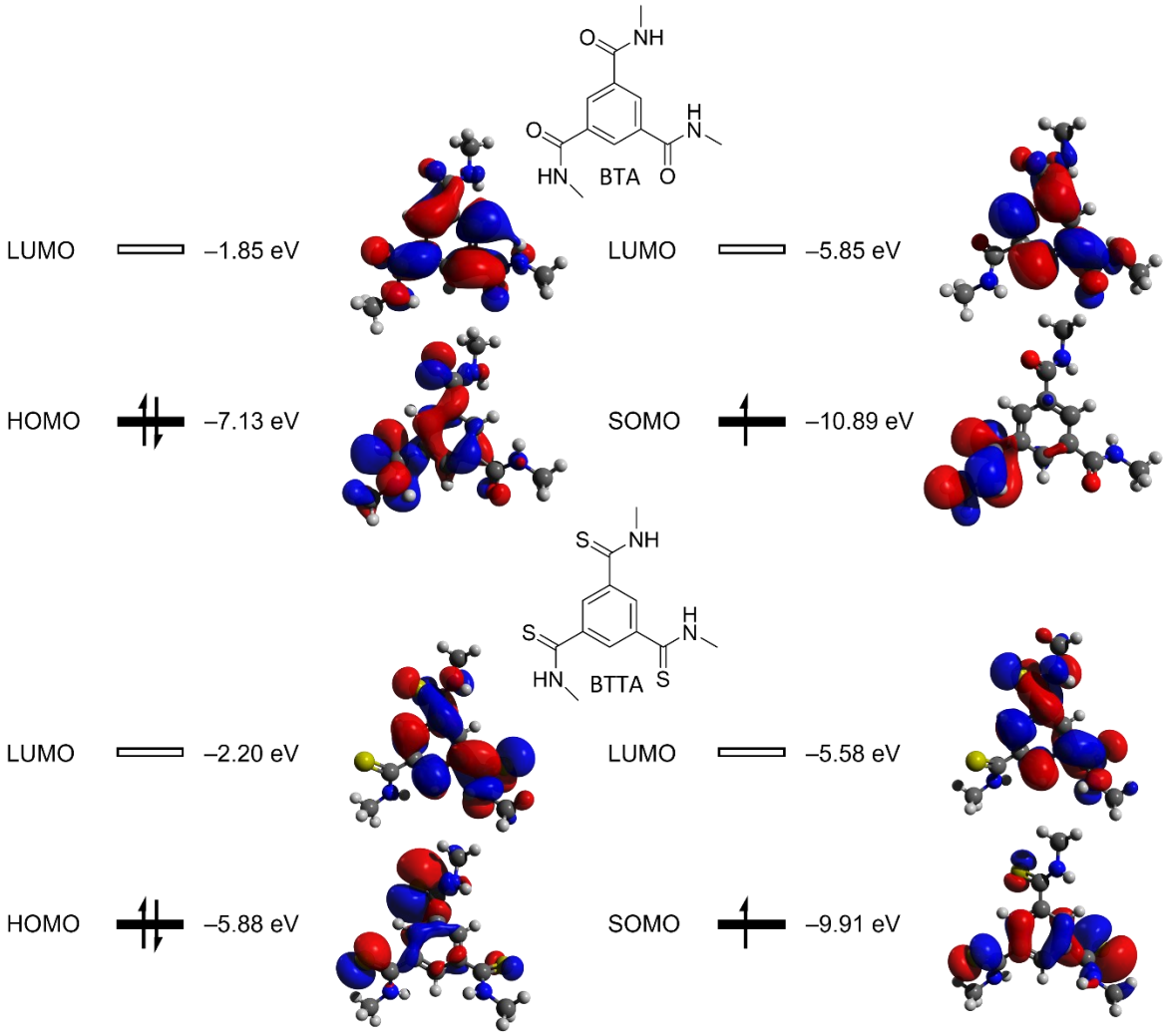

appendix Figure 2. Energy levels and electron wavefunction as calculated by DFT for BTA and BTTA.

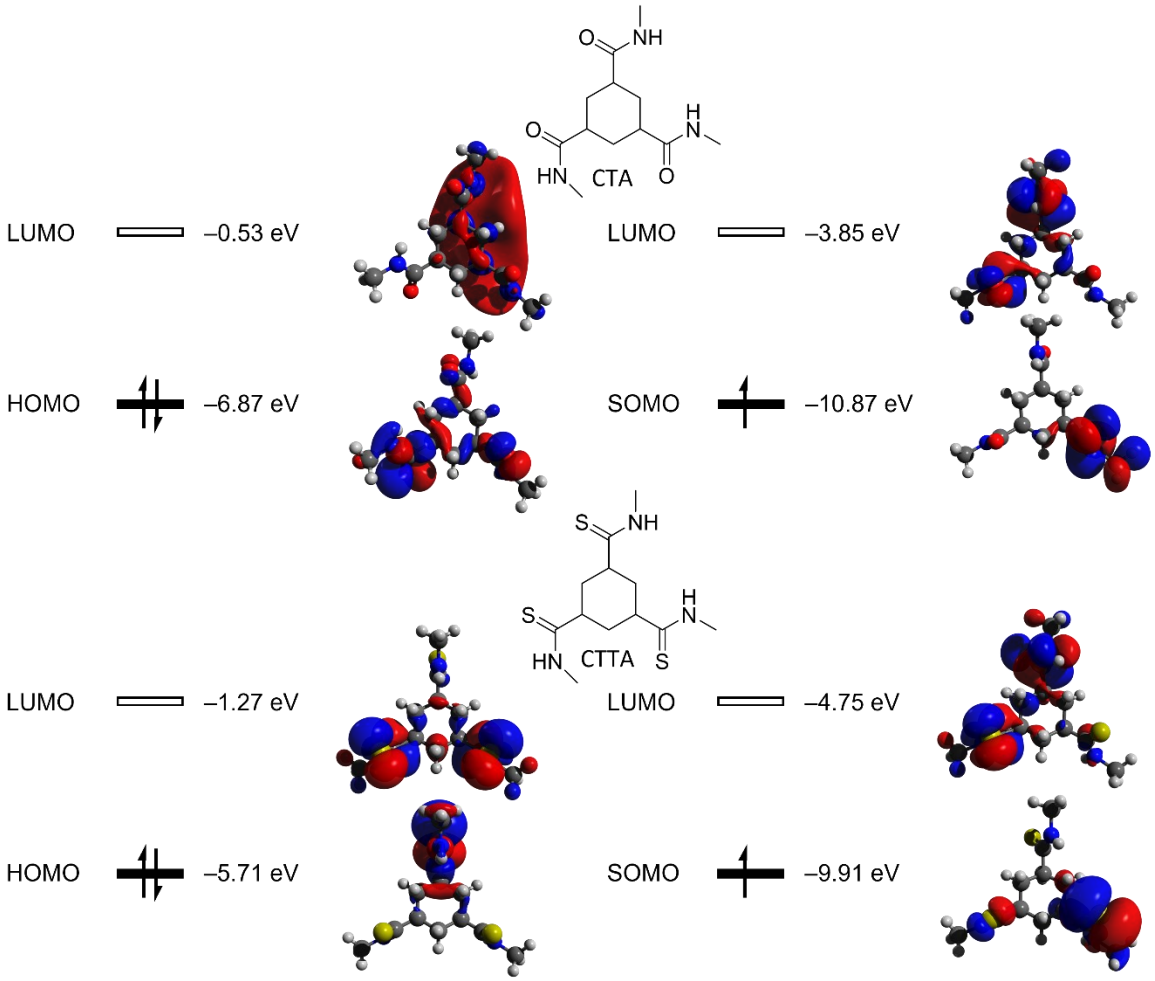

appendix Figure 3. Energy levels and electron wavefunction as calculated by DFT for CTA and CTTA.

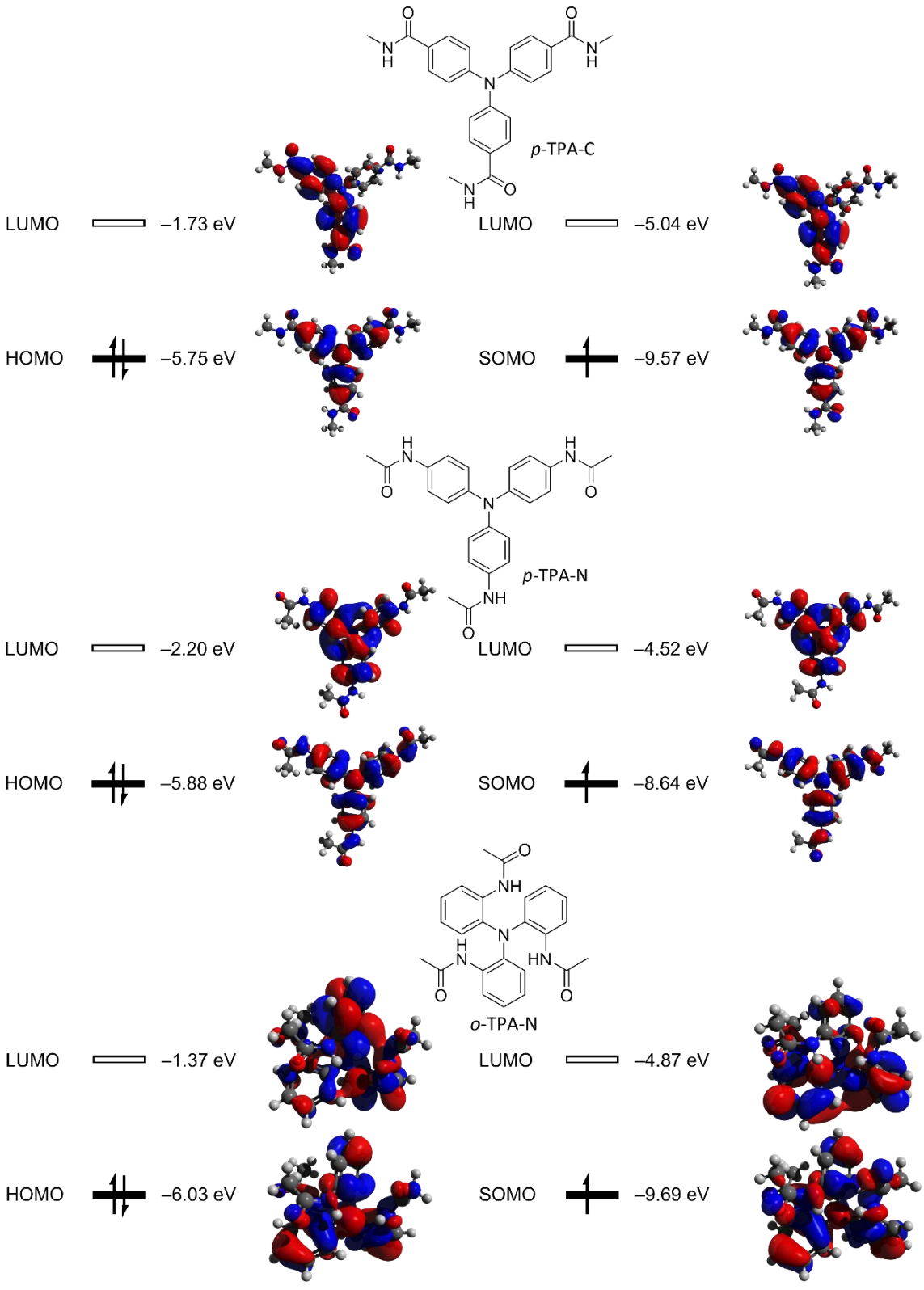

appendix Figure 4. Energy levels and electron wavefunction as calculated by DFT for *p*-TPA-C, *p*-TPA-N and *o*-TPA-N in descending order.

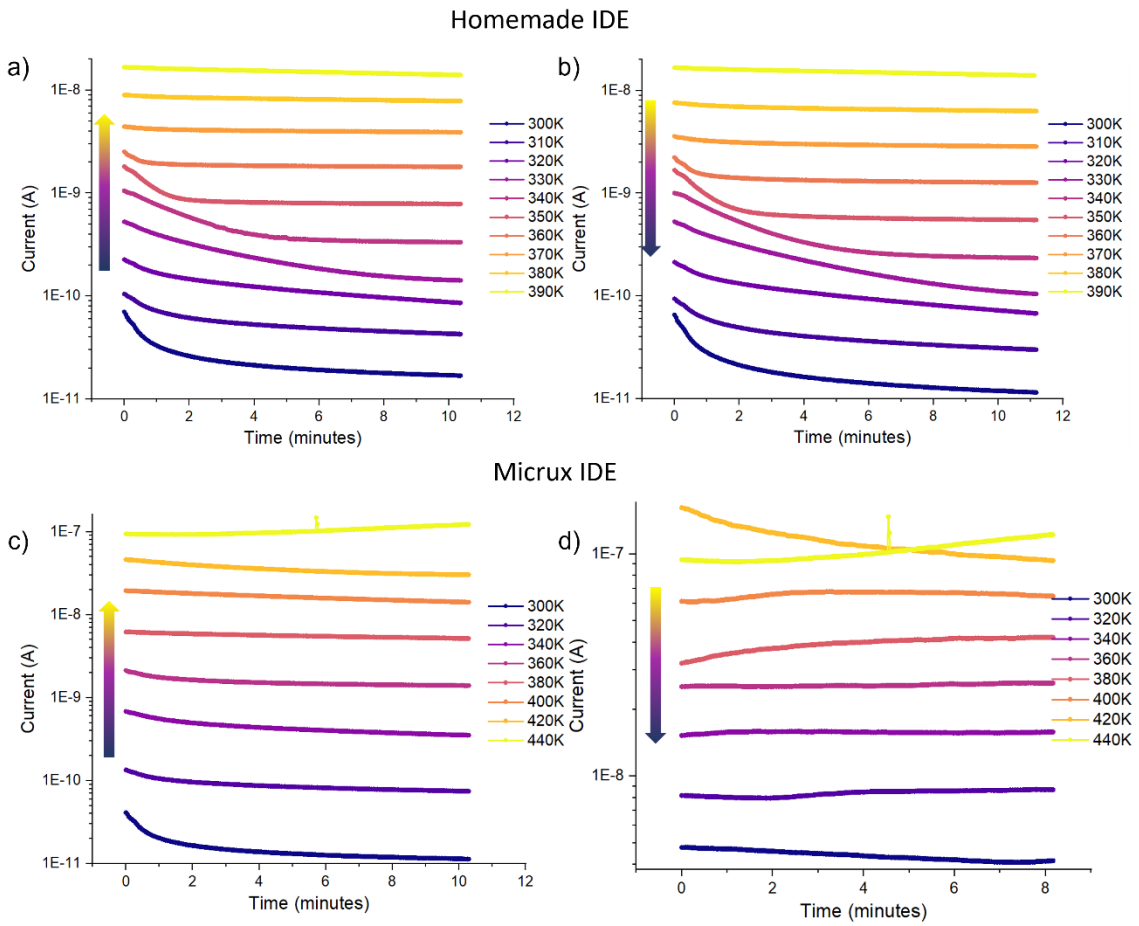

appendix Figure 5. Measured currents under a constant applied field of 20 V/µm for empty IDE substrates. The Micrux substrates show a permanently increased leakage current after annealing at 440 K. This is always considered in the discussion in the main text.

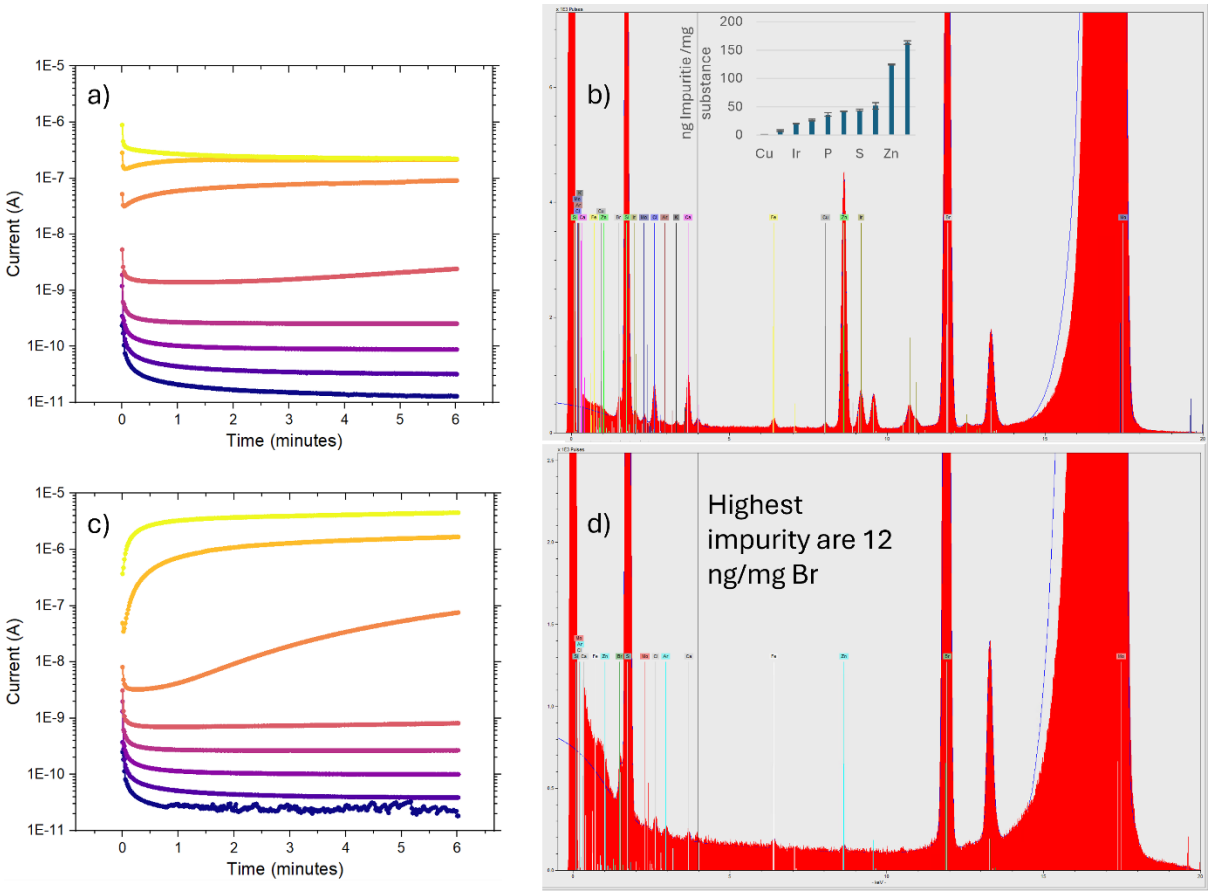

appendix Figure 6. Measured current over time at constant applied voltage for increasing temperature steps for FCH-C3-A samples of a batch with high impurity content (a) and low impurity content (c). b) and d) X-ray fluorescence data depicting the impurity concentration of the corresponding material batch. Note that the conductivity of the low impurity content batch is equal or higher than that of the high impurity content batch, ruling out that the observed conductivity is an impurity-related artefact. X-ray fluorescence data was provided by Shyamkumar Haridas.

For Total X-Ray Fluorescence analysis, a S2 Picofox (Bruker Nano GmbH, Berlin, Germany) equipped with high efficiency module and Mo X ray tube was used. Spectra were recorded at 50 kV and 600 µA over a live time of 1000 s. During measurement the system was purged with nitrogen gas (N2 5.0, mti Industriegase AG, Neu-Ulm, Germany).

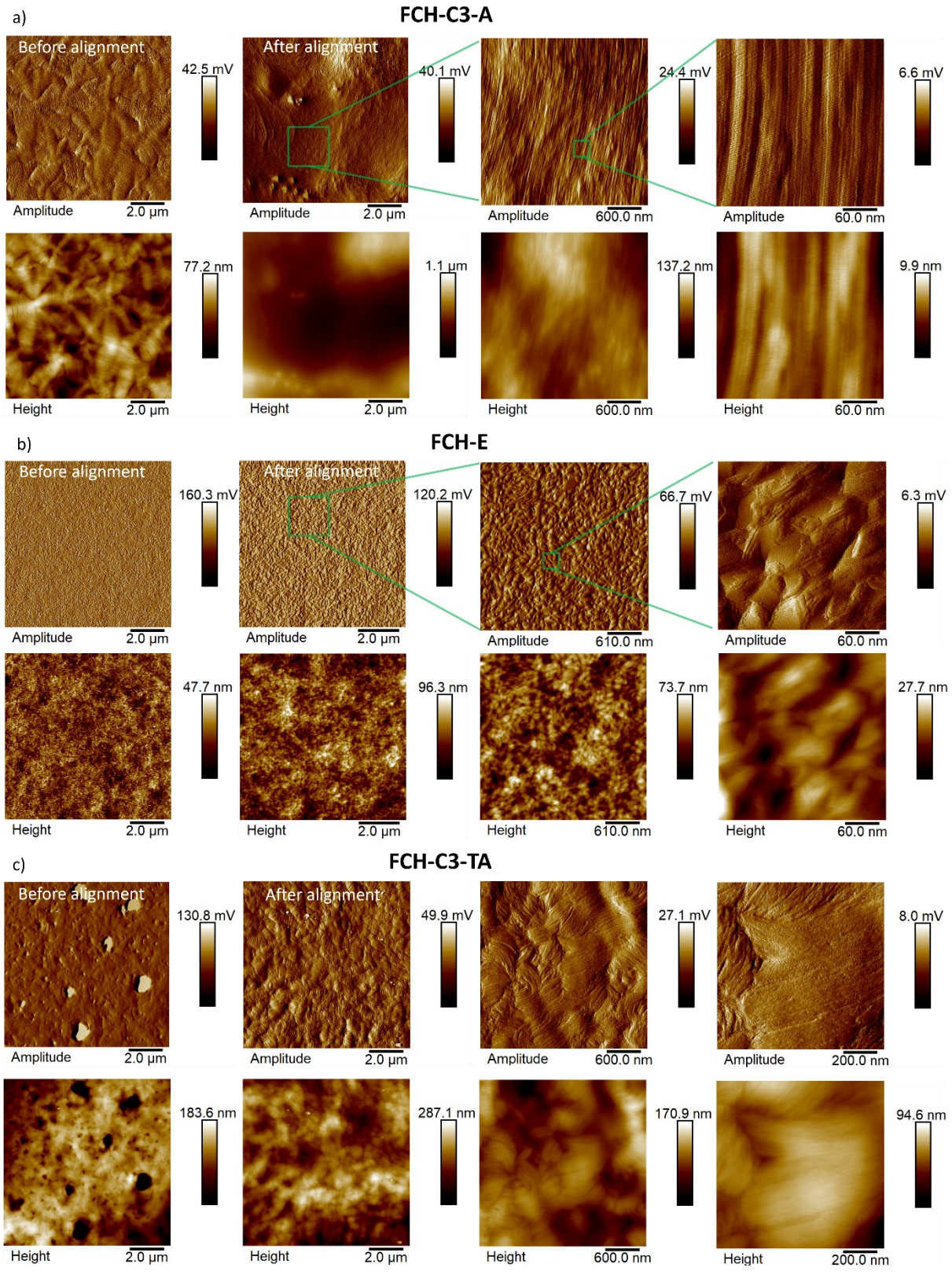

appendix Figure 7. AFM amplitude and corresponding topographic images of drop-casted and molten films before and after field annealing, for a) FCH-C3-A, b) FCH-E and FCH-C3-TA c).

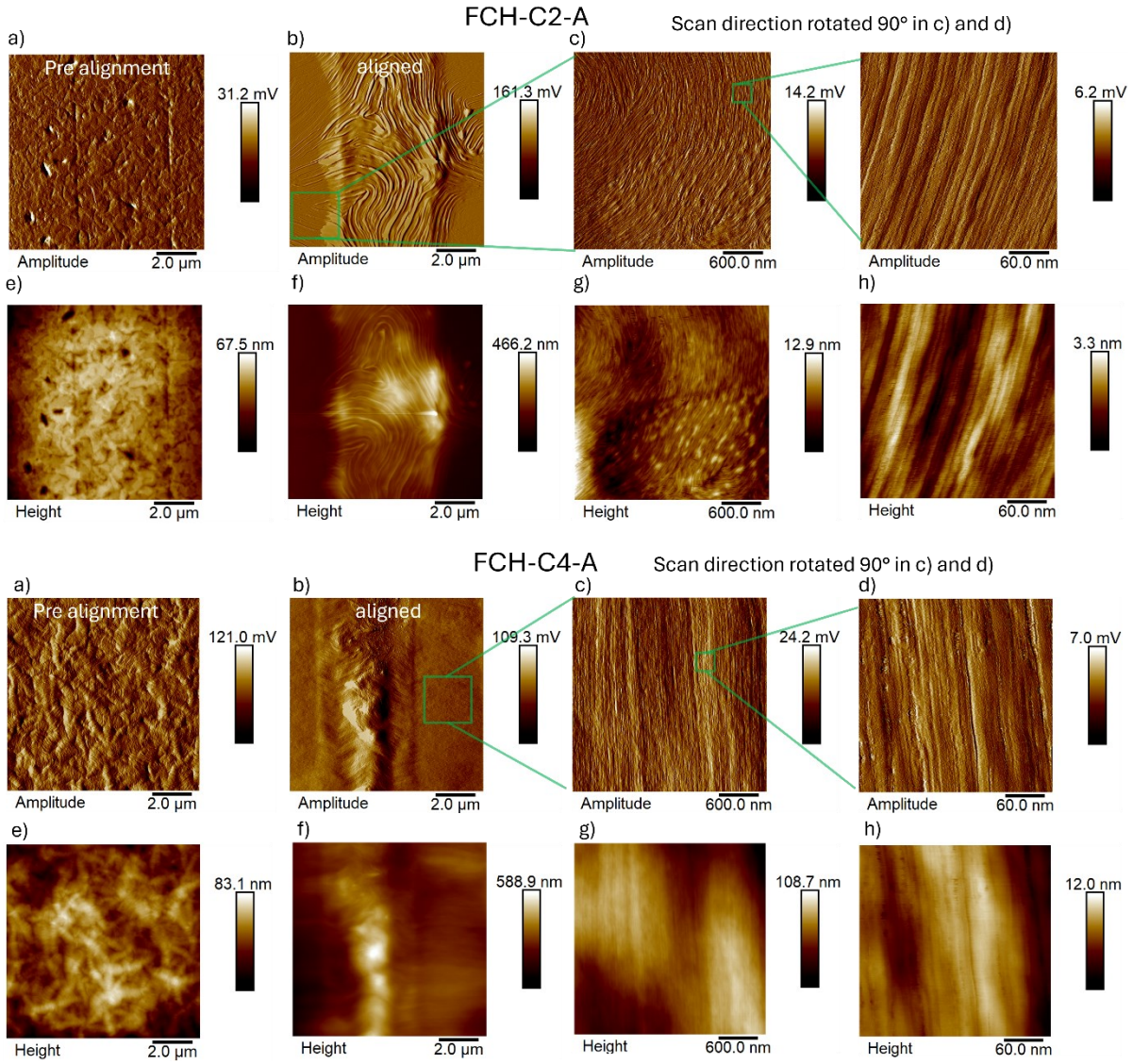

appendix Figure 8. AFM images of FCH-C2-A and FCH-C4-A. a)-d) show the height channel, e)-h) the amplitude channel. a) and e) are pre alignment, the rest are taken after field annealing. FCH-C2-A was field annealed under 20 V/µm at 120°C for an hour. FCH-C4-A was field annealed under 20 V/µm at 90°C for an hour.

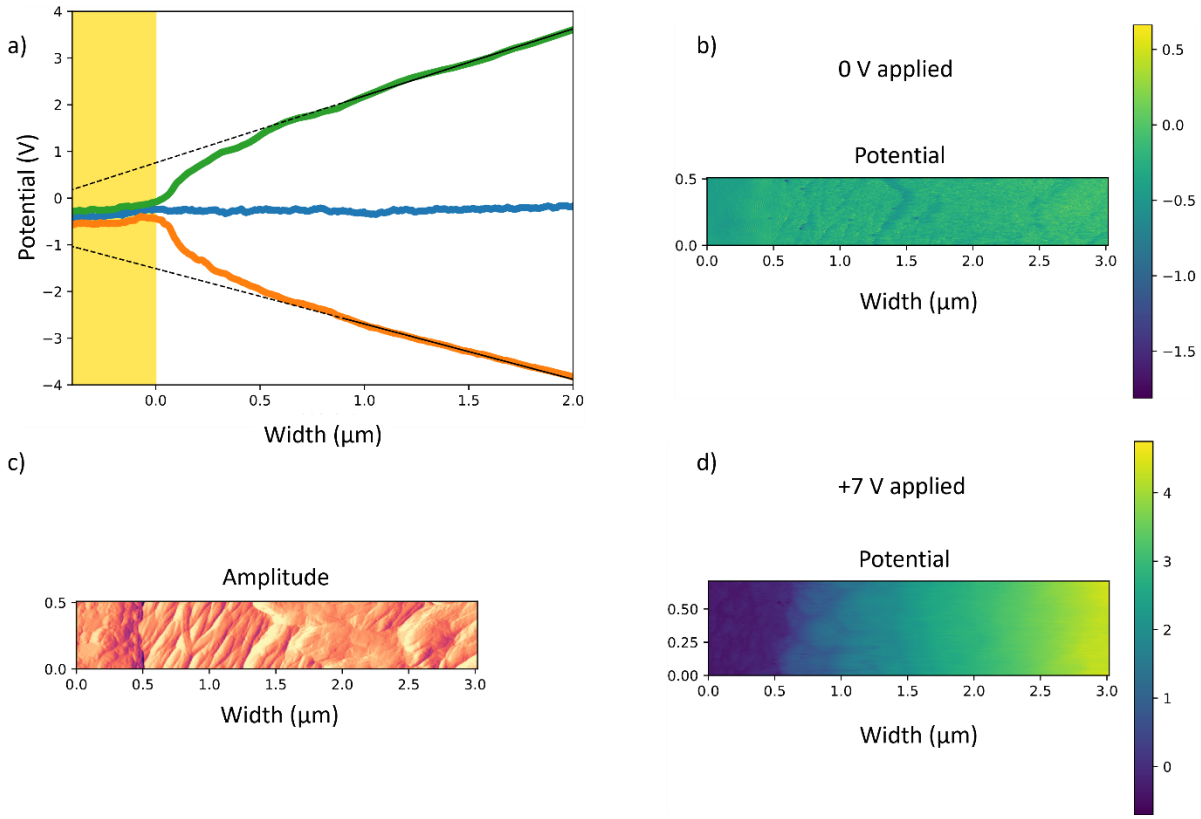

appendix Figure 9: a) shows the averaged potential against distance measured by KPFM in the vicinity of the grounded electrode for an applied bias of 7 V (green), 0 V (blue) and -7 V (orange). The black dotted lines are linear fits to extrapolate the potential step at the electrode-organic interface caused by the dipole density. in both cases a potential step of 1 V is observed. c) shows the corresponding amplitude image from which the position of the electrode was determined. b) and d) show the raw potential data of the 0 V and 7 V measurement plotted in a). KPFM images were measured by Sophia Klubertz with an Oxford Instruments Jupiter XR Asylum Research AFM.

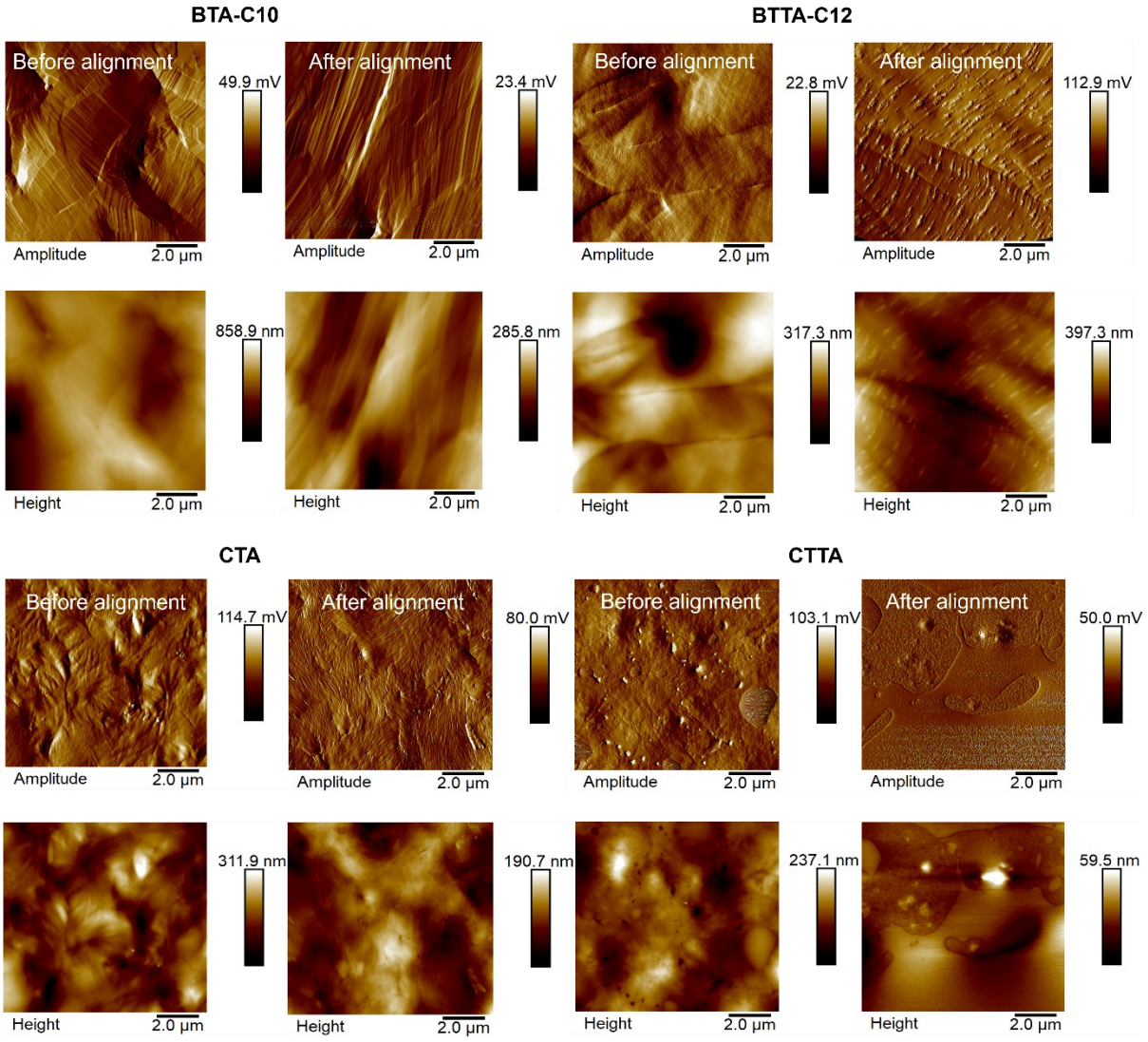

appendix Figure 10. AFM images of BTA-10, BTTA-C12, CTA and CTTA before and after field annealing.

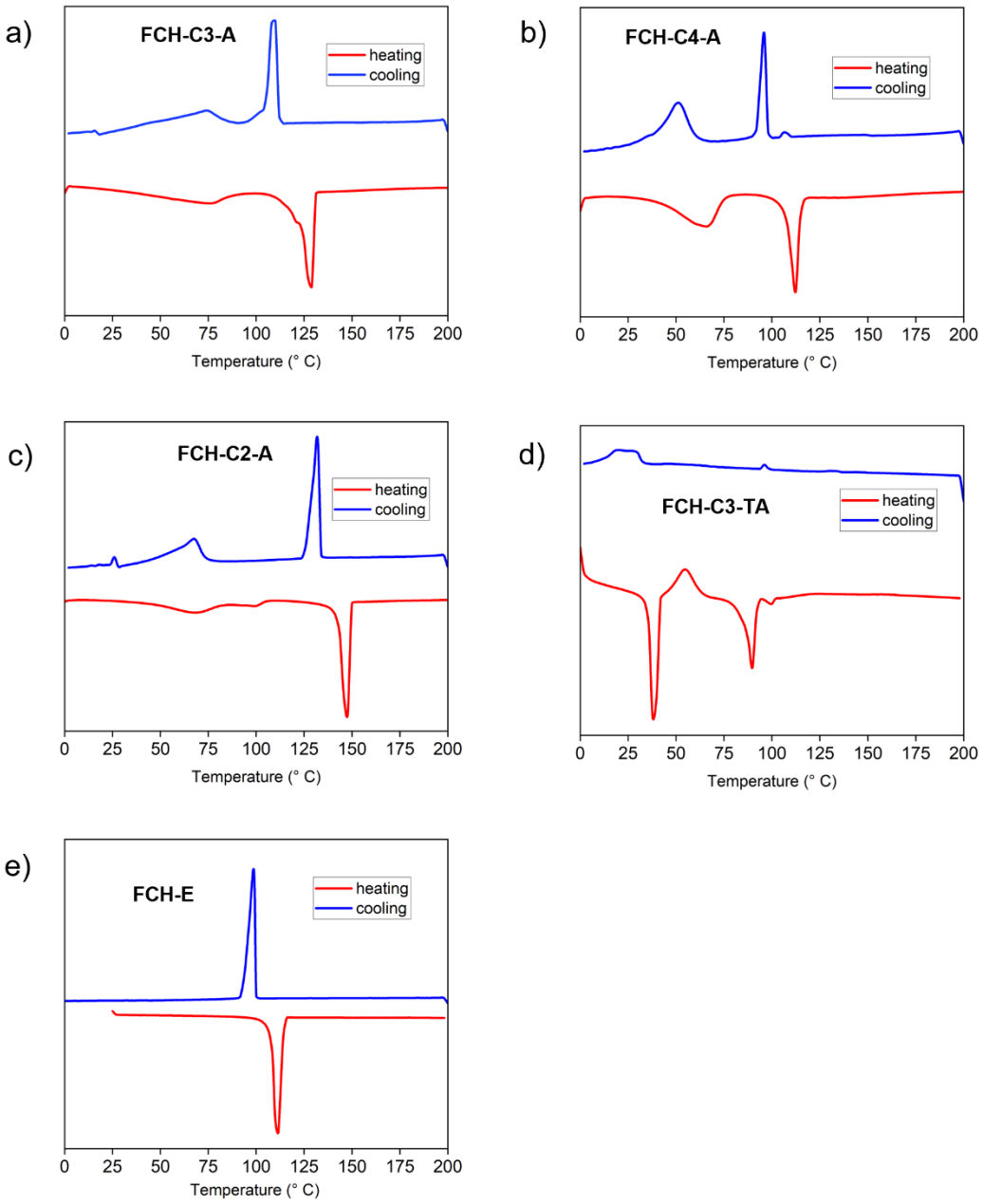

appendix Figure 11. Differential scanning calorimetry traces for all FCHs. The heating and cooling rate was 5°C/min. The large peaks are the respective melting and freezing points of the materials. The data was provided by Shyamkumar Harridas from the van Delius group at Ulm University.

DSC was conducted on a Mettler Toledo DSC 2 STARe system under nitrogen atmosphere.

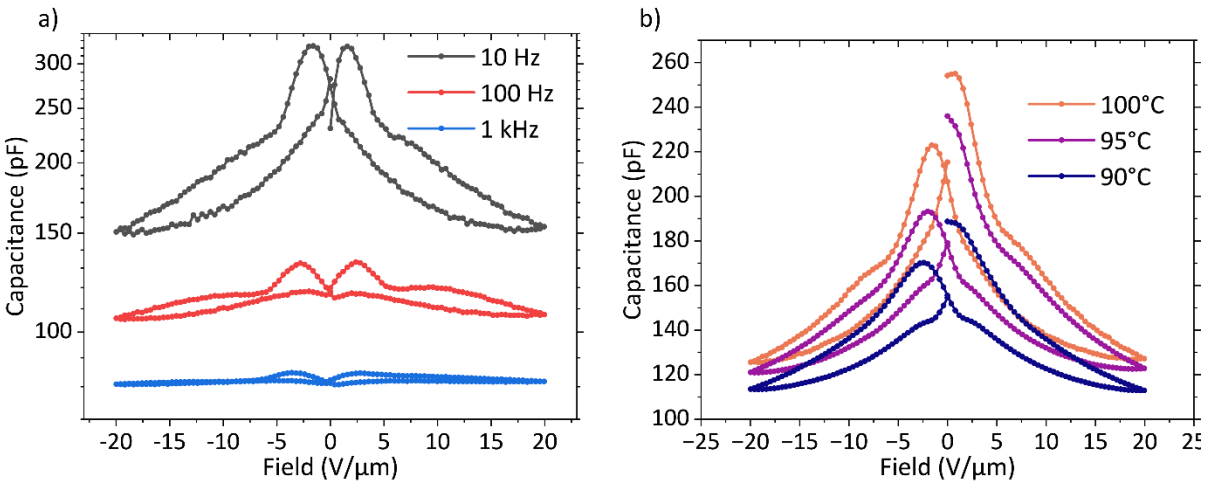

appendix Figure 12. CV measurements of FCH-C3-A. a) shows measurements at 110°C with different small signal frequencies and a small signal peak-to-peak amplitude of 200 mV/µm. b) shows temperature dependent measurements at a low small signal frequency of 10 Hz and a small signal peak-to-peak amplitude of 200 mV/µm.

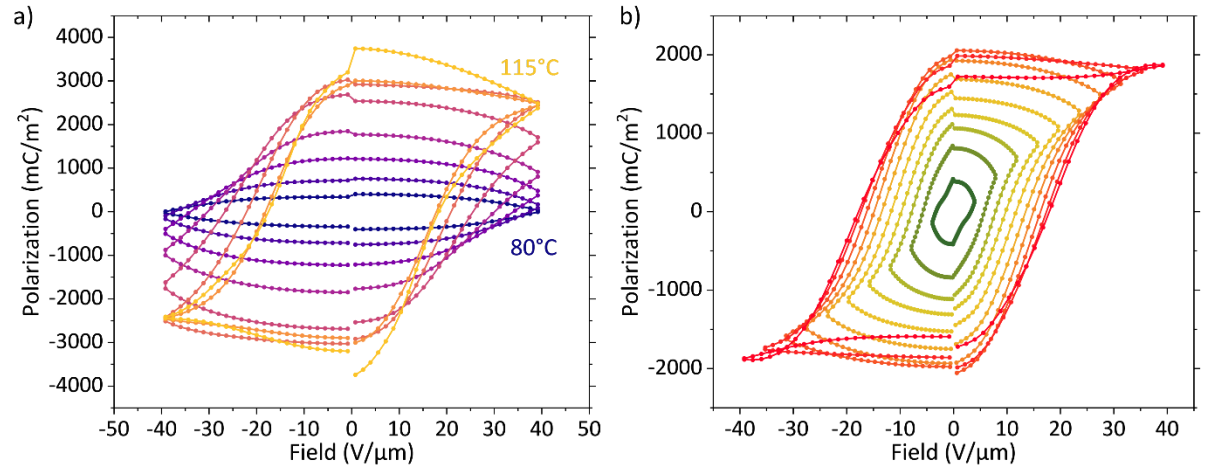

appendix Figure 13. "Polarization" hysteresis loops obtained from the DWM measurements on FCH-C3-A shown in Figure 45a) and c). While the typical high polarization values that completely exceed the theoretical ferroelectric polarization are observed, the loop growth seems to saturate or even invert for high temperatures and fields respectively. This was not commonly observed and is tentatively attributed to the onset of degradation in this specific sample.

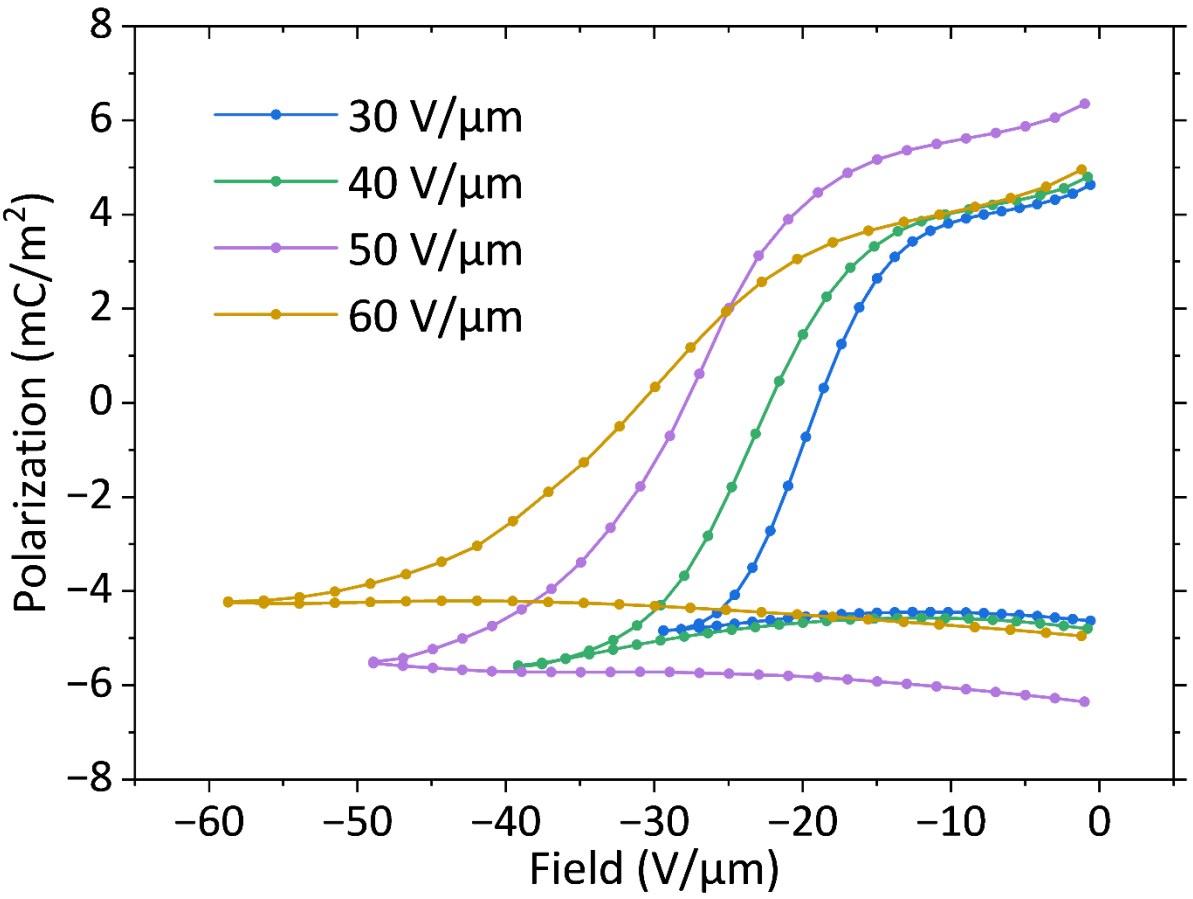

appendix Figure 14. Negative part of the polarization obtained from the maximum field dependent DWM measurements on FCH-E shown in Figure 47f), after scaling the background peaks to correct for ionic currents.

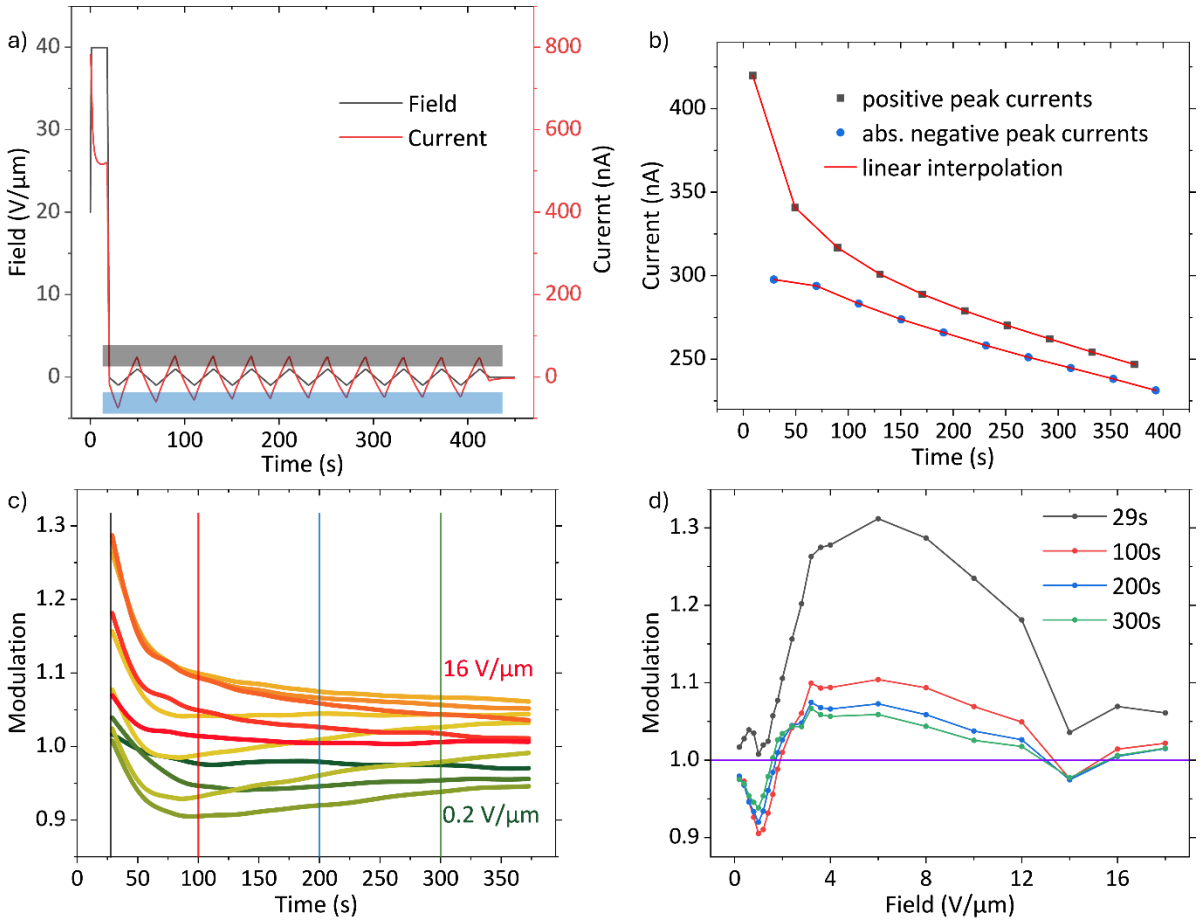

appendix Figure 15. Extrapolation of the conductivity modulation. a) shows an exemplary "zig-zag" measurement. In b) the peak currents from a) are plotted against the time and linearly extrapolated. Polynomial extrapolation would result in non-sensible behavior especially at lower fields. c) shows the modulation obtained from the extrapolated currents in b) for various fields after smoothing. The vertical lines indicate the field dependence of the modulation with the corresponding traces plotted in d). The quantitative and qualitative behavior is very similar to the modulation obtained from the peak ratios in Figure 51e).

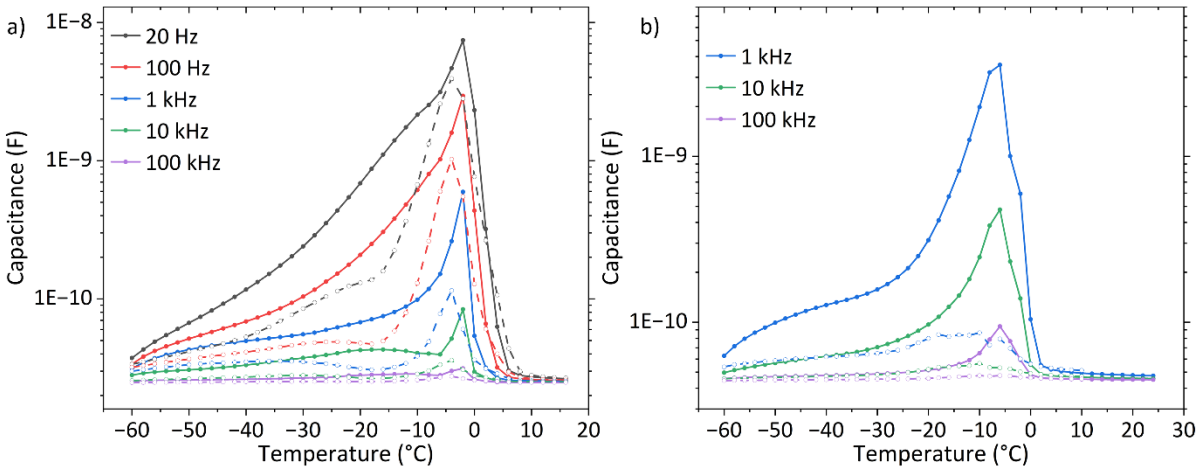

appendix Figure 16. Dielectric spectroscopy data showing measured capacitance versus temperature for various frequencies. Here, the first (solid lines) and second (dashed lines) heating traces are compared for NHTA:TCNE a) and NHTA:F4TCNQ b). The change in behavior between first and second heating, for NHTA:TCNE is only minor and attributed to small structural changes in the crystal while for the NHTA:F4TCNQ the major changes are possibly a sign of degradation. While the crystals did not significantly change in appearance, NHTA:F4TCNQ crystals were generally less stable during electric measurements. Changes in phase transition temperature (0°C to 5°C for NHTA:TCNE) were observed in a multitude of measurements in nitrogen atmosphere and for different samples, indicating that the phenomena behind the dielectric peak are rather caused by morphology changes than the freezing or unfreezing of water.

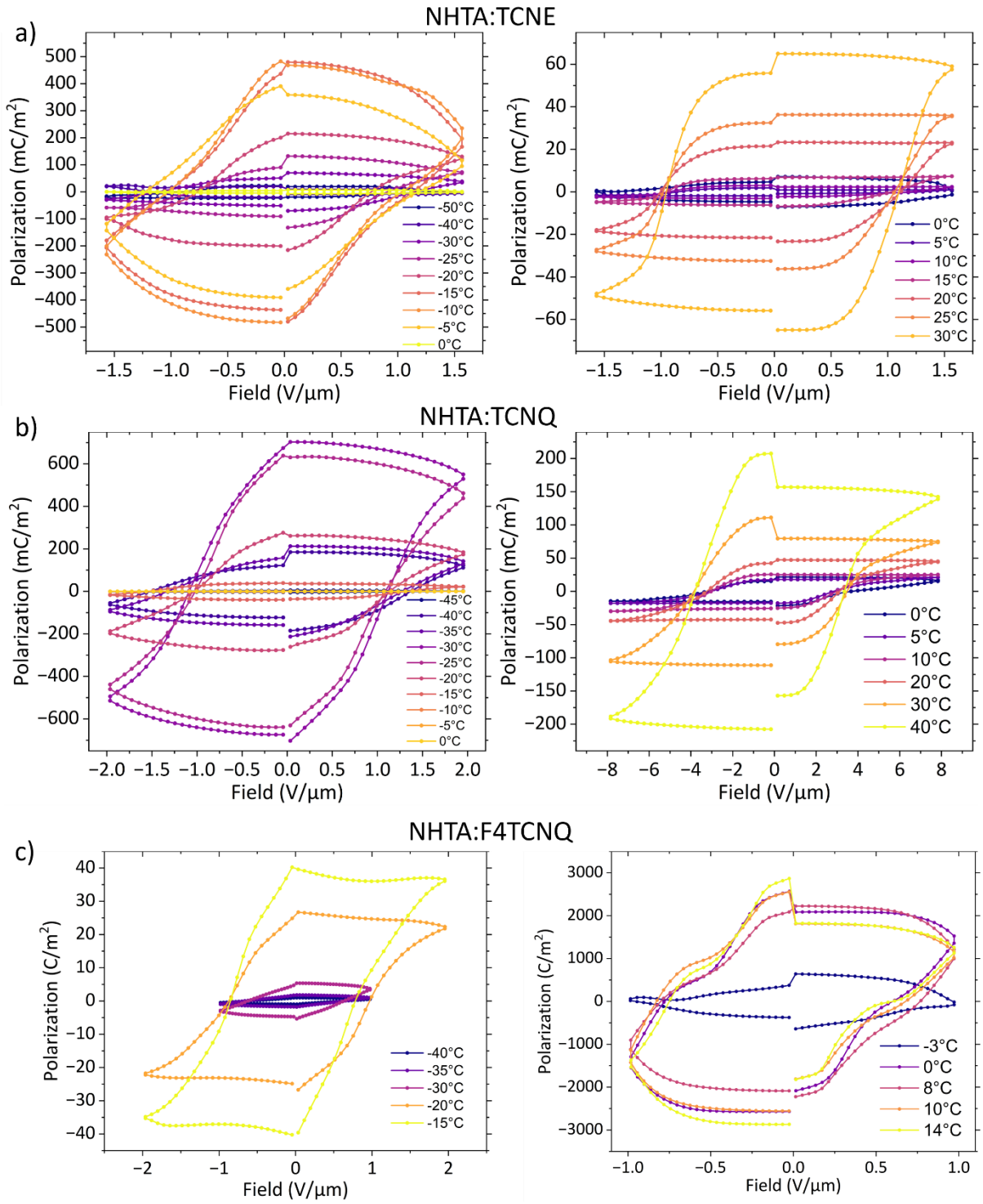

appendix Figure 17. Polarization hysteresis loops for stepwise temperature change for CTC1 a), CTC2 b) and CTC3 c). Polarization values are obtained via the DWM from the corresponding measurements shown in Figure 54.

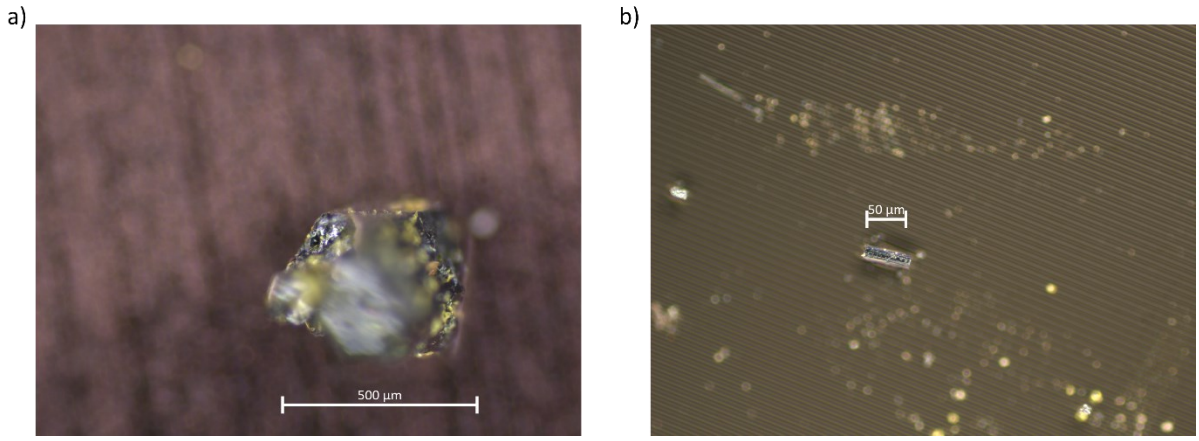

appendix Figure 18. Light microscope images of a NHTA:TCNQ single crystal a) and of a NHTA:F4TCNQ single crystal b), both placed on an IDE.

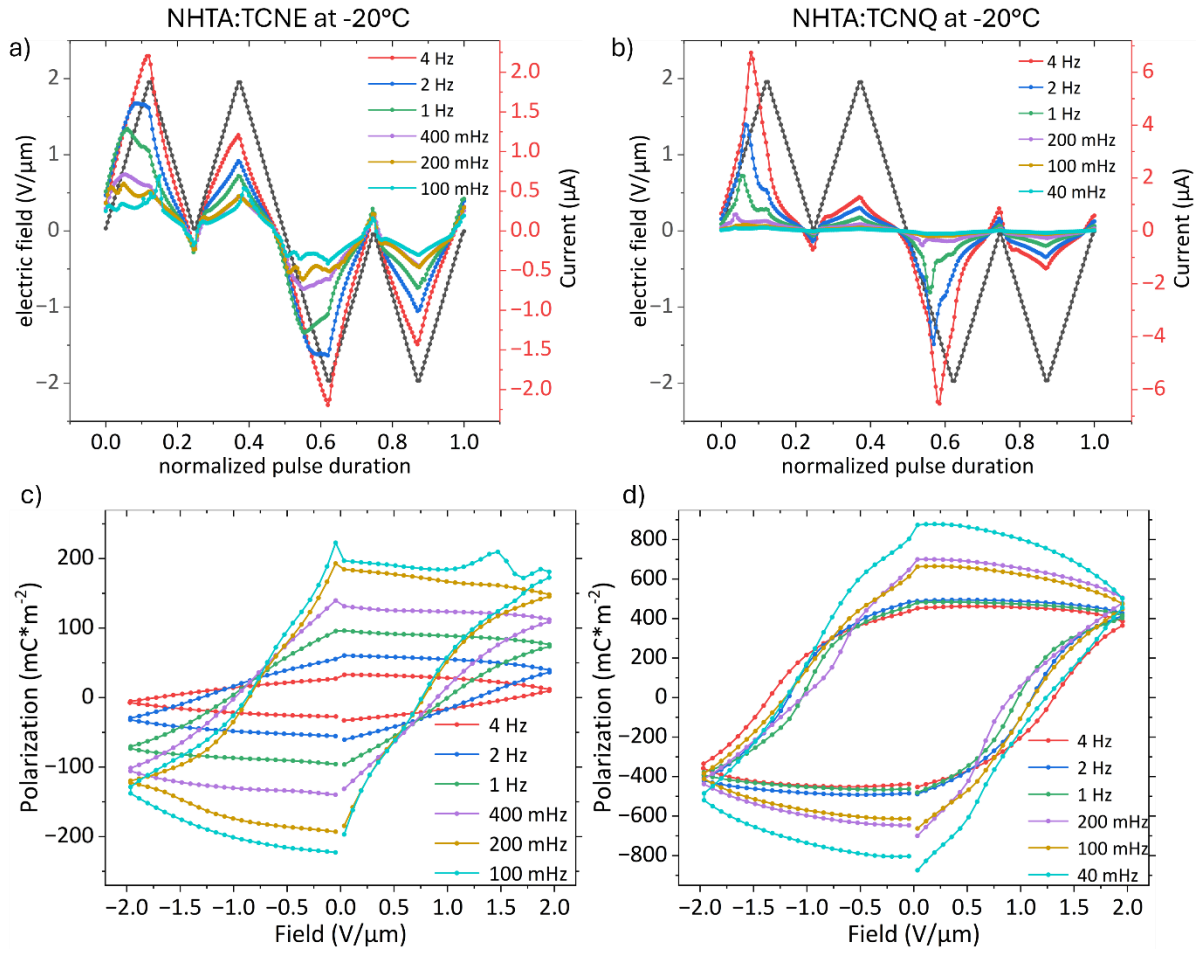

appendix Figure 19. Raw DWM data of CTC1 a) and CTC2 b) measured at – 20°C. c) and d) are the corresponding polarization hysteresis loops. In both case transient currents, presumably from ionic impurities, inflate the polarization, with the effect being stronger for CTC2. The double peak substructure for 100 mHz and 200 mHz for CTC1 is possibly caused by contributions from ferroic switching orthogonal to the main crystal stacking axis.

Tables

Material	Gaussian Disorder Fit σ (meV)	Murgatroyd SCLC Fit μ ($cm^2*V^{-1}*s^{-1}$)	Murgatroyd SCLC Fit γ ($cm^{1/2}*V^{-1/2}$)
FCH-C3-A	76 ± 2	7.9 ± 0.1 E-7 (300 K)	2.99 ± 0.03 E-3
FCH-C4-A	-	2.7 ± 0.2 E-8 (300 K)	5.7 ± 0.2 E-3
***o*-TPA-N**	59 ± 1	1.6 ± 0.1 E-9 (300 K)	5.7 ± 0.1 E-3
***p*-TPA-N**	57 ± 3	2.4 ± 0.1 E-6 (300 K)	1.1 ± 0.1 E-3
BTTA-C12	-	4.0 ± 0.1 E-7 (390 K)	6.5 ± 0.6 E-4
CTA	-	8.7 ± 0.2 E-7 (440 K)	2.2 ± 0.1 E-3

Table 1. Fit parameters from Figure 36 and Figure 37.

Fit parameter	Coercive field, low field peak
Fitted equation	$F_C(f,T) = \frac{w_\mathrm{b}}{P_\mathrm{s}} - \frac{k_\mathrm{b}T\ln\left(\frac{\nu_0}{\ln(2)\,f}\right)}{V^*P_\mathrm{s}}$
V^* [nm^3]	2.76469E-26 ± 2.51371E-27
w_b [eV/nm^3]	0.04287 ± 0.00374
Reduced χ^2	1.96481
R^2	0.97603
Adjusted R^2	0.96805

Table 2. TA-NLS fit parameters for Figure 42.

Fit parameter	Low field peak	High field peak
Fitted equation	$F_C(f,T) = \frac{w_\mathrm{b}}{P_\mathrm{s}} - \frac{k_\mathrm{b}T\ln\left(\frac{\nu_0}{\ln(2)\,f}\right)}{V^* P_\mathrm{s}}$	
V^* [nm^3]	3.31562E-26 ± 2.77957E-27	1.90526E-26 ± 1.74259E-27
w_b [eV/nm^3]	0.03316 ± 0.00258	0.06041 ± 0.0049
Reduced χ^2	0.68808	0.88153
R^2	0.97292	0.96793
Adjusted R^2	0.96615	0.95992

Table 3. TA-NLS fit parameters for Figure 43.

Fit parameter	Low field peak	High field peak
Fitted equation	$F_C(f,T) = B'/\sqrt{k_\mathrm{b}T\cdot\ln(f_0/f)}$	
B' [V/m*J$^{1/2}$]	0.00103 ± 1.68917E-4	0.00215 ± 1.44935E-4
f_0 [1/s]	3.85171 ± 0.70983	6.0853 ± 1.03532
Reduced χ^2	3.22106	1.14629
R^2	0.87324	0.9583
Adjusted R^2	0.84155	0.94788

Table 4. Du-Chen fit parameters for Figure 43.

Fit parameter	Low field peak	High field peak
Fitted equation	$F_C = C\cdot f^{\frac{d}{\alpha}}$	
C [V/m]	1.43635E7 ± 292490.96315	2.3841E7 ± 314549.03451
d	2.75614 ± 0.13545	1.6281 ± 0.07534
Reduced χ^2	0.17221	0.2076
R^2	0.99322	0.99245
Adjusted R^2	0.99153	0.99056

Table 5. KAI fit parameters for Figure 43.

Fit parameter	Coercive field
Fitted equation	$F_C(f,T) = \frac{w_\mathrm{b}}{P_\mathrm{s}} - \frac{k_\mathrm{b}T \ln\left(\frac{\nu_0}{\ln(2)\, f}\right)}{V^* P_\mathrm{s}}$
V^* [nm^3]	1.14908E-26 ± 1.22372E-27
w_b [eV/nm^3]	0.09932 ± 0.00979
Reduced χ^2	1.25488
R^2	0.95702
Adjusted R^2	0.94627

Table 6. TA-NLS fit parameters for the inset of Figure 45a).

Fit parameter	Coercive field
Fitted equation	$F_C(f,T) = \frac{w_\mathrm{b}}{P_\mathrm{s}} - \frac{k_\mathrm{b}T \ln\left(\frac{\nu_0}{\ln(2)\, f}\right)}{V^* P_\mathrm{s}}$
V^* [nm^3]	6.71374E-27 ± 3.03624E-28
w_b [eV/nm^3]	0.161 ± 0.00673
Reduced χ^2	0.20563
R^2	0.99396
Adjusted R^2	0.99195

Table 7. TA-NLS fit parameters for Figure 47.

Fit parameter	Coercive field
Fitted equation	$F_{\mathrm{C}}(f,T) = \frac{w_{\mathrm{b}}}{P_{\mathrm{s}}} - \frac{k_{\mathrm{b}} T \ln\left(\frac{\nu_0}{\ln(2)\, f}\right)}{V^* P_{\mathrm{s}}}$
V^* [nm^3]	1.21805E-26 ± 4.94948E-28
w_{b} [eV/nm^3]	0.09215 ± 0.00327
Reduced χ^2	0.06378
R^2	0.99674
Adjusted R^2	0.99511

Table 8. TA-NLS fit parameter for Figure 49d).

Fit parameter	Low field peak
Fitted equation	$F_{\mathrm{C}}(f,T) = B'/\sqrt{k_{\mathrm{b}} T \cdot \ln(f_0/f)}$
B' [V/m*J$^{1/2}$]	0.00284 ± 2.08187E-4
f_0 [1/s]	5.6716 ± 1.58293
Reduced χ^2	1.26772
R^2	0.96761
Adjusted R^2	0.95142

Table 9. Du-Chen fit parameter for Figure 49d).

Fit parameter	Low field peak
Fitted equation	$F_C = C \cdot f^{\frac{d}{\alpha}}$
C [V/m]	3.07979E7 ± 345442.5373
d	1.37726 ± 0.07597
Reduced χ^2	0.1123
R^2	0.99426
Adjusted R^2	0.99139

Table 10. KAI fit parameter for Figure 49d).

Fit parameter	CTC1	CTC2
Fitted equation	$F_C(f,T) = \frac{w_\mathrm{b}}{P_\mathrm{s}} - \frac{k_\mathrm{b}T \ln\left(\frac{\nu_0}{\ln(2)\, f}\right)}{V^* P_\mathrm{s}}$	
V^* [nm^3]	1.50596E-25 ± 4.1066E-26	2.86511E-25 ±5.81709E-26
w_b [eV/nm^3]	0.00504 ± 0.00114	0.00264 ± 0.00044
Reduced χ^2	1.72919	2.0506
R^2	0.81909	0.89092
Adjusted R^2	0.75879	0.85456

Table 11. TA-NLS fit parameter for Figure 56.

Fit parameter	CTC1	CTC2
Fitted equation	$F_C(f,T) = B'/\sqrt{k_\mathrm{b}T \cdot \ln(f_0/f)}$	
B' [V/m*J$^{1/2}$]	8.80321E-5 ± 6.50379E-6	8.29118E-5 ± 3.99155E-6
f_0 [1/s]	66.18621 ± 19.24152	98.20673 ± 14.58698
Reduced χ^2	0.50196	0.26084
R^2	0.94748	0.98612
Adjusted R^2	0.92998	0.9815

Table 12. Du-Chen fit parameter for Figure 56.

Fit parameter	CTC1	CTC2
Fitted equation	$F_C = C \cdot f^{\frac{d}{\alpha}}$	
C [V/m]	718602.87795 ± 58575.72406	634389.17253 ± 48266.81276
d	1.10548 ± 0.24886	1.18285 ± 0.16816
Reduced χ^2	1.27278	0.87081
R^2	0.86684	0.95368
Adjusted R^2	0.82245	0.93824

Table 13. KAI fit parameter for Figure 56.